Probing the Organisation and Function of Structured Starch Materials by Advanced NMR Techniques

Todor T. Koev

Biological and Medicinal Chemistry (MChem)

Thesis submitted to the School of Pharmacy, University of East Anglia in fulfilment of the requirement for the degree of Doctor of Philosophy (PhD).

October 2021

information derived there-from must be in accordance with current UK Copyright Law. In addition, any quotation or extract must include full attribution.

Acknowledgements

My PhD study at the Quadram Institute Bioscience and the University of East Anglia has been by far the best and most enjoyable period of my life to date. This journey would not have been possible without the help and support of many people, whom I would like to thank in this section of my thesis.

I am incredibly grateful and humbled by the constant support and patience my supervisors Dr Frederick J. Warren and Professor Yaroslav Z. Khimyak have shown me over the past 4 years. They have always been there for me in times of difficulty, but also in times of great joy and success. They have supported me through their vast knowledge and encouragement, as well as through their friendship and experience in all my times of need. They have shown nothing but patience when faced with my stubbornness, and have been nothing but constructive about it. But above all, I would like to thank both my supervisors for always giving me incredible amount of professional freedom, the ability to form collaborations on my own, to lead multiple projects throughout my PhD journey, and for always believing in my ability to see things through. They have been the best supervisors I could have asked for, and I feel incredibly lucky and humbled to have had them as beacons of guidance during my PhD journey.

I am forever grateful to Dr Juan Carlos Muñoz García and Dr Ignacio Delso for teaching me everything I know about NMR spectroscopy, and for making the process the most exciting of experiences. I want to also thank Juan for all the trips to the national solid-state NMR facility at the University of Warwick, and for the numerous late nights spent

at the 850 MHz spectrometer. Those were some of the most educational and transformative times of my PhD journey. I want to thank Dr Hannah C. Harris for teaching me proper aseptic technique, *in vitro* fermentation models, and also for being an indispensable friend throughout my PhD journey. I want to thank Dr Maria C. Hernández-Soriano for being a true friend, and always having nothing short of excellent advice for any conundrum of mine – be it scientific, or interpersonal. I want to also thank Jennifer McClure for being there from the very start, and for always holding me accountable for my words and actions, and for helping me be a better version of myself, even when I was a right mess. I also want to thank Dr Valeria Gabrielli for being a great companion during the late nights working in the NMR office.

I want to thank Dr Peter Ryden and Dr Louise Salt for helping me pick up *in vitro* digestion models and for always answering my many questions. I want to thank Dr Nikolaus (Klaus) Wellner and Dr Catherine Booth for teaching me all I know about IR spectroscopy, fluorescence and laser scanning confocal microscopy.

I want to thank Dr Dinu Iuga at the University of Warwick, who was always just a text message away whenever I was having difficulties with the 850 MHz solid-state spectrometer.

I also want to thank Professor Robert (Bob) Gilbert at the Yangzhou University in China, who welcomed me into his home and allowed me to use his SEC equipment when I was a visiting worker at his laboratory in China.

I also want to thank my mother who has always been there for me from the very beginning, in times of joy and misery, and has largely been supportive in most of my

endeavours. No part of this journey would have been possible without her help and support, for which I will forever be grateful.

I want to thank my partner Mr Chris A. John, who has always provided comfort and support in times of need, and who has been a great distraction when I have needed it.

Last, but not least, I want to extend my gratitude to everybody else who has been a part of my PhD journey, and has made it a memorable experience.

Abstract

Hydrogels have a complex and heterogeneous structure and organisation, making them promising candidates for applications in the biomedical, pharmaceutical and cosmetics industry. Starch is a particularly attractive material for producing hydrogels due to its low cost and biocompatibility, but the structural dynamics of polymer chains within starch hydrogels are not well understood, which has limited their development and utilisation. We employed a range of NMR methodologies to probe the structural organisation of these systems on various length scales, investigating the internal dynamics and intercomponent interactions within these heterogeneous systems. We report on a new level of structural organisation within starch gels – namely, highly dynamic solvated starch chains. Our findings provide new insights into the rationalisation of structure-function relationships governing the micro- and macroscopic properties of hydrogel assemblies.

Physiologically, starch hydrolysis by a-amylase occurs in several places in the human body and involves host's salivary and pancreatic a-amylase enzymes, as well as amylolytic enzymes of bacterial origin. There has been some research on the impact of

starch on the gut microbiota, but not much is known about the structure-function relationships governing starch hydrogels' interaction and impact on the full extent of the gastrointestinal tract (GIT).

We demonstrate a quick and easy method for the preparation of pharmaceutical excipients from easily accessible materials, and their ability to provide targeted release of orally administrable physiologically relevant small molecules in the colon, with minimal to no release in the upper GIT. Our work provides important insights into the role and function of starch hydrogel structure on its drug delivery properties, probing guest-host interactions, and elucidating starch gels' interaction with the human GIT. These insights provide important knowledge for the development of superior orally administrable targeted drug delivery systems with auxiliary physiologically relevant properties.

Table of Contents

Chapter 1: Introduction

1.1 Project Overview and Summary

1.2 Botanical Origin of Starch Granules

1.3. Starch Granule Composition, Organisation and Crystallinity

1.3.1 *Starch Granule Composition*

1.3.2 *Starch Granule Organisation and Crystallinity*

1.4. Industrial Significance and Utilisation of Starch

1.4.1 *Starch as Food*

1.4.2 *Starch in the Pharmaceutical and Biomedical Industry*

1.5. Human Gastrointestinal Physiology and *in vitro* Models of Human Digestion

1.6. Starch in the Human Gastrointestinal Tract

1.7. Hydrothermal Treatment of Starch

1.8. Starch Gel Structure and Organisation

1.9. Overall Project Objectives

Chapter 2: Materials and Methods

2.1 Materials

2.2 Methods

2.2.1 *Total Moisture Content*

2.2.2 *Total and Apparent Amylose Content*

2.2.3 *Swelling Power*

2.2.4 *Hydrogel Preparation*

2.2.5 *Differential scanning calorimetry (DSC)*

Principles

Experimental Procedures

2.2.6 *Sub-ambient DSC*

2.2.7 *Dynamic oscillatory rheology*

Principles

Experimental Procedures

2.2.8 *Powder X-ray diffraction and estimation of long range order*

Principles

Experimental Procedures

2.2.9 *Estimation of Long-range Molecular Order*

2.2.10 *NMR Spectroscopy*

Principles

Relaxation

Dipolar Coupling and Spin Diffusion

Electron Shielding Effects, Chemical Shift, and Chemical Shift Anisotropy

Solid-state Spectroscopic Techniques

High-resolution Magic-Angle Spinning (HR-MAS) techniques

Solution-state NMR techniques

Experimental Procedures

Cross Polarisation and Single Pulse Magic Angle Spinning (CP and CPSP/MAS) NMR Spectroscopy

Estimation of Short-range Molecular Order

Spectral deconvolution

Estimation of mobility

^{13}C Direct Polarisation (DP) with High Power ^{1}H Decoupling (HPDEC) NMR Spectroscopy

Water Polarisation Transfer Cross Polarisation (WPT-CP) NMR Spectroscopy

HR-MAS NMR Spectroscopy

Longitudinal Relaxation Measurements

Saturation Transfer Difference (STD) NMR Spectroscopy

Solution-state NMR Spectroscopy

2.2.11 *Simulated Digestion & Fermentation*

Enzyme Activity Measurement

Salivary α-amylase

Pepsin

Pancreatin Amylase Activity

In vitro Digestion

Oral phase

Gastric phase

Intestinal phase

Halting Digestion & Sample Collection

Quantification of Digested Starch Hydrogel

Identification of Oligosaccharides and Reducing Sugars in Starch Digesta

In vitro Fermentation

Participant Information & Ethics

Batch model colon fermentation media ingredient recipe

Faecal Sample Collection and Preparation for Inoculation

Final Fermentation Vessel Preparation and Sampling

Measurement of Total Gas Produced during Fermentation

Samples for Bacterial Metabolite Analysis

Samples for NMR structural analyses, FISH and LSCM

2.2.12 *Starch Branching Analyses*

2.2.13 *Bacterial Metabolite and Small Molecule (Drug) Release Quantification*

2.2.14 *Fluorescence in-situ Hybridisation (FISH)*

2.2.15 *Laser Scanning Confocal Microscopy Visualisation*

2.2.16 *Size-Exclusion Chromatography (SEC)*

Principles

Experimental Procedures

2.2.17 *Fluorophore-assisted carbohydrate electrophoresis (FACE)*

Principles

Experimental Procedures

2.2.18 *Statistical analyses*

Chapter 3: Structural Organisation of Starch Hydrogels

3.1 Introduction

3.2 Results and Discussion

3.2.1 *Bulk Properties of Starch Hydrogels*

Thermal properties

Mechanical Properties

3.2.2 *Molecular structural parameters, internal organisation, molecular mobility, and inter-component interactions*

Molecular Structural Parameters

Long-range ordering and Total Amorphous Contribution

Short-range order and dynamics

Role of water in hydrogel structure, organisation, and integrity

Effect of Storage Conditions on Local Mobility

3.3 Conclusions

Chapter 4: Starch Hydrogels in the Human Gastrointestinal Tract

4.1 Introduction

4.2 Materials and Methods

4.2.1 *Preparation of Drug-loaded Starch Hydrogels*

4.3 Results and Discussion

4.3.1 *Starch Hydrogel Bulk Properties & Molecular Organisation through the GIT*

Rheological Properties

Molecular Structural Parameters

Starch Hydrogel Internal Mobility

Starch Hydrogels' Viability as Targeted Colonic Drug Delivery Platforms

Commensal Bacteria's Interaction with Starch Hydrogels

4.4 Conclusions

Chapter 5: Solid-state NMR Methodology for Probing Guest-Host Interactions in Small Molecule-Complexed V-Amylose

5.1 Introduction

5.2 Materials and Methods

5.2.1 *Materials*

5.2.2 *Methods*

H_2O/D_2O Exchange

Proton-Driven Spin Diffusion (PDSD) NMR

Principle

^{1}H-^{13}C Heteronuclear Correlation (HETCOR) NMR

Principle

Experimental Procedures

^{1}H-^{1}H NOESY NMR

Principle

Experimental Procedures

Single Quantum-Double Quantum Back-to-Back (SQ-DQ BABA) NMR

Principle

Experimental Procedures

5.3 Results and Discussion

5.3.1 *V-amylose-1-naphthol ($V7_{III}$)*

5.3.2 *V-amylose-ibuprofen ($V7_{II}$)*

5.4 Conclusion

5.5 Future Work

Chapter 6: Overall Conclusions and Final Remarks

References

Appendix

Chapter 1: Introduction

1.1 Project Overview and Summary

Starch is an easily accessible, renewable, and environmentally friendly material, and a pivotal part of the human diet. Coupled with its broad range of rheological, physicochemical, and biochemical properties, starch has been extensively utilised in the food and beverage, structural, cosmetic, pharmaceutical, and biomedical industries.[1] Starch is synthesised by photosynthetic plants as their main storage carbohydrate, and is stored in seeds, rhizomes, roots, and tubers in the form of granules, featuring semi-crystalline structure and organisation. The size and morphology of starch granules is specific for each plant species, and their properties have been shown to be dependent on the plant's growth and harvesting conditions. Starch granules' internal structure and

organisation share a great degree of similarity between botanical sources, being comprised of growth rings, blocklets, and crystalline and amorphous lamellae, resulting in their semi-crystalline architecture.[1]

Starch exhibits the ability to associate into a range of semi-crystalline forms, and form a variety of hydrogels and aggregated structures as a result of a range of processing conditions. Despite its high degree of utilisation in a number of industrial processes, there are still gaps in our understanding of the structure-function links underpinning starch aggregates' physicochemical properties.

This project aimed at furthering our knowledge of how starch structure influences its ability to form hydrogels and to probe the inter-component interactions within these heterogeneous soft matter systems, governing their bulk and molecular-level properties. Furthermore, this work aimed at unravelling how the structure of starch hydrogels impacts their physicochemical properties and behaviour in the human gastrointestinal tract (GIT). We aim to achieve this using a combination of established and novel techniques, with an emphasis on solid- and solution-state, as well as high-resolution magic angle spinning (HR-MAS) nuclear magnetic resonance (NMR) spectroscopic methods. We probe starch hydrogels' structural arrangements on a range of scales – from macromolecular, to nuclear-level, and to follow the changes they experience under the influence of individual components of the GIT, such as endogenous amylolytic enzymes, as well as ones of commensal bacterial origin. This was followed by exploring starch hydrogels' viability as orally administrable drug delivery platforms, for targeted release in the large intestine, under simulated conditions, exploring the pharmacokinetic profile of a range of small guest molecules, and linking

these data to the structural changes starch hydrogels undergo as they traverse the entire length of the human GIT.

1.2 Botanical Origin of Starch Granules

Starch is the major energy storage carbohydrate in plants. Most higher plants deposit starch in their leaves, in plastids (such as chloroplasts) in the form of transitory starch, during the day to support growth during the night; and in non-photosynthetic plastids (such as amyloplasts) in seeds and vegetative storage organs, in the form of storage starch. [2]

The process of starch synthesis is widely conserved among different plant species and for the most part, involves three sets of enzymes – starch synthase enzymes (SSs), starch branching enzymes (SBs), and starch debranching enzymes (SDBs). [2] Outside of starch synthesis within the endosperm, once sucrose enters cells in the plant storage tissue or organ, it is converted to glucose 6-phosphate inside the cell's cytosol, with fructose, UDPglucose and glucose 1-phosphate as intermediates in this conversion process. Glucose 6-phosphate is transported inside the cell's plastid via the action of glucose 6-phosphate transporters, where it is converted to ADPglucose, via ADPglucose pyrophosphorylase and phosphoglucomutase. ADPglucose acts as the substrate for the polymerisation-type reaction which results in the elongation of glucan chains in the process of starch synthesis. Starch synthesis in the endorsperm of cereal crops, such as maize, occurs almost entirely in the cell's cytosol, where the synthesis of ADPglucose is carried out by a cytosolic form of AGPase, and the product of this reaction – ADPglucose, is transported into the plastid via nucleotide transporter system (Figure 1.1). [3]

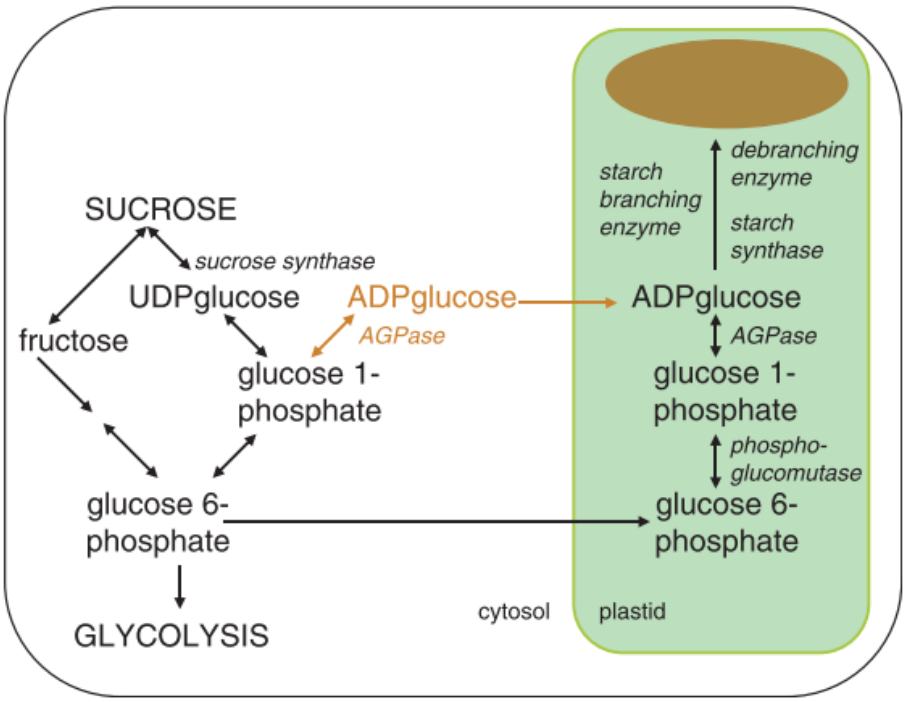

Figure 1.1: Graphical representation of the starch synthesis pathways in plant storage tissues and organs, adapted from Smith (2008). [4]

The exact mechanisms involved in the above processes are not very well understood, but the current scientific consensus is that it involves at least five different classes of SSs (SS I-IV and granule-bound starch synthase enzyme GBSS), and two classes of both SBs and SDBs.[5–8] SS IV has recently been linked to starch granule initiation.[9] GBSS has been linked to synthesis of amylose directly inside the developing starch granule, where it is outside of the reach of SBs. Amylopectin synthesis, on the other hand, is largely dependent on the action of SSs, where SS I synthesises short (up to degree of polymerisation, DP, of ≈10) chains, which are then elongated by the action of SS II and III [10] The α(1-6) branching in amylopectin molecules involves the action of SBs, which have been shown to cleave existing α(1-4) linkages and translocate them to a donor site by forming α(1-6) glycosidic bonds. Proper amylopectin synthesis further involved the

action of α(1-6)-specific SDBs (*a.k.a*. isoamylases I-II), which allow for the cleavage of mislocated and/or misshaped amylopectin branches. [2,11–18]

Unlike the relatively well-understood pathways involved in the synthesis of individual amylose and amylopectin molecules, there are still gaps in our knowledge on the mechanisms responsible for the complex architecture of starch granules, from nucleation to propagation and growth. [2]

1.3. Starch Granule Composition, Organisation and Crystallinity

1.3.1 *Starch Granule Composition*

Native starches from most botanical sources contain 15–30% amylose and 70-85% amylopectin, with the ratio of amylose being slightly higher in pulse starches, compared to tuber ones. The amylose and amylopectin content has also been shown to vary greatly, depending on individual cultivars, with some mutant species containing essentially 100% amylopectin (*e.g.*, waxy maize and waxy potato) and other ones containing up to 80% amylose (*e.g.*, amylomaize, Hylon VII®, Hi-Maize® and Gelose 80). The two polysaccharides comprise up to 98–99% of the dry weight of native starch granules, with the remainder being predominantly surface and internal lipids [19,20], proteins (both loosely associated storage proteins, and granule-associated proteins) [21], esterified phosphates and trace minerals (of up to 0.1% of the overall weight of granules), all of which can have an impact on the functional properties of the given starch. [22–25] Out of all of these, quantitatively, lipids have the most significant impact on starch granule organisation and properties, such as the granule's susceptibility to α-amylase digestion being influenced by the formation of amylose-lipid complexes, resistant to amylolytic degradation. [26–33]

Amylose is a predominantly unbranched structure made up of 600-6000 glucose units, linked primarily through α(1-4) bonds, resulting in an average molar mass of up to 10^5–10^6 g mol^{-1} (or Da). [19,27] The size of the largely linear polymer is more often reported as its degree of polymerisation (DP) than as molecular weight, with the exact size varying between botanical sources and growing conditions. Generally, amylose has a number-average degree of polymerisation (DP_n) of 1,000 – 10,000 units and weight-average degree of polymerisation (DP_w) of 1,000 to 7,000, forming a structure composed of 3–12 chains, with an average chain length (ACL) of 200–700 glucosyl residues per molecule. [19,27] Less than 0.5% of the glucose units in amylose molecules feature α(1-6) linkages, giving rise to amylose's characteristic highly linear overall architecture (Figure 1.2). [27,28]

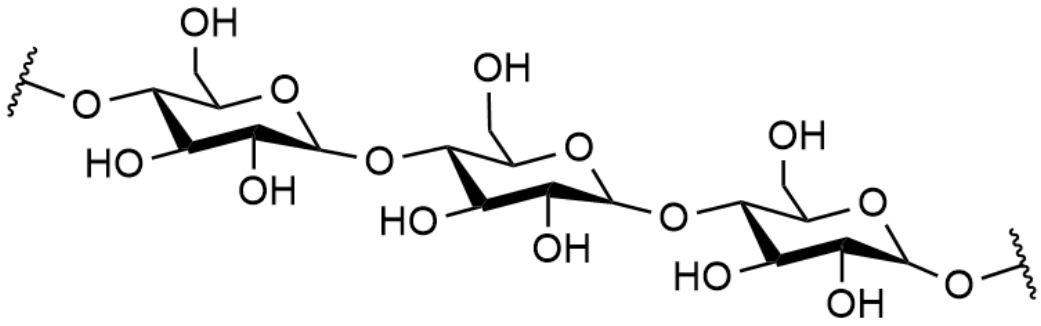

Figure 1.2: Structural representation of part of the linear amylose polysaccharide, with the anhydroglucose monomers given in the chair conformation.

It has been demonstrated that amylose chains in native granules are organised predominantly in single helical and random coil conformation, with only a small fraction involved in the formation of double helices. [29,34,35] Solubilised amylose has been documented to be able to form parallel packed, left-handed double helices, which organise in a V-type amylose helical packing when complexed with predominantly hydrophobic moieties. The V-type organisation and dimensions have been shown to

differ slightly depending on the complexing guest molecules, which are located within the hydrophobic core of V-amylose helix. [36] It has also been shown than this amylose organisation can also form without the presence of a complexing agent under the correct crystallisation conditions. [37] The most well-documented V-type amylose complex is the one formed in the presence of iodine, which gives rise to a complex with a characteristic deep blue [38,39], resulting from the alignment of iodine in the amylose helical groove, facilitating a change in the relay of electrons within the polyiodide ions (usually in the form of I^-_3). Other common complexing ligands are short- and medium-chain fatty acids, flavour compounds and alcohols. The formation of these V-type complexes has been suggested to be driven by the lower stability of the amylose single helical structures, compared to the stability of the complexes. [40]

Cross-sectional studies of starch granules of various botanical origin have shown that the concentration of amylose increases towards the edge of the granule, with the peripheral molecules exhibiting lower CL values, compared to the ones observed in the granular centre, making the former easier to be leached out than the latter during hydrothermal treatment of starch (more on starch processing further down). [41,42] In light of these observations, it has been hypothesised that the shorter CL amylose molecules located predominantly near the surface of granules are in single helical conformation, whilst the greater CL ones near the centre of granules are in double helical one or in further association with amylopectin molecules. [34]

Amylopectin is the other major component comprising the starch granule, with a highly branched architecture. It features multiple α(1-6) bonds (up to 5% of its total number of

glycosidic linkages, Figure 1.3), with the location and length of branches exhibiting great variability, depending on botanical source. [27,29,43]

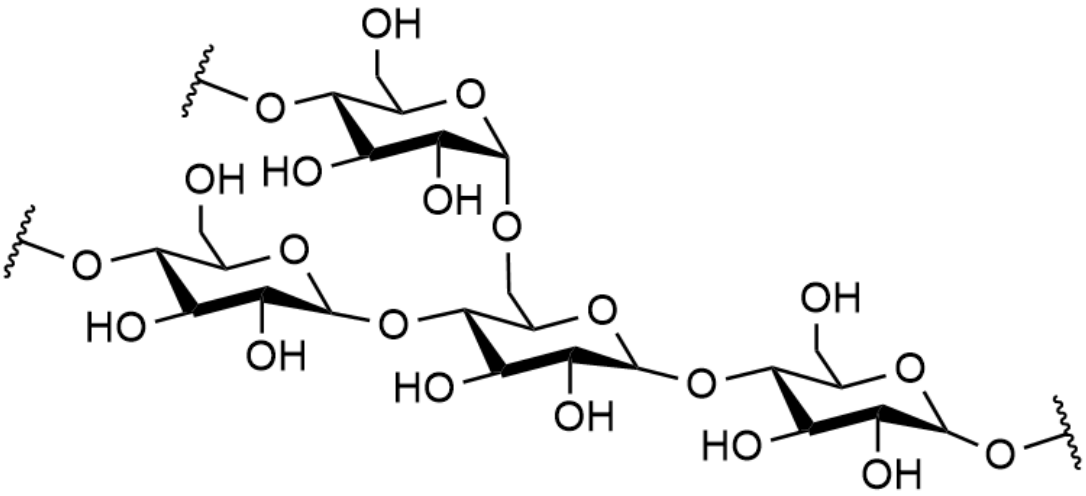

Figure 1.3: Structural representation of part of the branched amylopectin polysaccharide, with the anhydroglucose monomers given in the chair conformation.

Compared to amylose, amylopectin is a much larger molecule, with a much greater DP_w of up to and sometimes exceeding 1,000,000, DP_n of 4,800–15,000, molar mass as high as 10^7–10^9 g mol^{-1}, and ACL of only 18–29 glucose residues. [44–46] It has been shown that the ACL amylopectin molecules in high-amylose starches, such as amylomaize, Gelose 50 and Gelose 80 can be unusually high. [47–51]

The currently accepted model of the amylopectin architecture is based on the early works of Hanashiro *et al*.[52], which pointed towards amylopectin having a cluster-type (or tree-like) organisation with several longer chains and many more shorter chains branching out of them.

The amylopectin chains can be broadly divided in two types – short, containing 6–36 residues and long chains, made up of more than 36 residues. Amylopectin chains may also be classified according to their pattern of substitution, where A chains are unsubstituted, B chains are substituted by other chains, and there is a single C chain (per amylopectin molecule), structurally similar to B-type chains, carrying the reducing end (*a.k.a.* the 'backbone', Figure 1.4)[27,53,54]. The majority of A chains have been shown to form the external branches, whilst B ones – both external and internal chain regions (termed B_1 and B_2, respectively), with external ones having greater ACL, compared to internal chains. The external chains, A and B_1 have been documented to be able to form double helical structures within starch granules, which impacts on the crystallinity type of starch granules (A- B- or C-type crystallinity,). [19,29]

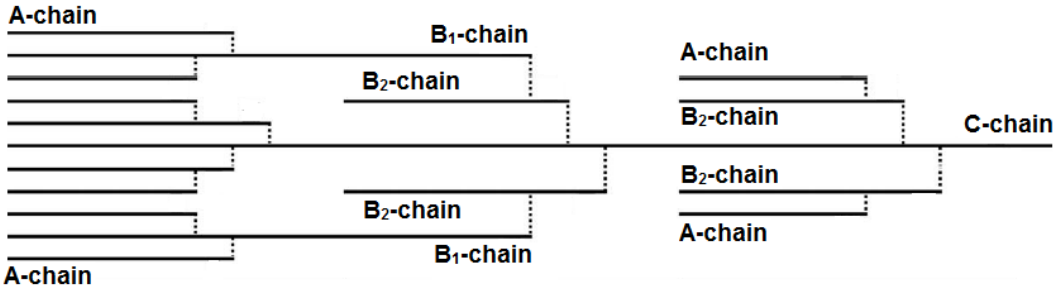

Figure 1.4: Schematic representation of the amylopectin polysaccharide featuring its characteristic α(1-4)- and α(1-6) linkages, with its characteristic nomenclature, adapted from the works of Hizukuri and Bertoft *et al*. [53,55]

According to synchrotron radiation X-ray microdiffraction data on the granular morphology of starches, the amylopectin double helices in crystalline lamellae are not uniform in directionality, but instead are radially oriented, *i.e.*, they are perpendicular to the granular surface.[56] Interestingly, advanced molecular modelling simulation techniques have pointed towards the energetic stability and feasibility of certain

internal chain length (ICL) values of amylopectin to lead to the folding of the molecules onto themselves, resulting in a parallel-type double helical structure. Such observations have led to the notion that some ICL may have a significant impact on the degree of local crystallinity within starch granules, and that CL and amylopectin branching pattern have a determining effect on the physicochemical properties of the starch in question. [34]

1.3.2 *Starch Granule Organisation and Crystallinity*

Native starches can be broadly classified in accordance with their predominant crystallinity pattern, as observed under powder X-ray diffraction (PXRD), *i.e.*, A-, B-, C-, or V-type (Figure 1.5), where A-type is largely observed in grains, B-type – in tubers and high-amylose grain mutants, and C-type – exhibiting characteristics of both A- and B-type – in pulses. [57] These crystalline patterns have been shown to be arising largely from the association between the external branches (A and B_1, Figure 1.4) of several amylopectin molecules. [43,58]

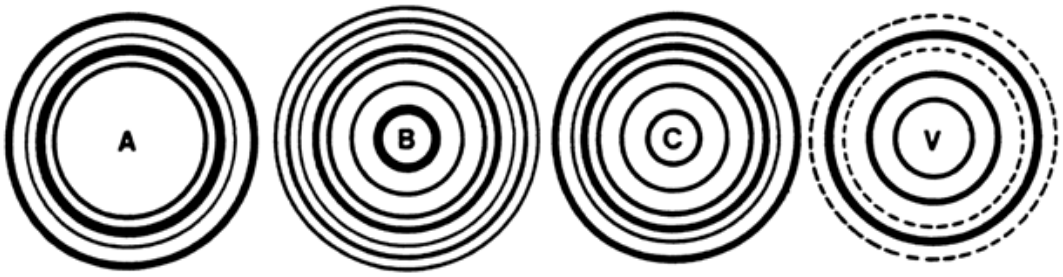

Figure 1.5. A-, B-, C- and V-type powder X-ray diffraction patterns from starch granules, adapted from the works of Zobel *et al.* [59]

A-, B- and C-type crystalline polymorphs vary in their space group types and unit cell dimensions, resulting in differences in the internal density of their helical arrangement. The A-type allomorph unit cell has a *B2* monoclinic space group and dimensions of a = 2.083 nm and b = 1.145 nm; and B-type has a $P6_1$ hexagonal space group and unit cell

dimensions of a = b = 1.851 nm (Figure 1.6). V-type crystallinity arises largely from amylose chains forming parallel packed, left-handed double helices, which organise in a unique helical packing, the dimensions of which differ from the above three crystalline polymorphs. [40]

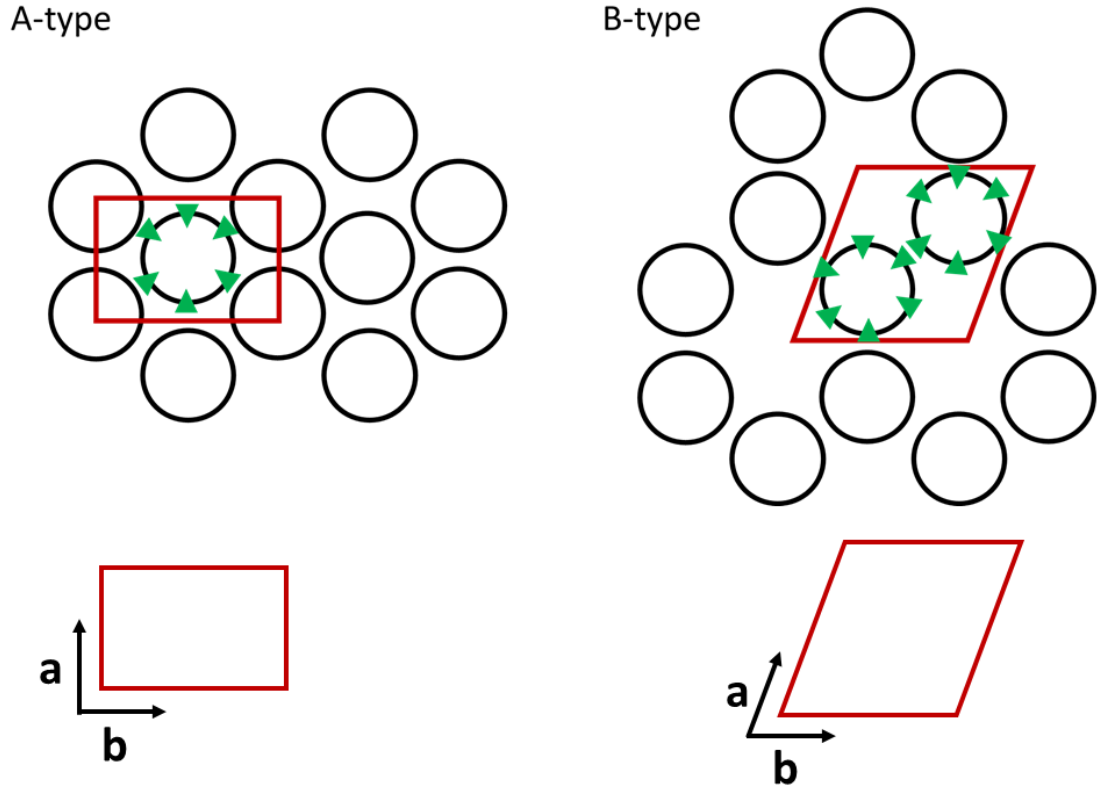

Figure 1.6: Visual representation of the double helical packing organisation of A- and B-type crystalline polymorphs, with the unit cell dimensions (a and b) underneath.

These differences lead to the double helices in the A-type polymorph being more compactly organised, whilst the B-type ones are more open, featuring a hydrated helical core (Figures 1.6 and 1.7), where the former contains 8 and the latter – 36 water molecules per unit cell, respectively.[19,29,60,61] Furthermore, the double helical organisation in A-type starches has been shown to adopt a two-fold packing symmetry, giving rise to three distinct residues per helical turn, whilst B-type starches have been shown to exhibit a three-fold packing symmetry, producing two residues per turn. The

C-type polymorph can be expected to have intermediate density of packing, given it features structural elements of both A- and B-types.[58,62,63]

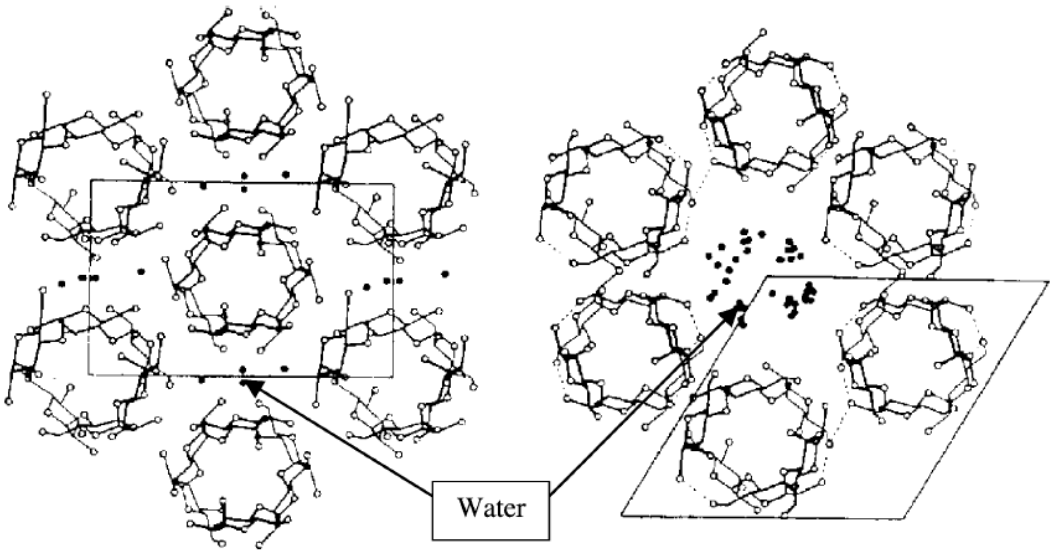

Figure 1.7: Visual representation of the double helical packing in the A- (left) and B-type (right) crystalline polymorphs in starches, adapted from the works of Tester *et al.*[19]

It is established that short-range order structures, such as glucan double helices, associate into long-range order organisations (*i.e.*, crystallites). [57] Native starches exhibit a great variability in their degree of long-range order (*a.k.a.* crystallinity), with typical values ranging from 15 to 45%, with lower levels being symptomatic of high-amylose starches, such as amylomaize, Hylon VII, Hi-Maize[64], whilst higher levels being characteristic of high-amylopectin ones, such as waxy maize. This has served as the basis for the hypothesis that amylose plays a role in the disruption of crystallinity established through the association of amylopectin molecules. It is important to note, however, that this correlation between glucan composition and long-range order lacks linearity, where two starches with comparable amylose content may have different degree of crystallinity. [65–67] Aside from their crystallinity, starch granules have further been shown

to vary in their degree of short-range order (with some botanical species exhibiting 20-25% crystallinity have been shown to possess 35-45% short-range order), as probed by ^{1}H-^{13}C CP/MAS NMR, suggesting that not all helical arrangements in starch granules are organised into crystallites (Table 1.1). [64,65,68]

Table 1.1: Crystalline and molecular order of native starch granules, adapted from the works of Gidley and Cooke. [65]

Botanical Source of Granule	Crystalline Order (%)	Molecular Order (%)
Wheat	20	39
Normal Maize	27	43
Waxy Maize	24	40
Potato	28	48
Tapioca	24	44

Starch granules exhibit a hierarchical structure, defined by a collection of concentric layers (*a.k.a.* growth rings) of progressively increasing diameter, growing out from the granule centre (*a.k.a.* the hilum) and in the direction of the granular periphery (Figure 1.8).

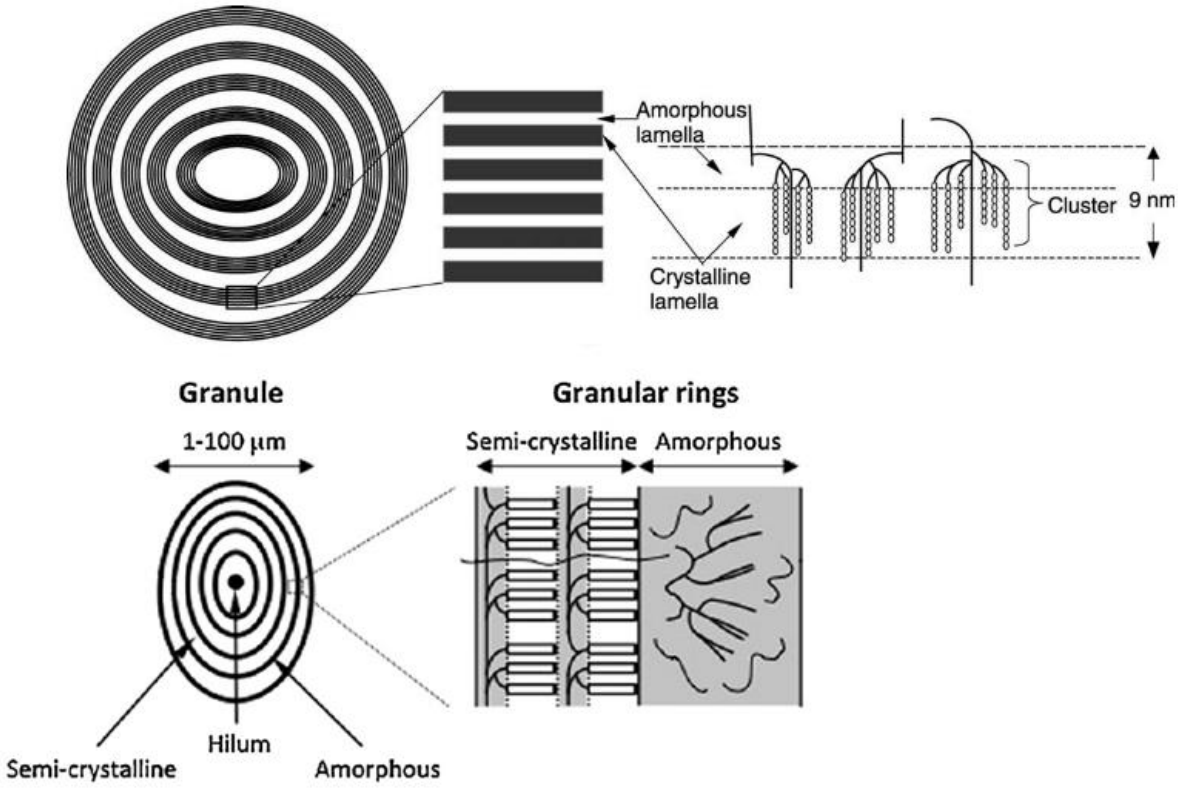

Figure 1.8: Graphical representation of the starch granule (left), featuring its centre of growth (a.k.a. the granular hilum) and its characteristic alternating semi-crystalline and amorphous growth rings (right), adapted from the works of Donald *et al.*[69], Buleon *et al.*[70] and Vamadevan and Bertoft. [29]

At present, there are two largely accepted models of the internal granule organisation – the cluster model and the building block model (Figure 1.9).[1]

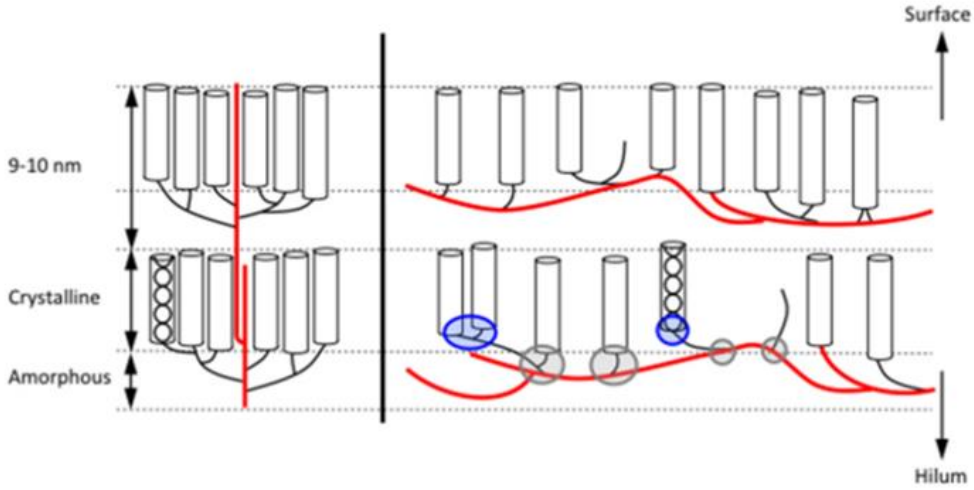

Figure 1.9: Amylopectin organisation within the semi-crystalline growth rings in starch granules, according to the cluster model (left), and the building block model (right). Adapted from the works of E. Bertoft. [1]

Across both models, it is generally accepted that the hilum is predominantly of amorphous nature. The growth rings are typically 100–400 nm in thickness and are comprised of multiple successive areas of increased (*i.e.*, semi-crystalline) and decreased (*i.e.*, amorphous) density. The semi-crystalline growth rings are organised in a lamellar fashion (9-11 nm in thickness, as evidenced by small angle X-ray scattering, SAXS), where the crystalline layers are primarily comprised of chains of amylopectin packed into a crystalline lattice, and the amorphous layers – predominantly of amylopectin branching points, along with disordered amylose and amylopectin molecules (Figure 1.9). [34,71] It has been shown, however, that effectively amylose-free starches, such as waxy potato and waxy maize, also possess the aforementioned amorphous regions, indicating that in those cases – it is amylopectin that is the primary composite of these regions. [29,72] The two models are somewhat similar, where the primary difference lies in that in the cluster model, the longer amylopectin chains which

interconnect the shorter ones organised in clusters, traverse the border between the amorphous and crystalline lamellae, whereas according to the building block model, the longer amylopectin chains are exclusively localised within the amorphous lamellae. [1]

Data obtained from AFM, SEM and other non-microscopy analyses suggests that there is an intermediate semi-crystalline arrangement existing in-between the aforementioned growth rings and amylopectin lamellae. Asymmetric individual blocklets (Figure 1.10) with diameter ranging from 20 to 500 nm (depending on the botanical source of the starch) and axial ratio of approximately 2.5:1, have been documented to exist in both the semi-crystalline and amorphous granule rings, with smaller blocklets (20–50 nm in diameter) being located primarily in the amorphous growth rings and larger ones (50–500 nm in diameter) – in the semi-crystalline rings.[34,60,73–75] These observations have given rise to another model – the blocklet model of Gallant *et al.*, which is compatible with the previous two models described. According to the blocklet model, starch granules are made up of blocklets, where larger blocklets form the semi-crystalline (*i.e.*, hard) layers, and smaller blocklets – the amorphous (*i.e.*, soft) layers of the granule. Blocklets, in turn, are made up of interchanging amorphous and crystalline lamellae, similar to the previous two models (Figure 1.9).[1,34,56,76–79]

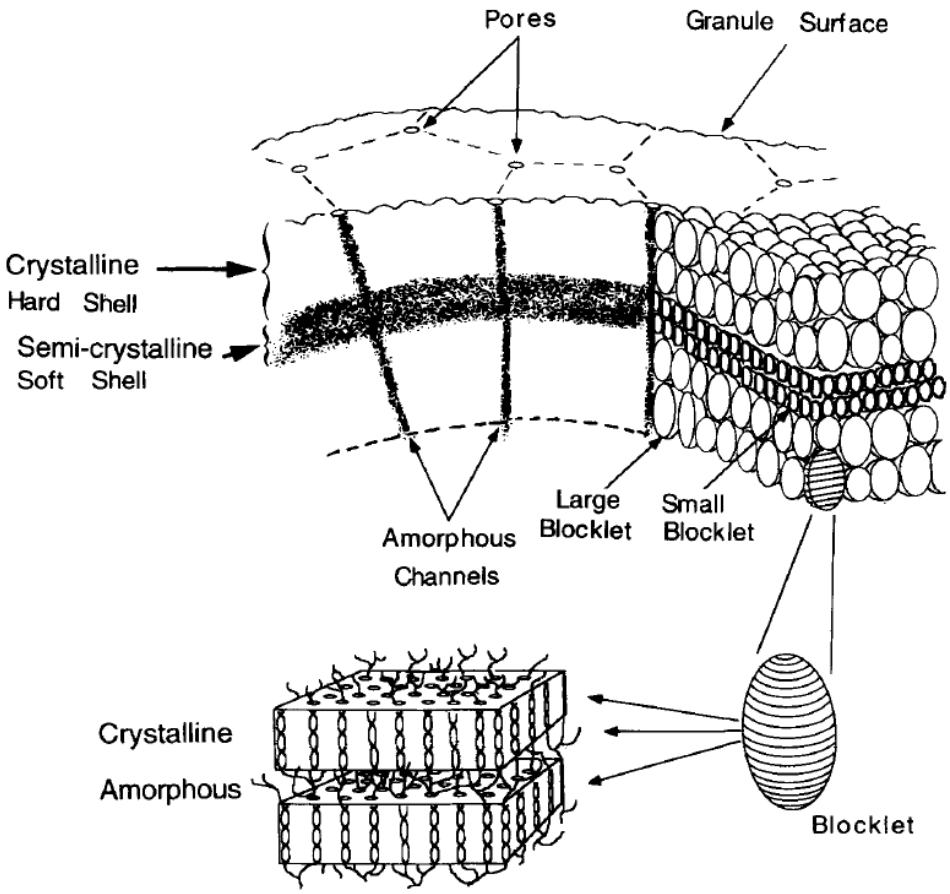

Figure 1.10: A graphical representation of the blocklet model of starch granule organisation, adapted from the works of Baldwin *et al.* [76]

Another model proposed by Waigh *et al*.[80], is based on the smectic to nematic to gel transitions in liquid crystals. This model accounts for evidence obtained by SAXS, SANS, DSC and ^{1}H-^{13}C CP/MAS NMR spectroscopy, as well as AFM and SEM. According to the side-chain liquid crystalline (SCLC) model of starch, amylopectin molecules in the amorphous regions of granules act as spacers, which link helical crystallites into cluster units (*a.k.a*. mesogens). On hydration, these spacers gain flexibility, which allows for alignment of helices and increase in overall crystallinity, which is in agreement with the observations of Bogracheva *et al*.[57,81] on starch crystallinity at various hydration levels. The SCLC model also accounts for the phase transitions between nematic, smectic and

gel states, on hydrothermal treatment of starch (Figure 1.11). This is a two-stage process in the presence of excess water, which commences with the slow dissociation of helices in a side-by-side fashion, followed by helical unwinding.

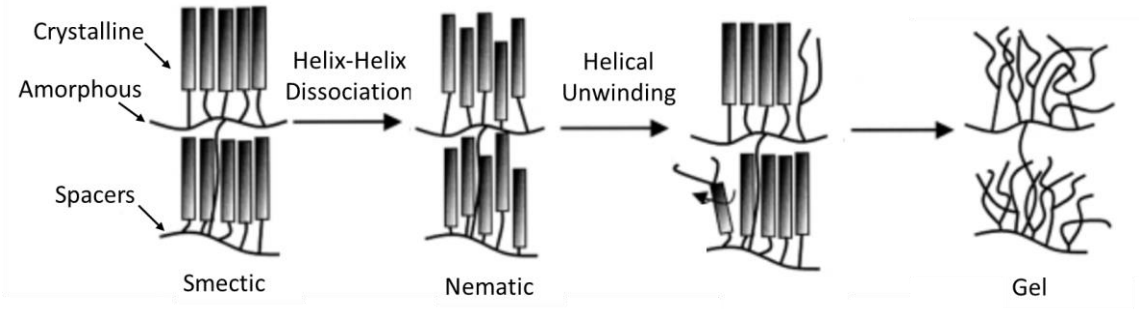

Figure 1.11: Side-chain liquid-crystalline model of starch and the structural transitions it undergoes on hydrothermal treatment. Adapted from the work of Waigh *et al.* [80]

1.4. Industrial Significance and Utilisation of Starch

1.4.1 *Starch as Food*

Starch is one of the most important components in our diet, as well as being used in a wide range of biomaterials. It serves as a fundamental energy reserve in higher plants and is of great significance to human nutrition and health. Providing an easily metabolised source of glucose, starch is a pivotal food macronutrient contributing 50–70% of the average caloric intake in Western populations, and up to 90% of the caloric intake in populations in developing countries.[82] Historically, it has played a fundamental role in human evolution and societal development, as an easily farmable and available agricultural source of energy.[83–86]

As a fundamental macronutrient in our diet, metabolism of starch is of great scientific interest, due to its numerous health consequences and possible medicinal applications. Over the past several decades, there has been an undeniable increase in food-related

diseases, such as type 2 diabetes mellitus, cardiovascular disease (CVD), coronary heart disease (CHD), obesity and others, largely due to the increased availability of rapidly digestible foods, contributing to irregular glycaemic response (the blood glucose and subsequent insulin spike, following ingestion of sugary foods) across populations from developed countries.[87–92] This, along with factors, such as the world's increasing population, rising competition for arable land, standards of food quality, climate change, and the need for new renewable functional materials have served as a driving force for the need to increase the efficiency and quality of food production.[93] This, however, requires increasing and improving our knowledge and understanding of the structure–function relationships of major food constituents of the modern day human diet. Around 60% of the global annual production of starch is utilised in the food industry for the manufacturing of a variety of food items, such as baked goods, confectionery, sauces and soups, snacks, fat replacers, coffee creamers, baby food, meat and beverage products; and 40% – in the pharmaceutical, agricultural, paper, textile, oil and structuring material industries (biodegradable bioplastics, cement, adhesives, building materials).[27,94–97] Despite being synthesised by all higher plants, starch for the purposes of food, is largely sourced from a small selection of crops, such as maize, wheat and tapioca, and to a lesser extent – rice, barley, sorghum, mung bean and potato.[47,98]

Even though the primary purpose of starch in the food industry is for the production of starch-based good, such as breads, pasta and cereals, starch is also extensively utilised as an additive for its functional impact on food properties, such as gelling and pasting. It is a common ingredient in soups, sauces, low-fat foods (as a fat replacer), spreads and dressings, due to its texture- and flavour-enhancing capacity. For these purposes, starch is often subjected to chemical modification (most often in the form of esterification and

cross-linking) in order to improve some of its desirable physicochemical properties, such as decreasing its susceptibility to syneresis.[47,98]

1.4.2 *Starch in the Pharmaceutical and Biomedical Industry*

Starch has also found a wide range of applications in the pharmaceutical and biomedical industries, primarily due to its green sourcing, biocompatibility, biodegradability, hydrophilicity, swelling, gel- and film-forming capacities, digestibility by human GIT enzymes, and relatively straightforward derivatisation.[99] Starch has been extensively used in numerous drug delivery vehicles, predominantly in its native and esterified states and in a combination with other carbohydrate polymers (*e.g.,* carboxymethylcellulose and hydroxypropyl methylcellulose[100], pectin[101], gums[102]), which have been shown to offer good *in vivo* excipient performance. By modifying factors influencing starch's swelling capacity and hydrophilicity, pharmaceutical companies have been using starch in a host of roles, such as a binder, disintegrant, matrix-former and encapsulating material, in the design of drug delivery matrices with superior pharmacokinetic properties.[103] Physical (*e.g.*, thermal, hydrothermal, pressure) and chemical (cross-linking, functional group introduction and interconversion) modifications for pharmaceutical and biomedical uses are aimed at attaining the optimal starch excipient structure possessing desirable functions, depending on the mode of drug administration, distribution, and metabolism, *i.e.*, transdermal, respiratory, gastric, intestinal, or colonic. For example, amorphous spheres have been used in the administration of aviscumine – a type II ribosome-inactivating N-glycosidase used for its ribotoxic properties on the 28S ribosomal subunit in the treatment of melanoma-related neoplasias[104]; and more crystalline, gastro-resistant forms of starch have been cross-

gelled with pectin, guar gum, methacrylic and polylactic acid, and employed as sustained release solid dosage forms (SDF) with targeted drug distribution and metabolism in the small and large intestine.[101,105–107] Furthermore, starch in its native, gelatinised and retrograded forms has been employed in the pharmaceutical formulation of topical creams, emulsions and suspensions for transdermal delivery of physiologically active molecules.[108]

There are many other industrial applications of starch, such as its use as a bulking agent and in the formulation of adhesives in the paper and packaging industries[109,110], with other uses in the textile and building materials industries detailed elsewhere.[111]

1.5. Human Gastrointestinal Physiology and *in vitro* Models of Human Digestion

In order to develop functional foods with health-promoting properties and next generation, highly tailored orally administrable drug delivery vehicles, it is important to have a detailed understanding of the human GI physiology. The human upper GIT can broadly be divided into three stages: the oral stage, characterised by mastication and salivary amylase; the gastric stage – featuring gastric peristalsis, gastric pepsin and lipase; and the small intestinal stage – featuring pancreatic enzymes (amylase, trypsin, chymotrypsin, lipase) and bile salts.[112]

Animal models (most often porcine[113]) and *in vitro* methods of upper GIT digestion are arguably the most advanced current tools for understanding the physicochemical changes foods and drug delivery platforms undergo as they travel through the human GIT.[114] There are several types of *in vitro* methods of upper GIT digestion, which can broadly be classified into two categories – dynamic and static, where these differ predominantly in the enzyme/substrate ratio and pH, where these are constant in the

static models, and change in the dynamic models. Both models have been shown to be of great utility in the food and pharmaceutical industries.[114–116] Unlike the dynamic models of *in vitro* digestion, which often require complex and expensive equipment, static models are relatively straightforward and require minimal setup. At present, the most widely accepted method of adult human upper GIT digestion is the INFOGEST method[112], which involves mimicking all three stages of the human upper GIT in succession (Figure 1.12), with enzyme activities, enzyme and electrolyte concentrations, pH and substrate transit times all defined on the basis of existing *in vivo* physiological data.[114] The method involves mixing the substrate with buffered electrolyte solutions with set pH (simulated salivary fluid, SSF, pH 7; simulated gastric fluid, SGF, pH 3; and simulated intestinal fluid, SIF, pH 7, Figure 1.12) in succession, and GI enzymes, mimicking the transit of foods and pharmaceutics from the oral cavity to the small intestine.

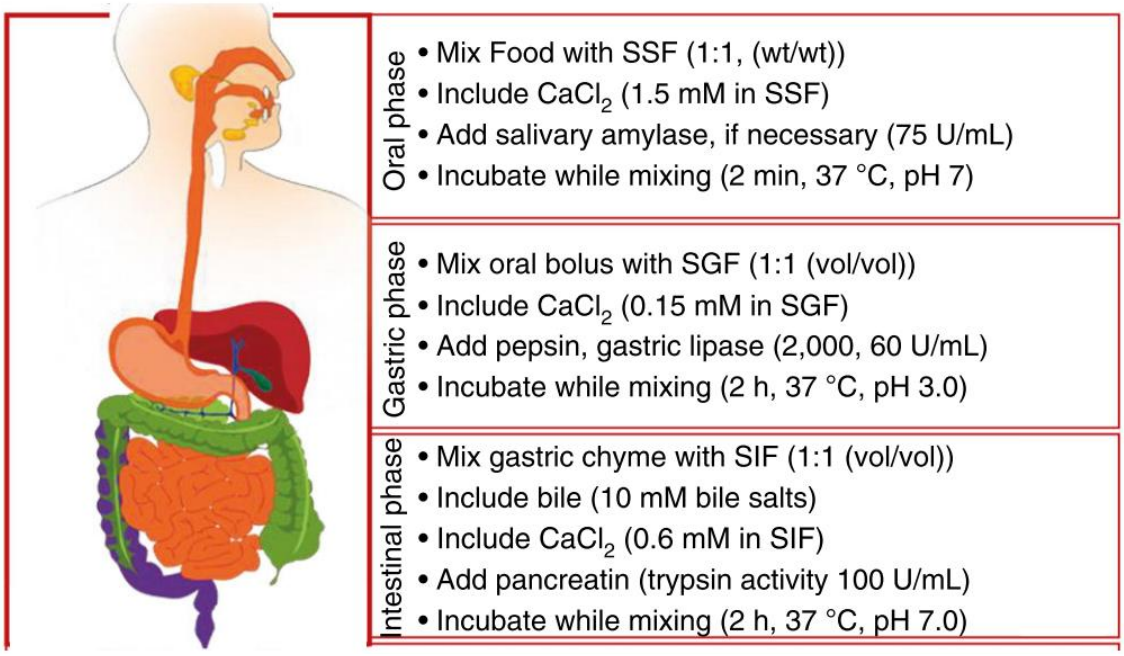

Figure 1.12: Overview of the INFOGEST method of upper GIT *in vitro* digestion. Adapted from Brodkorb *et al*. (2019).[114]

1.6. Starch in the Human Gastrointestinal Tract

Across the upper human GIT, starch is exposed to the cumulative action of human salivary and pancreatic α-amylases, as well as α-amylolytic enzymes of commensal bacterial origin in the colon. α-Amylases (*a.k.a*. glycoside hydrolase clan H, family 13, GH-13) are the primary starch hydrolysing enzymes throughout the mammalian world. In most mammals, there are three isoforms of α-amylase produced – salivary, as well as two forms of pancreatic α-amylase, which are structurally very similar.[117] Salivary α-amylase provides initial partial cleavage of starch into shorter oligomers. Some starch hydrolysis may continue in the gastric phase (*i.e.*, stomach) of the human GIT, prior to reaching the small intestine, where it is extensively hydrolysed by pancreatic α-amylase in the small intestinal lumen. The resulting mixture of oligosaccharides diffuses through the brush border membrane, where additional α-glucosidase enzymes degrade the products of starch digestion into glucose, which is transported to the blood stream by specific glucose transporters.[118]

The α-amylase family has a $(\beta/\alpha)_8$ barrel (*a.k.a*. triose-phosphate isomerase, TIM) catalytic domain, defined by a symmetrical arrangement of eight inner parallel β-strands, surrounded by eight α-helices. Whilst there is little homology strictly conserved across the entire amino acid sequence of mammalian α-amylases, most share a high degree of similarity of their super-secondary (folded) protein structure, made up of three domains – domain A and B, stabilised through a divalent Ca^{2+} ion, along with a more loosely associated domain C. Most mammalian α-amylases have a highly conserved amino acid sequence comprising their substrate binding and catalytic sites, defined by 7 amino acid residues – Asp96, His101, Arg195, Asp197, Glu233, His299 and

Asp300, with Asp197, Glu233 and Asp300 comprising the catalytic triad (Figure 1.13).[119–121]

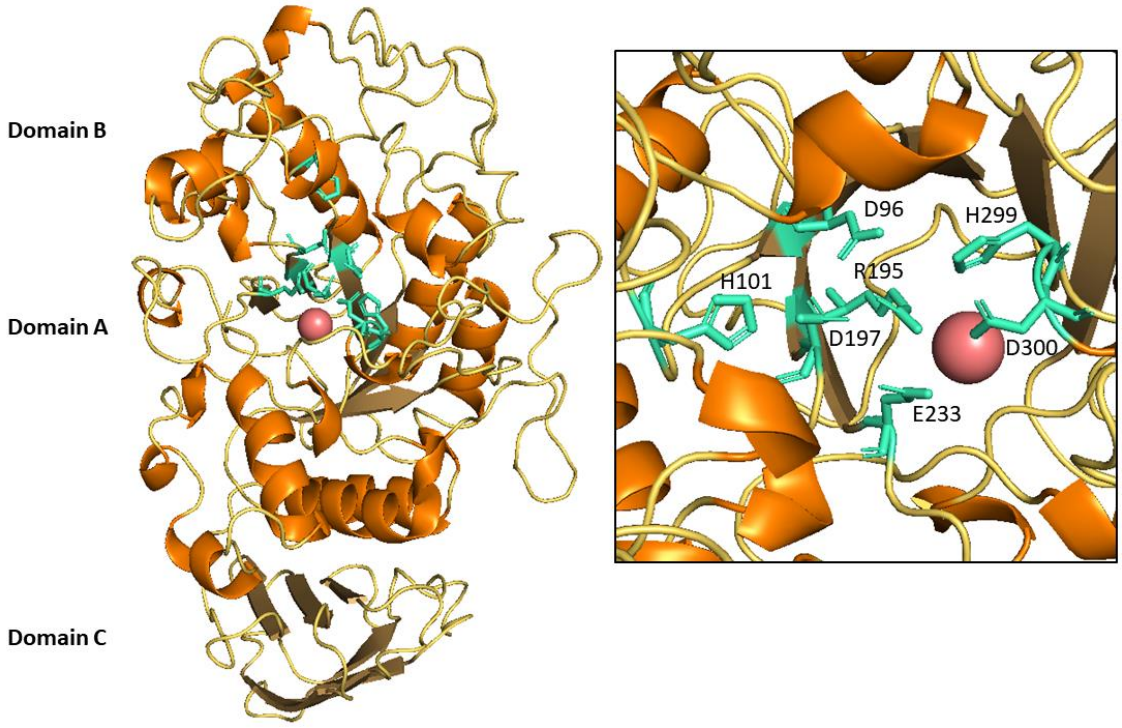

Figure 1.13: Human pancreatic α-amylase structure (1hny, PDB) with orientation towards the active site into the $(\beta/\alpha)_8$ barrel domain, with the amino acid residues involved in the catalytic hydrolysis and substrate binding shown in teal, the catalytic Cl^- shown in pink, α-helices shown in orange, β-sheets in brown, and loops in yellow. Inlay showing a close-up version of the active pocket. Visualised using PyMOL software package.

The catalytic activation in α-amylases is an example of acid-base catalysis. It is facilitated by a deprotonation of a hydroxyl residue in the catalytic pocket by Cl^-, facilitating a nucleophilic attack by aspartate and glutamate, forming a covalent intermediate (Figure 1.14).[117,122,123]

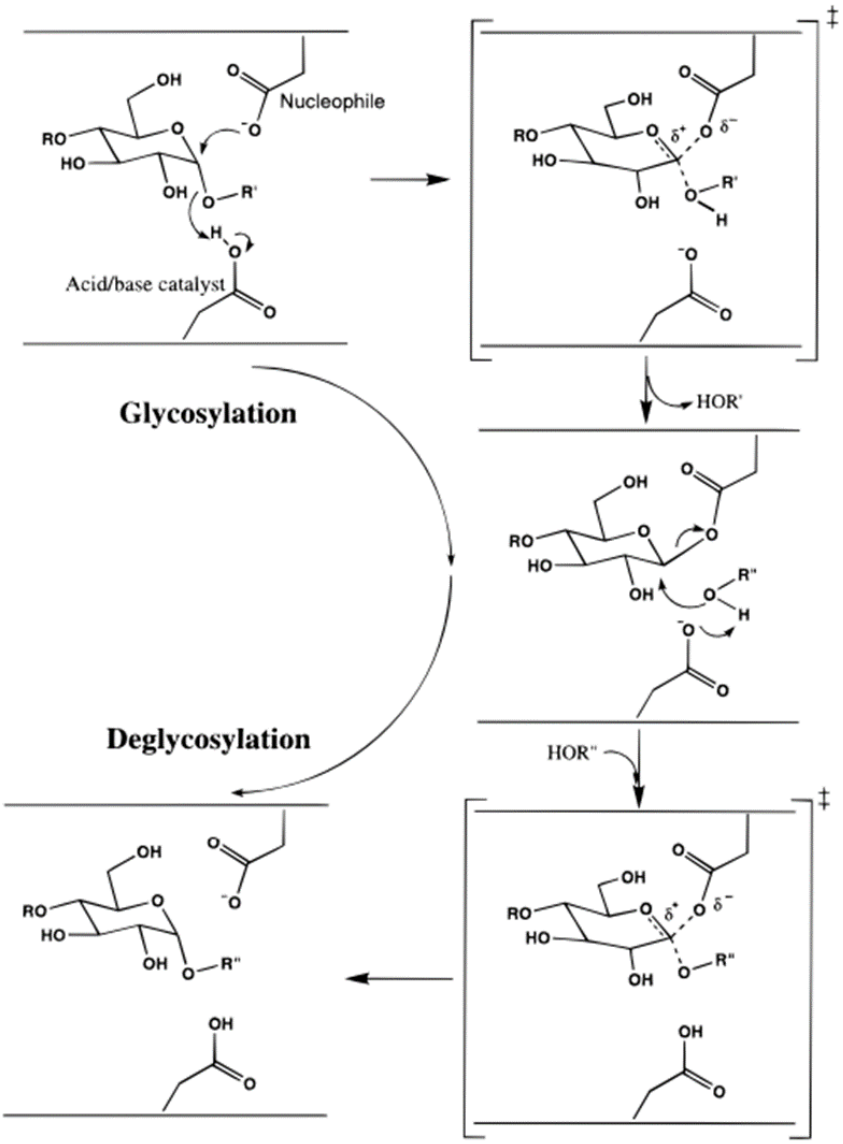

Figure 1.14: Schematic representation of the proposed mechanism of starch hydrolysis by pancreatic α-amylase, initiated by a nucleophilic attach by a deprotonated aspartate residue onto the primary carbon of an anhydroglucose monomer, followed by formation of an intermediate, and finalised by deglycosylation. As seen in the work of Brayer *et al.*[118]

Human pancreatic α-amylase is an example of an endo-acting enzyme, hydrolysing internal bonds of the substrate – linear regions of amylose and amylopectin, resulting in the production of shorter oligosaccharides as intermediate products, and maltose and

maltotriose as end-products of starch hydrolysis. Crystallographic data of porcine pancreatic α-amylase has shown the existence of 5 substrate (*i.e.*, glucose monomer) binding sites in the active site, allowing for the correct positioning of the substrate, prior to hydrolysis of the glycosidic bond linking glucose residues 3 and 4 (Figure 1.15).[124] Kinetic studies have shown that substrate binding is self-perpetuated, where glucose binding in one of the domains increases the strength of binding in the following (ΔG changing from -5 to -16 kJ/mol), with the exception of subsite 3, featuring the weakest (*i.e.*, least energetically favourable) binding (ΔG = +17.6 kJ/mol), resulting from conformational distortion of the glucose ring, prior to cleavage (Figure 1.14).[117,125]

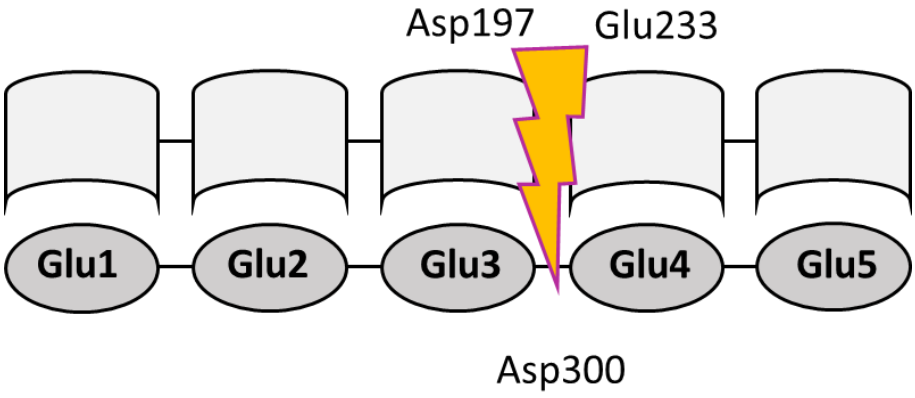

Figure 1.15: Substrate binding sites (light grey) at the active centre of mammalian pancreatic α-amylase. Glycosidic bond hydrolysis occurring between glucose residues 3 and 4 (glu3 and glu4, dark grey), facilitated by the catalytic triad of Asp197, Glu233 and Asp300. Adapted from Butterworth *et al.*[117]

Mathematical models applied to the context of starch hydrolysis by α-amylase have been reviewed extensively elsewhere[126–128], where what is relevant for this work is that starch fractions able to resist upper GIT amylolytic degradation, termed resistant starch (RS), can reach the large intestine where they are degraded by the cumulative action of

commensal bacterial amylolytic enzymes.[82,129–131] RS has been shown to have important health-promoting effects, through its impact on the production of short-chain fatty acids, nitrogen metabolism and gut health homeostasis.[86] The term RS was originated by Englyst *et al*. in 1982[132], initially identifying three different types of RS[86], whereas today this number has increased to five (RS I – V).[130] These have been reviewed extensively elsewhere[130,133,134], where for the purposes of this work, RS III – gelatinised and subsequently retrograded starch, and RS V – helical amylose complexed with lipids and other small molecules, would be the ones in focus.

1.7. Hydrothermal Treatment of Starch

The ability of starch granules to solubilise, absorb water, swell and retrograde are of great significance to many industrial processes. The most widely utilised method of starch processing is its hydrothermal treatment, where starch is heated in the presence of water, resulting in significant structural changes. When heated in excess water (>55% w/v), the insoluble native granules undergo an endothermic transition initiated by water entering the amorphous parts of granules, causing them to swell, expand and destabilise the crystalline regions. This proceeds with further granular swelling, melting of the crystalline regions, breaking of hydrogen bonds and disassociation of double helices, and ultimately resulting in the collapse of the granular organisation, granule breakdown, amylose and some amylopectin leaching into the surrounding liquid/solvent phase, collapse of the molecular and double helical order, as evidenced by X-ray diffraction, small angle X-ray scattering (SAXS), and ^{1}H-^{13}C cross polarisation magic angle spinning (CP/MAS) NMR.[45,65,98] The formation of granule ghosts – remnants of the starch granule, has been documented to form the discontinuous phase, whereas the leached amylose,

and to a lesser extent amylopectin molecules, forming the continuous phase.[135,136] This entire endothermic process is termed starch gelatinisation, in which water acts as a plasticiser, and its completion is also evidenced by the loss of birefringence of starch granules (*i.e.*, loss of Maltese crosses), as evidenced by polarised light microscopy.[137,138]

The degree of long-range ordering in starches has often been probed by means of DSC, which quantifies energy changes associated with exothermic (usually bond forming or associative) or endothermic (usually bond breaking or dissociative) transitions. Up to four distinct endothermic transitions may be detected by DSC, depending on the heating temperature and water conditions, designated as G, M1, M2 and Z endotherms. Endotherms G and M1, observed in the range of 50 to 80 °C (depending on the botanical source of starch) have been associated with the disruption of amylopectin structures – their gelatinisation (G endotherm) and melting (M1 endotherm), where the former is observed in intermediate to excess water contents, and the latter is observed in limited water conditions. The M1 endotherm has been suggested to result from crystallites' incomplete gelatinisation in the presence of limited water, resulting in their melting.[65,139] Endotherms M2 and Z, usually observed in the range of 90 to 135 °C, are ascribed to the dissociation of amylose–lipid complexes and the disruption of uncomplexed amylose crystallites, respectively. The presence of these endotherms depends largely on the hydrothermal conditions and the botanical source of the starch.[140] Previous works have shown that endotherms associated with amylose transitions reappear in subsequent heating cycles, whereas ones associated with amylopectin structures do not. This is likely a result of the different rate of recrystallisation of amylose and amylopectin molecules, where the linear glucan has been shown to recrystallise within hours, whereas the branched glucan – on the order

of days, due to the greater degree of steric hindrance experienced by the highly branched amylopectin molecules.[32,141–147]

Each endothermic transition can be defined by several parameters, such as onset temperature (T_O), indicating the starting point of starch gelatinisation; melting, sometimes referred to as peak temperature (T_M or T_P), conclusion temperature (T_C), indicating the end of the starch gelatinisation step; and overall enthalpy (ΔH), cumulatively referred to as gelatinisation parameters. High levels of crystallite perfection (*i.e.*, stability) in starch structures is usually associated with high values of T_M, whereas the range and magnitude of ΔH is linked to both degree of molecular order and amylopectin content.[29,65,143,145,148,149] The characteristic gelatinisation temperature range is defined as the endothermic breadth or as the difference between T_C and T_O (*i.e.*, $T_C - T_O$, or ΔT) and high values of this parameter are generally associated with more ordered structures, exhibiting higher stability.[32,141–144,150]

There has been some work on the association between endothermic transitions observed via DSC, and starch molecular order and crystallinity, as quantified by ^{1}H-^{13}C CP/MAS NMR and PXRD, respectively. As originally suggested by Cooke and Gidley, and further explored by Perry and Donald, Waigh *et al*., and Bogracheva *et al*., endothermic transitions in hydrothermally treated starch result from the combined loss of double helical order and crystallinity, where the enthalpy (ΔH) of transitions can be used to quantify the degree of both double helical order, and crystallinity.[57,65,80,81,139]

Hydrothermal treatment of starch leads to changes in its physical and micromechanical behaviour, which is most commonly probed by means of rapid viscoanalyser (RVA), due to its ability to emulate the heating and cooling conditions of regular hydrothermal

treatment by exposing a suspension of starch in water to heat and shear, with the simultaneous recording of the ensuing changes in the mixture's viscosity profile as a function of time and temperature. The typical viscosity profile of starch suspensions in water is described by an initial increase in viscosity with the increase in temperature ranging from 50 to 95 °C, ascribed to the swelling of the starch granules and the initial release of polysaccharides into the aqueous medium – predominantly leached amylose, and some amylopectin. This is followed by a drop in viscosity caused by the combined continuous input of high temperature and shear, leading to the disintegration of the granules, which in turn, is followed by an increase in viscosity as the temperature is lowered, resulting from the re-association (recrystallisation) of the solubilised glucan chains making up the continuous phase.[26,29,75,151–154]

This glucan reassociation or retrogradation – a process defined by the reassociation of glucans (both amylose and amylopectin) in the gelatinised suspension, through the formation of inter- and intramolecular hydrogen bonds and through van der Waals forces, ultimately gives rise to a different crystalline ordered structure to its native, unprocessed analogue (Figure 1.16).[29,44,75,140,145,155]

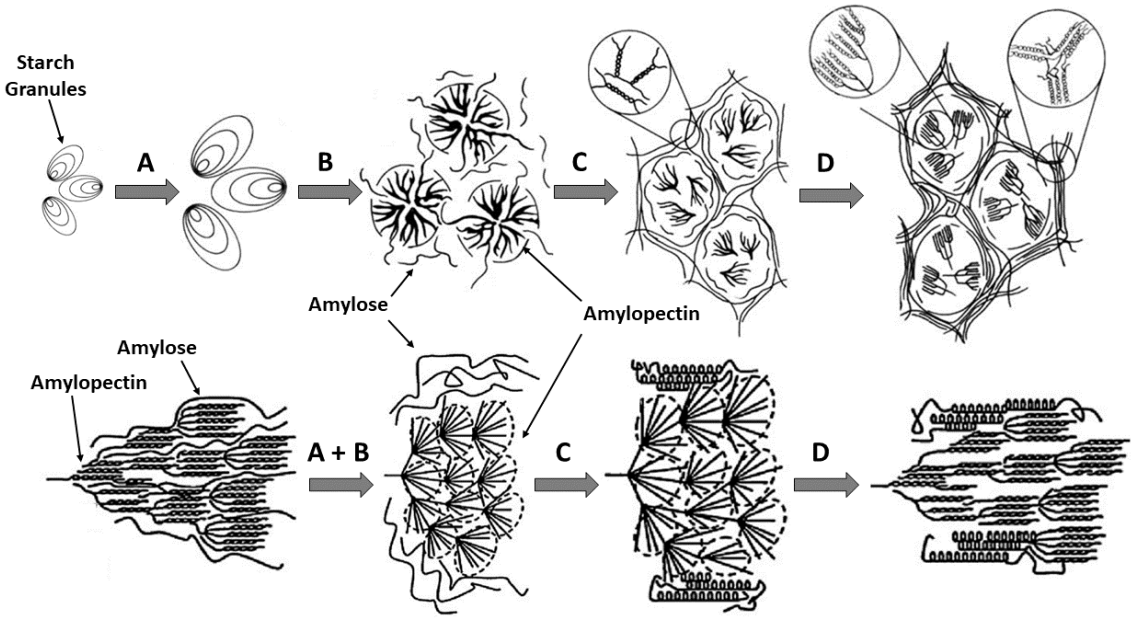

Figure 1.16: Graphical representation of starch gelatinisation and retrogradation, indicating each individual stage: granule swelling (A), granule disruption and amylose leaching (B), glucan reassociation on cooling (C) and further glucan association and cross-linking with storage (D), adapted from the works of Goesart *et al.*[145] and Yu and Christie[156].

Gelatinisation and subsequent retrogradation have also been shown to lead to a change in crystalline polymorphs in A-type starch, where most retrograded starch exhibits B-type crystallinity, similar to native tuber and high-amylose cereal starches.[157] The process of retrogradation plays an important role in the nutritional and pharmaceutical industries, as it increases the material's respective resistance to α-amylase digestion, which has an impact on its ability to escape upper GIT digestion and reach the large intestine structurally intact.[82,86,88,158]

1.8. Starch Gel Structure and Organisation

Hydrogels resulting from the gelatinisation and subsequent retrogradation of starch-water suspensions undergo structural changes in their short- and long-range order, ultimately resulting in a structural ensemble different from the one exhibited by the native starch prior to hydrothermal treatment. On retrogradation, starch pastes form gels, where in general, mechanically stronger gels are associated with higher amylose content starches, whereas weaker ones – with low amylose and amylose-free (waxy) starches.[75] Furthermore, kinetic analyses on the formation of starch gels point towards the rapid recrystallisation of amylose being responsible for the initial stages of hydrogel structure formation, giving high-amylose starch gels their characteristic robustness and resistance to deformation, whereas the slower reassociating amylopectin imparts stickiness and adhesiveness.[75,159]

Previous research on starch hydrogel formation and organisation employing thermal, microscopic, rheological, diffraction and spectroscopic techniques, has pointed towards starch gels exhibiting a lower degree of both short- and long-range order, compared to their native starch analogues, a largely amorphous diffraction pattern, and a change in the mobility and dynamics of ^{1}H within starch gels.[75] The early work by Leloup *et al*.[160] on the porosity of amylose and amylopectin gels, investigated by the diffusion of macromolecular probes (*e.g*., bovine serum albumin, BSA, ovalbumin and lysozyme), revealed the possibility of molecules of various sizes to diffuse into a starch hydrogel network, where there was a linear relationship between the change in probe diffusion coefficient and the starch concentration. This and following studies by the same group[161] on the glucan concentration dependence on the density of the hydrogel network, gave

rise to the initially proposed models of starch hydrogel organisation, whereby the gel network largely resembled a three-dimensional (3-D) fishnet-type assembly, with average pore size (ξ) described by the diameter of the cavity formed between entanglement points in the 3-D network. The works of Imberty and Perez[162], Kalichevsky and Ring[163], Jane and Robyt[164] and Leloup *et al*.[161] further developed this understanding to derive the discontinuous and continuous models of amylose gels (Figures 1.17 and 1.18, respectively). The former model proposes amylose gel organisation to be separated into crystalline and amorphous regions, where these two regions differ largely in the chain length of the amylose chains they are comprised of.

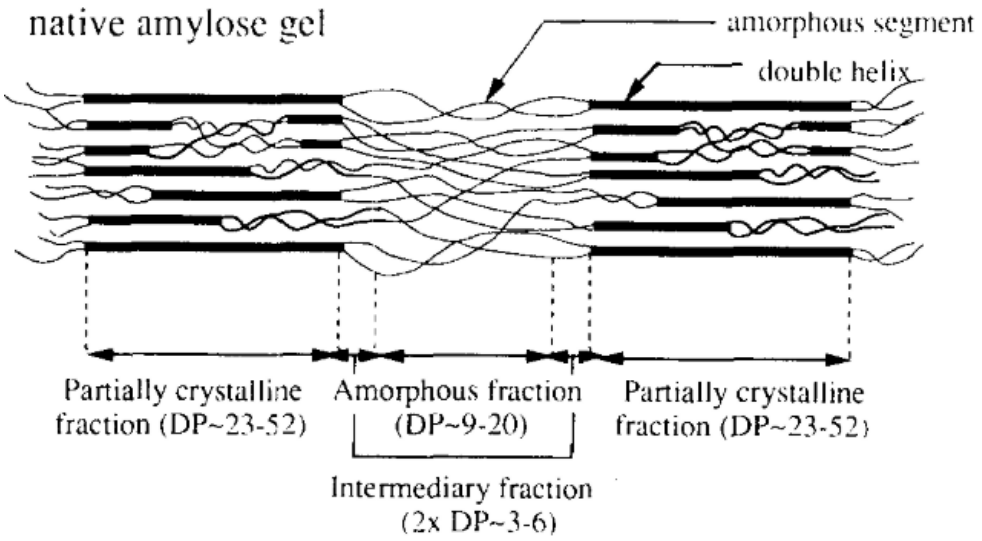

Figure 1.17: Schematic representation of the discontinuous model of amylose gels, as seen in the works of Jane and Robyt.[164]

The latter model, on the other hand, further incorporates electron microscopy data to propose a continuous 3-D network, consisting of both parallel and antiparallel packed helices, interconnected by amorphous amylose segments "dangling" within the porous cavities within the overall hydrogel matrix.

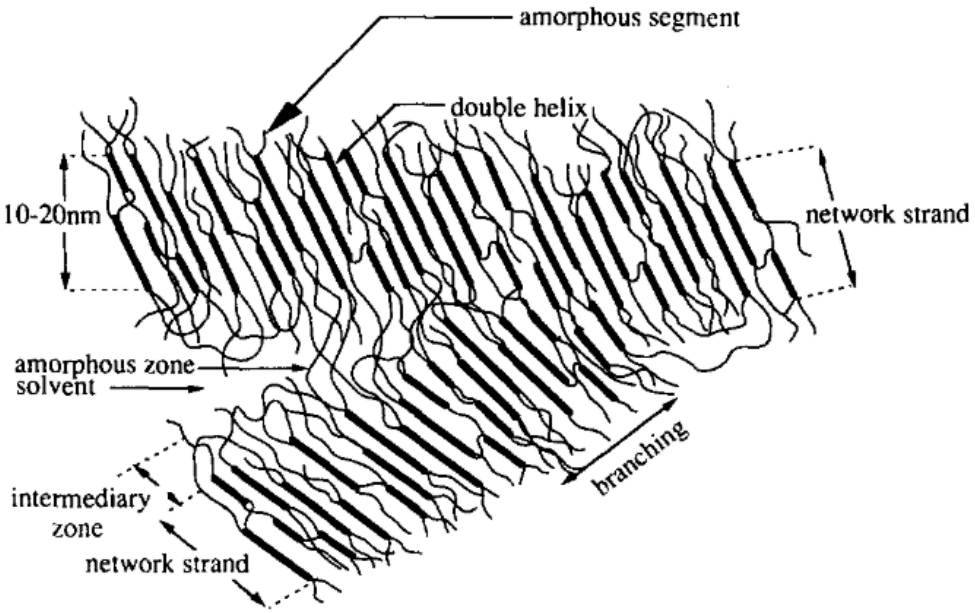

Figure 1.18: Schematic representation of the contiguous model of amylose gels, as seen in the work of Leloup et al.[161]

There have been few further proposed models of amylose, amylopectin, and starch hydrogel organisation, with the most recent one being proposed by Gong *et al.*[165], according to which amylose chains in starch hydrogels organise in circular arrangements ("cells", Figure 1.19), where shorter amylose chains allow for greater degree of recrystallisation on cooling of hydrothermally treated starch, thus resulting in 3-D structures exhibiting decreased susceptibility to α-amylase degradation, as a function of decreased enzyme accessibility.

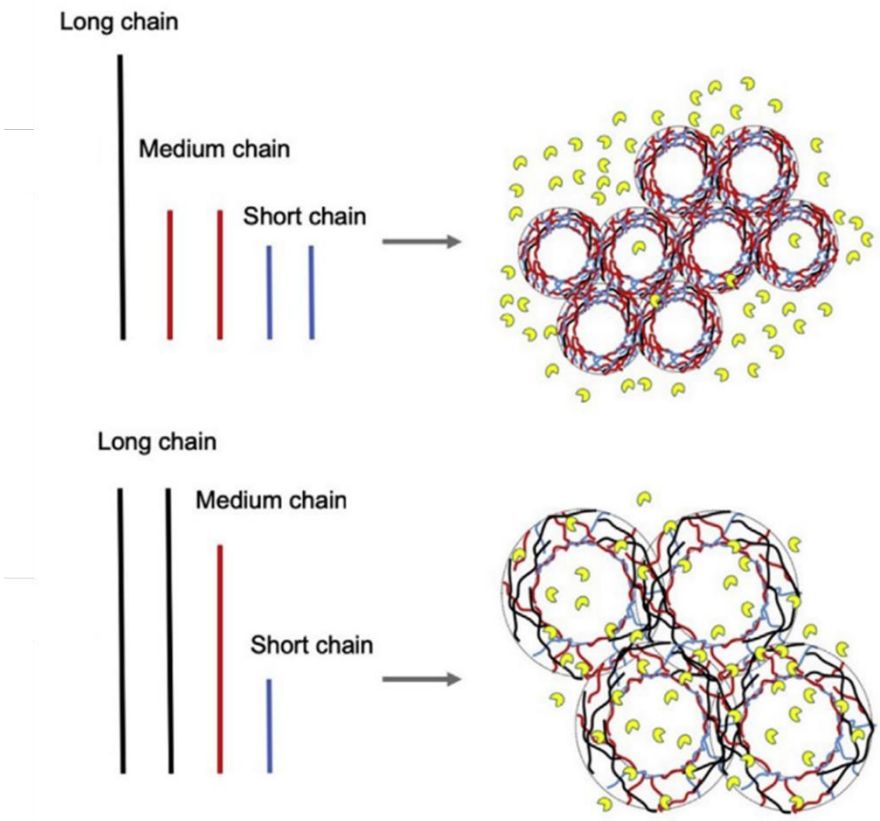

Figure 19: Schematic representation of the influence of amylose chain length on the network organisation of starch gels, as seen in the work of Gong *et al.*[165]

1.9. Overall Project Objectives

The currently existing models of starch gels provide a good foundation for the understanding of their porous internal organisation, and the influence of glucan composition on their physicochemical properties. However, there is little knowledge and understanding of the molecular-level organisation and structural heterogeneities within starch hydrogels, and how these link to hydrogels' bulk structural properties and behaviour. Polysaccharide hydrogels are employed more and more in an array of industries, but there is little knowledge linking their structure and function, which limits their utilisation. In this work we set out to bridge this gap in knowledge and understanding of starch hydrogel structure and function, by probing their

heterogeneous structural and motional organisation, and to show how these impact bulk behaviour, and properties. We do this by probing hydrogel organisation on a macro and molecular scale of a collection of maize starches of varying amylose content.

We probe the viability of starch gels to act as targeted colonic drug delivery platforms, focusing on how structure impacts their pharmacokinetic properties, and demonstrate how they interact with the human GIT, probing the interplay between starch gels, GI enzymes, and commensal bacteria.

We then extend this to V-amylose complexed with small molecules, probing the structural arrangement and internal organisation of these complexes, guest-host interactions, and functional properties in the context of next generation drug delivery vehicles.

In this work we employ an array of characterisation techniques – on a range of length scales, with an emphasis on solid-, solution-state and high-resolution magic angle spinning (HR-MAS) NMR spectroscopy.

Chapter 2: Materials and Methods

2.1 Materials

Waxy maize, normal maize and amylomaize were purchased from Merck (formerly Sigma-Aldrich, Dermstadt, Germany). Hylon VII® and Hi-Maize 260® were kindly provided as a gift by Ingredion Incorporated (Manchester, UK).

Human salivary alpha-amylase (CAS: 9000-90-2, A1031: type XIII-A lyophilized powder, AA from human saliva, 1357 IU), pepsin from porcine mucosa (CAS: 9001-75-6, P7012: pepsin from porcine gastric mucosa, 2074 IU), porcine pancreatin (CAS: 8049-47-6,

P7545: pancreatin from porcine pancreas, 2422 IU amylase activity), bovine bile (CAS: 8008-63-7), KH_2PO_4 (CAS: 7778-77-0), bis-tris (CAS: 6976-37-0), $NaHCO_3$ (CAS: 144-55-8), *p*AHBAH (CAS: 5351-23-5), KCl CAS: 7447-40-7), NaCl (CAS: 7647-14-5), $MgCl_2.6H_2O$ (CAS: 7791-18-6), $CaCl_2.2H_2O$ (CAS: 10035-04-8), haemin (CAS: 16009-13-5), resazurin (CAS: 62758-13-8), NaOH (CAS: 1310-73-2), acetic acid (CAS: 64-19-7), propionic acid (CAS: 79-09-04), butyric acid (CAS: 107-92-6), isobutyric acid (CAS: 79-31-2), 2-methylbutyric acid (CAS: 116-53-0), valeric acid (CAS: 109-52-4), isovaleric acid (CAS: 503-74-2), $NiCl_2.6H_2O$ (CAS: 7791-20-0), SeO_2 (CAS: 7446-08-4), $MnCl_2.4H_2O$ (CAS: 13446-34-9), $FeSO_4.7H_2O$ (CAS: 7782-63-0), $ZnCl_2$ (CAS: 7646-85-7), $CuCl_2.2H_2O$ (CAS: 10125-13-0), $CoCl_2.6H_2O$ (CAS: 7791-13-1), $NaMoO_4.2H_2O$ (CAS: 10102-40-6), $NaVaO_3$ (CAS: 13718-26-8), and H_3BO_3 (CAS: 10043-35-3), as well as all other reagents were purchased from Merck (Dorset, UK), unless specified otherwise. All enzymes were used as provided by the manufacturer, without any further purification.

2.2 Methods

2.2.1 *Total Moisture Content*

Moisture content (%) of all starch powders was measured using the weight loss following air-oven drying at 135 °C for 120 min, until the weight remains constant, using the iAACC 44-19.01 official method (*Equation 2.1*).[166]

$$\%\ Moisture\ Content = \frac{Initial\ Weight - Final\ Weight}{Initial\ Weight} \times 100 \quad \textit{Equation 2.1}$$

2.2.2 *Total and Apparent Amylose Content*

This was performed as per the methodology of Knutson.[167] A 6.0 mM iodine solution was prepared by dissolving 0.229 g of iodine in 210 mL DMSO and 90 mL *dd*H_2O. A

standard curve of known amylose (from potato, >88% pure, CAS 9005-82-7) concentration was prepared by adding 0 to 5.0 mg of amylose to 15-mL Corning® tubes (6 tubes in total), followed by adding 5.0 mg of each starch type to further 5 tubes in triplicate (15 tubes in total). To each of the 21 tubes, 10 mL of the 6.0 mM iodine solution was added, and the tubes were placed on an end-over-end mixer overnight. The following day, 200 µL of each tube were added to 800 µL of *dd*H_2O, and left aside for 1 hour for the amylose-iodine complex to form. The absorbance of all samples was recorded using a UV-Vis spectrophotometer (Biochrom Libra S50 UV/Vis Spectrophotometer, λ_{max} = 600 nm). The obtained apparent amylose content value was corrected to give the % total amylose content (*Equation* 2.2).[38]

$$\%\ Amylose = \frac{\%\ Apparent\ Amylose - 6.2}{93.8} \qquad \textit{Equation 2.2}$$

2.2.3 *Swelling Power*

The swelling power of the five starch powder samples was analysed as per the methodology described by Leech *et al*.[168] In brief, starch/water suspensions (0.1% w/v) were incubated in a shaking water bath (60 °C, 150 rpm, 30 min), followed by centrifugation (1600 rpm, 20 min), removal of the supernatant and calculating the difference in wet and dry mass (*Equation 2.3*).

$$Swelling\ Power = \frac{W_{wet}}{W_{dry}} \qquad \textit{Equation 2.3}$$

where W_{wet} and W_{dry} are the weights of the starch sample following centrifugation and removal of the supernatant, and the dry starch powder prior to the addition of water, respectively.

2.2.4 *Hydrogel Preparation*

Gelatinisation and subsequent storage of all starch gel samples was performed in triplicate by preparing 10% (w/v) starch/deionised water suspensions in 25.0-mL Pyrex® screw-top vials, vortex mixed and autoclaved (121 °C, 15 psig) for 20 min, followed by their storage for the total duration of 8 days at three different conditions: one set was stored at a constant temperature of 4 °C for the whole duration of 8 days (*i.e.*, low temperature isothermal); another set of gels was stored at 30 °C for the full duration of 8 days (*i.e.*, high temperature isothermal); and the third set of starches was stored at 30 °C for 4 days, followed by storage at 4 °C for further 4 days (*i.e.*, thermocycled conditions), all of which resulted in the formation of opaque white gels.[169] These conditions were chosen, due to the available literature on the impact of these storage conditions on the bulk properties of cooked starches[169,170], allowing for comparison, and further elucidation of the molecular underpinnings of macromolecular observations.

All hydrogels intended for micromechanical analysis, PXRD, solid-state NMR and HR-MAS NMR, simulated digestion and fermentation were carefully excised using a 10 mm cork borer (Breckland Scientific Supplies Ltd., Stafford, UK) and cut into cylinders, 10 mm in height, using a surgical blade (Swann Morton Ltd., Sheffield, UK).

Hydrogels intended for solution-state NMR experiments were prepared using D_2O (99.9% ^2H) instead of H_2O, following the exact same procedures as above, where the total starch/D_2O suspension volume was 700 µL.

2.2.5 *Differential scanning calorimetry (DSC)*

Principles

DSC is often employed for the characterisation of raw materials, amorphous, crystalline, and semi-crystalline polymers, pharmaceutical drugs, and excipients, and is instrumental in the structural analysis of starch, where heat flow changes associated with first and second order transitions in polysaccharide materials can be detected and quantified across a wide range of conditions (*e.g.*, moisture content, temperature range). This technique involves the detection and quantification of heat changes and thermal events (both endo and exothermic) in samples, induced by the application of controlled conditions – heating, cooling or isothermal, under a defined, usually inert atmosphere (*e.g.*, N_2).[27,171,172] In this work, DSC (DSC 2500) and multi-cell DSC (MC-DSC) are used, where both of these are heat-flux instruments, which use either 2 (DSC 2500) or 4 (MC-DSC) pans (Hastelloy crucibles) – one (or three) for the sample(s), and one for the reference – usually left either empty, or filled with degassed, deionised, and distilled water (*dd*H_2O), depending on the research question and sample of interest. Heat-flux differential scanning calorimeters heat all pans simultaneously under the same conditions, and the difference in between the sample pan(s) and the reference pan is detected and converted into energy (J or J/g), where the heat flow from the furnace to each pan can be described by Equation 2.4.

$$\frac{\Delta Q}{\Delta t} = \frac{\Delta T}{R} \qquad \textit{Equation 2.4}$$

Where ΔQ/Δt is the heat flow over time, and ΔT is the temperature difference between the sample(s) and the reference pan, and R is the thermal resistance between the furnace and the Hastelloy ampoules.[173]

In the context of polymers, such as starch, four thermal parameters are usually reported on for every thermal event – the onset, peak (sometimes referred to as melting) and concluding temperature (T_O, T_m and T_C), as well as the enthalpy of transition (ΔH).

The gelatinisation parameters of starches can be influenced by the rate of heating and cooling employed, where slower rates are generally preferred, as they have been argued to be more representative of the actual thermal behaviour.[148] Slower rates of thermal exposure have the advantage of maintaining pseudo steady state conditions, allowing for the minimisation of kinetic effects, the presence of which can lead to an overestimation of the peak temperature, due to lagging of the transition behind the temperature at the given time point.

Experimental Procedures

DSC experiments were performed on a TA Instrument (TA Instruments Ltd., New Castle, USA) multicell differential scanning calorimeter (MC-DSC), equipped with three sample Hastelloy ampoules and one reference Hastelloy ampoule, where the reference pan was filled with deionised water. The furnace was continuously flushed with dry Nitrogen at a rate of 50 mL.min^{-1}. For native starch samples, 100 mg of starch powder were made up with 0.9 mL degassed, deionised H_2O (*i.e.,* 10% w/v suspensions), where the individual amount of water added to each sample was adjusted depending on their respective moisture content data. The vessels were hermetically sealed, and samples were analysed in the range of 10–150 °C, with a heating rate of 1 °C min^{-1}, a cooling rate of 2 °C min^{-1}, followed by a second heating cycle at 1 °C min^{-1}.

For all hydrogel samples, approximately 800 mg of stored sample were accurately weighed into each Hastelloy ampoule. The vessels were sealed, and all measurements

taken against an empty reference ampoule. All gel samples were subjected to a single heating cycle at a heating rate of 1 °C min^{-1}. All thermal data was analysed using TA Universal Analysis software package, establishing the onset, peak and conclusion temperature (T_O, T_P and T_C, respectively), and the overall enthalpy of each thermal transition (ΔH). All scans were run at least in triplicate and all obtained results are presented as means.

2.2.6 *Sub-ambient DSC*

Sub-ambient DSC experiments were performed on a TA Instruments Discovery Series DSC2500, using TA Instruments Tzero® pans and hermetic lids (reference numbers 901683.901 and 901684.901, respectively), sealed using Tzero® sample press die. Approximately 3.5–5.0 mg of each hydrogel sample were loaded into each pan and hermetically sealed. All measurements were referenced against a sealed, empty pan. All gel samples were subjected to a single cooling cycle from 20 to -40 °C min^{-1}, at 5 °C min^{-1}. The furnace was flushed with dry nitrogen at a rate of 50 $mL.min^{-1}$. All thermal data was analysed using TA TRIOS software package, establishing the onset, conclusion temperature (T_O, and T_C, respectively), and the overall enthalpy of each thermal transition (ΔH). All scans were run at least in triplicate and all obtained results are presented as means.

2.2.7 *Dynamic oscillatory rheology*

Principles

Unlike plastic solids, which undergo continuous structural deformation even after their elastic limit, our materials are nonfluid colloidal polymer networks, featuring finite yield stress, and as such are classified as gels[174] (Appendix, Figure S1). Since these hydrogels

resemble viscoelastic solids, exhibiting time-dependence, predominantly dynamic (*i.e.*, sinusoidal) shear flow (*i.e.*, oscillatory rheology) has been used throughout this work. In this type of micromechanical technique, a solid sample (a viscoelastic gel) is fixed between a moving part and a fixed one, and mechanical stress (σ) is applied to it, where the material responds through a generated strain (*γ*), depending on its viscoelastic properties. Stress is the ratio of force (*F*) to the area (A) over which that force is exerted, and is also direction-dependent. According to Newton's law, σ is related to γ through a sample's density or viscosity (η, *Equation 2.5*).

$$\eta = \frac{\sigma}{\gamma} \qquad \textit{Equation 2.5}$$

In the context of viscoelastic solids, directional shear stress (σ) applied on the sample, resulting in a sinusoidal varying deformation, generating strain (γ), are related through Equations 2.6 and 2.7.

$$\gamma = \gamma_0 \times \sin(\omega t) \qquad \textit{Equation 2.6}$$

$$\sigma = \sigma_0 \times \sin(\omega t + \delta) \qquad \textit{Equation 2.7}$$

where σ_0 and γ_0 are the stress- and strain-amplitudes (*i.e.*, the maximum stress and deformation applied to the sample, respectively), ω is the oscillation frequency, t is the given time period, and δ is the phase angle difference (*i.e.*, shift) between the sinusoidal stress and strain waveforms (*figure 2.1*).[174–177]

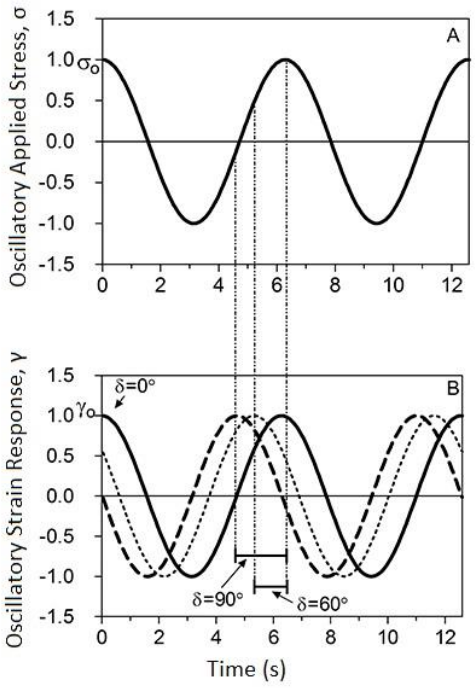

Figure 2.1: Example diagram of the applied oscillatory sinusoidal stress wave and the resulting response strain wave of a plastic gel, with three different phase angles (δ) shown, adapted from the works of Marangoni and Peyronel.[177]

Using trigonometric function decomposition (described elsewhere)[174], the stress waveform can be decomposed into two components correlating with two material functions – elastic (storage) modulus (*G'*) and a viscous (loss) modulus (*G''*), where the former is indicative of the energy storing properties and solid-like nature of the sample; and the latter provides information regarding the material's viscous and liquid-like nature, and about the dissipation of energy by the sample. These dynamic moduli can be used for the classification of a dispersion systems into four distinct sub-groups – dilute solutions, entangled networks, weak, and strong gels, and can be expressed by Equations 2.8 and 2.9.

$$G' = \sigma_0/\gamma_0 \times \cos(\delta) \qquad \textit{Equation 2.8}$$

$$G'' = \sigma_0/\gamma_0 \times \sin(\delta) \qquad \textit{Equation 2.9}$$

The ratio of the dynamic moduli is directly related to the phase angle (δ) through Equation 2.10, and are frequently utilised for the characterisation of the viscoelastic behaviour of various polymers of interest, where classic strong gels can be described by *tan*(δ) values of 0.01-0.1.[178–180]

$$\tan(\delta) = G''/G' \qquad \textit{Equation 2.10}$$

In the context of viscoelastic solids and traditional gels, the micromechanical properties of these materials are independent of the strain amplitude up to a point, beyond which G' and G'' lose linearity with respect to the applied strain. A strain sweep, *i.e.*, an experimental set-up involving constant frequency of oscillation and progressive strain applied to the samples, determines the extent of this linear region, often referred to as the linear viscoelastic (LVE) regime. Once the LVE regime of the material has been defined, the sample is subjected to a frequency sweep, defined by a constant strain, the value of which is within the established LVE, and a progressively increasing frequency. Below the critical strain, the elastic modulus G' is often nearly independent of frequency, as would be expected from a structured or solid-like material. The more frequency dependent the elastic modulus is, the more fluid-like is the material.[181–183]

Hydrogel-type materials usually exhibit a frequency-independent *G'* (where *G'*>>*G''*) at predominantly low frequency values. This behaviour changes at higher frequencies, resulting from bond rupture and/or internal structural entanglements, which can be experimentally observed by the sudden decrease of *G'* and a temporary increase in *G"* and *δ* (*a.k.a.* yield point), followed by the former's sharp decrease, ultimately resulting

in the intersection of the dynamic moduli curves (*a.k.a.* G crossover point). The breaking point, indicative of a permanent physical deformation and/or fracture of the sample, usually occurs shortly prior to the crossover of the dynamic moduli and the phase angle curves (Figure 2.2).[177]

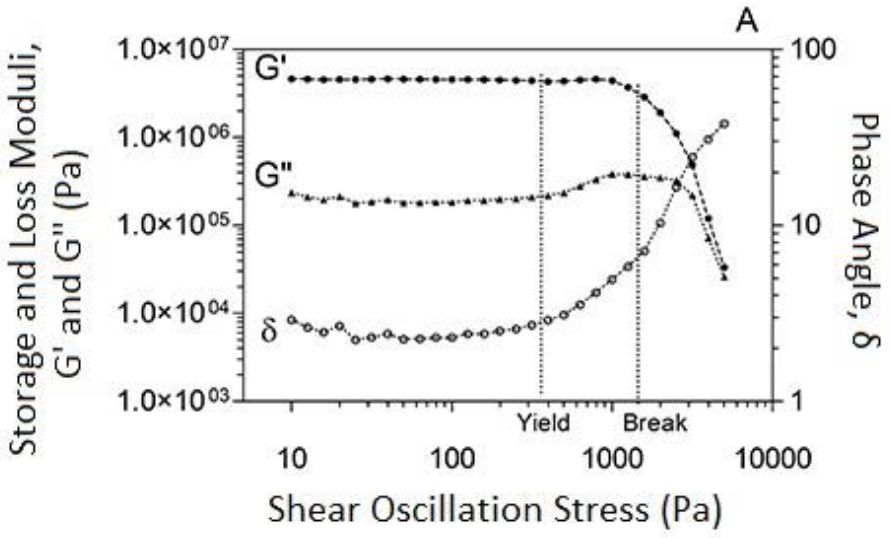

Figure 2.2: Example diagram of behaviour of the dynamic moduli (G' and G'') and the phase angle (δ) in the linear viscoelastic region of a plastic gel, as a logarithmic function of the shear oscillation stress, adapted from the works of Marangoni and Peyronel.[177]

In this work, oscillatory rheology is largely used to assess hydrogels' overall bulk properties, differences in structural integrity between different types of starch hydrogels, as well as to probe changes in structural integrity as a result of exposure to a variety of *in vitro* physiological conditions.

Experimental Procedures

Micromechanical analyses were performed on a TA Instrument (TA Instruments Ltd., New Castle, USA) Rheometer AR2000, with 13 mm parallel plate geometry (non-sand blasted, so as to avoid microtears into the hydrogel surface where the substrates make

contact with the top plate), equipped with a Peltier device for temperature control, where hydrogel samples were carefully excised using a 13-mm cork borer (Breckland Scientific Supplies Ltd., Stafford, UK) and cut into discs, 10 mm in height, using a surgical blade (Swann-Morton Ltd., Sheffield, UK). All samples were analysed at a constant temperature of 5.0 °C and the inter-plate gap was set to 10 mm. All starch hydrogels were loaded onto the sensor plate and allowed to equilibrate for 2 min to allow for temperature to equilibrate throughout the sample. Parallel plate configuration was chosen due to the solid-like nature of these materials, and their proneness to slipping due to their highly hydrated state. Strain sweeps were performed in the range of 0.01–100% at a constant frequency of 1.0 Hz to ascertain the materials' linear viscoelastic (LVE) range. This was followed by frequency sweep analyses in the range of 0.1–10.0 Hz (*i.e*., 0.6283–62.83 rad/sec) at a constant strain of 0.3% to determine the samples' storage and loss moduli (G' and G'). All measurements were taken at regular time intervals, analysed using TA Data Analysis software package, and presented as averages of a minimum of three runs, where deviation in the obtained parameters between runs of the same samples were less than 10%.

2.2.8 *Powder X-ray diffraction and estimation of long range order*

Principles

Crystalline samples are made up of regular, periodic spacing of atoms. In 3-D space, a crystal can be viewed as an arrangement of coordinates in a crystal lattice, the smallest reproducible unit of which is referred to as a unit cell. A unit cell is defined by three vectors in space – *a*, *b* and *c*, along with the interaxial angles between them – α, β, and γ. A plane intersecting a lattice and thus passing through three non-aligned lattice points

is referred to as a lattice plane. In crystals, two parallel lattice planes are linked through the Miller indices – *h*, *k* and *l*, as well as the *x*, *y* and *z* coordinates of the points where two lattice planes satisfy Equation 2.11

$$hx + ky + lz = n \qquad \textit{Equation 2.11}$$

where *n* is an integer number.[184]

The filtered X-ray wavelength is in the range of λ = 0.01 to 10 nm, allowing it to induce changes in the electron cloud (density) of molecules, due to their nm length scale.

On irradiation, a beam of X-rays strikes a sample and diffracts into many specific directions, the angles and intensities of which depends on the specific electron density distribution within the sample. X-ray interference is the result of the interaction of correlated waves, where this can be constrictive or destructive in nature, depending on whether the X-ray waves are in-phase or out of phase, respectively. On irradiation with X-rays with wavelength λ, falling at an incidence angle θ, part of the energy beam is scattered in accordance with Bragg's diffraction (Figure 2.3). The two energy beams reflected by the two planes, separated by a given distance *d* (*a.k.a.* d-spacing), have a path length difference of 2*dsin*θ. The two energy beams enhance each other's intensity (*a.k.a.* constructive interference) under the conditions satisfying Bragg's law – when 2*dsin*θ is an integer number (*n*) multiple of the X-ray wavelength (λ, Equation 2.12), or the order of the beam (1, 2, 3, *etc*.) A diffraction of a crystalline or semi-crystalline sample (such as starch) yields a pattern featuring distinct peaks, where each peak corresponds to different *d*-spacing and a different set of Miller indices in 3-D space.[184,185]

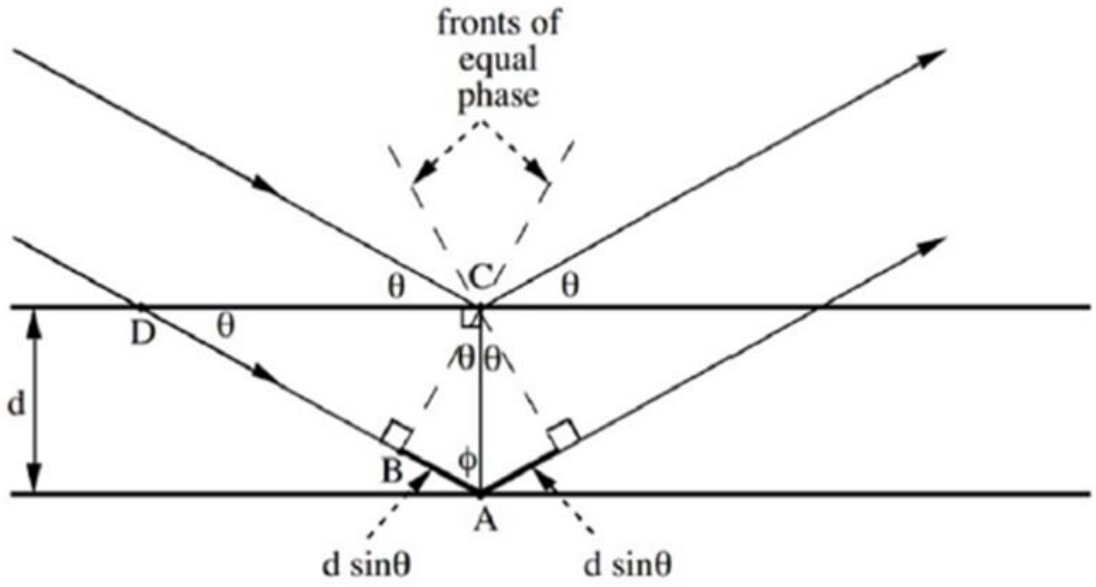

Figure 2.3: Schematic representation of incident X-rays scattered by two crystal planes in a sample, separated by d-spacing.[184]

$$2dsin\theta = n\lambda \qquad \textit{Equation 2.12}$$

Our powder X-ray diffraction set-up is comprised of an X-ray source, a detector and the sample loading disc. The set-up involves placing the irradiation source at an angle θ to the sample, and the angle between the beam projection and the detector being 2θ. In this work, PXRD is largely used quantitatively to determine the total amorphous contribution in starch samples – both native powders and their lyophilised hydrogel counterparts.

Experimental Procedures

Powder X-ray diffraction (PXRD) patterns of all starch powders were measured on an ARL™ X'Tra Powder Diffractometer (Thermo Scientific™). All samples were scanned with Cu K_α radiation (λ = 0.154 nm), and reflections were detected via a scintillation detector over the angular range of *2*θ = 5.0–54.99°, with a step interval of 0.01°, and step duration

of 0.6 s. The X-ray generator was set at 45 kV and 40 mA. Approximately 600 mg of each sample were packed into the loading dish to a depth of 4 mm and levelled with a razor blade. Diffraction patterns of all starch hydrogels were obtained following freeze-drying of the gel samples and grinding using a mortar and pestle.

2.2.9 *Estimation of Total Amorphous Contribution*

The total amorphous contribution of both powders and gels was estimated following the approach described by Lopez-Rubio *et al.*[186] In brief, peaks in the diffraction patterns of all starch samples were manually fitted using a combination of Lorentzian and Gaussian functions, utilising the PeakFit (SigmaPlot, Systat Software Inc.©) software package, where 10 peaks were selected for starches of A-type crystallinity (*i.e.,* waxy maize and normal maize) and 11 peaks for starches of B-type crystallinity (*i.e.,* amylomaize, Hylon VII® and Hi-Maize 260®), with the addition of an amorphous "background" peak in the range of 2Θ 15-17° for each diffraction pattern (Figure 2.4). The total percentile amorphous contribution in our samples was calculated based on the ratio between the sum of the total area under the whole diffractogram (A_{total}), and the area under each crystalline peak (either A- or B-type, $A_{A/B\text{-}type}$, *Equation 2.13*).[187]

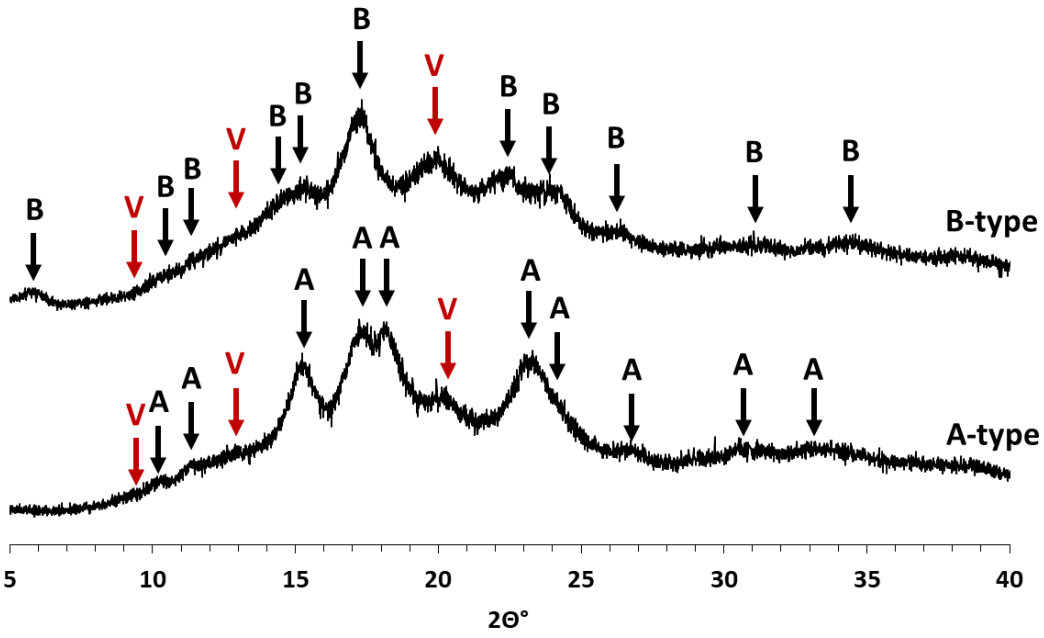

Figure 2.4: Powder X-ray Diffraction pattern of A- and B-type powder starches (normal and Hylon VII™ maize powders shown here, respectively), with black arrows indicating the peaks associated with A- and B-type type crystallinity chosen for peak fitting (10 for A-type and 11 for B-type), and red arrows indicating the peaks associated with V-type amylose arrangements.

$$Amorphous\ Contribution\ (\%) = \frac{\Sigma A_{total} - \Sigma(A_{A/B-type})}{\Sigma A_{total}} \quad \textit{Equation 2.13}$$

2.2.10 *NMR Spectroscopy*

Since most samples analysed by NMR spectroscopy in this work are considered solid-like, an emphasis would be placed on solid-state NMR techniques in this section.

Principles

Atomic nuclei contain both protons and neutrons, and as such have the properties of mass and charge. Nuclei also possess an intrinsic property of angular momentum, *a.k.a.* nuclear spin (*I*). As a charged particle with a spin property, nuclei generate a magnetic

field, resulting in a magnetic moment (μ), proportional to their *I* (Equation 2.14) and their nuclear gyromagnetic ratio (γ), which is constant for a given nucleus, and both μ and *I* being vector properties with magnitude and direction.[188–190]

$$\mu = \gamma I \qquad \textit{Equation 2.14}$$

In order for nuclei to be magnetically active, and thus detectable by NMR spectroscopy, nuclei must possess a non-zero spin quantum number (*I* = 1/2, 1, 3/2, *etc*.), where all nuclei with spin quantum number of zero (*I* = 0) are referred to as NMR-silent.[188–190]

The net magnetisation in a sample, equivalent to the bulk magnetic moment (M), can be expressed as the sum of the magnetic moment of all nuclei in the sample (*Equation 2.15*).

$$M = \Sigma\mu \qquad \textit{Equation 2.15}$$

When a sample is placed in a uniform magnetic field (B), a torque is exerted on M, and M precesses about B at a fixed rate (*i.e.*, frequency, ω, Equation 2.16).

$$\omega = \gamma B \qquad \textit{Equation 2.16}$$

In the context of NMR spectroscopy, the external fixed B is usually designated as B_0 and in the laboratory frame of reference[191] it is arbitrarily chosen to be oriented along the z-axis, and the frequency with which M precesses about B_0 is defined as the Larmor frequency (ω_0, Equation 2.17), where the motion and direction of this precession is dependent on the nuclear γ, and as such is unique to each nucleus.

$$\omega_0 = -\gamma B_0 \qquad \textit{Equation 2.17}$$

When not under the influence of B_0, nuclear μ are randomly oriented in space. When placed in B_0, nuclear spins orient in $2I+1$ non-degenerate energy populations (*i.e.*, for spin I ½ nuclei, there are 2 x ½ + 1 = 2), separated by an energy gap (ΔE, *a.k.a.* Zeeman splitting, Figure 2.5), proportional to the B_0 field strength, and the nuclear γ. In this state, nuclear spins achieve thermal equilibrium (different at different temperatures) of distribution, referred to as the Boltzmann distribution (Equation 2.18), where n is the total number of nuclear spins in either population, k is Boltzmann's constant, and T is the temperature for the particular thermal equilibrium in Kelvin.[188–190]

$$\frac{nI_{+1/2}}{nI_{-1/2}} = e^{\frac{\Delta E}{kT}} \qquad \textit{Equation 2.18}$$

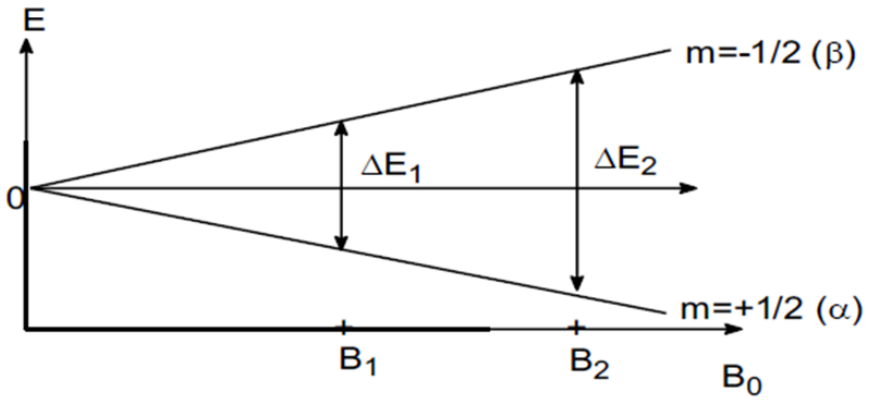

Figure 2.5. Zeeman splitting of a spin ½ nucleus in an external magnetic field B_0, resulting in two spin populations – low energy (+½ α), and a high-energy (-½ β), with the size of the Zeeman splitting (ΔE_1 and ΔE_2) proportional to the strength of B_0. [188–190]

In NMR spectroscopy, radiofrequency (*r.f.*) pulses oscillating at the Larmor frequency are applied to the sample at angle θ (*a.k.a*. flip angle), which make up the basis of most NMR experiments. These *r.f*. pulses result in an oscillating magnetic field (B_1) along the direction of the applied pulse, which in turn, exerts a torque on M perpendicular to B_1,

displacing M_0 away from its equilibrium position along the *z*-axis, and towards the transverse *xy*-plane (M_1, Figure 2.6), where the precession frequency follows Equation 2.17 (where ω_0 is ω_1, and B_0 is B_1). [188–190]

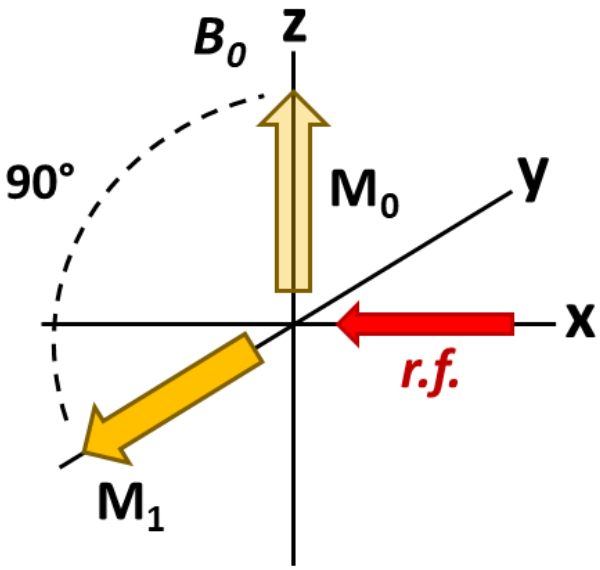

Figure 2.6: Schematic representation of the change in placement of the bulk magnetisation (M) from its equilibrium (z-axis) position towards the xy-plane (-y-axis) under the influence of a (90°) *r.f.* pulse along the x-axis.

Relaxation

Following the application of an *r.f.* pulse, the Boltzmann distribution of nuclear spins at the given magnetic field is perturbed. Spins return to their original (*i.e.*, equilibrium) energy levels through nuclear relaxation mechanisms, mediated by dipolar interactions, spin rotation and chemical shift anisotropy. Nuclear relaxation can broadly be categorised as resulting from spin-lattice interactions (*a.k.a.* longitudinal, T_1), and spin-spin relaxation (*a.k.a.* transverse, T_2). In most systems, nuclear relaxation is on the order of magnitude of a few seconds to minutes.[188–190]

Longitudinal relaxation is the exponential recovery of M along the *z*-axis (Figure 2.7), mediated by the loss of magnetisation of spins through thermal contact with the lattice (hence spin-lattice relaxation) until reaching thermal equilibrium. The recovery of z-magnetisation follows first-order kinetics, as demonstrated by Bloch's theory, were T_1 is the time period necessary to recovery approximately 63% of the bulk z-magnetisation (Figure 2.8). [188–190]

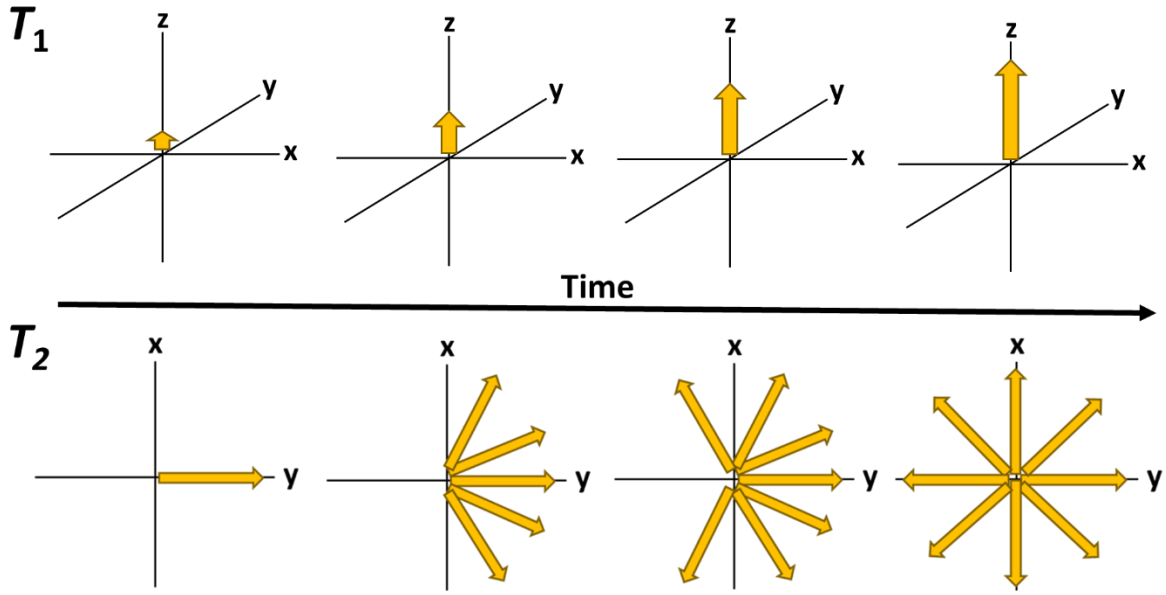

Figure 2.7: Graphical representation of the longitudinal (T_1) relaxation through the time-dependent recovery of *z*-magnetisation (up), and of the transverse (T_2) relaxation through the time-dependent loss of spin coherence within the *xy*-plane (down).

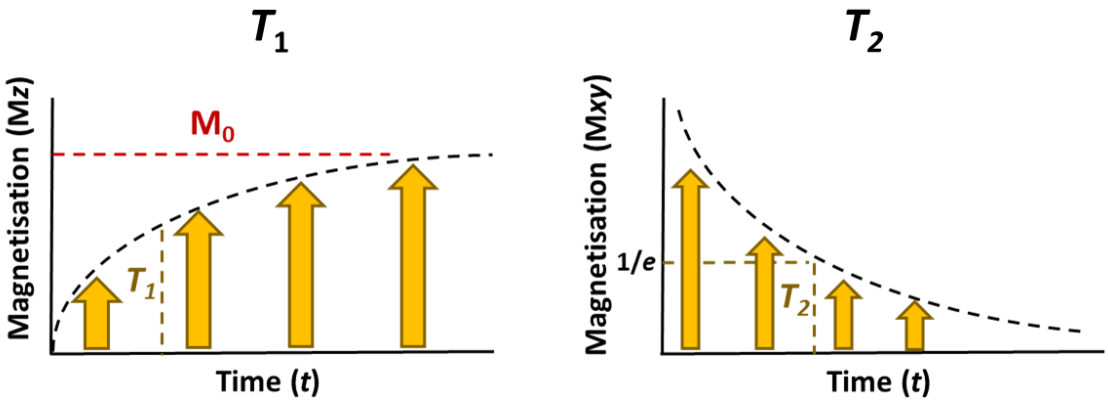

Figure 2.8: First-order exponential growth curve of longitudinal relaxation, where T_1 represents the time period needed for recovery of 63% of the bulk *z*-magnetisation (M_z, left), and first-order exponential decay curve of transverse relaxation, where T_2 represents the time period needed for the drop of the M_{xy} magnetisation to approximately 37% (1/*e*) of its original magnitude (right).

Transverse relaxation represents the time-dependent loss of spin coherence (*i.e.,* spin dephasing) in the transverse (*xy*) plane, hence spin-spin relaxation (although spin-spin interactions are only one mechanism involved in transverse relaxation, Figure 2.7). This loss of coherence follows a first-order exponential decay, where T_2 is the time period required for the transverse magnetisation to fall to approximately 37% (Figure 2.8), and for most samples T_2 occurs hand-in-hand with T_1 relaxation, although there have been cases documented where T_2 relaxation occurs without T_1.[188–190]

Both longitudinal and transverse relaxation depend on the molecular tumbling (*i.e.*, correlation time, τ_c). In molecules exhibiting fast molecular motions and correlation time, the contribution of T_1 and T_2 is very similar. In the slow motional regime, T_1 dominates molecular relaxation, where the contribution of T_2 is negligible (*i.e.*, very fast T_2, Figure 2.9).[188–190]

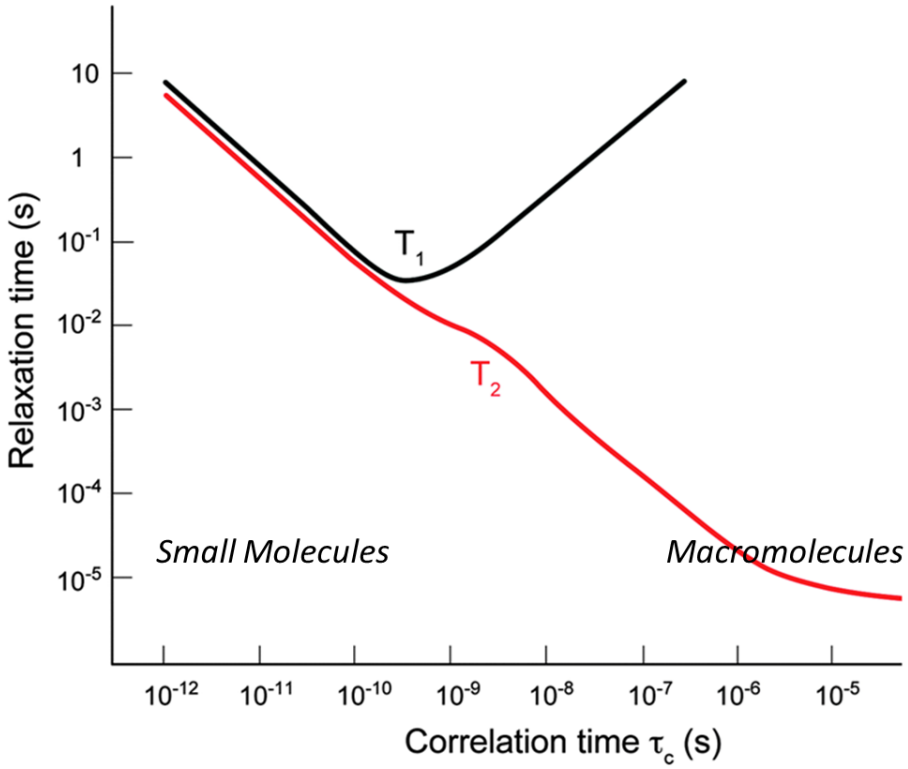

Figure 2.9: T_1 and T_2 dependence on molecular correlation time (τ_c), as seen in work of Keshari and Wilson.[192]

Dipolar Coupling and Spin Diffusion

Nuclei in close proximity (<10 Å) can interact through their magnetic moments – a through space effect referred to as dipolar coupling. This can occur between the same nuclei (homonuclear dipolar coupling, *I*, *I*) and different nuclei (heteronuclear dipolar coupling, *I*, *S*). Both homonuclear and heteronuclear dipolar interactions are dependent on the internuclear distance and the nuclear *γ*, where in the context of like nuclei (*I*, *I*), proximal abundant nuclei with high *γ*-values exhibit very strong dipolar interactions and spin diffusion properties (*e.g.*, ^{1}H-^{1}H), unlike proximal dilute nuclei with low *γ*-values (*e.g.*, ^{13}C-^{13}C). Unlike homonuclear dipolar coupling, in heteronuclear dipolar coupling spin diffusion is not observed, due to the difference in resonating frequencies between

heteronuclei (*e.g.*, ^{1}H and ^{13}C).[188–190] The homonuclear dipolar coupling Hamiltonian for a two spin system ($\hat{H}_{I,I}$) can be expressed by Equation 2.19.

$$\hat{H}_{I,I} = -\left(\frac{\mu_0}{4\pi}\right)\frac{\hbar\gamma_{I_1}\gamma_{I_2}}{r^3{}_{I_1I_2}}\left(3cos^2\theta_{I_1I_2} - 1\right)[3I_{1z}I_{2z} - (I_1I_2)] \quad \textit{Equation 2.19}$$

Where the dipolar constant (*d*) is equal to $\left(\frac{\mu_0}{4\pi}\right)\frac{\hbar\gamma_{I_1}\gamma_{I_2}}{r^3{}_{I_1I_2}}$, $r^3{}_{I_1I_2}$ is the internuclear distance between the two like spins, and μ_0 is the permeability of free space ($\mu_0 = 4\pi \times 10^7 NA^{-2}$.

Spin diffusion is an energy conserving "flip-flop" mechanism in which energy is transferred from a spin in a higher energy state (I_β), to one in a lower energy state (I_α), leading to the relaxation of the former to a lower energy state (I_α), and promotion of the latter to a higher energy state (I_β): $I_\beta I_\alpha \rightarrow I_\alpha I_\beta$. It should be noted, that "diffusion" is a misleading term, as the phenomenon of spin diffusion is a coherent and a reversible process.[188–190]

Electron Shielding Effects, Chemical Shift, and Chemical Shift Anisotropy

Electrons making up the electron shell around nuclei influence the magnetic field nuclei experience when placed in B_0, resulting in a modulated magnetic field. This is referred to as a shielding effect and is depending on nuclei's shielding constant (σ), proximal nuclei of higher electronegativity (χ), through space interactions with other nuclei and hydrogen bonding, all of which can exert a shielding or a deshielding effect on the nuclei of interest.

The formal relationship between the chemical shift and the shielding tensors is given below (*Equation 2.20*):

$$\delta = 1\sigma_{iso} - \sigma \qquad \textit{Equation 2.20}$$

Where δ is the chemical shift tensor, σ is the shielding tensor, 1 is the unit matrix, and σ_{iso} is the isotropic value of the shielding tensor of the standard reference used in the NMR experiments. [193]

The formal definition of the components of the shielding tensor can be seen below (*Equation 2.21*):

$$\sigma_{\alpha\beta} = \frac{\partial^2 E}{\partial \mu_a \partial B_\beta} \qquad \textit{Equation 2.21}$$

Where *E* is the total electronic energy of the molecule.

Since different nuclei have different degree of electronic shielding, they also have a unique chemical shift (δ), which is expressed in parts per million (ppm) of B_0.

The chemical shift of a nucleus is defined by the difference between the nuclear frequency (ν) and the frequency of a reference compound (ν_{ref}) – usually tetramethylsilane (TMS) for referencing ^{1}H and ^{13}C nuclei. (*Equation 2.22*).[188–190]

$$\delta_{ppm} = 10^6\left(\frac{\nu - \nu_{ref}}{\nu_{ref}}\right) \qquad \textit{Equation 2.22}$$

Since the distribution of electron density around nuclei is not spherical, and oriented along bonds or *p*-orbitals in *sp* and sp^2 hybridised nuclei, its effect on the magnetic field experienced by the nucleus is orientation-dependent (*i.e.*, anisotropic). This leads to differences in the electron shielding, depending on the orientation of the electron density along the *x*-, *y*- and *z*-axes, leading to slight changes in the nuclear chemical shift,

depending on its orientation with respect to B_0. This effect is referred to as chemical shift anisotropy (CSA), and leads to a broader distribution of the chemical shift.[188–190]

In solutions (and solution-state NMR spectroscopy), the orientation of nuclei in space is averaged out due to rapid isotropic tumbling, which minimises the effect of CSA and dipolar coupling, leading to narrow peaks. In solids, however, the low degree molecular mobility and molecular tumbling leads to significant line broadening, due to the presence of strong dipolar interactions and significant CSA contribution. For a shielding tensor with axial symmetry, the CSA Hamiltonian ($\hat{H}_{CS}$) can be expressed by Equation 2.23

$$\hat{H}_{CS} = \gamma B_0 I_z[\delta_{iso} + \frac{1}{2}\delta_{CSA}(3cos^2\theta - 1)] \qquad \textit{Equation 2.23}$$

where δ_{iso} and δ_{CSA} are the isotropic and anisotropic chemical shift factors.[188–190]

Solid-state Spectroscopic Techniques

The geometric component of the chemical shift and dipolar interaction Hamiltonians ($\hat{H}_{CS}$ and $\hat{H}_{I,I}$, respectively) has an angular dependence expressed by the term $3\cos^2(\theta) - 1$ (Equations 2.19 and 2.23). This term is cancelled to zero when the sample is spun at an angle of θ = 54.74° with respect to B_0, which minimises dipolar couplings and the anisotropic contribution to the chemical shift Hamiltonian ($\hat{H}_{CS}$). This technique is referred to as magic-angle spinning (MAS, Figure 2.12) and is based on the isotropic tumbling of molecules in solutions, and is fundamental for obtaining high-resolution spectra in solid-state NMR spectroscopy, where the two overlapping powder patterns may result in very difficult (or impossible) to interpret spectra (Figure 2.13).[188] In order to minimise effects, such as CSA and heteronuclear dipolar coupling, the spinning speed

needs to be 3-4-fold higher than the strength of the interaction (*e.g.*, to eliminate the effect of ^{1}H-^{13}C heteronuclear dipolar coupling, spinning speeds of 5-15 kHz are sufficient). In the case of strong homonuclear or heteronuclear dipolar interactions of abundant nuclei of high *γ* (*e.g.*, ^{1}H-^{1}H or ^{1}H-^{19}F), one usually requires spinning speeds of more than 65 kHz.

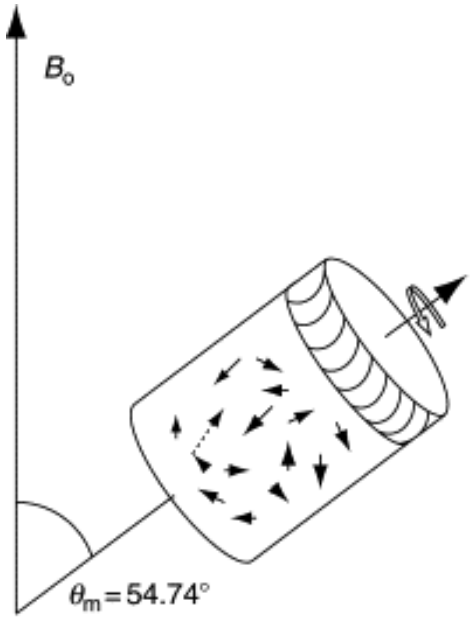

Figure 2.12: Magic-angle spinning (MAS) and its effect on the orientation dependence of nuclear spins with respect to the externally applied magnetic field (B_0), adapted from the work of Melinda J. Duer.[188]

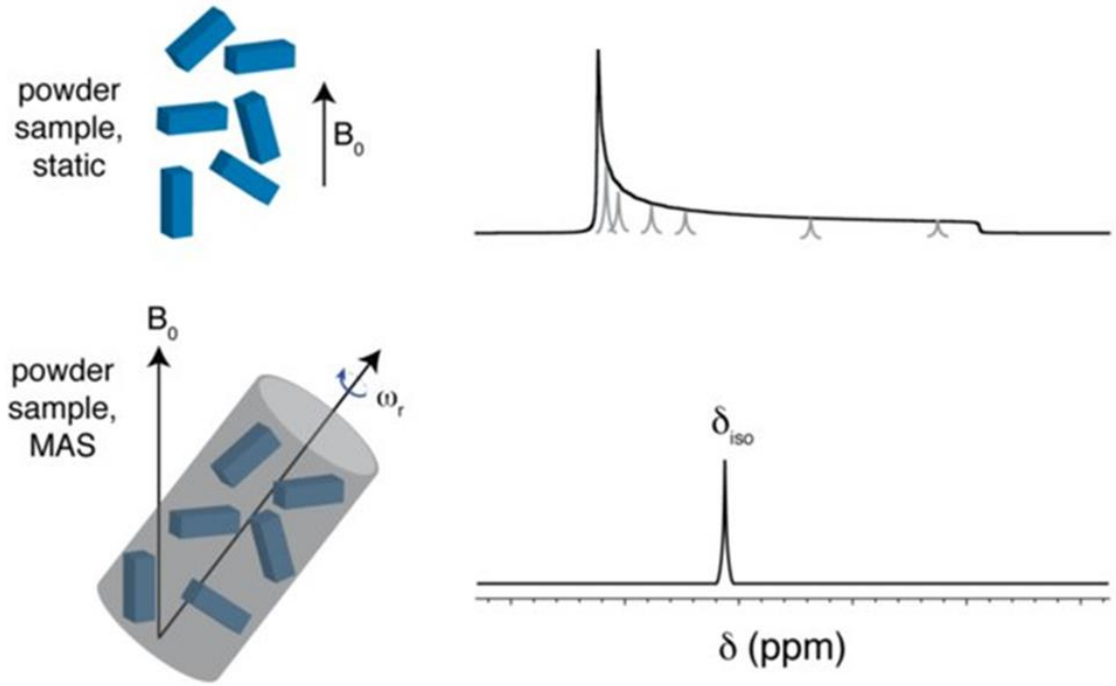

Figure 2.13: Schematic representation of a powder sample under static (up) and MAS conditions (down), and the associated anisotropic and isotropic chemical shift distributions resulting from the two conditions, respectively. Adapted from Forse (2013).[194]

When MAS rates are lower than the strength of the CSA contribution, there is incomplete averaging of the direction dependent electron density ellipsoid, resulting in the appearance of spinning sidebands (ssb), which are sharp lines, at a distance equal to an integer of the spinning rate from the peak (line) of isotropic chemical shift. This can usually be overcome by spinning at faster rates, where the ssb are much greater at spinning frequencies of 1 kHz, compared to 3, 5 and 10 kHz. Other methods of removing ssb involve the use of sequential 90 and 180° *r.f.* pulses in a technique known as total suppression of spinning sidebands (TOSS).[188]

An important consideration of applying MAS conditions to gel-type samples, is the production of heat and shear effects (as a result of centrifugal forces), proportional to

the MAS rate, which can introduce changes into the gel structure and organisation, depending on the thermal responsivity and structural integrity of the hydrogel system.[195,196] The impact of heat can be partially mitigated through controlling the experimental temperature conditions through the variable temperature unit (VTU), coupled to the NMR probe, which provides carefully controlled flow of gas at a constant temperature over the duration of the experiment. The influence of centrifugal forces can be partially modulated through the use of different size and shape spinning rotors, where smaller and more spherical rotors decrease the strength of the centrifugal forces exerted on the sample under MAS conditions.[195,196]

Since most of this work deals with structural characterisation of samples, making use of nuclei of low natural abundance and *γ*, such as ^{13}C, most NMR experiments rely on the simultaneous application of MAS, alongside cross-polarisation (CP) and high-power heteronuclear (^{1}H-^{13}C) decoupling.

CP is usually utilised in order to observe dilute nuclei, using the high polarisability of abundant nuclei of high *γ* values. CP is mediated by the dipolar interactions between two heteronuclei (*I* and *S*), but since dipolar interactions between heteronuclei are unfavourable, these need to be made likely through the use of carefully calculated *r.f.* pulses. This is discussed in quantum mechanical details elsewhere[188], but for the purposes of this work, using precise *r.f.* pulses the transfer of magnetisation from the abundant nuclei (*e.g.*, ^{1}H) to the dilute nuclei (*e.g.*, ^{13}C) is made favourable by modulating the contact pulse amplitude in accordance with the Hartmann-Hahn condition, *i.e.*, $\gamma_I B_I = \gamma_S B_S$.

The efficiency of polarisation transfer (*a.k.a.* CP efficiency) is dependent on the strength of the heteronuclear dipolar interaction under these conditions, where the stronger the interaction, the more efficient the polarisation transfer is. CP efficiency is further enhanced by the lack or decrease in intermediate motions, due to the detrimental effect of motional modulation on dipolar interactions and the efficiency of magnetisation transfer. For example, viscoelastic gels with strong viscous liquid contribution are likely to experience decreased CP efficiency, compared to analogous elastic solid gels.[188]

Since most nuclei observed within this work are ^{13}C nuclei, heteronuclear dipolar decoupling is extensively used in the NMR experiments described. Two-pulse phase modulation (TPPM) and its "offspring" SPINAL-64 – the most common types of heteronuclear decoupling techniques used in this work, involve the use of two high-power *r.f.* pulses with a defined phased shift of 10-70° in the case of the former, and a supercycle 64 cycles of this two-pulse set-up.[197]

Due to the reduced quantitative aspect of traditional ^{1}H-^{13}C CP/MAS spectroscopy, particularly in the context of polymers where moieties of different dynamics co-exist (*e.g.*, rigid and mobile domains), an adaptation to the traditional CP/MAS pulse train is utilised for the purpose of quantitative probing of such heterogeneous systems, known as CP single-pulse (CPSP) MAS NMR spectroscopy, pioneered by Shu *et al*.[198] and discussed in more detail in the works of Courtier-Murias *et al*.[199] Where the CPSP/MAS pulse train differs from the traditional CP-ramp is that both ^{1}H and ^{13}C nuclei are brought into the transverse (*xy*) plane, followed by both ^{1}H and ^{13}C magnetisation being spin-locked under the Hartmann-Hahn conditions, during the subsequent contact pulse. The role of the ^{13}C spin lock is two-fold: to transfer magnetisation from the high-γ ^{1}H nuclei

to ^{13}C ones, much like in the traditional CP/MAS pulse train, and also to prevent the ^{13}C magnetisation of the mobile moieties from dephasing during the contact pulse. One of the advantage of the CPSP pulse train is that ensures baseline ^{13}C magnetisation by the direct pulse in the ^{13}C channel, and doesn't rely on the ^{13}C magnetisation coming exclusively from ^{1}H nuclei via the CP element under Hartmann-Hahn conditions.[199]

High-resolution Magic-Angle Spinning (HR-MAS) techniques

HR-MAS spectroscopy is the combined application of traditional high-resolution, solution-state spectroscopic methods, along with anisotropic and dipolar interaction-averaging MAS, as seen in traditional solid-state settings. The advancement of NMR hardware, the availability of gradient coils in combination with pneumatic MAS units has allowed for many modern high-resolution techniques to be applied to semi-solid, gel-like, soft matter samples, such as self-healing polymers, organogels, food samples, as well as biological samples, such as tissues. [200,201] HR-MAS allows for the acquisition of NMR spectral data featuring narrower peaks compared to traditional solid-state NMR spectroscopy. HR-MAS allows for the merging of solution- and solid-state techniques, due to the pronounced increase in resolution, as well as the residual anisotropic interactions at moderate MAS speeds (typically 4-6 kHz). Some of the key traditional solution-state experiments applied to the context of starch hydrogels through the use of HR-MAS NMR spectroscopy are ^{1}H-^{1}H correlation spectroscopy (COSY), ^{1}H-^{13}C heteronuclear multiple bond correlation spectroscopy (HMBC) and saturation transfer difference (STD) spectroscopy.[202–206]

Solution-state NMR techniques

^{1}H Solution-state techniques are particularly useful for investigation of the kinetic aspects of gelation and supramolecular organisation from low-molecular weight gelator species, due to its quantitative aspect, coupled with the changes in NMR peak intensity and shape (full-width and half-height) as rapidly tumbling molecules in solution (well resolved, narrow intense peaks) transition to being organised in a motionally constrained, macromolecular network (less intense, broader peaks).

In the context of this work, solution-state NMR is largely used for the qualitative identification of products of starch hydrogel digestion by amylolytic enzymes (*e.g.*, glucose, maltose, maltotriose, limit dextrins), as a function of starch hydrogel transit through the human GIT; as well as for quantifying primary and secondary commensal bacterial metabolites, produced as a result of starch hydrogel fermentation in the simulated large intestine (*i.e.*, colon).

Unlike solid-state and HR-MAS techniques, solution-state NMR involves the use of solvent species in the sample preparation (*e.g.*, DMSO, H_2O/D_2O). In ^{1}H NMR experiments, depending on the chemical shifts of the molecules and samples of interest, it may be necessary to use deuterated solvents (99-99.9% deuteration, depending on chemical vendor, solvent age, and good laboratory practice of users), such as DMSO-d_6 and D_2O. This largely reduces the residual solvent peak in ^{1}H NMR spectra. Depending on the chemical shift of the ^{1}H peaks of the sample of interest, the residual solvent peak may partially or fully obscure ^{1}H peaks of interest (*e.g.*, H_2O ^{1}H signal at 4.7 ppm partially overlaps with H-1 ^{1}H in the glucose monomer in starch at 5.1 ppm). This can be overcome with gradient-based NMR techniques of solvent-suppression.

In the context of this work, this is largely used in the quantification of commensal bacterial metabolites, as well as the quantification of drug release from the starch hydrogel excipients. This is achieved through a series of low-power pre-saturation pulses on the residual H_2O peaks during relaxation and mixing time of the '*noesygppr1d*' Bruker pulse sequence, minimising the solvent ^1H contribution during FID acquisition.

Experimental Procedures

Cross Polarisation and Single Pulse Magic Angle Spinning (CP and CPSP/MAS) NMR Spectroscopy

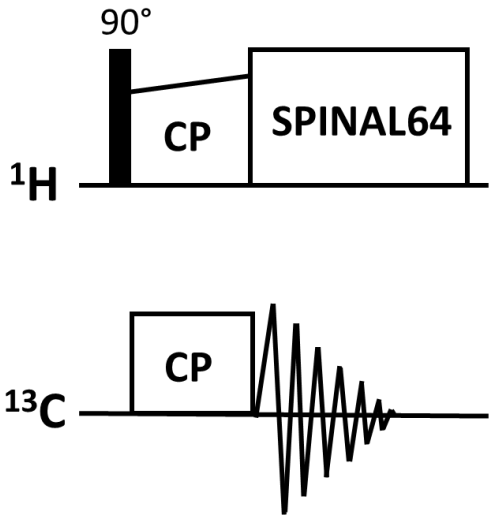

Figure 2.14: Pulse sequence of the ^1H-^{13}C CP/MAS train, consisting of a π/2 *r.f*. pulse on ^1H, followed by a contact time (CP), and FID acquisition with simultaneous heteronuclear decoupling.

Solid-state ^1H-^{13}C CP/MAS experiments were carried out for powder samples using a Bruker Avance III 300 MHz spectrometer, equipped with an HX 4-mm probe, at a ^{13}C frequency of 75.47 MHz and MAS rate of 12 kHz. Approximately 100–120 mg of solid samples were packed into a 4-mm zirconium oxide rotor with a Kel-F end cap. The ^1H-^{13}C CP/MAS NMR experimental acquisition and processing parameters were π/2 ^1H *rf* pulse

length of 3.50 μs and π/2 ^{13}C *rf* pulse length of 4.50 μs, a contact time of 1000 μs, a recycle delay of 10 s, and a minimum of 5120 number of scans. All ^{1}H and ^{13}C spectra were referenced with respect to tetramethylsilane (TMS). The measurements were carried out at *ca.* 25 °C.

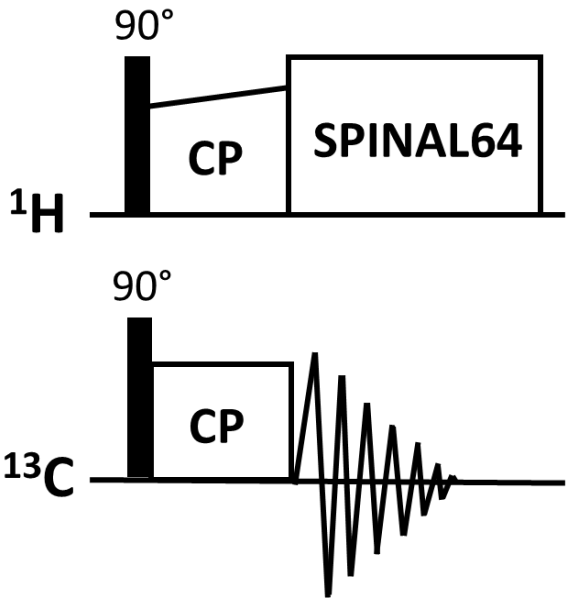

Figure 2.15: Pulse sequence of the ^{1}H-^{13}C CPSP/MAS train, consisting of π/2 *r.f*. pulses on both ^{1}H and ^{13}C, followed by a contact time (CP), and FID acquisition with simultaneous heteronuclear decoupling.

Solid-state ^{1}H-^{13}C CP and CPSP/MAS NMR experiments were carried out for the starch gels using a Bruker Avance III 400 MHz spectrometer, equipped with an HXY 4-mm probe, at a ^{13}C frequency of 100.64 MHz, and MAS rate of 6 kHz. Gel samples were packed into an insert, enclosed with a stopper and a screw cap, and placed inside a 4-mm cylindrical rotor with a Kel-F end cap. The ^{1}H-^{13}C CP/MAS NMR experimental acquisition and processing parameters were π/2 ^{1}H rf pulse of 3.20 μs and π/2 ^{13}C rf pulse of 3.86 μs, a contact time of 1000 μs, a recycle delay of 5 s, with a minimum of 6000 scans. ^{1}H and ^{13}C chemical shifts were referenced to tetramethylsilane (TMS). The spectra were

measured at approximately 5 °C. These experiments were also performed at variable temperature (VT) in the range of +5.0 to -25.0 °C in steps of 5 °C, where these were performed with a total of 2000 number of scans per temperature step and all other parameters were kept the same.

Estimation of Short-range Molecular Order

Short-range starch molecular ordering was estimated using the method described by Flanagan *et al*. [207] In brief, following the acquisition of the free induction decay, the data were Fourier transformed, phase corrected and zero-filled to 4096 data points. The spectra were then subjected to partial least squares (PLS) fit using a large library of experimental ^{1}H-^{13}C CP/MAS NMR spectra of both raw granular and processed starches of various botanical origins, featuring all crystalline polymorphs (A-, B- and V-type). The short range order of the samples was obtained by multiple linear regression fitting to parameters obtained from the PLS model.

Spectral deconvolution

Spectral deconvolution was performed using the MestReNova software v14 (MestreLab Research©) at high resolution with a minimum of 20 fitting cycles, using a mixture of Lorentzian and Gaussian functions, with minimal manual adjustment of peak position. This was performed iteratively until the acquisition of minimal outlier residuals.

Estimation of mobility

Estimation of mobility levels across all peaks of interest was calculated as shown below (*Equation 2.22*).

$$\%\ Mobility = \frac{I_{CPSP} - I_{CP}}{I_{CPSP}} \times 100 \qquad \textit{Equation 2.22}$$

where I_{CPSP} and I_{CP} are the ^{13}C peaks' normalised intensity values in their CPSP and CP/MAS NMR spectra, respectively.

2.2.10.8.5 *^{13}C Direct Polarisation (DP) with High Power ^{1}H Decoupling (HPDEC) NMR Spectroscopy*

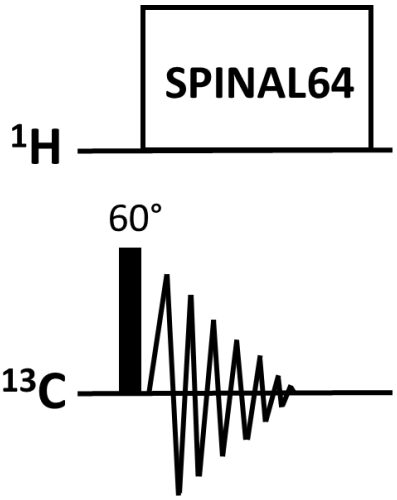

Figure 2.16: Pulse sequence of the direct polarisation with high-power decoupling (HPDEC) train, consisting of a π/3 *r.f*. pulse on ^{13}C, followed by FID acquisition with simultaneous heteronuclear decoupling.

DP experiments were performed on a Bruker AVANCE III 850 MHz solid-state NMR spectrometer (UK National 850 Solid-State NMR facility at the University of Warwick) equipped with a 4 mm HX H13892B probe, using π/2 angle on ^{13}C of 3.5 μs, relaxation delay of 2 s, at MAS rate 10 kHz, at 5 °C and with a minimum of 256 scans.

Further DP experiments with long relaxation delays were performed on a Bruker Avance III 400 MHz spectrometer, equipped with an HXY 4-mm probe. The acquisition

parameters were π/2 angle on ^{13}C of 3.3 µs, recycle delay of 10, 20 and 150 s, at MAS rate of 6 kHz, at 5 °C, and with a minimum of 1024 scans.

2.2.10.8.6 *Water Polarisation Transfer Cross Polarisation (WPT-CP) NMR Spectroscopy*

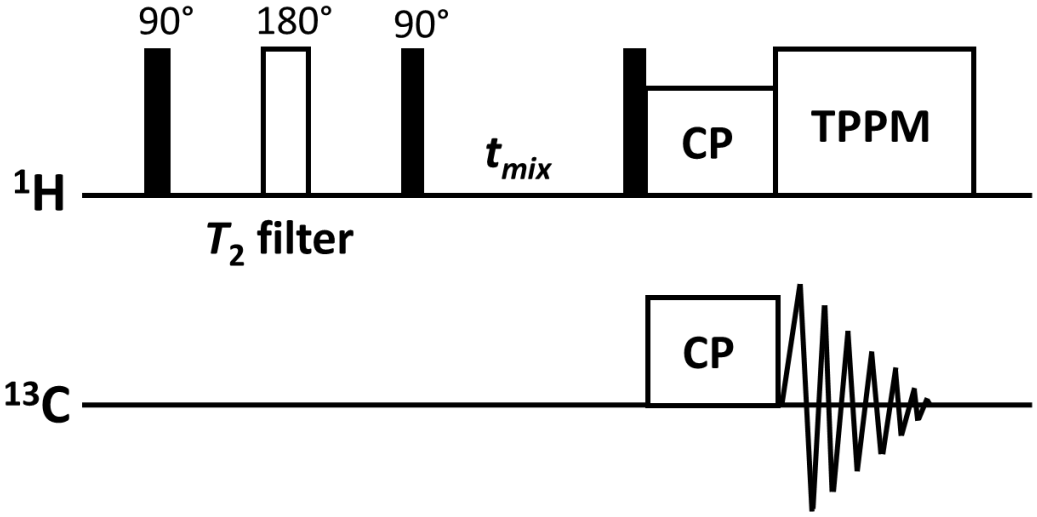

Figure 2.17: Pulse sequence of the water polarisation transfer-cross-polarisation (WPT-CP) train, consisting of a T_2 filter, followed by mixing time, and a traditional CP/MAS ramp.

WPT-CP NMR experiments have been shown to be particularly useful for probing water-polysaccharide interactions in semisolid materials, for instance plant cell walls.[208] The experiment starts by filtering out ^1H magnetisation from immobile components (*e.g.*, starch particle network; short T_2) while keeping ^1H magnetisation from mobile components (*e.g.*, water; long T_2). Subsequently, the latter is transferred to the particle network during a variable mixing period (t_{mix}) via three different mechanisms, (i) ^1H spin diffusion, (ii) ^1H intermolecular nuclear Overhauser effect (nOe) and (iii) ^1H chemical exchange. It should be noted that, in comparison with mechanisms (i) and (iii), nOe contributes to a lesser extent to magnetisation transfer at low-to-moderate MAS

rates.[208] Finally, ^{1}H magnetisation is transferred to ^{13}C *via* CP and the ^{13}C spectrum is acquired under conditions of high power ^{1}H decoupling.

The acquisition parameters were 90° ^{1}H and ^{13}C rf pulses of 3.20 and 3.86 µs, respectively. A total T_2 filter period (2Δ + 180° pulse length) of 4 ms and mixing times of 25 ms was used. To minimise the contribution of intramolecular spin diffusion during the CP period a contact time of 500 µs was employed. The short mixing time and low CP efficiency of starch hydrogels precluded running complete WPT-CP build-up curves at variable mixing times. All WPT-CP experiments were carried out at 5 °C, MAS rate of 6 kHz with a minimum of 6k scans. Peak intensities were normalised against a reference spectrum obtained with very short T_2 filter duration and mixing times (both set as 1.0 µs). The percentage of water polarisation transfer (% WPT-CP) was calculated for C-1, C-2,3,5 and C-6 carbon peaks as the ratio of the peak intensities at 25 ms mixing time (*i.e.,* build-up) and the reference spectrum (*Equation 2.23*)

$$\%\, WPT - CP = \frac{A_{25ms}}{A_{REF}} \times 100 \qquad \textit{Equation 2.23}$$

where A_{25ms} and A_{REF} are the carbon peak intensities of WPT-CP spectra acquired at 25 and 0 ms, respectively. The C-4 peak was disregarded, due to its low intensity. The peak intensity in WPT-CP curves depends on the number, distance, and mobility of water molecules at a given ^{13}C environment. Hence, peaks corresponding to less sterically constrained vicinities showing faster WPT-CP growth at shorter mixing times (*i.e.,* 25 ms), compared to sterically hindered ones.

HR-MAS NMR Spectroscopy

Direct ^{13}C detection and ^{1}H-^{13}C HSQC experiments on starch gels were carried out on a Bruker Avance III 800 MHz spectrometer, equipped with a high-resolution magic angle spinning (HR-MAS) 4 mm double resonance probe. All experiments were carried out at 5 °C and at MAS rate of 6 kHz.

The ^{13}C direct detection experiments were carried out with a 90° ^{13}C pulse of 6.7 µs, a relaxation delay of 1.0 s and a minimum of 4k scans, and the 2D ^{1}H-^{13}C HSQC experiments were performed with a π/2 flip angle of 7.72 µs, relaxation delay of 5.0 s and 128 increments in the indirect (F1) dimension.

2.2.10.8.8 *Longitudinal Relaxation Measurements*

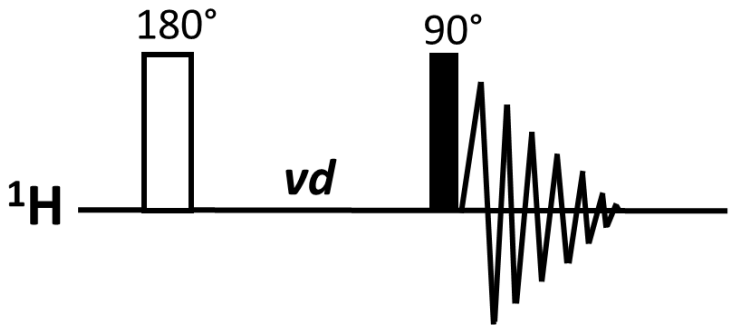

Figure 2.18: Pulse sequence of inversion-recovery train for measuring ^{1}H T_1, consisting of a π *r.f*. pulse on ^{1}H, followed by variable delay, a π/2 *r.f*. pulse and acquisition of the FID.

^{1}H longitudinal relaxation times (T_1) were measured using the inversion recovery pulse sequence, using recycle delay of 10 s. A total of 16 points were recorded with time delays ranging from 0.05 to 20 s for all hydrogel samples. This was also performed at variable temperature in the range of +5.0 to -15.0 °C in steps of 5 °C for normal maize starch hydrogels. The evolution of spectral intensities of all ^{1}H peaks of the starch hydrogels

and the one for HDO were mathematically fitted to the monoexponential function below (*Equation 2.24*), using Bruker TopSpin v3.6.3:

$$M_z(\tau) = M_0 \times [1 - 2e^{\left(\frac{-\tau}{T_1}\right)}] \qquad \textit{Equation 2.24}$$

where M_z is the z-component of magnetisation, M_0 is the equilibrium magnetisation and τ is the time delay.[209,210]

Saturation Transfer Difference (STD) NMR Spectroscopy

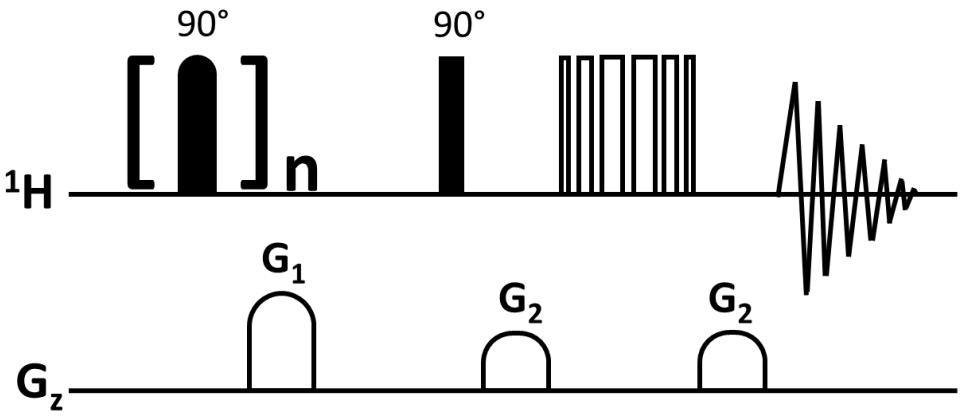

Figure 2.19: Pulse sequence of the STD NMR train, consisting of a selective saturation π/2 *r.f*. pulse, followed by spin-lock, solvent suppression, and FID acquisition.

STD NMR spectroscopy is a nuclear Overhauser effect (nOe)-based pulse sequence, where a molecule is selectively saturated at two separate frequencies – an on-resonance (typically in the range of 3 to -1.5 ppm) which allows for the fast effective saturation of the molecule through ^{1}H-^{1}H spin diffusion and intramolecular nOe; and an off-resonance (typically around 40-50 ppm) frequency, which provides a reference spectrum. The magnetisation in the saturated (on-resonance) spectrum is then transferred intermolecularly to proximal ^{1}H within reasonable distances (<5 Å).[211] The mathematical

subtraction of the two spectra allows for the identification of ^{1}H peaks resulting from the most spatially proximal moieties of the two molecules of interest. In this work, STD NMR is predominantly used for probing the through-space interactions between guest (pharmaceutical drugs) and host molecules (starch hydrogels), as well as investigation of the proximity between H_2O molecules and the starch backbone in the hydrogel systems to complement WPT-CP NMR data.

STD NMR experiments of drug-loaded starch hydrogels were acquired using a Bruker Avance II 800 MHz spectrometer equipped with a triple resonance HR-MAS probe. Samples were spun at 6 kHz and experiments were carried out at 308 K, using π/2 *rf* of 8.62 μs, 64 scans and 16 dummy scans. All STD experiments were performed using a pulse a train of 50 ms shaped pulses for selective saturation of the starch matrix, using on- and off-resonance frequencies of 3.5 ppm and 50 ppm, respectively. Saturation times ranged from 0.1 to 10 s. A constant experiment length (saturation time + recycle delay) of 12 s was used.

To calculate the STD response (%), the peak intensities in the difference spectrum (STD_{OFF} - STD_{ON}, STD_{Δ}) were integrated relative to the peak intensities in the off-resonance (STD_0)[212], according to the Equation 2.25.

$$STD\ (\%) = \frac{STD_{\Delta}}{STD_0} \times 100 \qquad \textit{Equation 2.25}$$

Solution-state NMR Spectroscopy

Direct polarisation ^{13}C {^{1}H} Solution-state NMR spectra were acquired on a Bruker Avance I spectrometer, operating at ^{13}C frequency of 125.79 MHz, equipped with a 5 mm probe. Hydrogels were prepared directly in Pyrex® NMR tubes (Norell Inc.®),

starting with 10% (w/v) starch/D_2O suspensions with total volume of 700 µL and following all other gelatinisation and storage procedures (*see Hydrogel preparation section*). All ^{1}H and direct ^{13}C {^{1}H} detection experiments were acquired with a 10 µs ^{13}C *rf* pulse, 2.0 s relaxation delay, a minimum of 2000 scans and carried out at 25 °C. The short recycle delay was chosen to probe the structure of the liquid-like components in the hydrogels.

2.2.11 *Simulated Digestion and Fermentation*

Enzyme Activity Measurement

Salivary α-amylase

A 100-mg sample of soluble potato starch (Merck, CAS: 9005-25-8) was placed in a 20-mL volumetric flask, followed by the addition of PBS (0.01 M) to a total volume of 20 mL, the sample was inverted by hand and its contents transferred to a 25-mL conical flask, containing a stirrer bar. The vessel was clamped on a stand in a water bath set at 90 °C, and set to stir at 600 rpm for 20 min, allowing for the complete gelatinisation of the soluble potato starch. Once done, the sample was removed from the water bath and placed in incubator pre-set at 37 °C for 1 hour to allow for the temperature to equilibrate. 5-mL gelatinised starch samples were transferred to three 15-mL Corning® tubes, and placed on an end-over-end mixer in the incubator for further 5 min. Sample blanks (100 µL) were taken out to account for any reducing sugars already present in the starch sample, and added to centrifuge tubes containing $NaHCO_3$ (0.3 M, stop solution). This was followed by the addition of 100 µL of the salivary amylase of unknown activity to each of the three 15-mL sample tubes, and they were returned to the mixer inside the incubator. At pre-determined time points (3, 6, 9 and 12 min), 100-µL aliquots were

taken out of each digestion mixture and placed in further centrifuge tubes containing stop solution.

The concentration of reducing sugars in at each time point was quantified against a standard curve of known maltose concentrations (0, 50, 100, 250, 500, 750 and 1000 µM). This was done by doing a 20-fold dilution the reducing sugar samples of unknown concentration, and transferring 100 µL of the diluted samples, and of the samples containing maltose of known concentrations to new centrifuge tubes, followed by the addition of *para*-hydroxybenzoic acid hydrazine (*p*AHBAH, 250 mg, made up HCl (0.5 M, 4.75 mL), and NaOH (0.5 M, 45 mL)). The samples were placed in a water bath (99 °C) for 5 mi, then they were left to cool down for 15 min before measuring their absorbance on a UV/Vis spectrophotometer (Biochrom Libra S50 UV/Vis Spectrophotometer, λ_{max} = 405 nm).[213] The enzyme activity was expressed in units, where the definition of a unit is 1 mg enzyme liberating 1 mg of substrate every 3 min.

Pepsin

Pepsin (5 mg) was dissolved in NaCl (0.15 M, 5 mL), and the pH was adjusted to 6.5, using NaOH (0.1 M). This stock solution was serially diluted to make up samples of known concentrations of 5, 10, 15, 20 and 25 µg/mL in HCl (10 mM).

Bovine blood haemoglobin, Merck, CAS: 9008-02-0) was dissolved in HCl (60 mM), giving a final concentration of 2% w/v.

500 µL aliquots of the haemoglobin stock solution (2% w/v) were placed in five 2-mL centrifuge tubes at 37 °C for 30 min to allow for temperature equilibration, followed by the addition of the prepared pepsin (100 µL) solutions of known concentration. The samples were vortex mixed and incubated with end-over-end mixing at 37 °C for 10 min.

The assay was stopped by pipetting 1-mL aliquots of trichloroacetic acid (TCA, 5% w/v). The samples were then spun down (6000 g, 20 min), the supernatant was placed in plastic cuvettes and the absorbance was read at λ_{max} = 280 nm.[214,215]

The activity was calculated according to Equation 2.26.

$$Pepsin\ Activity\ \ U/mg = \frac{A_{\lambda 280}}{[Pepsin]} \times 100 \quad \textit{Equation 2.26}$$

Where [Pepsin] is the enzyme concentration in the sample. All pepsin activity values are within 20 units of each other (linear region).

Pancreatin Amylase Activity

The amylolytic activity of pancreatin was measured using the same protocol as for salivary α-amylase, with the only modification being that the samples were spun down (6000 g, 15 min) to remove the pancreatin agglomerates. The concentration of reducing sugars in the supernatants were then quantified using *p*-AHBAH (see salivary α-amylase section).

According to the INFOGEST protocol, pancreatin's activity is quantified against its trypsin activity[112], but for the purposes of this work, we have standardised it against its amylolytic activity, due to the nature of our pure starch substrates.

In vitro Digestion

Digestion was carried out in triplicate using a standardised static simulated digestion model developed by Minekus *et al*.,[112] modified to substitute $NaHCO_3$ and $[NH_4]HCO_3$ with bis-tris[216], due to the latter's higher buffering capacity in the range of pH 6.0 – 7.2.

Oral phase

Simulated salivary fluid (SSF, KCl (15.1 mM), KH_2PO_4 (3.7 mM), bis-tris (13.66 mM), $MgCl_2.6H_2O$ (0.15 mM), $CaCl_2.2H_2O$ (1.5 mM)) was added in a 1:1 ratio (v/w) to the hydrogel samples in 50.0-mL Corning® tubes, where the weight of each hydrogel sample was 2.0 g (± 0.1 g), where the total starch content in each hydrogel was 200 mg (± 20 mg). The temperature in the vessels was equilibrated at 37 °C, followed by the addition salivary a-amylase to give a final concentration of 75.0 IU mL^{-1}. All tubes were set up on an end-over-end rotator at a rate of 30 rpm and were incubated at 37.0 °C for 2 min.

Gastric phase

At the end of the oral phase, the pH of all samples was adjusted to 2.9 (± 0.05) using HCl (1.0 M), simulated gastric fluid (SGF, KCl (6.9 mM), KH_2PO_4 (0.9 mM), bis-tris (25.5 mM), NaCl (47.2 mM), $MgCl_2.6H_2O$ (0.1 mM), $CaCl_2.2H_2O$ (0.15 mM)) was added in a 1:1 ratio (v/v) to the oral phase mixture. Finally, pepsin was added to the digestion mixture to give a final concentration of 2000 IU mL^{-1}, and the gastric phase was incubated in an end-over-end rotator at a rate of 30 rpm, at 37 °C for 2 h.

Intestinal phase

Immediately after completion of the gastric phase the pH was raised to 7.0 (± 0.05) using NaOH (1.0 M), simulated intestinal fluid (SIF, KCl (6.8 mM), KH_2PO_4 (0.8 mM), bis-tris (85.0 mM), NaCl (38.4 mM), $MgCl_2.6H_2O$ (0.33 mM), $CaCl_2.2H_2O$ (0.6 mM), and bile (10.0 mM)) was added in a 1:1 (v/v) ratio with the gastric phase and finally pancreatin was added to give a final concentration of 100 IU mL^{-1}. The intestinal phase was incubated in an end-over-end rotator at a rate of 30 rpm, at 37 °C for 2 h.

Halting Digestion and Sample Collection

At the end of each simulated phase and at the mid-point of both the simulated gastric and small intestinal digestion steps (oral, O; gastric, G1 and G2; duodenal, D1 and D2), vessels were removed from the incubator, and the pH was raised to pH 9.0 (± 0.5) using $NaHCO_3$ (1.0 M) to halt enzymatic activity. The partially digested hydrogel substrates were rinsed in $NaHCO_3$ (1.0 M) twice more, and placed in phosphate buffered saline (PBS, 0.01 M) containing NaN_3 (0.02% w/v) and stored at 4 °C until further analysis. The digesta were stored at -20 °C for further analysis.

Quantification of Digested Starch Hydrogel

The starch hydrogel digesta were thawed out, vortex mixed for 10 s and spun down (Eppendorf Centrifuge 5810R) at 13,000 x g for 5 min, and the supernatant removed to a clean tube for analysis. The concentration of reducing sugars in the supernatant was analysed using the *p*AHBAH method against maltose standards.[213] The absorbance was measured using a UV-Vis spectrophotometer (Biochrom Libra S50 UV/Vis Spectrophotometer, λ_{max} = 405 nm).

Identification of Oligosaccharides and Reducing Sugars in Starch Digesta

The supernatants collected after spinning down the starch digesta were analysed on a Bruker Avance I spectrometer, operating at ^{13}C frequency of 125.79 MHz, equipped with a 5 mm probe. Aliquots of 600 µL were loaded into NMR tubes (Norell Inc.®). Direct ^{13}C detection with ^{1}H decoupling experiments were acquired with a 10 µs ^{13}C *rf* pulse, 4.0 s relaxation delay, a minimum of 256 scans, and carried out at 25 °C.

In vitro Fermentation

Participant Information and Ethics

Faecal sample was obtained from four adults (≥ 18 years old), free-living, healthy donors who had not taken antibiotics in the 3 months prior to donation, and were free from gastrointestinal disease. Ethical approval was granted by Human Research Governance Committee at the Quadram Institute (IFR01/2015) and London - Westminster Research Ethics Committee (15/LO/2169) and the trial was registered on clinicaltrials.gov (NCT02653001). A signed informed consent was obtained from the participant prior to donation. The stool sample was collected by the participant, stored in a closed container under ambient conditions, transferred to the laboratory and prepared for inoculation within 2 hours of excretion.

Batch model colon fermentation media ingredient recipe

Haemin solution was prepared by dissolving haemin (CAS: 16009-13-5, 0.05 g) in NaOH (0.05 M, 25.0 mL) and made up to 500 mL with boiled *dd*H_2O .

Resazurin solution was prepared by dissolving resazurin sodium salt (CAS: 62758-13-8, 0.05 g) in *dd*H_2O (50 mL).

Fatty acids solution was prepared by dissolving the following fatty acids in NaOH (0.2 M, 200 mL): acetic acid (1.37 mL), propionic acid (0.6 mL), butyric acid (0.368 mL), isobutyric acid (0.094 mL), 2-methylbutyric acid (0.11 mL), valeric acid (0.11 mL), and isovaleric acid (0.11 mL).

Trace minerals solution was prepared by dissolving the following salts in *dd*H_2O (1.0 L): manganese chloride tetrahydrate ($MnCl_2.4H_2O$), 25.0 mg), ferrous sulphate

heptahydrate ($FeSO_4.7H_2O$, 20.0 mg), zinc chloride ($ZnCl_2$, 25.0 mg), copper chloride dihydrate ($CuCl_2.2H_2O$, 25.0 mg), cobalt chloride hexahydrate ($CoCl_2.6H_2O$, 50.0 mg), selenium dioxide (SeO_2, 50.0 mg), nickel chloride hexahydrate ($NiCl_2.6H_2O$, 250 mg), sodium molybdate dihydrate ($NaMoO_4.2H_2O$, 250 mg), sodium metavanadate ($NaVaO_3$, 31.4 mg), boric acid (H_3BO_3, 250 mg).

Basal solution was prepared by the following in *dd*H_2O (4.0 L): potassium chloride (KCl, 3.57 g), sodium chloride (NaCl, 3.57 g), calcium chloride dihydrate ($CaCl_2.2H_2O$, 1.19 g), magnesium sulfate heptahydrate ($MgSO_4.7H_2O$, 2.97 g), 1,4-piperazinediethanesulfonic acid (Pipes, 7.84 g), ammonium chloride (NH_4Cl, 3.21 g), trypticase (5.95 g), resazurin solution (5.87 mL), trace minerals solution (59.46 mL), haemin solution (59.46 mL), fatty acids solution (59.46 mL). The pH was adjusted to 6.8 with concentrated potassium hydroxide (KOH) and the solution was made up to 5.0 L with *dd*H_2O. The basal solution was bubbled with CO_2 overnight, dispensed into sterilised serum bottles in aliquots of 76.0 mL, the vessels were sealed and autoclaved at 121 °C for 15 min.

Vitamins and phosphate solution was prepared by dissolving monobasic potassium phosphate (KH_2PO_4, 27.35 g) in *dd*H_2O (500 mL), followed by the addition of the following sequentially: biotin (10.2 mg), folic acid (10.3 mg), calcium (D)-pantothenate (82.0 mg), nicotinamide (82.0 mg), riboflavin (82.0 mg), thiamine hydrochloride (82.0 mg), pyridoxine hydrochloride (82.0 mg), p-aminobenzoic acid (10.2 mg), cyanocobalamin (10.3 mg). The solution was filter sterilised (0.22 µm, polyethersulfone membrane filter).

Carbonate buffer solution was prepared by dissolving sodium carbonate (Na_2CO_3, 41.0 g) in boiled *dd*H_2O (500 mL), dispensed into sterilised serum bottles in aliquots of 60.0

mL, sealed and autoclaved at 121 °C for 15 min. The vessels were bubbled through with CO_2 for 2 h shortly prior to use.

Reducing agent solution was prepared by dissolving (L)-cysteine hydrochloride (1.0 g) and sodium sulfide nonahydrate ($Na_2S{\cdot}9H_2O$, 1.0 g) in boiled *dd*H_2O, followed by adjusting the pH to 10.0 with concentrated NaOH.

Vitamin-phosphate/carbonate solution was prepared by the addition of vitamin and phosphate solution (see above, 15.0 mL) to each of the vessels containing carbonate buffer solution (see above) by injecting through the septa.

Faecal Sample Collection and Preparation for Inoculation

Faecal samples were obtained from 4 different subjects (see participant information and ethics section). Each volunteer was given a sample collection kit with instructions. The samples were produced inside sterilised plastic bags, sealed with a plastic clip, and placed in sealed plastic containers within 2 hours of inoculation. The containers were transferred to a sterilised class II safety cabinet (Walker Ltd, UK). An average of 30.0 g of donor stool sample was homogenised with sterile PBS (0.01 M) reduced in an anaerobic chamber overnight, in a ratio of 1:10, in a strainer bag (BA6141/STR, Seward Limited, UK) using a Stomacher® 400 Circulator (Seward Limited, UK) set to 200 r.p.m. for a duration of 30 s, resulting in diluted faecal slurry intended for inoculation.

Final Fermentation Vessel Preparation and Sampling

Simulated fermentation experiments were performed following the methodology of Williams *et al*. with some adaptations.[217] In brief, 100-mL sterile, septa-sealed fermentation vessels (76.0 mL basal solution, 5.0 mL vitamin-phosphate/carbonate

solution, 1.0 mL sulfide reducing solution) containing pre-digested (INFOGEST-treated) starch hydrogels (*ca*. 1.9 ± 0.1 g of pre-digested gel sample), were placed under CO_2 for 3 min each, and were left to equilibrate in an incubator at 37.0 °C the evening before inoculation. On the following day, inoculation was performed by injecting diluted faecal slurry (3.0 mL) directly through the septa of each fermentation bottle, using sterile 19G hypodermic needles and 10.0 mL syringes. Inoculation was carried out in a class II safety cabinet. All vessels were returned to the incubator immediately following inoculation.

Measurement of Total Gas Produced during Fermentation

At pre-determined time points (12, 24, 48 and 72 h after inoculation) bottles were taken out of the incubator and the gas produced was measured directly through the septa, using sterile 19G needles and 20 mL syringes, where the volume of gas measured at each time point was equal to the volume in the syringe (*i.e.,* distance of the plunger) being displaced.

Samples for Bacterial Metabolite Analysis

At pre-determined time points (0, 6, 12, 24, 48 and 72 h after inoculation) bottles were taken out of the incubator and the fermentation media was sampled (2.0 mL) in triplicate through the septa, using sterile 23G needles and 5.0 mL syringes. The samples were placed in labelled 2.0-mL screw-cap centrifuge tubes, spun down at 3,000 x g for 5 min at 4 °C (Thermo Heraeus Fresco 17 centrifuge). The supernatant was collected without disturbing the pellet, where both were retained and stored at -20.0 °C for further analyses.

Samples for NMR structural analyses, FISH and LSCM

At pre-determined time points (12, 24, 48 and 72 h following inoculation), vessels were removed from the incubator and placed in an ice bath for 10 min. The starch hydrogels intended for solid-state NMR analyses were tipped out into 5.0 mL sterile vessels containing $NaHCO_3$ (1.0 M), swirled gently for 1.0 min and placed under PBS (0.01 M), containing NaN_3 (0.02% w/v); and the hydrogels intended for hybridisation and microscopy – in sterile vessels containing cold (4.0 °C) formaldehyde (4.0% in 0.01 M PBS) and left in the fixative at 4.0 °C overnight. Hydrogel sampling was performed in duplicate for each time point of the *in vitro* fermentation.

2.2.12 *Starch Branching Analyses*

Starch Branching analysis was performed as described in Tizzotti *et al*.[218] Starch hydrogels sampled at the end of the simulated digestion treatment and after 24, 48 and 72 hours of *in vitro* fermentation were flash frozen in liquid N_2, freeze-dried (Thermo ModuLyod freeze drier) for 3 days, manually ground using mortar and pestle, and dissolved in DMSO-d_6 (containing LiBr 0.5% w/v) at a concentration of 2.85 mg mL^{-1}. Samples were vortex-mixed for 10 s, followed by the addition of 600-µL aliquots of the solutions directly into NMR tubes (Norell® Select Series™, 5 mm). A single drop of TFA-d_1 was added to each NMR tube immediately prior to spectral acquisition using a Pasteur pipette. The NMR experiments were performed on a Bruker Avance II NMR spectrometer, operating at a ^1H frequency of 500.11 MHz, equipped with an inverse triple resonance z-gradient probe. The acquisition parameters were π/2 *rf* pulse on ^1H of 10 s, recycle delay of 12 s, acquisition time of 3.2 s, and 128 scans. All experiments were performed in triplicate. The degree of branching (DB) was determined as the percentage of the integration of the peak at 4.78 ppm, out of the combined proportion

of the peaks at 5.10 and 4.78 ppm, associated with α(1-4) and α(1-6) glycosidic linkages, respectively.

2.2.13 *Bacterial Metabolite and Small Molecule (Drug) Release Quantification*

The samples containing the supernatant from the fermentation media were thawed out, spun down (3,000 x g for 3 min) and 400 µL aliquots were pipetted directly into NMR tubes (Norell® Standard Series™, 5 mm), followed by the addition of 200 µL of phosphate buffer (NaH_2PO_4 (21.7 mM), K_2HPO_4 (82.7 mM), NaN_3 (8.6 mM), 3-(trimethylsilyl)-propionate-d_4 (TMSP, 1.0 mM)).[219] The spectra were recorded on a Bruker Avance III 800 MHz spectrometer, equipped with an inverse triple resonance z-gradient probe. All ^1H NMR spectra acquired on the 800 MHz spectrometer were obtained using 256 scans, a spectral width of 9615 Hz, acquisition time of 0.83 s, using Bruker's '*noesygppr1d*' pulse sequence, featuring selective low-power pre-saturation (p16 = 1.0 ms) on the residual H_2O peak frequency during relaxation delay and mixing time for effective solvent suppression. Spectra were apodised using 0.1 Hz line broadening and referenced using the TMSP peak (0.0 ppm). Recycle delay was set to 10 s, the mixing time used was 0.1 s, and the π/2 *rf* pulse was 9.08 µs. Acetate, propionate, butyrate, succinate, lactate, glucose and maltose were quantified using the NMR Suite v7.6 Profiler (Chenomx®, Edmonton, Canada).

The small molecular release in the fermentation media was quantified against the TMSP reference, using the acquisition parameters above, on the basis of standard curves of known concentrations of small molecules in phosphate buffer.

Standard curves of known concentrations of the three model drugs chosen were made up in NMR buffer, where each sample was made up of 600 µL NMR buffer, containing

0.1, 0.2, 0.5, 0.75, 1.0, 1.5 and 2.0 mM of the small molecule of choice. Standard curves were built based on the ratio between the known concentration of small molecule and the ratio of the area under the peak of TMSP (-CH_3, 0 ppm) and the ^{1}H peak of choice of each of the small molecules (CHO, 9.6 ppm, VNL; NH, 7.7 ppm, 5FU; Ar ^{1}H, 7.9 ppm, DOX).

2.2.14 *Fluorescence in-situ Hybridisation (FISH)*

The fixed hydrogel samples were removed from the formaldehyde solution, placed in 2.5 mL embedding plastic boats, and covered in mounting medium (PolyFreeze O.C.T. medium, Merck SHH0026). The embedding boats were gently placed in an EtOH/dry ice bath until fully solidified. Embedded samples were mounted on cryostubs and sectioned on a CryoStat (Thermo CryoStar NX70) equilibrated at -10.0 °C, at 20.0 µm width, placed directly on sterile polysine adhesion microscopy slides (Thermo Scientific™ 10219280) and left to air dry in a fume cabinet overnight. Hybridisation was performed following the methodology described in the work of Gorham *et al*.,[113] with some adjustments, where 10.0 µL of hybridisation buffer (NaCl 5.0 M, Tris.HCl 1.0 M, formamide 25%, sodium dodecyl sulfate (SDS) 10%) was placed on top of each section, followed by the addition of 20.0 µL of each probe (Table 2.1), where the concentration of each probe was 50.0 ng μL^{-1}. Slides were placed in aluminium foil-wrapped 50.0-mL Corning® tubes and placed horizontally in an incubator set at 58.0 °C, and left overnight to hybridise. After hybridisation, the slides were recovered and washing buffer (NaCl 5.0 M, Tris.HCl 1.0 M, ethylenediaminetetraacetic acid (EDTA) 0.5 M, SDS 10%) was gently pipetted on top of each hydrogel section twice, followed by cold *dd*H_2O and leaving the slides to air dry in the dark. Prior to visualization, approximately 10.0 µL of Vectashield® anti-fade

medium (VectorLabs, Maravai LifeSciences, Peterborough, UK) was gently pipetted on top of each resin, followed by placing a glass coversheet on top.

The deviations from the original protocol by Gorham *et al*.,[113] such as the increased volume of hybridisation buffer per sample (10.0 *vs*. 8.0 µL in the original protocol), and volume of bacterial probes (20.0 *vs.* 0.5 µL), as well as the duration (overnight *vs*. 1 h in the original protocol), and temperature of hybridisation (58.0 *vs*. 46.0 °C in the original protocol) were adopted, due to the high surface area of our sectioned samples, relative to those in Gorham *et al*., as well as due to the increased resistance to digestion and fermentation of our retrograded hydrogel substrates, compared to the feeds used in the study by Gorham *et al*.[113]

Table 2.1. List of fluorescent probe-tagged oligonucleotides for sequence-specific hybridisation with commensal bacteria in fermented starch matrices.

Probe name	Sequence (5' - 3')	Concentration (ng μL^{-1})	Storage Solution	Modification	Purchased From
Rbro730	TAAAGCCCAGYAGGCCG	50.0	Tris.HCl 10 mM, EDTA 1 mM, pH 8.1	5'-AF350	*Eurofins*
Bif164	CATCCGGCATTACCACCC	50.0	Tris.HCl 10 mM, EDTA 1 mM, pH 8.1	5'-ATTO740	*Eurofins*
Bac303	CCAATGTGGGGGACCTT	50.0	Tris.HCl 10 mM, EDTA 1 mM, pH 8.1	5'-RED	*Eurofins*
Eub338I	GCTGCCTCCCGTAGGAG	50.0	Tris.HCl 1 mM, EDTA 0.1 mM, pH 6.9	5'-CY5	*Eurofins*
Eub338II	GCAGCCACCCGTAGGTG	50.0	Tris.HCl 1 mM, EDTA 0.1 mM, pH 6.9	5'-CY5	*Eurofins*
Eub338III	GCTGCCACCCGTAGGTG	50.0	Tris.HCl 1 mM, EDTA 0.1 mM, pH 6.9	5'-CY5	*Eurofins*

2.2.15 *Laser Scanning Confocal Microscopy Visualisation*

Slides were visualised on a Zeiss LSM 880 Confocal Microscope, equipped with a fluorescent mercury lamp, a diode (405 nm), Ar (458, 488, 514 nm), DPSS (561 nm) and He-Ne (594,633 nm) lasers for visualisation of AF350 (λ_{ex} = 350 nm), TxRed (λ_{ex} = 595 nm), CY5 (λ_{ex} = 645 nm) and ATTO740 (λ_{ex} = 743 nm) fluorescent tags. All images were

taken under x10 (0.45, air) and x20 (0.8, air) magnification objectives, obtained and processed using the ZEN® Pro software package (Carl Zeiss Microscopy GmbH, Jena, Germany).

2.2.16 *Size-Exclusion Chromatography (SEC)*

Principles

The determination of the molecular structural parameters of amylose and amylopectin molecules in starch is pivotal for drawing structure-function links regarding starch' physicochemical properties and behaviour in the human GIT. Size-exclusion chromatography (SEC, *a.k.a.* gel permeation chromatography, GPC) is one of most common means of separating polymers based on their molecular size (not molecular weight), and more specifically – based on their hydrodynamic volume (V_h), where the IUPAC definition of V_h is based on the volume of a hydrodynamically equivalent impenetrable sphere, exhibiting the same frictional effect in a hydrodynamic field, as the polymer molecule. V_h is related to the hydrodynamic radius (R_h) of a polymer through Equation 2.27, and the size of a polymer quantified through SEC is usually reported either as its V_h or R_h, and not based on the elution time of the polymer fraction, as this latter property is heavily dependent on the instrument set-up, and day-to-day variability in separation processes.[220]

$$V_h = \frac{4}{3}\pi R_h^3 \qquad \textit{Equation 2.27}$$

The instrument is usually calibrated through a combination of polymers of narrow dispersity (pullulans – glucose polymers in this case, see below), through their molecular

weight (*Mw*), intrinsic viscosity for a given molecular weight ($[\eta]_{Mw}$, established viscometrically), and Avogadro's constant (N_A) through Equation 2.28.

$$V_h = \frac{2}{5}\frac{Mw[\eta]_{Mw}}{N_A} \qquad \textit{Equation 2.28}$$

The relationship between V_h and *Mw* is then fitted to the Mark-Houwink relation (Equation 2.29).

$$V_h = \frac{2}{5}\frac{KMw^{1+a}}{N_A} \qquad \textit{Equation 2.29}$$

Where *K* and α are Mark-Houwink parameters which depend on the polymer-solvent system. The pullulan standards are then used to relate elution time (t_{el}), elution volume (V_{el}) and V_h. All SEC data (both branched and debranched) in this work is obtained through a differential refractive index (DRI) detector, which relates the V_{el} detector signal $S_{DRI}(V_{el})$ to the weight distribution of the polymer - $w(\log V_h)$, through Equation 2.30.

$$w(logV_h) = S_{DRI}(V_{el})\frac{\Delta V_{el}}{\Delta logV_h} \qquad \textit{Equation 2.30}$$

It should be noted that the normalisation (if any) of $w(\log V_h)$ is arbitrary. Most research using SEC of starch make use of normalisation against the amylopectin peak distribution of greatest intensity, but this can artificially conceal small differences and changes in the overall weight distribution.[221–223] In light of this, for the purposes of this work, we have chosen to carry out standard normal variate and 0-order detrend (Appendix) in order to avoid artificially concealing potentially relevant changes in the weight distribution of the samples.

Sample preparation and column running conditions are very important in SEC in both branched and debranched polymers, in order to avoid artefacts generated from shear scission of highly branched molecules, such as amylopectin, which can result in artificial band broadening and misleading results, thus disabling one from gaining quantitative information about the amylopectin distribution in branched samples. This is one of the reasons why it is usually recommended to run both branched and debranched samples when probing the size distributions in starch through means of SEC. [224] Furthermore, a solvent (mobile phase) needs to be optimised for the sample, in order to achieve maximal (ideally complete) solubility of the sample. In the case of starch, this has been extensively investigated, where the optimal solvent found for most starch samples is filtered DMSO, containing LiBr (0.5% w/v) acting as a hydrogen bond disruptor. [224]

Experimental Procedures

Undigested, digested, and fermented hydrogel samples intended for SEC and fluorophore-assisted carbohydrate electrophoresis (FACE) were flash frozen under liquid N_2 and freeze-dried for 5 days, followed by manual grinding using a mortar and pestle. Samples for debranched SEC and FACE were debranched following Wu *et al*.[225]

Starch samples intended for debranching (5.0 mg) were dissolved in DMSO/LiBr (1.5 mL, 0.5% w/v), followed by being placed in a thermomixer at 80 °C, at 600 rpm over 24 hours. The following day, the samples were spun down (4000 g, 10 min), and the supernatant was removed, followed by the addition of *dd*H_2O (0.9 mL), and placing the samples in a water bath (95 °C, 1 hour).

The samples were then cooled to room temperature, NaOAc was added (0.1 M, 0.1 mL, pH 3.5), followed by the addition of isoamylase (2.5 µL, Megazyme, CAS: 9067-73-6), and

the mixture was placed on a thermomixer at 37 °C for 3 hours. The solution was neutralised (NaOH, 0.1 M), followed by being heated at 80 °C for 1 hour. The samples were then flash frozen in liquid N_2 and freeze-dried over 3 days.

Branched at debranched samples were then dissolved in DMSO/LiBr (0.5% w/v) at 2 $mg.mL^{-1}$ and 4 $mg.mL^{-1}$, respectively, and placed on a thermomixer at 80 °C, at 600 rpm overnight. The samples were recovered, spun down (4000 g, 5 min), and the supernatant was transferred to HPLC vials (Fischer Scientific, 10080952).[225] All samples were run at 80.0 °C, with DMSO/LiBr (0.5%) as the mobile phase, at a flow rate of 0.3 and 0.6 mL min^{-1} for branched and debranched samples, respectively. The mobile phase was prepared by dissolving LiBr (0.5% w/v) in DMSO under sonication for 1 h, followed by filtration under pressure (0.45 µm, PTFE membrane).

The molecular structural parameters of whole starch molecules in the hydrogels were characterised using an Agilent 1100 series SEC system (Agilent Technologies, Santa Clara, CA) equipped with a Shimadzu RID-10A differential refractive index detector (Shimadzu Corporation, Kyoto, Japan). Fully branched samples were run using GRAM 30 and GRAM 3000 columns (Polymer Standards Service (PSS), GmbH, Mainz, Germany) connected sequentially, providing separation in the range of 5_X10^3 – 5_X10^6 Da (R_h of 0.5 – 50.0 nm), whereas debranched samples were analysed using GRAM 30 and GRAM 1000 columns, appropriate for separation in the range of 100 – 10^6 Da. The samples were run alongside a series of pullulan standards (PSS, GmbH, Mainz, Germany) in the range of 180 Da – 1.2_X10^6 Da for calibration purposes (*see above*), using the methods described in Li *et al*.[226] Elution time was converted to R_h, and (for debranched samples)

from R_h – to the degree of polymerization (DP) X, using the Mark-Houwink relation[227], giving X (R_h).

2.2.17 *Fluorophore-assisted carbohydrate electrophoresis (FACE)*

Principles

FACE relies on the separation of polymeric carbohydrates based on labelling the single reducing end of polysaccharides of various lengths using either aromatic primary amines or polysulfonic acid derivatives of naphthalene, containing both a fluorophore and a charged end. In this work, 8-aminopyrene-1,3,6-trisulfonate (APTS) was used as the label, where the NH_2 group performs a nucleophilic attack on the reducing end (in the hemiacetal form) of linear (*i.e.*, debranched) starch, forming a Schiff's base-type amine, which is further reduced with $NaCNBH_3$ resulting in the formation of a secondary amine and a covalently linked label (Figure 2.20). The presence of both a fluorophore and a charge on the label allows for the electrophoretic size separation of linear glucans, and their detection via spectrophotometric (fluorescence detection) methods. The introduction of a single label per starch chain (single reducing end to act as an electrophile) allows for quantification of both length and mass, provided the molar mass of the monomer is known, and the polymer in question is homopolymeric.[225,228,229]

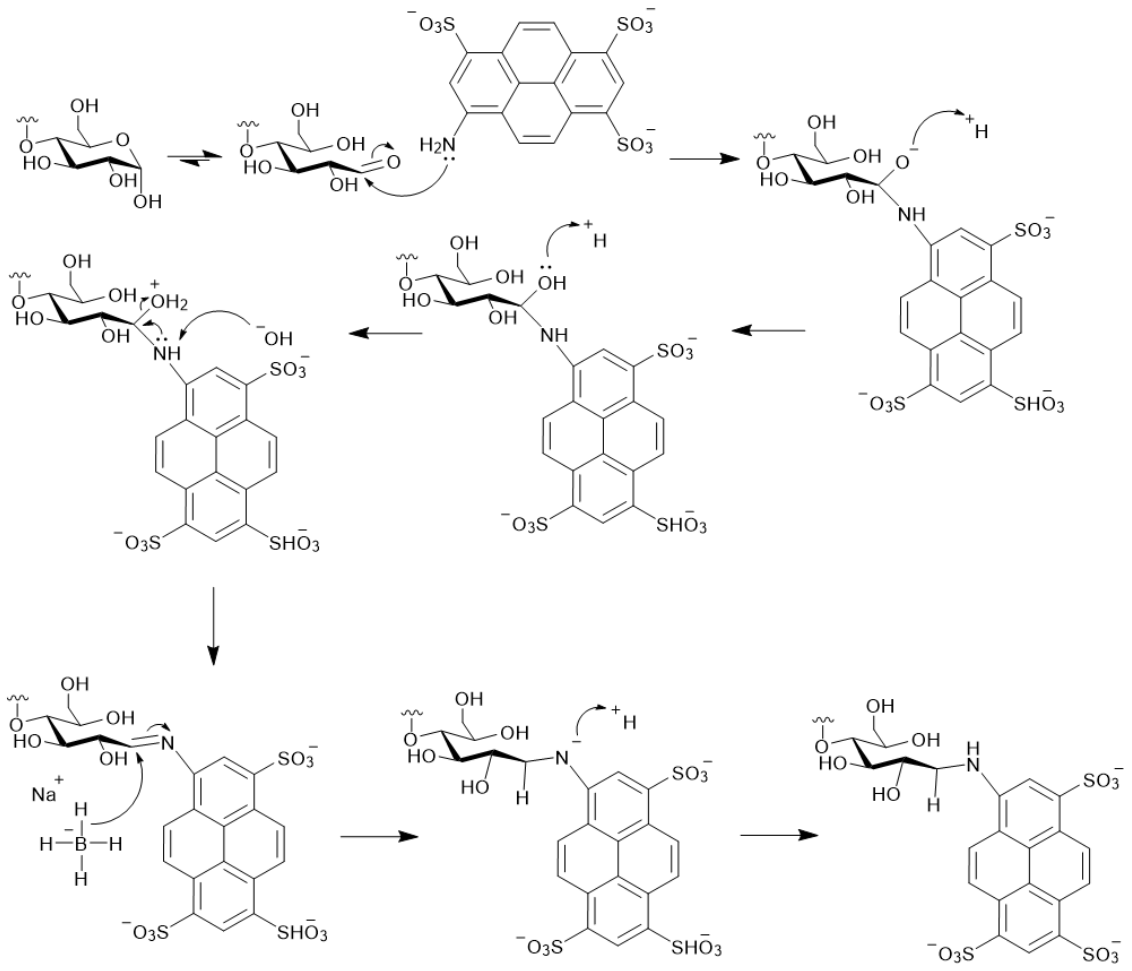

Figure 2.20: Mechanism for labelling the reducing end of starch with APTS through a nucleophilic substitution, followed by reductive amination using $NaCNBH_3$.

Experimental Procedures

The debranched samples intended for FACE analysis were labelled using APTS (Carbohydrate Labelling and Analysis Kit, Beckman Coulter, Brea, CA, USA) according to Wu *et al*.[225] (*see* above). The samples were analysed on a PA-800 Plus FACE System (Beckman-Coulter, Brea, CA, USA), coupled with a solid-state laser-induced fluorescence (LIF) detector and an argon-ion laser as the excitation source. The separation was carried out in an N-CHO-coated capillary (50.0-µm in diameter, Carbohydrate Labelling and Analysis Kit). The sample was introduced into the capillary in a carbohydrate separation

buffer (Beckman-Coulter, 477623) by pressure injection for 3.0 s at 0.5 psi. Separation of the labelled linear glucans was achieved using an applied voltage of 28–30.0 kV (≈14.0 mA) at 25.0 °C, where the first ≈120 peaks were separated over a total time of 60 min. Under these conditions, the chain length distribution (CLD) of all debranched samples was analysed and presented as percentile contribution of each DP to the total CLD, where DP is the number-average degree of polymerisation. min. Elution time was converted to R_h, and (for debranched samples) from R_h – to the degree of polymerization (DP) X, using the Mark-Houwink relation[227], giving X (R_h).

2.2.18 *Statistical analyses*

A two-tailed, paired t test was performed on all quantitative NMR measurements with a confidence interval of 95%. The statistical significance of the changes in degree of branching following *in vitro* digestion and fermentation, as well as the changes in the concentration of bacterial metabolites in the presence of the three guest molecules – vanillin, 5-fluorouracil and doxorubicin compared to the controls, were assessed using a 2-way analysis of variance (ANOVA) with Tukey's multiple comparisons test with a 95% confidence interval, using GraphPad Prism 9.0.0 (GraphPad Software, Inc.) statistical software.

Chapter 3: Structural Organisation of Starch Hydrogels

Results from this chapter are largely published in:

Todor T. Koev, Juan C. Muñoz-García, Dinu Iuga, Yaroslav Z. Khimyak, Frederick J. Warren. *Carbohydrate Polymers* (2020). 249 (1): 116834

3.1 Introduction

In order to fully understand the behaviour of starch hydrogels in different environments, we must first obtain a highly detailed characterisation of the structural assemblies making up their supramolecular organisation, the dynamic and motional effects of their structural moieties, intercomponent interactions, and how all of these contribute to the molecular- and bulk-level structural properties we observe.

We aim to establish the presence of components of disparate dynamics, and to quantify their molecular motions, and to correlate these with bulk system properties, such as gel micromechanics. We aim to explore the role of water molecules in the internal assembly of starch gel networks, and discriminate between tightly-associated and loosely bound water molecules in the hydrogel systems. We aim to build on the currently existing structural understanding and models of amylose gels, initially developed by Jane and Robyt[164] and Leloup *et al*.[161], and establish a model for the internal organisation of starch hydrogels. The purpose of this investigation is to establish structure-function links within starch hydrogels, which would be exploited for their application-driven tuning of properties. Our work also aims to develop a toolkit of advanced NMR spectroscopic techniques for establishing links between molecular level structural organisation, dynamics, and bulk system properties within highly heterogeneous soft matter starch hydrogel systems.

The impact of amylose content on the physicochemical properties of starch has been well documented in the literature.[142,148,230] In this chapter we aim to investigate the molecular-level structural parameters of maize starch gels of different amylose content, ranging from less than 1% to *ca*. 70%, and how these contribute to the bulk structural

behaviour of the starch hydrogel systems. We probe the effect of glucan (amylose and amylopectin) composition, short- and long-range molecular order, molecular mobility, molecular structural parameters (hydrodynamic radius, R_h, degree of polymerisation, DP, and chain length distribution, CLD), and the role of water in macromolecular hydrogel assembly and structural integrity. We also investigate the effect of storage conditions following gelatinisation on the starch gel strength, degree of crystallinity, and molecular mobility.

We discuss our findings in the context of existing models of starch hydrogel organisation, with the aim of contributing to the currently existing models of amylose gel organisation, originated by Jane and Robyt[164] and Leloup *et al*.[161] In particular, we expand on the continuous model of amylose gels made up of closely packed helices, interconnected by amorphous "dangling" chains within the porous cavities of the gel matrices, by providing quantitative data on the mobile nature of these moieties, and how this relates to the gels' bulk system properties.

3.2 Results and Discussion

3.2.1 *Bulk Properties of Starch Hydrogels*

We characterised the composition and properties of the granular starches used for the production of hydrogels, namely waxy maize (WM), normal maize (NM), amylomaize (AM), Hylon VII® (H7) and Hi-maize 260® (HM) starch. The results of moisture and amylose contents, swelling power and short-range order, and total amorphous contribution of all five starch powders are presented in Table 3.1, and images of the outer physical appearance of all five starch gels can be seen in Figure 3.1. All results are in good overall agreement with previously reported data. [1,141,186,231–233] All of these bulk

properties have been shown to have an impact on the physicochemical behaviour of starch. [1,141,186,232] In this chapter, we aim to probe the origin of and contributions to starch hydrogels' micromechanical, thermal and hydration properties on a molecular level, focusing on starch chain length, solvation, mobility, and dynamics.

Table 3.1: Material characterisation data of waxy maize (WM), normal maize (NM), amylomaize (AM), Hylon VII® and Hi-maize 260® (HM) starch powder samples.

Starch Type	Moisture Content (%)	Amylose Content (%)	Swelling Power (wet/dry weight)	Short-Range Order via CP/MAS NMR (%)[207]	Amorphous Content via PXRD (%)[186]
WM	12.2 (±0.2)	1.1 (±0.6)	10.7 (±0.1)	38.4 (±1.5)	66.3 (R^2 = 0.9800)
NM	12.2 (±0.2)	23.1 (±0.4)	13.3 (±0.9)	36.6 (±1.5)	69.7 (R^2 = 0.9900)
AM	11.3 (±0.1)	51.8 (±0.5)	4.6 (±0.3)	25.3 (±1.0)	77.0 (R^2 = 0.9810)
H7	11.5 (±0.6)	69.5 (±0.4)	4.8 (±0.5)	21.8 (±0.9)	80.8 (R^2 = 0.9800)
HM	11.2 (±0.2)	69.7 (±0.7)	2.8 (±0.2)	30.8 (±1.2)	70.8 (R^2 = 0.9910)

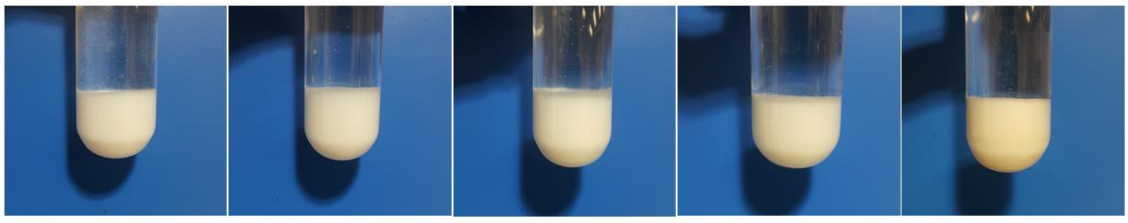

Figure 3.1: Photo of the five starch hydrogels in 25-mL Pyrex® vials, in order of increasing amylose content, produced from waxy maize (WM), normal maize (NM), amylomaize (AM), Hylon VII® (H7) and Hi-maize 270® starch, following gelatinisation and subsequent 8-day storage at 4 °C (retrogradation).

Thermal properties

DSC thermograms of all five maize starch powders and all starch can be seen in Figure 3.2, along with the thermal parameters defining each endothermic transition detected in their respective thermograms in Tables 3.2-3.5. The data collected for the starch powder samples were in good overall agreement with previously published data.[140,143]

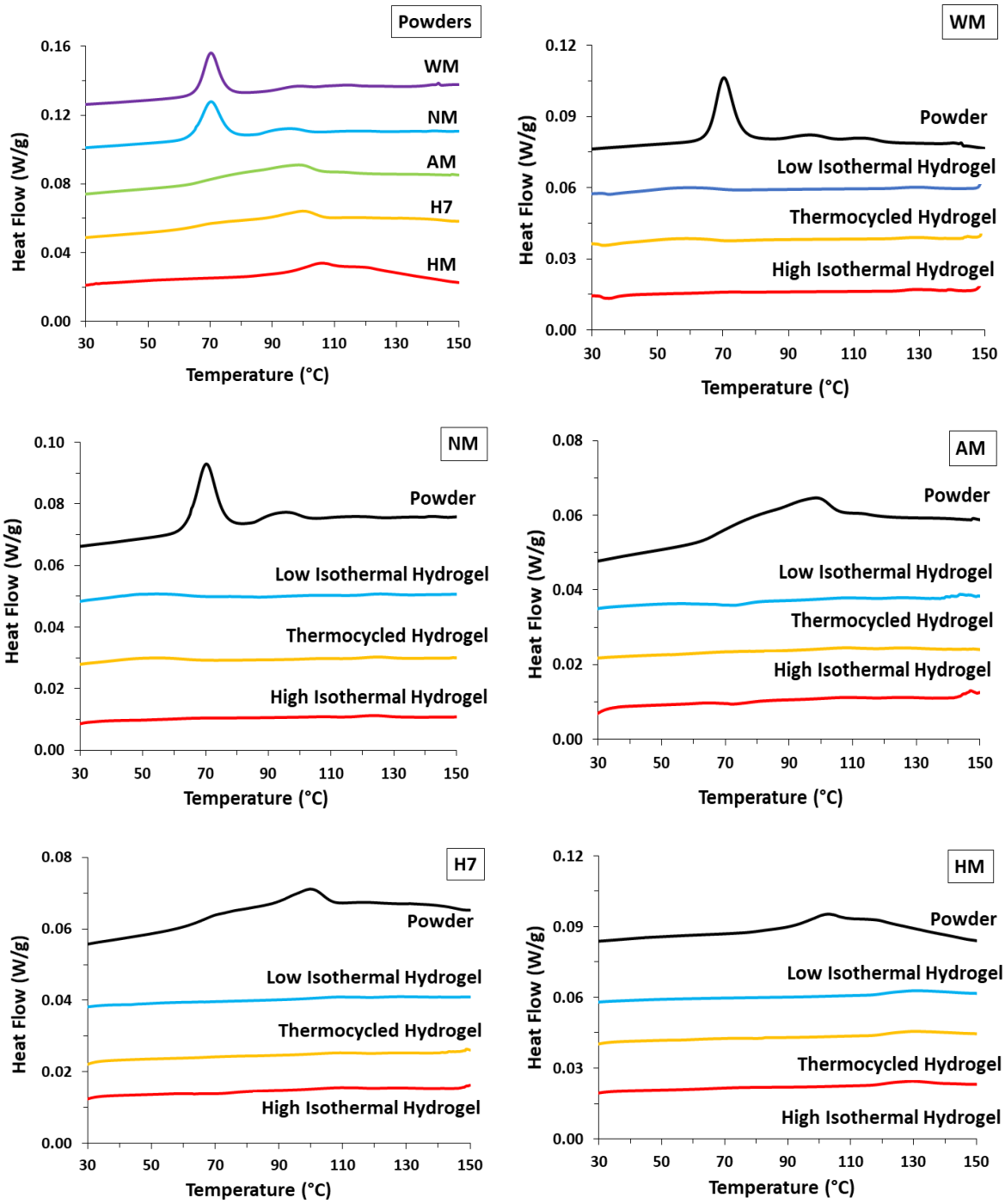

Figure 3.2: Composite DSC thermograms of waxy maize (WM), normal maize (NM), amylomaize (AM), Hylon VII™ (H7) and Hi-Maize 260™ (HM) starch powders, and their corresponding hydrogels prepared under different storage conditions (see materials and methods). Curves have been offset for visual clarity purposes.

Table 3.2: Gelatinisation parameters (onset temperature, T_O; peak temperature, T_P; concluding temperature, T_C; and enthalpy of transition, ΔH) defining each endothermic transition in the thermograms of waxy maize (WM), normal maize (NM), amylomaize (AM), Hylon VII® (H7), Hi-maize 260® (HM) starch powders.

Gelatinisation parameters	Starch Powders													
	WM			NM			AM		H7			HM		
T_O (°C)	61.2± 1.2	87.6± 0.8	108.4± 0.8	64.2± 1.1	85.4± 1.5	107.3± 1.0	62.8± 1.4	108.7± 1.1	60.7± 0.9	110.5± 1.4	129.2± 1.3	89.1± 0.8	110.9± 1.2	138.3± 1.6
T_P (°C)	70.2± 1.6	96.6± 1.0	113.6± 1.1	71.2± 1.4	94.7± 1.7	116.7± 2.1	96.1± 1.2	113.1± 1.5	99.4± 1.1	117.9± 1.1	139.1± 1.1	102.9± 1.1	118.2± 1.4	146.1± 1.2
T_C (°C)	81.2± 0.8	105.5± 1.4	120.4± 1.6	81.0± 1.2	107.3± 0.8	127.0± 1.8	107.4± 1.0	124.2± 1.6	108.2± 0.9	124.5± 1.2	147.0± 0.9	108.7± 1.2	122.6± 1.1	148.1± 1.8
$T_C - T_O$ (°C)	20.0± 2.0	17.8± 1.1	12.0± 0.8	16.9± 0.8	21.9± 1.8	19.7± 1.7	44.5± 1.8	15.5± 0.6	47.5± 2.1	14.0± 0.3	17.8± 0.5	19.6± 0.9	11.8± 0.3	9.8± 0.2
ΔH (J/g)	10.6± 0.9	1.0± 0.2	0.5± 0.1	9.8± 0.8	1.8± 0.4	0.4± 0.1	9.2± 1.2	0.01± 0.0	7.5± 0.6	0.0± 0.0	0.4± 0.1	1.2± 0.2	0.3± 0.0	0.0± 0.0

Table 3.3: Gelatinisation parameters (onset temperature, T_O; peak temperature, T_P; concluding temperature, T_C; and enthalpy of transition, ΔH) defining each endothermic transition in the thermograms of waxy maize (WM), normal maize (NM), amylomaize (AM), Hylon VII® (H7), Hi-maize 260® (HM) low isothermally stored hydrogels (*see materials and methods*).

Gelatinisation parameters	Low Isothermal															
	WM		NM			AM				H7				HM		
T_O (°C)	25.0 ±1.1	110.6 ±1.0	29.0 ±0.4	82.8± 1.2	108.5 ±1.4	24.3 ±1.2	68.4± 1.1	88.3± 1.0	109.4 ±1.1	26.8 ±1.2	87.7± 1.2	110.2 ±0.8	134.9 ±1.4	26.0 ±1.4	100.6 ±1.1	142.8 ±0.9
T_P (°C)	46.5 ±1.0	119.5 ±0.8	45.4 ±0.9	95.5± 1.4	114.7 ±1.6	43.0 ±1.2	98.7± 1.7	98.7± 1.2	115.1 ±1.9	34.5 ±1.7	98.9± 0.9	116.7 ±0.4	138.5 ±1.8	44.0 ±1.9	111.6 ±0.9	147.2 ±1.1
$_C$ (°C)	62.0 ±1.4	127.8 ±0.9	63.3 ±1.1	104.7 ±1.2	122.5 ±1.1	66.1 ±1.5	108.2 ±1.9	107.9 ±1.2	122.9 ±1.6	68.3 ±1.8	108.9 ±1.4	123.7 ±1.2	140.7 ±1.3	76.6 ±0.9	126.6 ±1.2	149.4 ±1.3
$T_C - T_O$ (°C)	37.0 ±0.5	17.3± 0.2	34.3 ±1.2	21.9± 1.0	14.0± 0.8	41.8 ±1.7	39.8± 1.9	19.7± 0.6	13.5± 0.2	41.5 ±2.1	21.2± 07	13.6± 0.3	5.8± 0.1	50.5 ±1.4	26.0± 1.0	6.6± 0.2
ΔH (J/g)	2.3± 0.2	0.4± 0.1	2.0± 0.2	0.2± 0.0	0.2± 0.0	2.5± 0.1	0.2± 0.0	0.3± 0.0	0.1± 0.0	0.6± 0.1	0.25± 0.0	0.1± 0.0	0.1± 0.0	1.0± 0.0	1.5± 0.1	0.2± 0.0

Table 3.4: Gelatinisation parameters (onset temperature, T_O; peak temperature, T_P; concluding temperature, T_C; and enthalpy of transition, ΔH) defining each endothermic transition in the thermograms of waxy maize (WM), normal maize (NM), amylomaize (AM), Hylon VII® (H7), Hi-maize 260® (HM) thermocycled starch hydrogels (*see materials and methods*).

Gelatinisation parameters	Thermocycled															
	WM		NM			AM				H7				HM		
T_O (°C)	23.2 ±0.9	111.3 ±1.2	25.0 ±0.9	90.9± 1.2	107.0 ±1.4	23.9 ±1.0	52.0 ±1.4	85.1± 1.6	108.6 ±1.7	33.4 ±0.7	88.2± 1.1	110.3 ±1.7	133.5 ±0.8	25.6 ±.09	101.0 ±2.1	140.6 ±1.2
T_P (°C)	45.4 ±1.1	118.9 ±1.6	45.1 ±1.1	98.2± 1.6	114.1 ±1.0	31.0 ±0.8	64.1 ±0.8	98.2± 1.2	115.8 ±1.1	67.3 ±0.9	99.2± 1.0	116.3 ±1.2	135.9 ±1.2	33.8 ±1.1	111.7 ±1.7	142.0 ±1.5
T_C (°C)	61.6 ±1.4	126.4 ±1.9	63.2 ±1.3	103.1 ±1.2	121.3 ±1.1	49.6 ±1.5	78.5 ±1.1	106.9 ±1.2	123.5 ±1.0	77.5 ±1.5	108.6 ±0.8	124.6 ±1.9	139.2 ±1.4	69.5 ±1.2	129.3 ±2.2	144.1 ±1.6
$T_C - T_O$ (°C)	38.4 ±0.9	15.1± 0.6	38.2 ±1.8	12.2± 0.7	13.8± 0.4	25.7 ±1.6	26.5 ±1.2	21.8± 1.1	14.9± 0.6	44.2 ±1.9	20.4± 0.4	14.3± 0.2	5.7± 0.1	43.9 ±2.3	28.3± 1.2	3.5± 0.4
Δ*H* (J/g)	2.3± 0.3	0.3± 0.0	2.5± 0.1	0.1± 0.0	0.2± 0.0	0.4± 0.0	0.2± 0.0	0.3± 0.0	0.1± 0.0	0.2± 0.0	0.2± 0.0	0.1± 0.0	0.1± 0.0	1.7± 0.2	1.8± 0.2	0.02± 0.0

Table 3.5: Gelatinisation parameters (onset temperature, T_O; peak temperature, T_P; concluding temperature, T_C; and enthalpy of transition, ΔH) defining each endothermic transition in the thermograms of waxy maize (WM), normal maize (NM), amylomaize (AM), Hylon VII® (H7), Hi-maize 260® (HM) high isothermally stored starch hydrogels (*see materials and methods*).

Gelatinisation parameters	High Isothermal																
	WM		NM			AM				H7					HM		
T_O (°C)	26.0 ±0.8	112.2 ±1.7	26.8 ±1.1	93.03 ±2.1	106.5 ±1.4	50.7 ±1.1	69.4 ±1.4	87.7± 1.8	109.0 ±0.0	32.9 ±0.1	67.7 ±0.1	89.6 ±0.2	110.9 ±0.1	136.0 ±0.1	25.9 ±0.1	100.7 ±0.2	133.6 ±0.1
T_P (°C)	33.0 ±1.1	118.7 ±2.1	34.8 ±1.3	98.1± 1.4	113.2 ±1.1	59.2 ±1.2	74.7 ±2.1	98.1± 1.5	114.1 ±0.1	52.9 ±0.2	73.9 ±0.1	99.6 ±0.1	116.9 ±0.2	138.2 ±0.2	32.6 ±0.1	111.1 ±0.1	140.1 ±0.2
T_C (°C)	60.6 ±1.4	127.9 ±1.4	62.6 ±1.2	104.8 ±1.8	120.0 ±0.9	66.7 ±1.1	86.4 ±1.7	108.2 ±1.2	119.6 ±0.1	63.6 ±0.1	82.3 ±0.1	108. ±0.2	125.1 ±0.2	141.1 ±0.1	71.1 ±0.3	126.0 ±0.2	142.7 ±0.1
$T_C - T_O$ (°C)	34.7 ±2.1	15.7± 0.9	35.8 ±1.9	11.9± 0.5	13.5± 0.7	16.0 ±0.5	17.0 ±0.4	20.5± 1.0	10.6± 0.5	30.7 ±1.2	14.6 ±0.4	19.1 ±0.7	14.2± 0.3	4.9± 0.2	45.2 ±2.1	25.3± 0.7	9.2± 0.4
ΔH (J/g)	1.1± 0.3	0.3± 0.0	1.1± 0.2	0.05± 0.0	0.2± 0.0	0.2± 0.0	0.2± 0.0	0.2± 0.0	0.1± 0.0	0.2± 0.0	0.1± 0.0	0.2± 0.0	0.1± 0.0	0.2± 0.0	1.0± 0.1	1.3± 0.2	0.0± 0.0

Up to four endothermic transitions were identified from the DSC data, where all thermal parameters are in agreement with previous works.[143,186,234–238] Waxy and normal maize starch powders displayed a single endothermic event in the range of 61 – 86 °C, associated with the melting of amylopectin crystallites, and low-enthalpy transitions in the range of 98 – 125 °C, associated with the disassociation of amylose crystallites.[164,239,240] In the case of amylomaize, Hylon VII® and Hi-Maize 260®, all endothermic transitions occurred as one broad multitherm lacking clearly differentiated maxima (*i.e.*, T_P), which could be linked to a broader distribution of crystalline structural arrangements, compared to the ones in waxy and normal maize. These observations

were in line with previously reported works on high-amylose starch exhibiting broad endotherms, irrespective of heating rate (2-10 °C/min). [236,241–243] The onset of gelatinisation of Hi-Maize 260® was delayed significantly compared to amylomaize and Hylon VII®, indicative of the greater crystallite stability and greater level of long-range ordering in the sample, further supported by its higher degree of crystallinity and short-range ordering, as per our PXRD and ^{1}H-^{13}C CP/MAS NMR data, respectively (Table 3.1). The majority of thermal transitions detected in the starch powders were of significantly lower enthalpy in their hydrogel analogues (J/g of the carbohydrate component), where the transitions associated with amylopectin crystallites were almost entirely absent (Tables 3.2-3.5). Furthermore, low isothermal and thermocycled storage conditions resulted in marginally greater helical reassociation, as evidenced by the slightly higher enthalpy of transitions compared to their high isothermal hydrogel counterparts. These observations are in agreement with previous works[244], and confirm the lower degree of short-range ordering in the hydrogel systems.

Mechanical Properties

Micromechanical results are shown in figures 3.3-3.6. All hydrogels' properties were in agreement with the established classic gel network parameters, documented in the works Burchard and Ross-Murphy[245] and Almdal *et al*.[246], where the parameterisation of strong gels rests on the samples exhibiting higher storage than loss moduli (G'>>G'') through the samples' LVE region, and *tan*δ values in the range of 0.01-1.00.

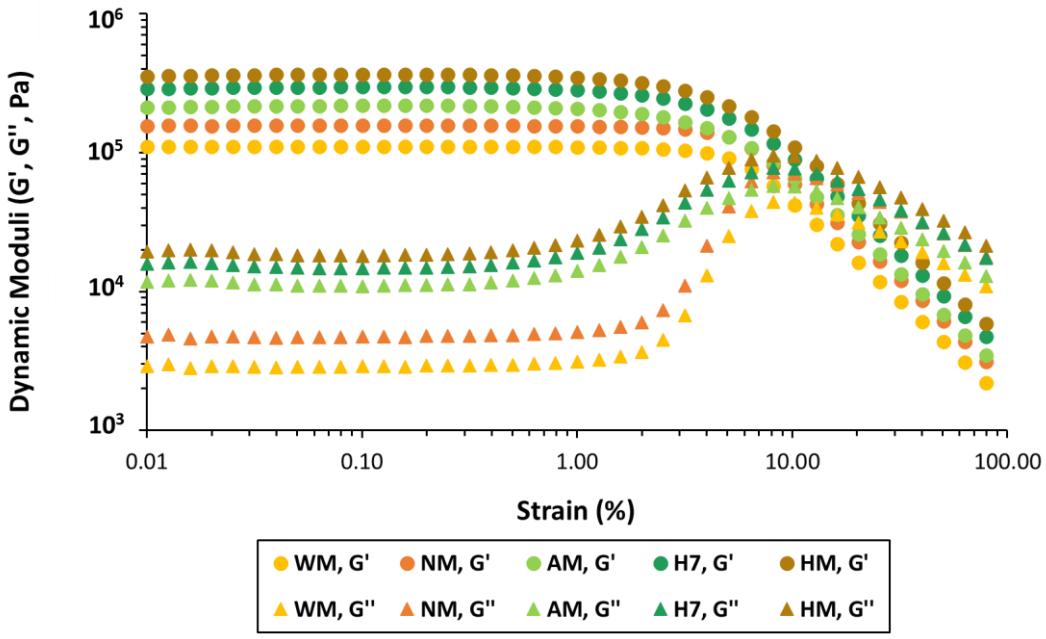

Figure 3.3: Storage and loss moduli (G’ and G’’, respectively) of all five maize starch hydrogels stored at low temperature isothermal conditions, as a function of applied strain, with constant frequency of 0.1 Hz, for ascertaining the hydrogels’ linear viscoelastic (LVE) region. Results presented are averages of a minimum of three repeats, where all repeats are within 10% of each other. Error bars have been omitted for visual clarity.

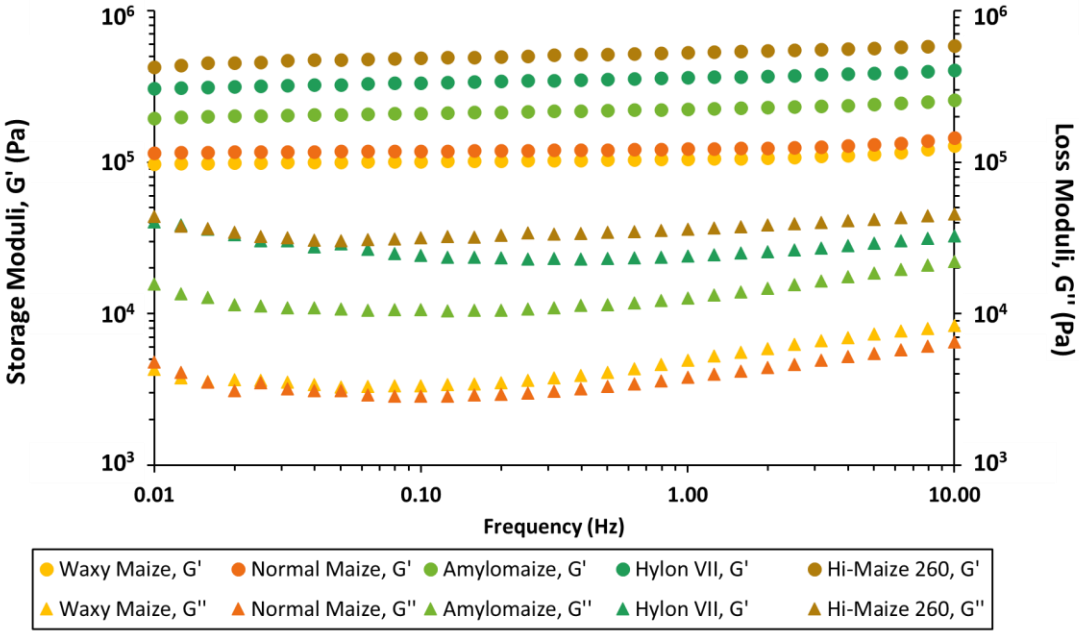

Figure 3.4: Storage and loss moduli (G’ and G’’, respectively) of all five maize starch hydrogels stored at low temperature isothermal conditions, as a function of applied frequency. Results presented are averages of a minimum of three repeats, where all repeats are within 10% of each other. Error bars have been omitted for visual clarity.

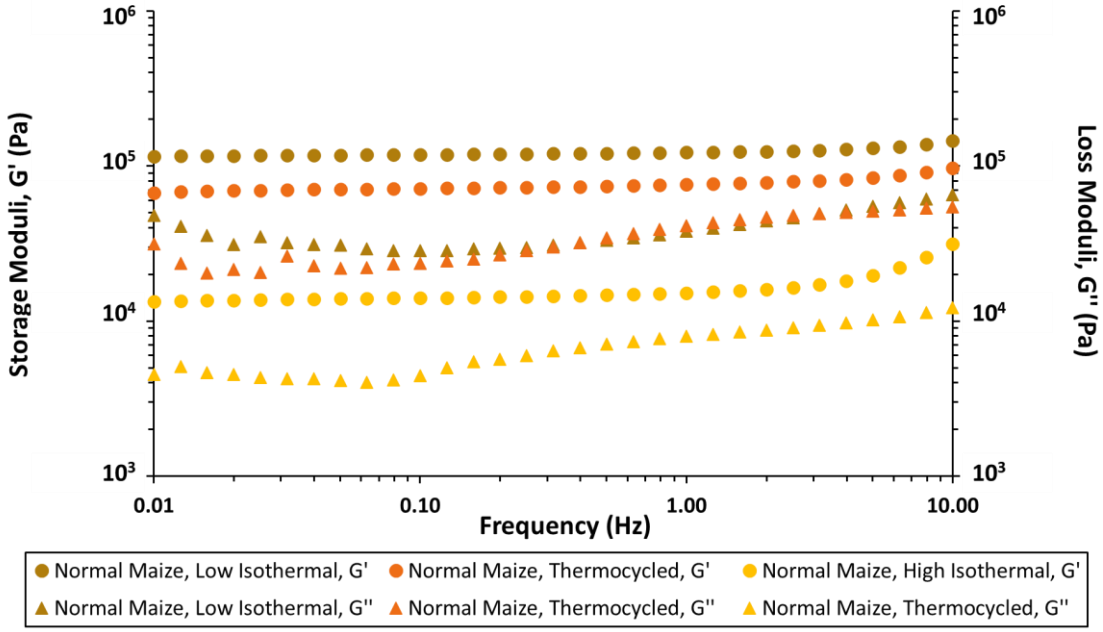

Figure 3.5: Storage and loss moduli (G’ and G’’, respectively) of all normal maize starch hydrogels stored at all three different conditions. Results presented are averages of a minimum of three repeats, where all repeats are within 10% of each other. Error bars have been omitted for visual clarity.

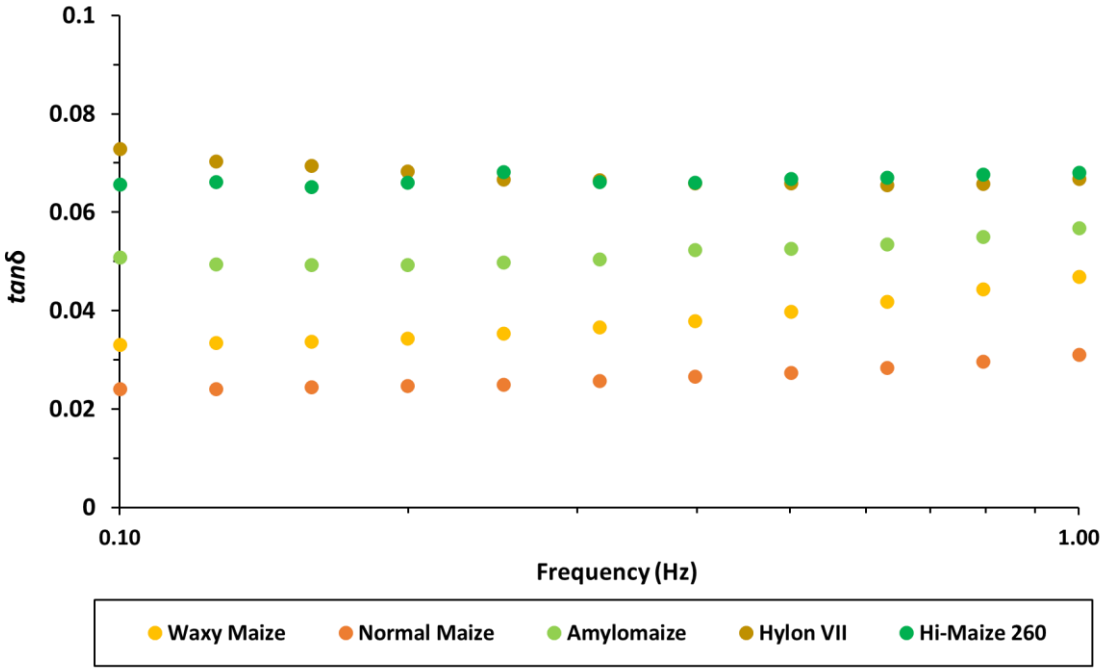

Figure 3.6: *tan*δ values of all five maize starch hydrogels stored at low temperature isothermal conditions, as a function of applied frequency. The narrower frequency range was selected, so as to probe *tan*δ within the stable region of G' and G'' only.

The extent of the LVE range of the hydrogels (under constant frequency of 0.1 Hz) spanned from 0.03 to 0.5% strain (Figure 3.3). At low strain (<0.3%) the dynamic storage moduli (G') remained independent of changes in the applied frequency until 1.0 Hz across all hydrogel samples, while their loss moduli (G'') exhibited marginal fluctuations (Figure 3.4), typical of hydrogel-type materials[247], potentially indicating low levels of compensatory structural rearrangements of glucan chains and/or redistribution of water fractions within the hydrogel network in its dissipation of stress throughout the system.[248] Alternative techniques that could have been used to probe these include dynamic mechanical analysis (DMA), and texture profile analysis (TPA). [249]

The viscoelastic solid nature of our starch hydrogels was confirmed by their low *tan*(δ) values, ranging from G''/G' = 0.024 – 0.073 within the stable part of the storage and loss

moduli (0.1 – 1.0 Hz, Figure 3.6), characteristic of strong soft matter materials, with a strong solid-like contribution.[250] Upon analyses of the micromechanical profiles of all maize starch hydrogels, there was a correlation (R^2 = 0.9305, Figure 3.7) between amylose content and storage modulus values (G', averaged across all gels at 0.25 Hz applied frequency). This was in agreement with previous works.[183,251]

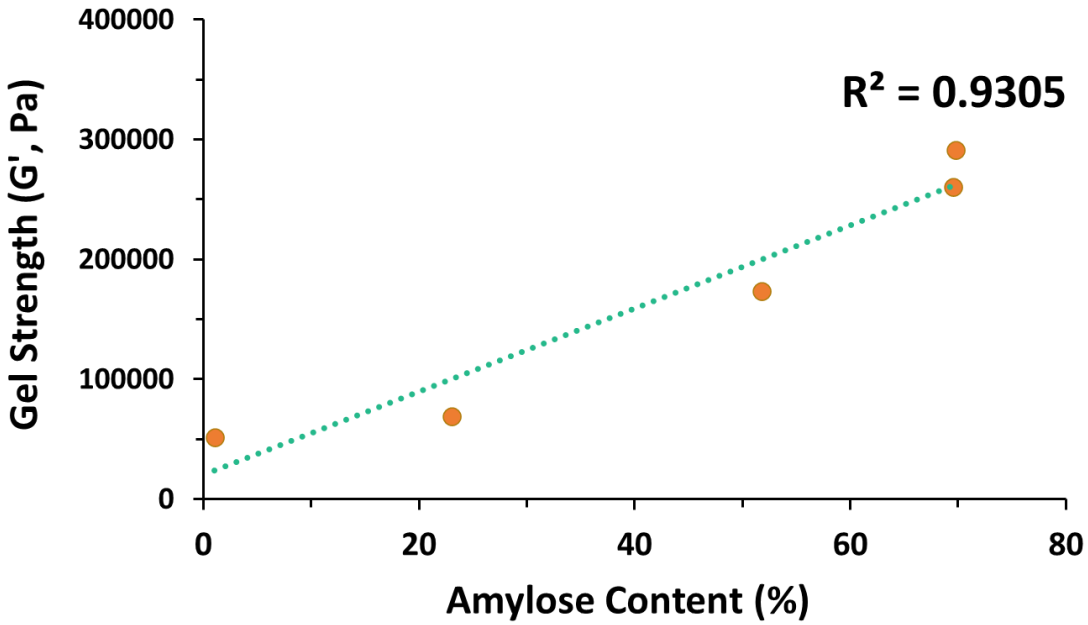

Figure 3.7: Linear correlation plot between maize starch hydrogels' strength (G', Pa) and respective amylose content (%), with displayed trendline and R^2 value.

Since G' values are related to the rigidity (density of junctions and cross-linking) of a viscoelastic material[181], the dependence of the storage moduli of starch hydrogels on their individual concentration and total amylose and amylopectin content has been interpreted to be a consequence of the phase transformations occurring during the biphasic model of retrogradation, resulting in the formation of hydrogels – namely the inter-glucan chain reassociations and formation of junction zones.[252] Following granular decomposition and amylose leaching into the surrounding medium, the greater kinetic

energy in the system facilitates the inter-glucan association, the susceptibility to which is dependent on the amylose and amylopectin macromolecular structural parameters. The predominantly linear amylose chains can partially align and interact with each other with far greater ease on the timescale of our experiments (8 days total storage duration), compared to the globular/ellipsoid highly branched amylopectin clusters, due to the lower steric effects experienced by the former when compared to the latter of the two glucans.[253] It is also worth noting that unlike the consistent and progressive increase in storage moduli with increasing amylose content observed for the majority of the samples, upon inspection of all starch hydrogels' individual G'' values, it was evident that it was normal maize starch hydrogels that exhibited the lowest loss moduli, and not waxy maize starch (*ca.* 2.99 kPa *vs* 3.63 kPa, at 0.25 Hz, respectively, Figure 3.4), pointing towards the presence of multiple contributions to the hydrogels' micromechanical properties, outside of their individual amylose and amylopectin content. Overall, our results demonstrate that maize starch hydrogels exhibit significant micromechanical strength, with G' values comparable to, and in some cases higher than, synthetic and natural-synthetic hybrid gels, commonly employed in the pharmaceutical industry.[102,254]

3.2.2 *Molecular structural parameters, internal organisation, molecular mobility, and inter-component interactions*

Molecular Structural Parameters

The molecular size distributions of both branched and debranched gels (Figures 3.8 and 3.9) revealed differences in the molecular structural parameters (hydrodynamic radius, R_h; and degree of polymerisation, DP) among all five starch hydrogels.

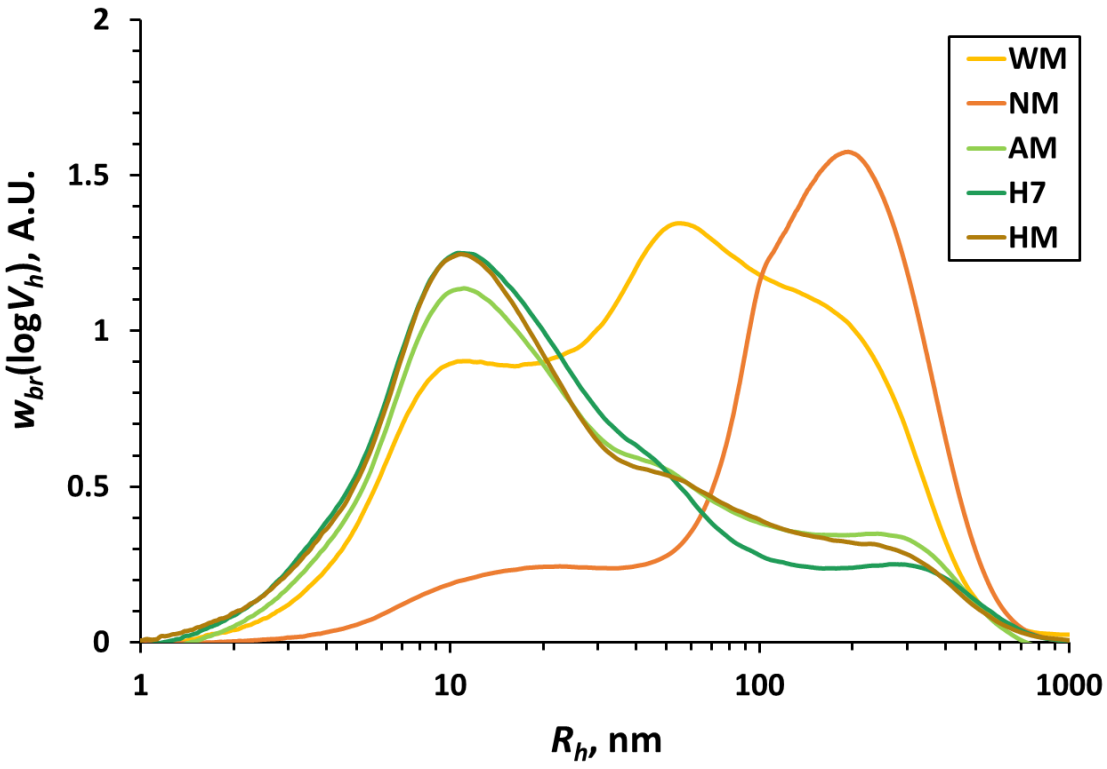

Figure 3.8: Size exclusion chromatography whole molecule weight distributions waxy maize (WM), normal maize (NM), amylomaize (AM), Hylon VII® (H7) and Hi-maize 260® (HM) starch hydrogels, $w_{br}\log(V_h)$ (A.U.) *vs.* R_h (nm). All distributions have been 0-order detrend- and standard normal variate-normalised.

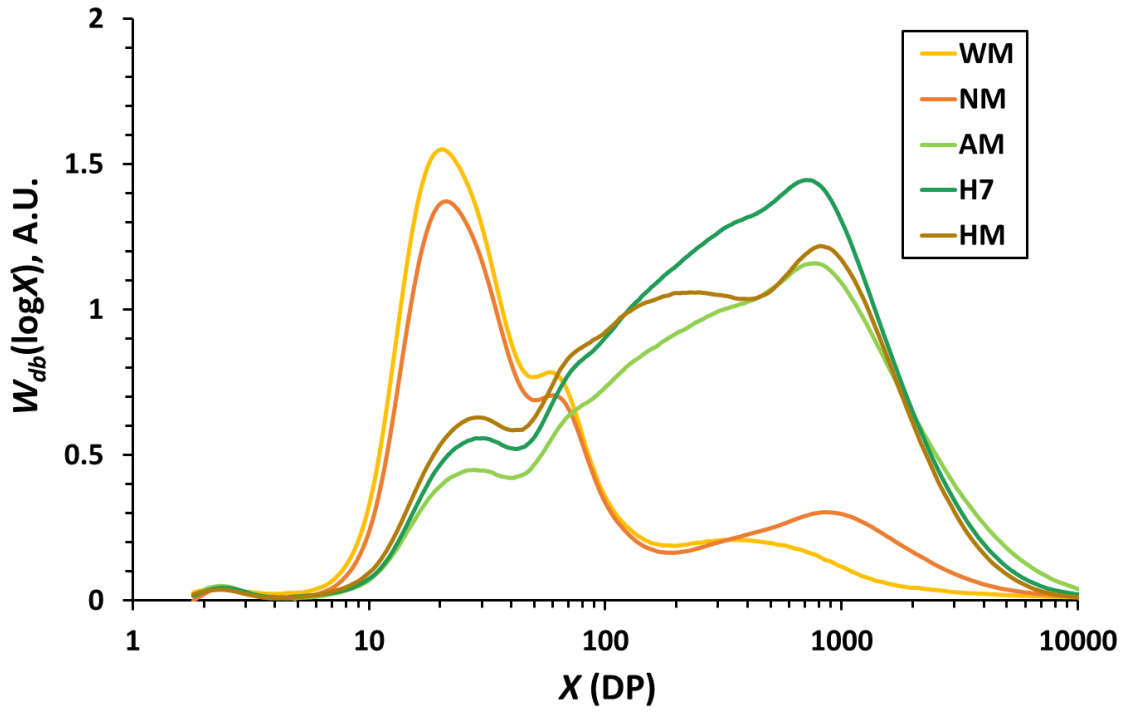

Figure 3.9: Size exclusion chromatography weight distributions of debranched waxy maize (WM), normal maize (NM), amylomaize (AM), Hylon VII® (H7) and Hi-maize 260® (HM) starch hydrogels, w_{db}log(X) (A.U.) *vs.* X(DP). All distributions have been 0-order detrend- and standard normal variate-normalised.

All three high-amylose starch gels (AM, H7 and HM) displayed very similar branched molecular weight distributions (Figure 3.8), where the primary differences were a slightly greater amylopectin contribution in AM (*ca*. R_h = 200 – 400 nm)[255–257], compared to H7 and HM, which is in agreement with their glucan composition (Table 3.1).

Both WM and NM exhibited a significant amylopectin contribution in their whole molecular weight distributions, due to their amylopectin content (*ca*. 99% and 77%, respectively). Unlike NM, which displayed a narrower distribution of its amylopectin fraction (*ca*. R_h = 100 – 300 nm)[255–257], the amylopectin-associated peak displayed a wider distribution, with a peak at *ca*. R_h = 60 nm, and a broad shoulder at *ca*. R_h = 100 – 200 nm (Figure 3.8).[255–257] These data, along with the WM peak at *ca.* R_h = 10 nm, usually

associated with an amylose contribution, and the very low amylose content of this starch sample (*ca*. 1%, Table 3.1), are likely an indication of shear scission having affected WM in its transit through the separation column, resulting in fractionation of the highly branched polymer.[224,258] This is further supported by WM's debranched size distribution, which did not exhibit a significant weight contribution in the amylose-associated region (*ca*. DP = 700 – 1000, Figure 3.9).

Long-range ordering and Total Amorphous Contribution

XRD patterns of all starch powders and corresponding low temperature isothermally stored hydrogels (Figure 3.10) were in good overall agreement with previous data where available.[186] The diffraction peaks used for quantification of the total amorphous contribution (Table 3.1)[187], associated with A-, B- or V-type crystallinity can be seen in Figure 3.11.[187]

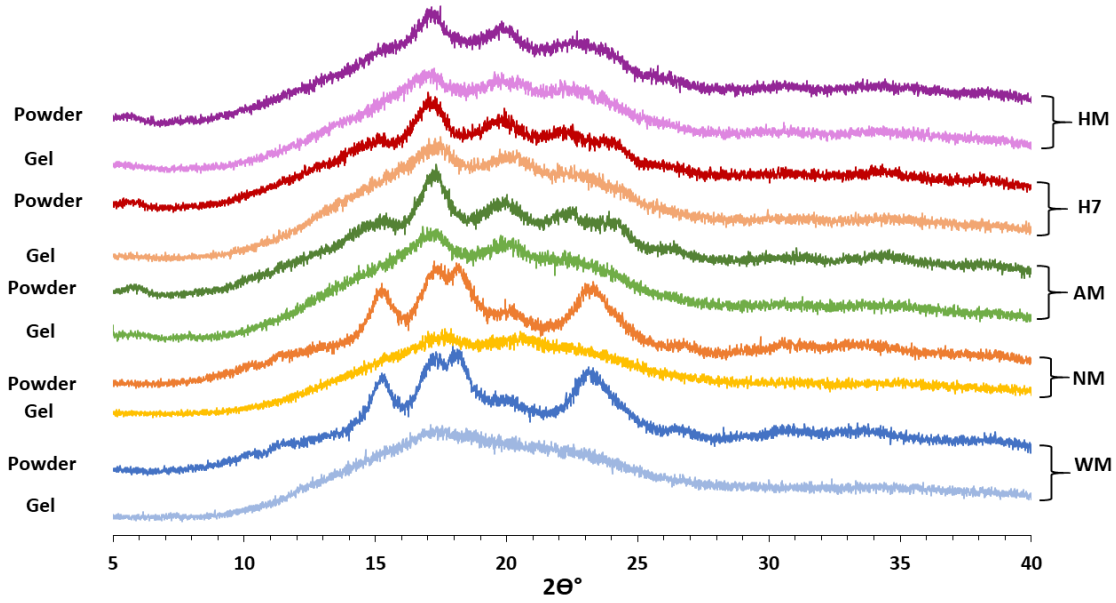

Figure 3.10: Powder X-ray Diffraction patterns of waxy maize (WM), normal maize (NM), amylomaize (AM), Hylon VII™ (H7) and Hi-Maize 260™ (HM) powder samples and their respective hydrogels prepared at low temperature isothermal conditions. Diffractograms have been displaced for visual clarity purposes.

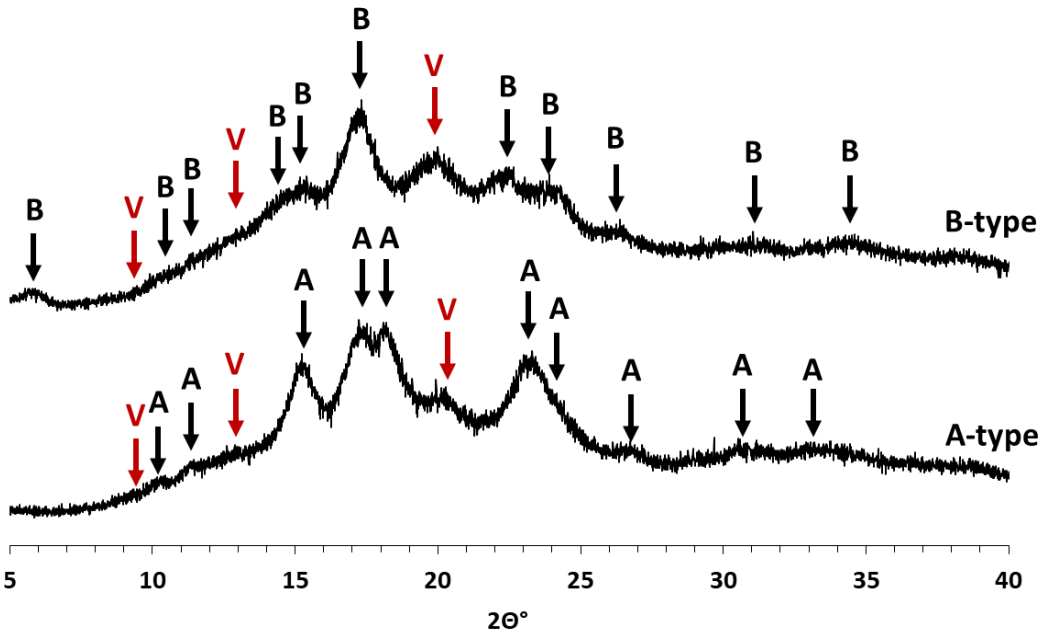

Figure 3.11: Powder X-ray Diffraction patterns of A- and B-type powder starches (normal and Hylon VII™ maize powders, respectively), with black arrows indicating the peaks (10 for A-type and 11 for B-type) associated with A- and B-type type crystallinity chosen for peak fitting, and red arrows indicating the peaks associated with V-type amylose arrangements. Peak assignment is according to Lopez-Rubio *et al.*[187]

The low-amylose starches (WM and NM) displayed A-type diffraction patterns, whereas their high-amylose counterparts (AM, H7 and HM) exhibited B-type ones (Figures 3.10 and 3.11).[187]

On hydrothermal treatment and storage, the low-amylose containing starches produced gels with practically no detectable long-rage ordering. The only discernible features were observed as broad peaks in normal maize gels (*ca*. 2θ° = 20), indicative of the presence of V-type amylose[187,259], and a change in helical packing from A- to the more stable B-type allomorph (Figures 3.10 and 3.11).[157,236]

In contrast, the high-amylose samples yielded hydrogels of significantly more pronounced B-type organisation, and higher degree of ordering, further confirming their decreased susceptibility to hydrothermal treatment, evidenced by their delayed thermal transitions (Figure 3.2). These observations were most likely also influenced by the differences in the retrogradation rates between amylose and amylopectin (hours *vs.* days, respectively).[134,260,261]

Short-range order and dynamics

Assignment of ^{13}C chemical shifts in all starch powder and hydrogel NMR spectra (Table 3.6, Figures 3.12 and 3.13) was performed based on previous works.[158,262–264]

Table 3.6: Assignment of carbon site resonances in all maize starch solid powders analysed, in accordance with published literature available.

Starch Type	Chemical Shift (ppm)								
	C-1		C-4		C-2,3,5		C-6		Published Literature
	Signal Range	Signal Peaks	Signal Range	Signal Peaks	Signal Range	Signal Peaks	Signal Range	Signal Peaks	
WM	95 - 105	99.4; 101.5; 102.7	79 - 85	81.9	68 - 78	72.4	58 - 65	62.3	262,263
NM	97 - 105	99.7; 101.6; 103.0	78 - 85	81.8	67 - 78	72.5	58 - 64	62.2	262,263
AM	97 - 105	100.8; 103.0	79 - 85	82.3	68 - 77	72.5	59 - 64	61.9	262,263
H7	93 - 104	100.1; 102.9	78 - 85	81.9	68 - 78	72.5	58 - 64	62.1	158
HM	94 - 105	99.8; 102.1	79 - 84	81.4	68 - 78	72.5	58 - 64	61.9	*N/A*

The ^{1}H-^{13}C CP/MAS NMR spectra of maize starch powders and their corresponding low temperature isothermally stored hydrogels (Figure 3.12) show considerably increased resolution in the spectra of hydrogels.

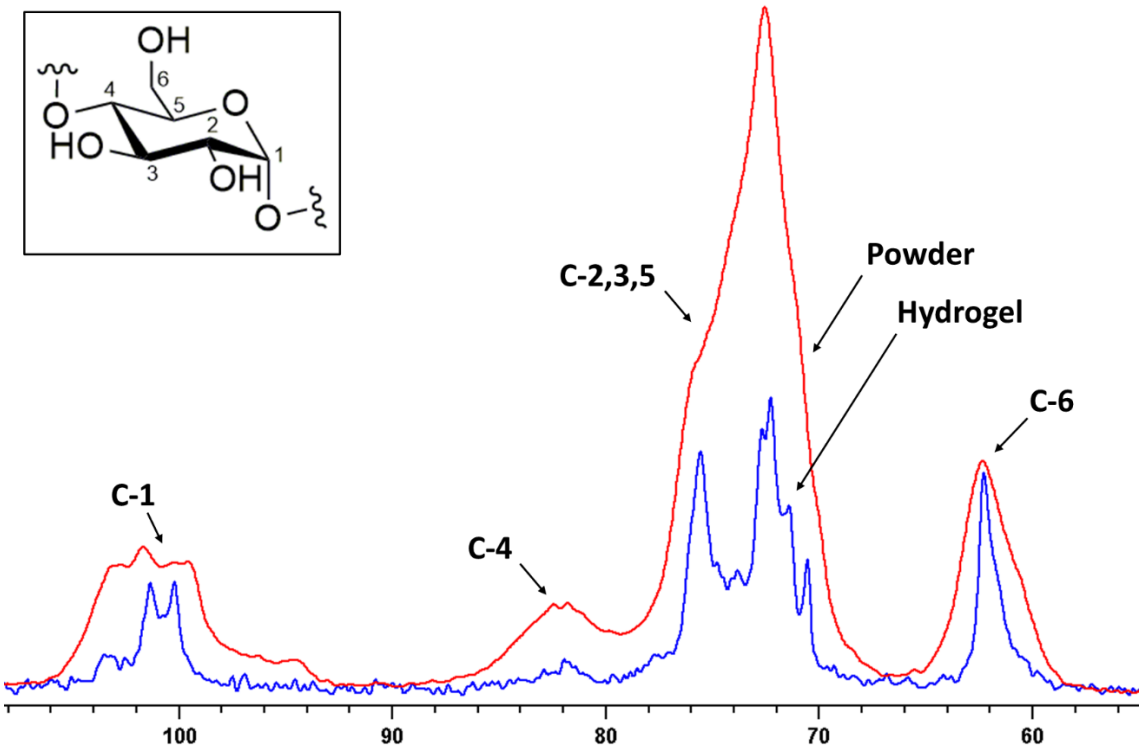

Figure 3.12: ^{1}H-^{13}C CP/MAS NMR spectra of normal maize powder (red) and low temperature isothermally stored hydrogel (blue). Inlay showing the glucose monomer with ^{13}C atomic numbering, and arrows pointing towards each of the 4 peak regions attributed to ^{13}C nuclei in the starch monomer.

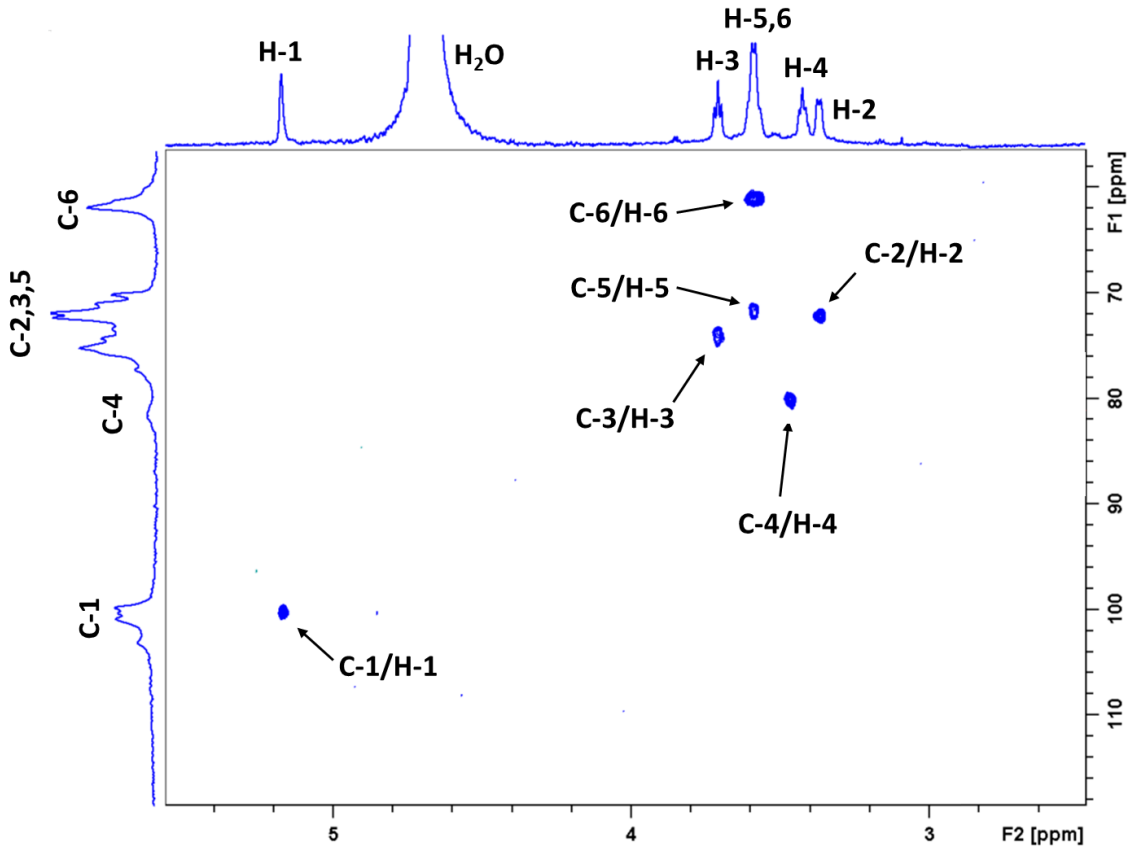

Figure 3.13: ^{1}H-^{13}C HSQC NMR spectrum of low temperature isothermally stored amylomaize starch hydrogel with ^{1}H and ^{13}C peak and ^{1}H-^{13}C cross-peak assignment. The ^{13}C spectrum in the indirect (F1) dimension is an external ^{1}H-^{13}C CPSP/MAS NMR spectrum.

Hydration and hydrothermal treatments have been shown to increase mobility in the more structurally disordered fractions of starch.[265,266] This has been linked to the state of the amorphous component in starches, which is highly susceptible to hydration effects.[57,81] It has further been associated with the impact of hydration on the crystalline regions in starch, where hydration allows for misaligned helices to align, increasing the degree of their association, resulting in better resolved and more intense peaks in the gel state, compared to the powders (Figure 3.12).[57,81]

The ^{1}H-^{13}C CP/MAS NMR spectra of all five maize starch hydrogels revealed differences primarily in the shoulder region of 100–104 ppm (green dashed line, Figure 3.14), ascribed to a combination of amorphous and V-type amylose crystalline arrangements.[62] These differences were most pronounced when comparing low to high amylose starch hydrogels (*e.g.,* WM to HM gels, Figure 3.14). Waxy maize gels displayed a broader chemical shift distribution compared to Hi-maize 260® gels, which was expected, as a consequence of the latter's higher V-type amylose content, as evidenced by its PXRD diffraction patterns (Figures 3.10 and 3.11).[135,263,266]

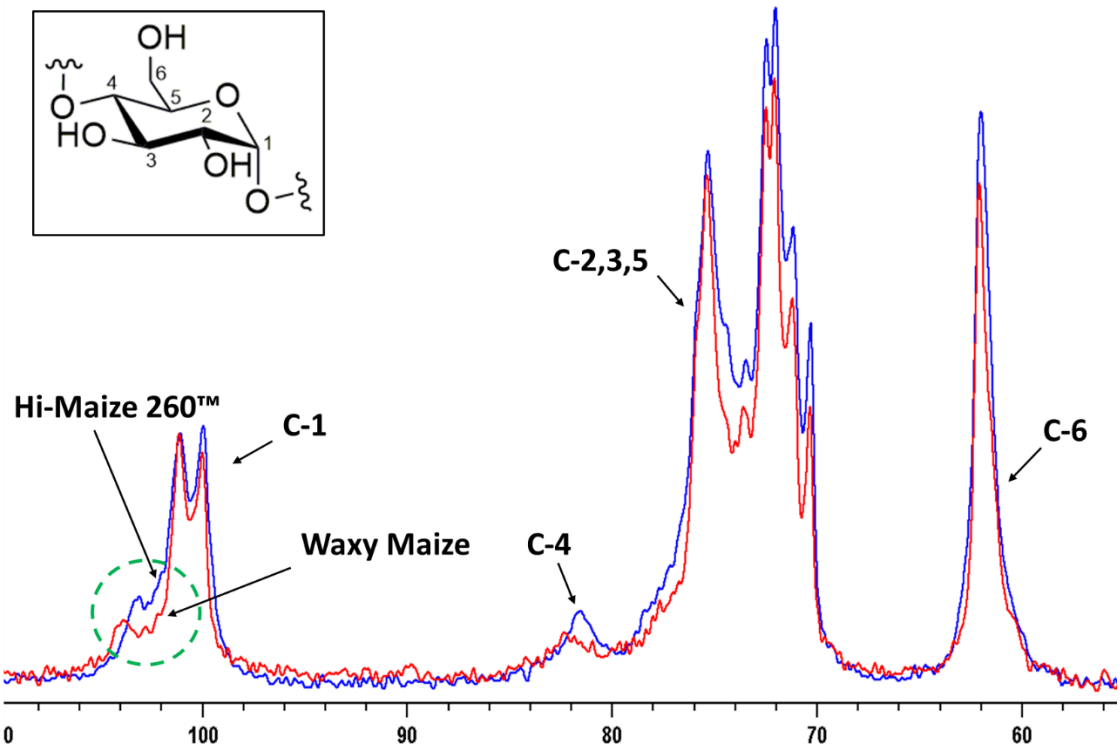

Figure 3.14: ^{1}H-^{13}C CP/MAS NMR spectra of waxy maize (WM, red) and Hi-Maize 260™ (HM, blue) low temperature isothermally stored hydrogels, where area in green shows the 100-104 ppm regions ascribed to V-type amylose and amorphous starch content. Inlay showing the glucose monomer with ^{13}C atomic numbering, and arrows pointing towards each of the 4 peak regions attributed to ^{13}C nuclei in the starch monomer.

The solid-state ^{1}H-^{13}C CP and CPSP/MAS NMR spectra of all starch hydrogels revealed the presence of structural domains of significant local mobility existing in C-1, C-2,3,5, and C-6 environments, in all maize variety hydrogels (Figures 3.15 and 3.16).[64]

Some of these peaks are only observable under CPSP conditions (Figure 3.15-A, in green), emphasising their considerable structural mobility, rendering them undetectable under CP conditions. The ^{1}H-^{13}C CPSP/MAS spectra of all starch hydrogels revealed the presence of three separate peaks within the anomeric carbon (C-1) environment (99.0–101.8 ppm), where the sites corresponding to peaks 99.8 and 100.8

ppm exhibited significantly lower levels local mobility, compared to the central peak (100.3 ppm) within the C-1 environment (Figures 3.15-A and 3.15-B). All three peaks were present in the CPSP spectra of all hydrogels (Appendix Figure S2). These data further confirm the changes in helical packing (the transition of A-type granular starches into B-type diffraction pattern in the corresponding hydrogels) initially observed in our PXRD data (Figure 3.9), and also supported by PXRD analyses in previous works.[147,262,267] Full spectral deconvolution (Figure 3.16, and Appendix Figures S3-S7)[64] allowed for the quantification of local mobility at each ^{13}C site (Figure 3.15B).

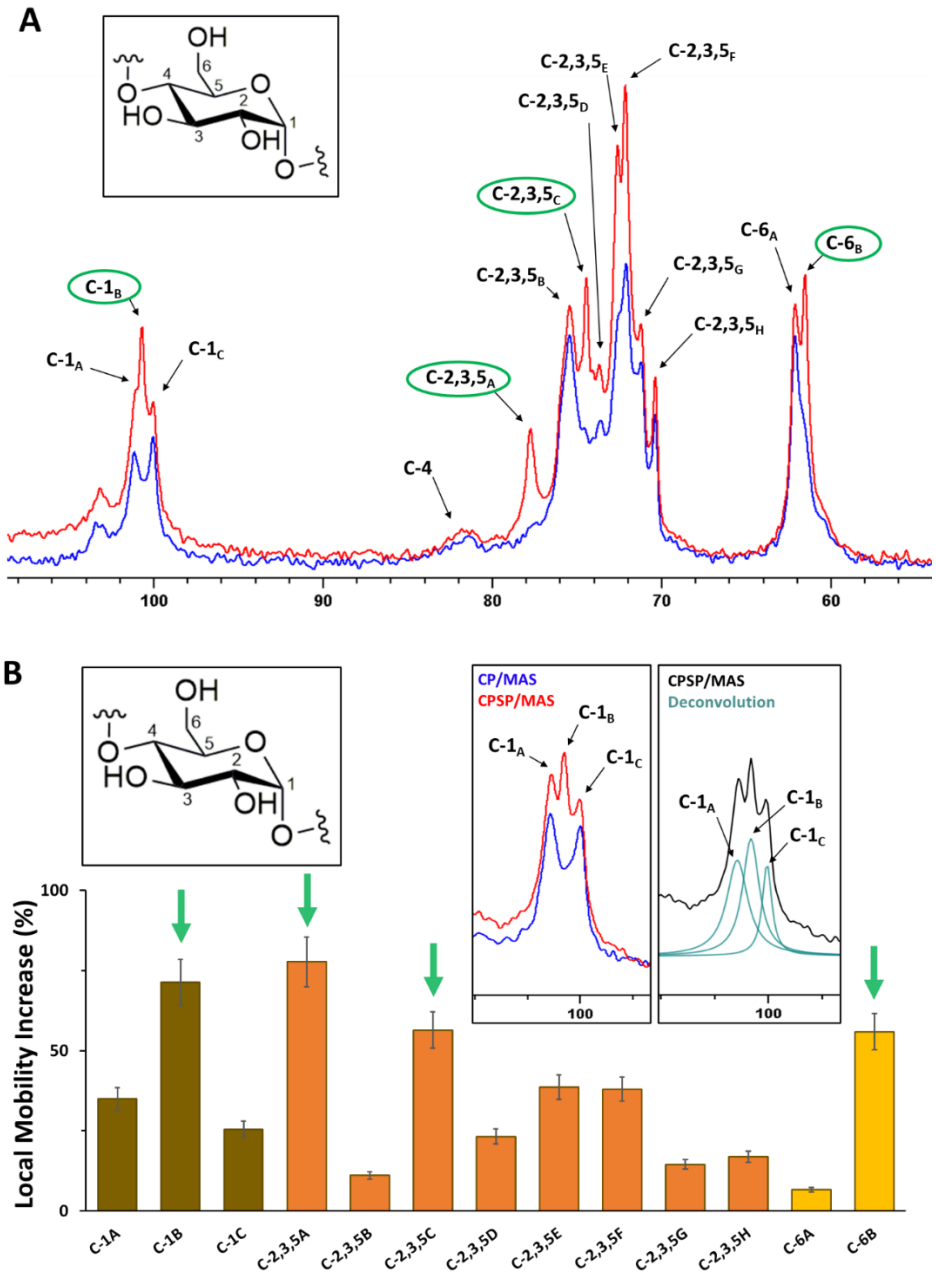

Figure 3.15: (A) An overlay of ^{1}H-^{13}C CP and CPSP/MAS NMR spectra of low temperature isothermally stored normal maize hydrogels with peak assignment. Peaks corresponding to sites with significantly increased local mobility are shown in green. (B) Bar chart of estimated levels of local mobility per peak across all carbon nuclear environments with arrows indicating peaks of increased local mobility. Inlays showing spectral excerpts featuring composite peak deconvolution and assignments; and glucose monomer with ^{13}C atomic numbering. Error bars based on the S/N ratio of all spectral data.

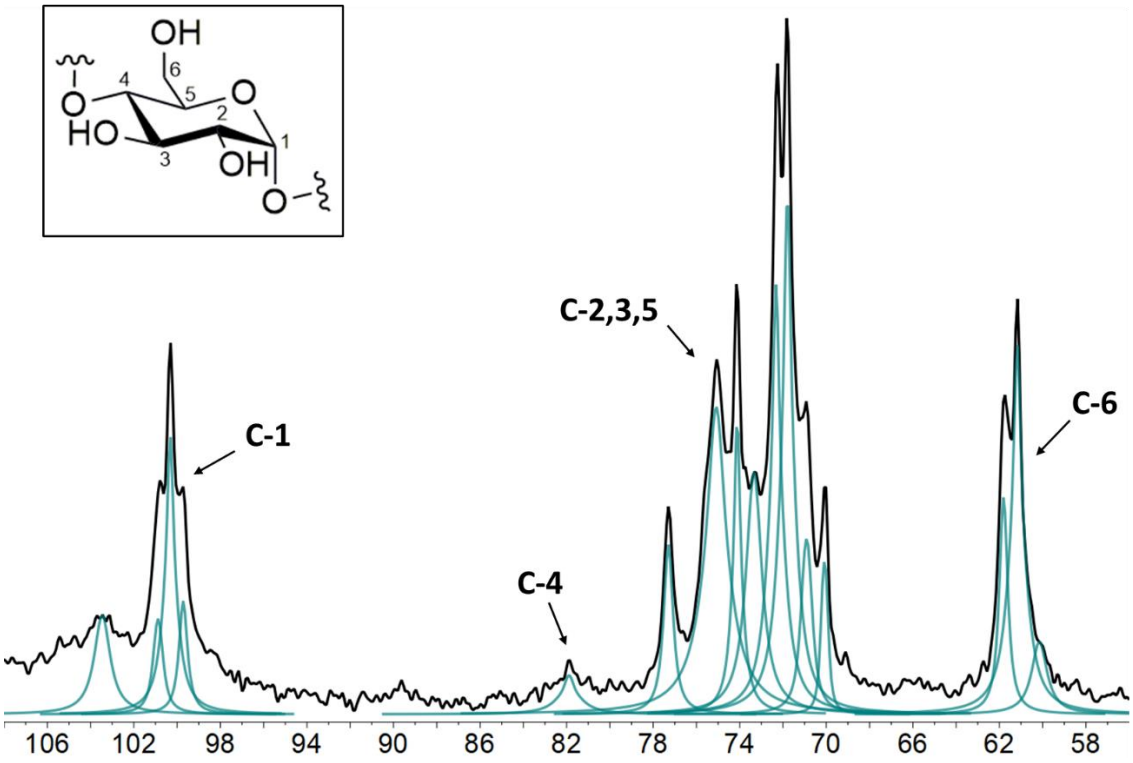

Figure 3.16: Deconvoluted ^{1}H-^{13}C CPSP/MAS NMR spectrum of all waxy maize (WM) starch hydrogels prepared under low isothermal conditions. Deconvolution performed using MNova global spectral deconvolution algorithm.

Combined application of solid-, solution-state and HR-MAS ^{13}C NMR experiments revealed that the peaks observed in solution-state and HR-MAS spectra correspond to those detected under ^{1}H-^{13}C CPSP/MAS NMR conditions (Figure 3.17), further affirming their highly dynamic nature. The rigid components in the starch hydrogels became observable under longer recycle delay (150 s) conditions (Figure 3.18). The observed line broadenings across all peaks in our solution state spectra was expected due to the solid-like state of the overall starch hydrogel matrix and CSA. The orientation dependence of the chemical shift was partially mitigated under HR-MAS conditions, resulting in improved signal resolution, evident by the lower line broadening compared to solution-state experimental settings (Figure 3.16, Solution state *vs.* HR-MAS).

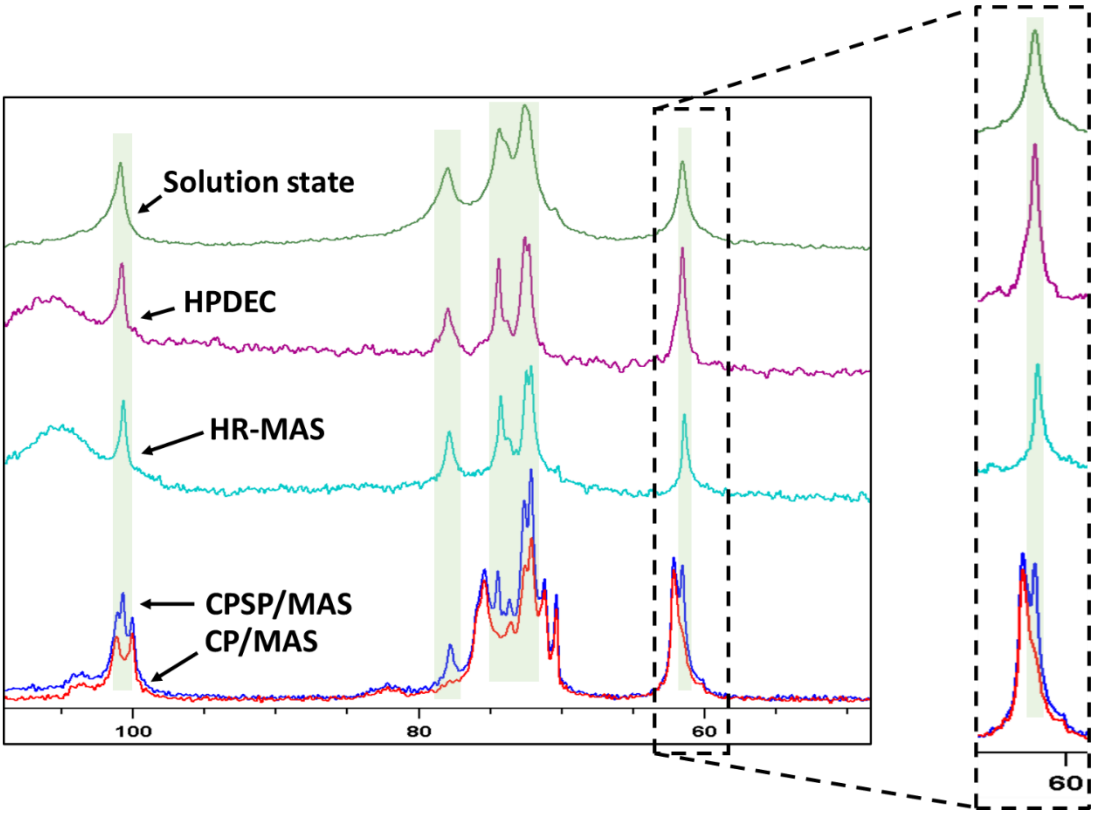

Figure 3.17: Overlay of $^{13}C\{^{1}H\}$ HR-MAS (turquoise), $^{13}C\{^{1}H\}$ solution state (green), $^{13}C\{^{1}H\}$ MAS (recycle delay of 2 s, purple) and ^{1}H-^{13}C CP and CPSP/MAS solid-state NMR spectra (red and blue, respectively) of low temperature isothermally stored waxy maize starch hydrogel in D_2O. Dashed lines shows overlapping peaks. A zoomed-in image of the C-2,3,5 and C-6 chemical shift region is shown in inlay.

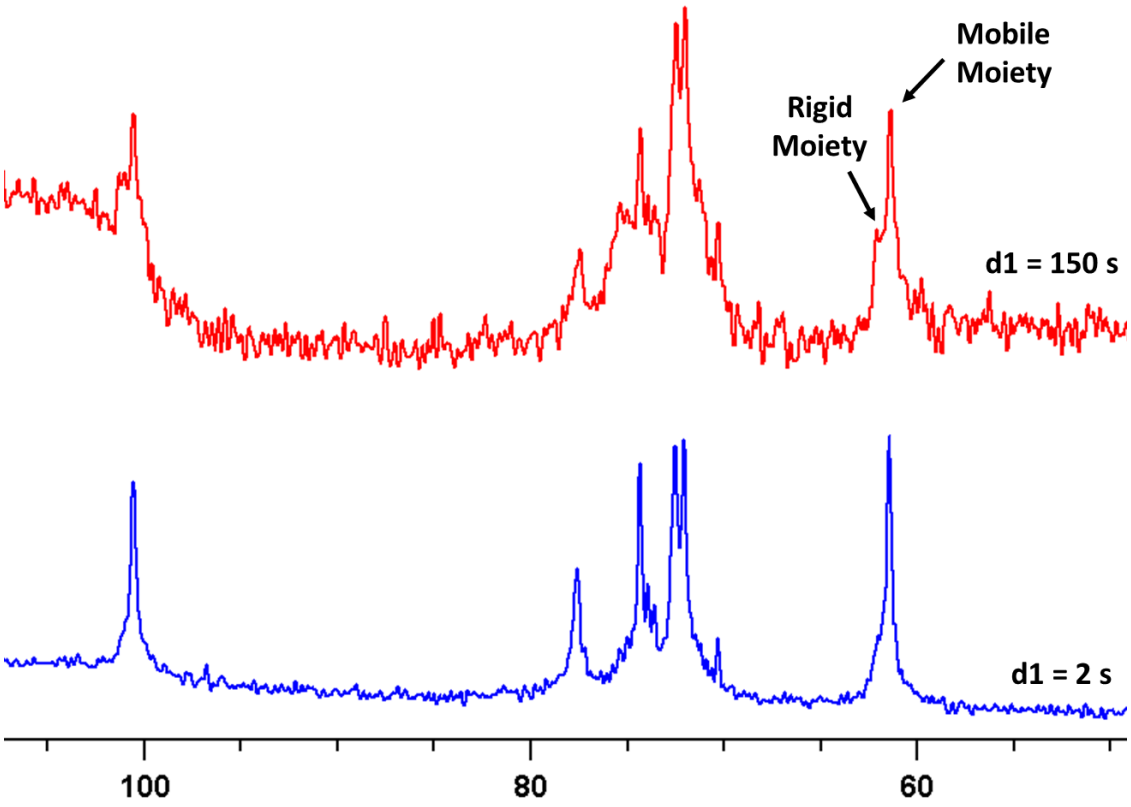

Figure 3.18: ^{13}C Direct polarisation with high power ^{1}H decoupling (HPDEC) NMR spectra of low temperature isothermally stored normal maize starch hydrogels with short (blue, recycle delay of 2 s) and long (red, recycle delay of 150 s) recycle delays. Both spectra are on the same scale. The decreased S/N ratio of the top spectrum is due to the lower number of scans obtained, compared to the bottom spectrum.

The mobile behaviour of these solvated moieties exhibited temperature dependence, where the degree of molecular mobility decreased progressively with lowering of the temperature in the range of -25 – 5 °C (Figure 3.19). The peaks associated with mobile domains are not detectable at temperatures below -10 °C (Figures 3.19 and 3.20).

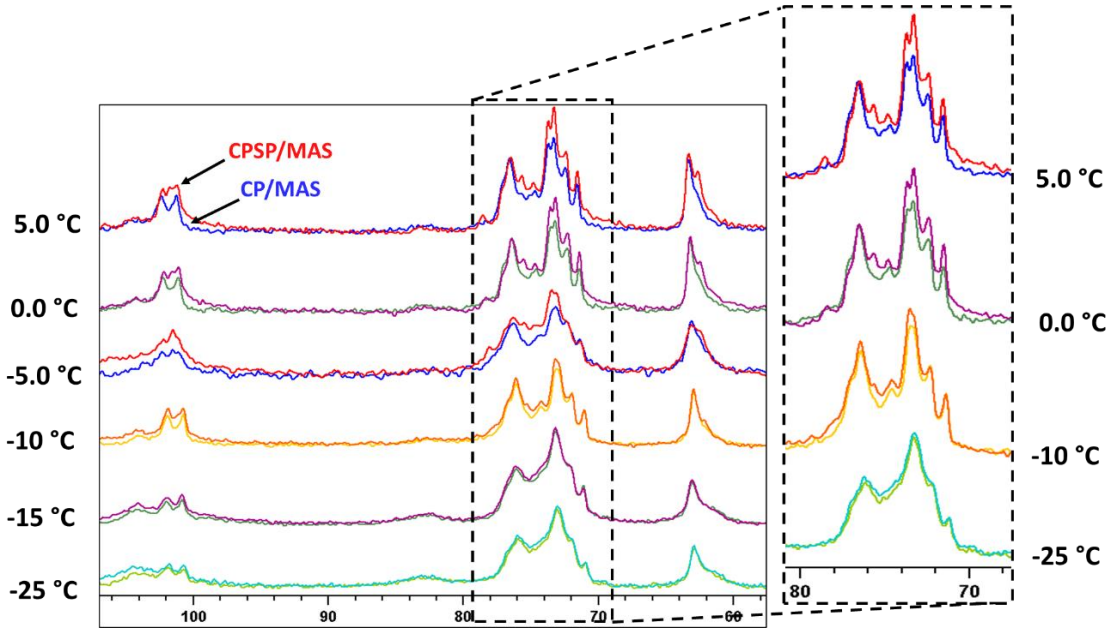

Figure 3.19: Overlay ^{1}H-^{13}C CP and CPSP/MAS NMR spectra of low isothermally stored normal maize starch hydrogels, obtained at variable temperatures, with inlay showing a zoomed in version of the C-2,3,5 spectral region. All experiments were acquired with a minimum of 2000 scans.

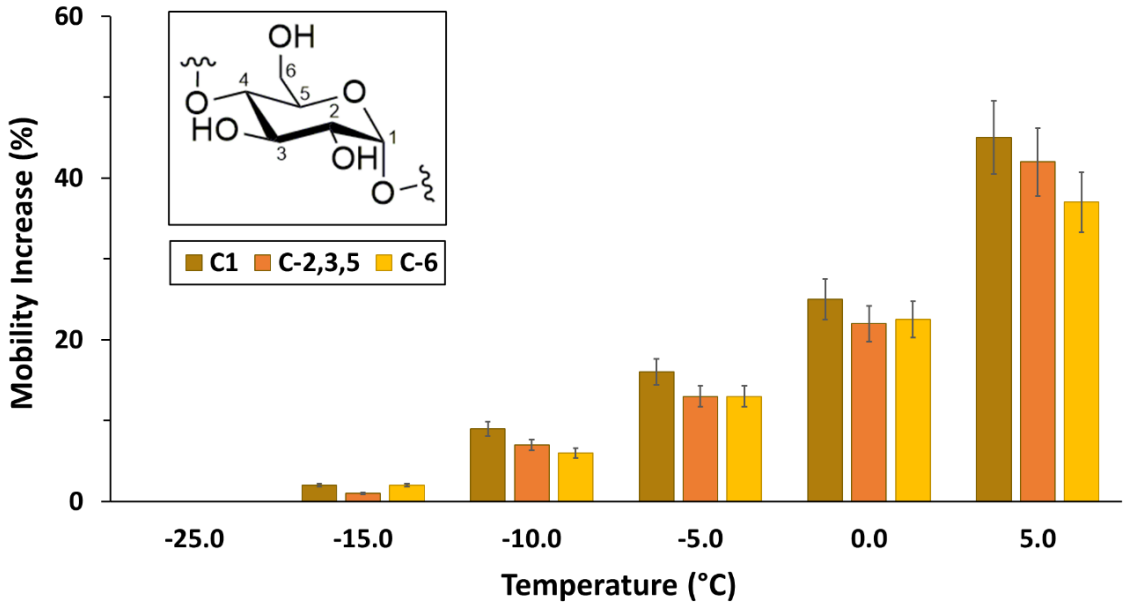

Figure 3.20: Estimated average mobility levels (%) in low temperature isothermally stored normal maize hydrogels across C-1, C-2,3,5, and C-6 atomic regions, as a function of temperature. All experiments were acquired with a minimum of 2000 scans. Error bars based on the S/N ratio of all spectral data.

The change in dynamics regime was also reflected in the hydrogels' longitudinal relaxation (T_1) across all ^{1}H nuclei, which exhibited a decrease at temperatures below -10 °C (Figure 3.21). These data are in agreement with the expected increase in correlation time characteristic of the transition from a hydrogel to a more rigid and solid network, and a more dynamically constrained or bound state of mobile moieties.[192]

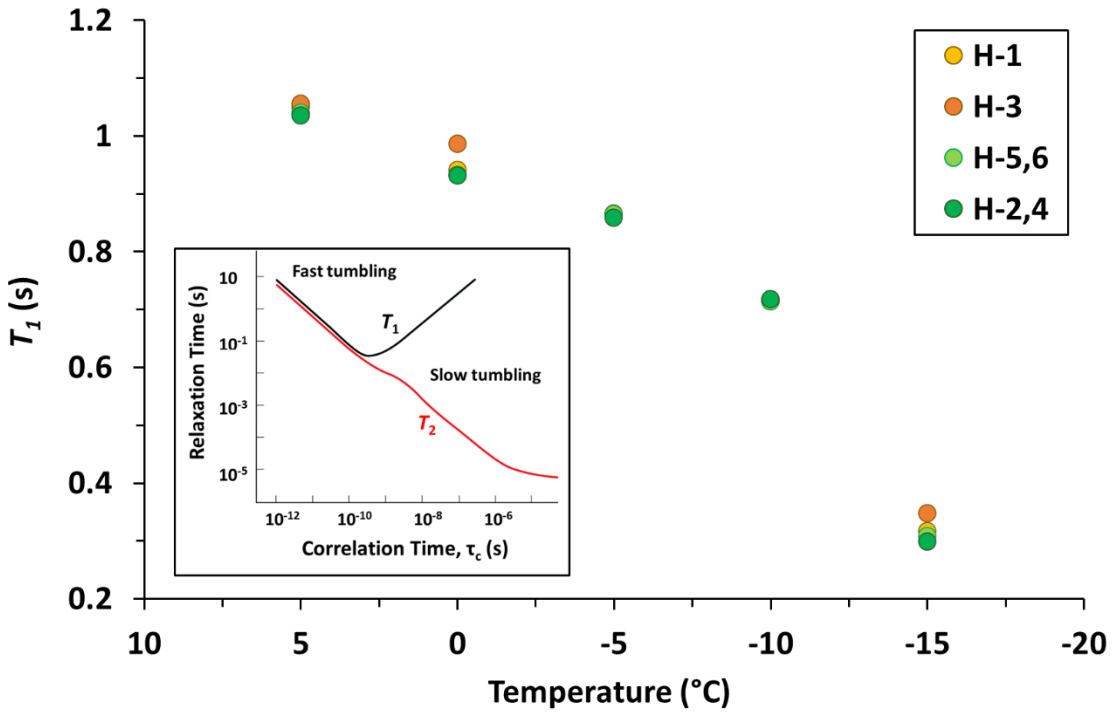

Figure 3.21: ^{1}H HR-MAS NMR longitudinal relaxation (T_1) times (s) of low temperature isothermally stored normal maize starch hydrogels in the range of -15.0 to 5.0 °C. Inlay showing T_1 and T_2 dependence on molecular correlation time (τ_c), adapted from the work of Keshari and Wilson.[192]

The majority of water population within our starch hydrogels behaved as freezeable bound water, as evidenced by our DSC data. The exothermic freezing event of this H_2O population occurred in the range of -13 to -25 °C for all starch gels (Table 3.7, Appendix Figure S8).

Table 3.7: Sub-ambient exothermic transition parameters (onset temperature, T_O, concluding temperature, T_C and enthalpy of transition, ΔH) of all low temperature isothermally stored starch hydrogels, with units given in parentheses.

Starch Type	Cooling Cycle, 5 °C.min^{-1}		
	Onset Point (°C)	Concluding Point (°C)	ΔH (J/g)
WM	-15.66	-25.31	189.63
NM	-13.73	-23.95	212.86
AM	-17.98	-25.63	182.35
H7	-15.58	-24.73	195.94
HM	-15.77	-22.80	137.82

The confined nature of the water population within our gels was further confirmed by its longitudinal relaxation times (Table 3.8), which were several times lower than the ones characteristic of free water (*ca*. 4 s)[268], indicative of restricted molecular motions. Furthermore, the total enthalpy (ΔH) of the exothermic freezing event of water populations in the starch gels (Table 3.7) followed the same order as the T_1 relaxation times of the water populations in the starch hydrogels, further validating the confined nature of the water molecules making up the freezable bound water population in these gel networks.

It should be noted, however, that the relaxation characteristics of the HDO peak represent an average across the water populations within our gels (due to the presence of spin diffusion), where this may be a contribution of several microenvironments with variable degree of molecular motions.

Table 3.8: ^{1}H HR-MAS NMR T_1 times (s) of the HDO peak (at ca. 4.7 ppm) in low temperature isothermally stored maize starch hydrogels measured at 5 °C. Results presented are averaged across a minimum of three measurements.

Starch Hydrogel	HDO T_1 (s)
Waxy Maize	1.352 (±0.02)
Normal Maize	1.570 (±0.04)
Amylomaize	1.283 (±0.02)
Hylon VII™	1.350 (±0.03)
Hi-Maize 260™	1.199 (±0.02)

Cumulatively, these data led to the hypothesis on the origin of these mobile fractions being highly solvent-exposed and/or partially solvated starch matrix structural elements (*i.e.*, chains) confined within the overall rigid hydrogel bulk matrix. The physicochemical properties of the mobile chains are being dominated by the surrounding water environment. Together these structurally and motionally distinct moieties comprise the overall structural heterogeneity of starch hydrogel systems. These data build on earlier works on low-temperature NMR spectroscopic experiments on starches.[269,270] Colquhoun *et al*.[270] built on the continuous model of amylose gels, proposed by Leloup *et al*.[271], by demonstrating the presence of both a rigid, and a mobile fraction within amylose gels, characterised by distinct T_2 relaxation times. In our work we quantify the degree of molecular mobility of these moieties, and demonstrate how their dynamic behaviour correlates to the properties of the system as a whole (*e.g.*, micromechanics).

Role of water in hydrogel structure, organisation, and integrity

WPT-CP experiments can reveal information on the structuration of water molecules around the starch backbone within starch hydrogels. WPT-CP build-up curves can be used to probe more confined structuration of H_2O molecules around the starch backbone, due to the nature of the WPT-CP pulse train, which removes magnetisation present in free water molecules by way of a T_2 filter, and transfers the magnetisation remaining in confined water molecules to the starch backbone by means of cross-polarisation (CP, Figure 2.15).[272]

Comparative build-up curves of the normalised levels of magnetisation transferred from "structured" water molecules to the starch backbone at the mid-point of build-up (t_{mix} = 25 ms) revealed that this transfer is most efficient from H_2O molecules proximal to C-2,3,5, and C-6 nuclei, compared to C-1 nuclei (Figures 3.22 and 3.23). This was explained by anomeric carbon's involvement in α(1-4) bonds within starch, contributing to a more confined vicinity around these nuclei, compared to C-6, due to its lesser involvement in α(1-6) glycosidic linkages. These observations were consistent across all our hydrogel samples. The C-4 peak was disregarded in this analysis, due to its low intensity and difficulty to integrate reliably. It should be noted that t_{mix} = 25 ms was used for comparison between spectral data sets, as it represents a mid-point during the signal build-up phase (*i.e.*, polarisation transfer), whereas almost all of the magnetisation was transferred at t_{mix} = 100 ms across all samples.

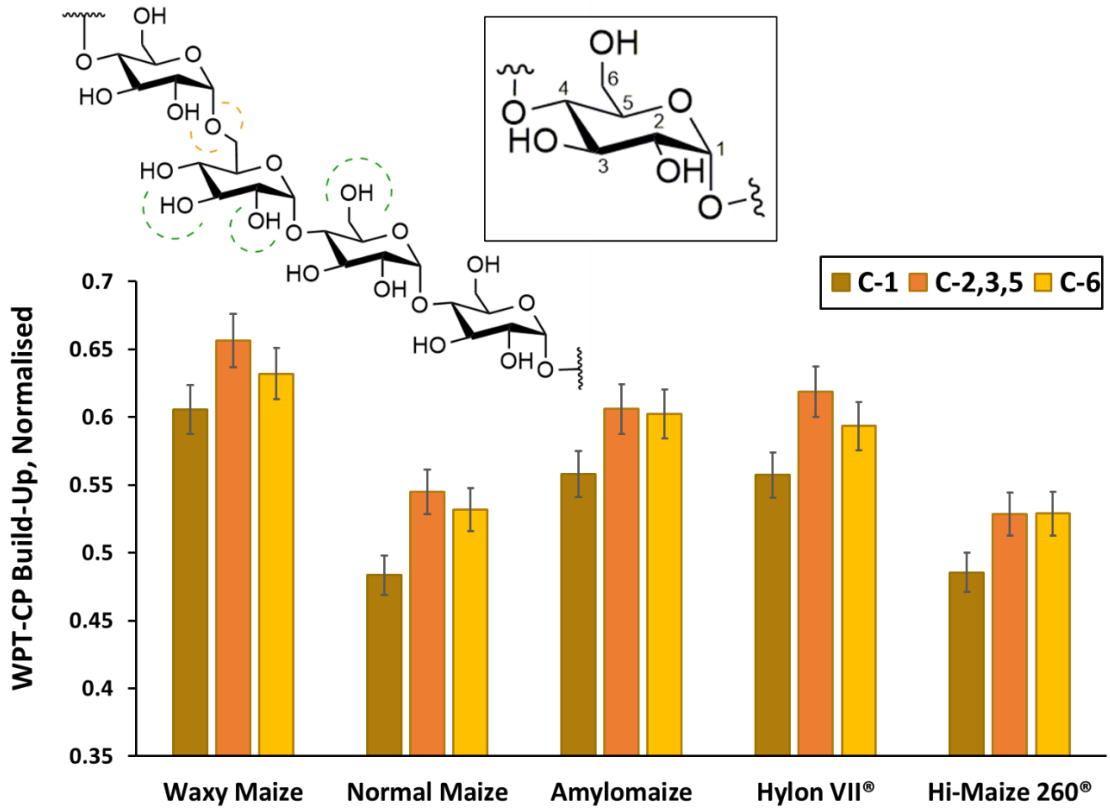

Figure 3.22: WPT-CP build-up across all five low temperature isothermally stored maize hydrogels (t_{mix} = 25 ms). Inlays showing a glucose monomer and part of a starch chain featuring α(1-4) and α(1-6) linkages, where dashed lines indicate the relative steric constraints around nuclei, with green indicating low, orange – moderate and red – high levels of steric confinement. Error bars based on the S/N ratio of our spectral data.

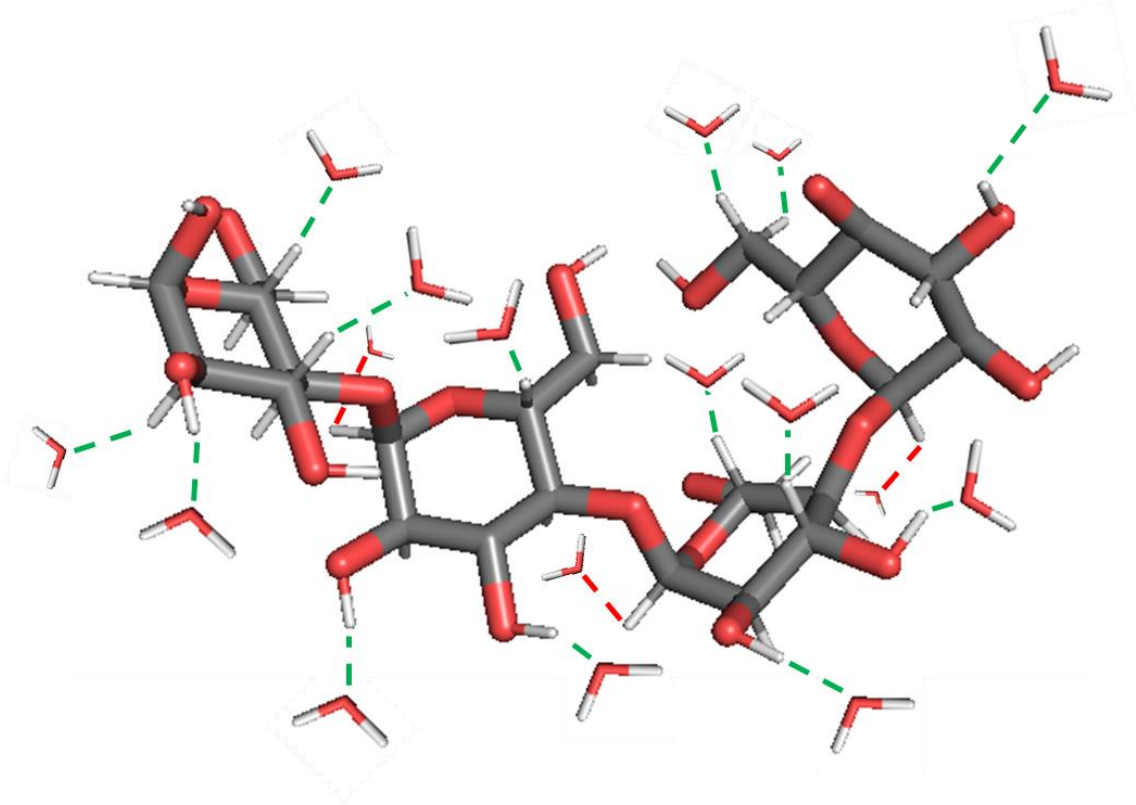

Figure 3.23: Starch chain fragment (maltotetraose) with carbon atoms in grey, oxygen atoms in red and hydrogen atoms in white; and structured water molecules surrounding the starch chain fragment, associating through hydrogen bonding (dashed lines), where the hydrogen bonds within a more confined space (O---H-C-1) are shown in red, whereas the ones in less confined space (O---H-C-2,3,5, and O---H-C-6) – in green. Image generated using UCSF Chimera software package, via the pseudobond wizard.

The five maize starch hydrogel types behaved in a very similar manner with respect to their through-space (nOe-mediated) interaction with water molecules, as evidenced by STD NMR experiments (Figure 3.24) probing the rate of transfer of magnetisation through space from the bulk hydrogel backbone to the water molecules within the hydrogel network. This offers further support for the origin of the observed mobile starch moieties, as it eliminates the possibility of differences in the organisation of water

molecules within the hydrogel network being the governing factor for the observed differences in molecular mobility.

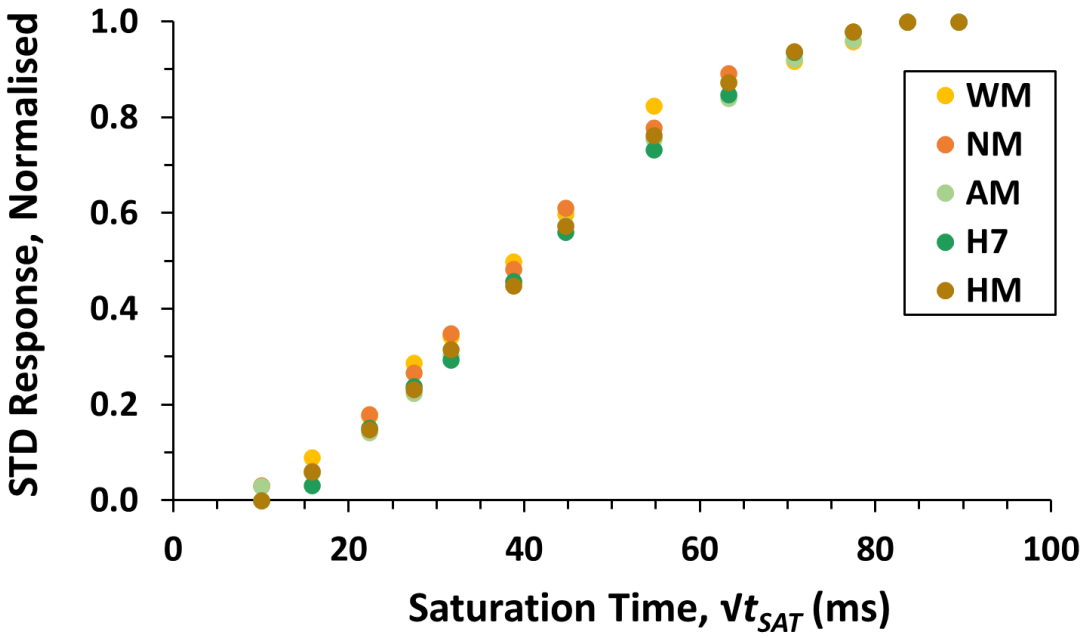

Figure 3.24: Saturation-transfer difference (STD) build-up curve (normalised) of the magnetisation transferred from the starch backbone to the water molecules in all five starch hydrogels, prepared at low-temperature isothermal conditions.

Effect of Storage Conditions on Local Mobility

Previous works have shown that the subsequent storage conditions following starch gelatinisation can have a pronounced impact on starch pastes and gels' degree of retrogradation.[244,273] So far in our work, we had observed marked differences in the bulk structural integrity of our starch gels, dependent on their storage conditions, where the micromechanical gel strength, as probed by the gels' storage moduli (G') followed the order of low temperature isothermal > thermocycled > high temperature isothermally stored (Figure 3.5).

The ^{1}H-^{13}C CPSP/MAS NMR spectra of our differentially stored starch hydrogels revealed that the levels of local mobility followed the order of high isothermal > thermocycled > low isothermal hydrogels (Figure 3.25). Furthermore, hydrogel local structural mobility correlated with their levels of mechanical resilience (R^2 = 0.8511, Figure 3.26), where low-amylose and structurally weaker gels exhibited higher local mobility levels and vice versa (Figure 3.24).

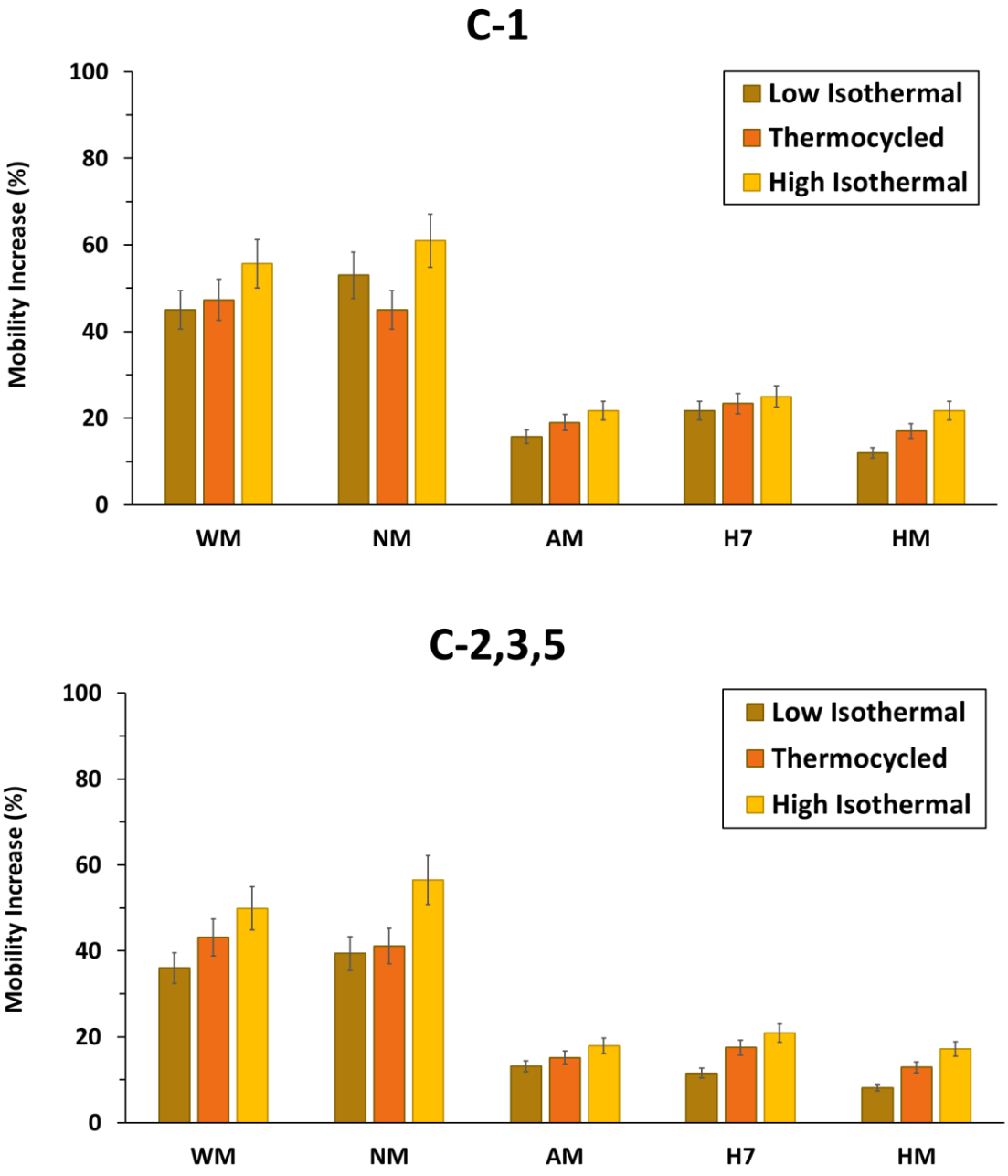

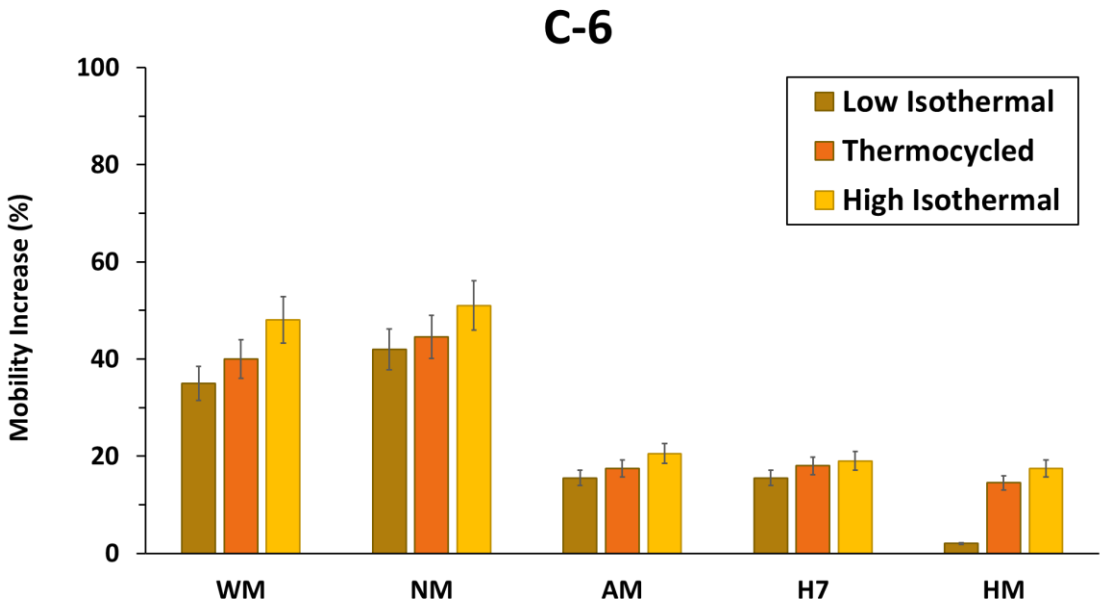

Figure 3.25: Overall increase in local structural mobility in waxy maize (WM), normal maize (NM), amylomaize (AM), Hylon VII® (H7) and Hi-Maize 260® (HM) starch hydrogels prepared with different storage conditions (low temperature isothermal, thermocycles and high temperature isothermal), organised by ^{13}C nuclear environment (C-1, C-2,3,5, and C-6).

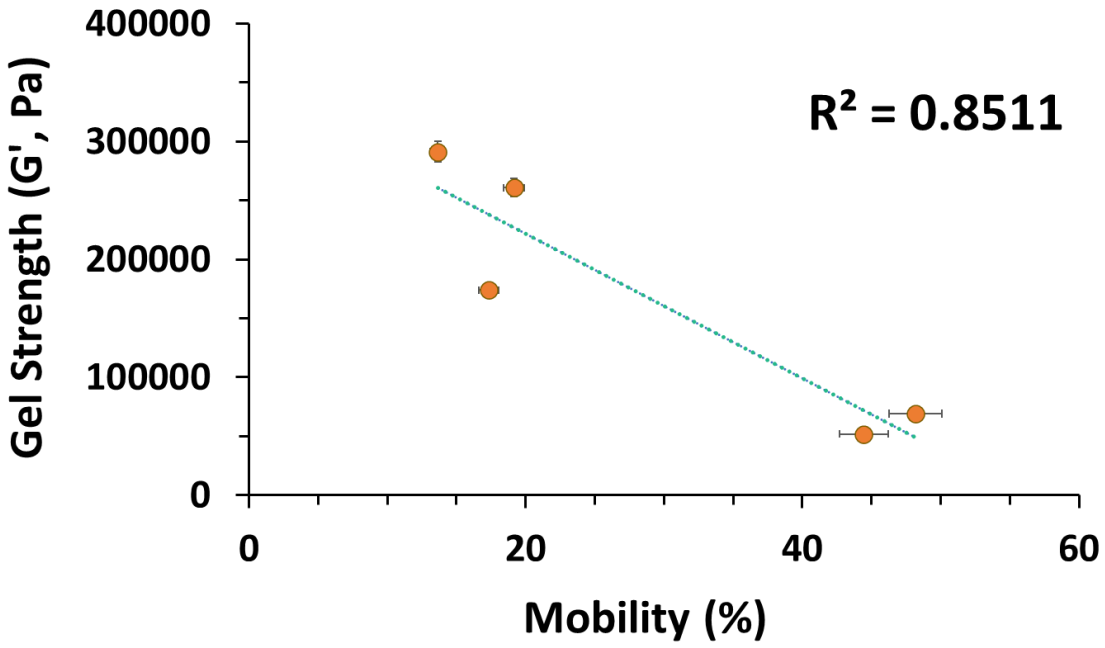

Figure 3.26: Linear correlation plot between low temperature isothermal maize starch hydrogels' strength (G', Pa) and estimated local structural mobility levels (%), with displayed trendline and R^2 value. Error bars based on the standard deviation between a minimum of three replicates.

The observed differences were interpreted as being a consequence of the differences in the rate of reassociation and retrogradation between amylose and amylopectin, or the presence of one glucan precluding optimum reassociation of another (*e.g.*, the presence of larger amylopectin molecules perturbing the effective association of linear amylose chains). The greater rate and propensity for reassociation of amylose chains, compared to amylopectin[243], likely contributes to a more tightly organised network in high-amylose starches (such as AM *vs*. WM, Figure 3.27), which in turn, may lead to restricting the motional freedom of the solvated starch chains, resulting in a lower degree of molecular mobility. An alternative explanation may be that the structurally mobile components arise largely from the amylopectin fraction of starch hydrogels, which

would result in lower degree of observable molecular mobility in high-amylose starches. This, however, is less likely, considering the original models[274] proposing the existence of mobile glucan chains existing in the pores and cavities of such hydrogel systems, were based on pure amylose gels.

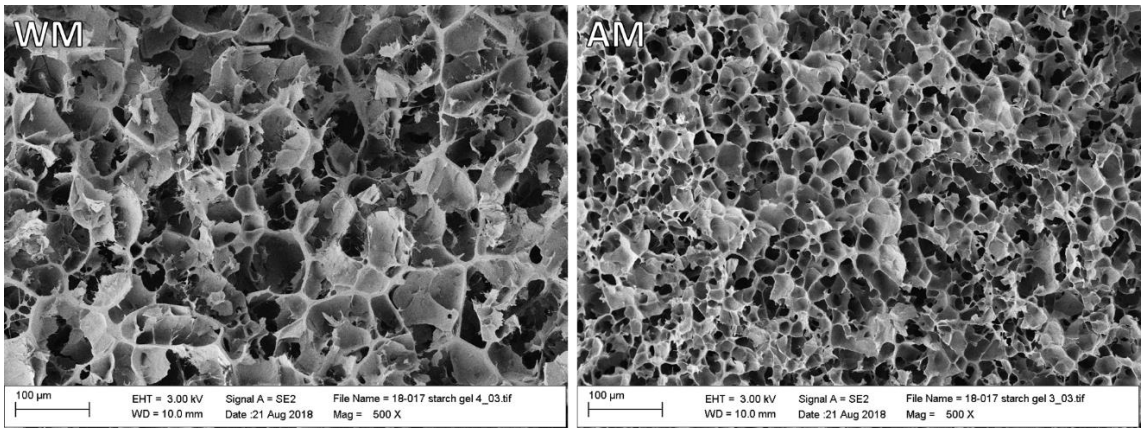

Figure 3.27: Environmental scanning electron microscopy images of waxy maize (WM, left) and amylomaize (AM, right) starch hydrogels at 500x magnification, acquired at a working distance of *ca*. 10 mm, and electron beam voltage of 3.0 kV.

3.3 Conclusions

In this work we provide insight into the molecular level organisation of starch hydrogels, probing intercomponent interactions and molecular dynamics, and show how these link to bulk system properties. We provide further evidence for and build on previously proposed models of amylose gel organisation[164,271] by quantifying the degree of mobility of solvated starch chains existing exclusively within the solvent phase of the hydrogel matrix. We demonstrate how one can modify their choice of starch type to fine-tune its hydrogel's molecular-level and bulk properties, which allows for manufacturing application-driven hydrogels for industrial applications.

Chapter 4: Starch Hydrogels in the Human Gastrointestinal Tract

Results from this chapter are largely published in:

Todor T. Koev, Hannah C. Harris, Sara Kiamehr, Yaroslav Z. Khimyak, Frederick J. Warren. *Carbohydrate Polymers* (2022). 289 (1): 119413

4.1 Introduction

In our previous chapter we demonstrated how one can alter their choice of starch type, in order to modulate its corresponding hydrogel's bulk structural and molecular-level physicochemical properties. In this chapter we continue this investigation by trying to answer the question of whether starch hydrogels can serve as viable orally administrable targeted colonic drug delivery platforms, and what structure-function links underpin their properties as pharmaceutical excipients. We also aim to explore the interaction between starch hydrogels and components of the human gastrointestinal tract (GIT), and how starch gel structure and organisation dictate its behaviour in a simulated GI environment.

Orally administrable targeted colonic drug delivery systems have been of great scientific interest over the past decade[101,275], due to their potential to improve the administration of currently existing treatments for common colorectal pathologies (*e.g.*, ulcerative colitis, Crohn's disease, colorectal cancer). This is largely achieved by providing localised release and distribution of drug molecules at higher concentrations in the colon, whilst limiting upper gastrointestinal tract (GIT) drug release, systemic absorption, and metabolism. Drug carriers' structural integrity has a significant impact on their role as excipients, as well as on the pharmacokinetic profile of the loaded drug molecules.

Depending on the primary mode of drug delivery – drug diffusion-dominated, matrix disintegration-dominated, or matrix deformation/swelling-dominated (Figure 4.1), structural integrity and matrix organisation play a major role in achieving optimal release kinetics.[276] Probing structural changes in the drug delivery scaffold, as well as quantifying the amount of drug release as a function of GIT transit time can help identify the primary mechanism of drug release.[277]

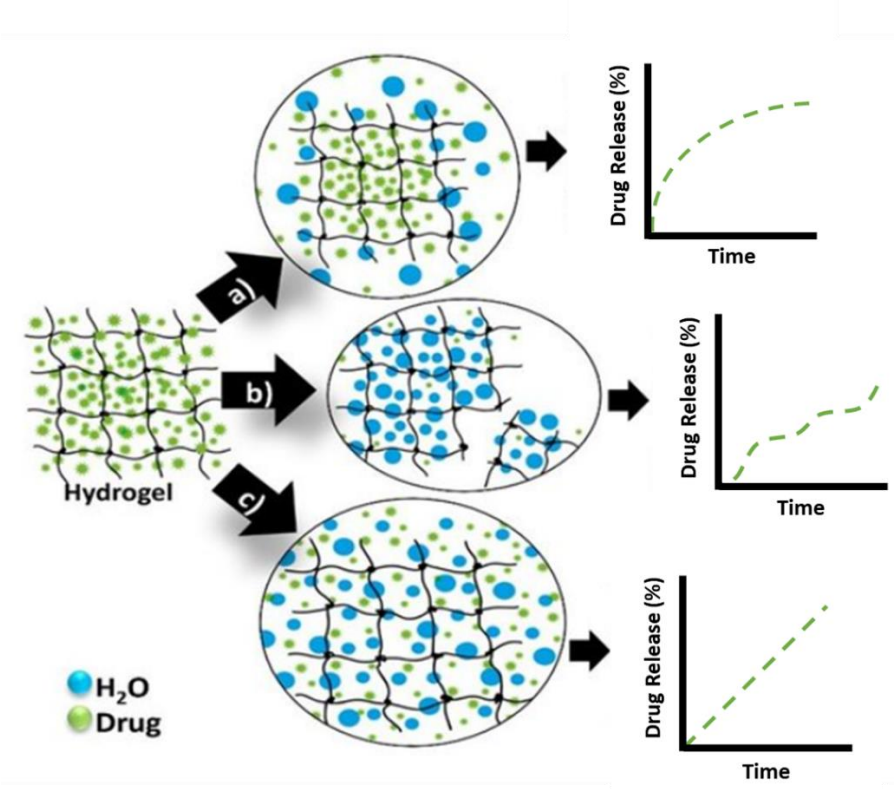

Figure 4.1: Hydrogels drug release mechanisms and their respective pharmacokinetic profiles: drug diffusion-dominated mechanism (a); matrix degradation-dominated mechanism (b); matrix deformation/swelling-dominated mechanism (c). Adapted from Rocha-García *et al*. (2016).[277]

At present, the most promising candidates for orally administrable targeted colonic pharmaceutical excipients are biocompatible natural polysaccharides such as starch, cellulose and pectins, and non-biodegradable and non-absorbable polymers like

Eudragit S.[278,279] Most starch-based systems for colonic drug delivery involve combining multiple polysaccharides[107], proteins[280], and organic acids[105] in the formulation, which results in longer and more complex excipient formulation.

Hydrothermally treated and subsequently retrograded starch forms hydrogel structures able to resist small intestinal digestion (RS III)[281–283], but instead reach the colon structurally intact, where they are fermented by commensal bacteria.[86,134,284,285] There has been some research on the impact of starch on the gut microbiota[131,284,286], but not much is known about the structure-function relationships governing starch hydrogels' interaction and impact on the full extent of the GIT.[64]

The human GIT (oral[287], small[288] and large intestinal[289–293]) microbiome has been shown to be populated by tens of trillions of microorganisms, providing its host with physiologically relevant enzymes, not natively secreted by the host. Many gut bacteria have been shown to be capable of starch fermentation and/or degradation.[289] RS fermented in the large intestine has been shown to lead to the production of gases, short-chain fatty acids (SCFAs) and low levels of alcohols.[129] Gut bacteria-mediated amylolysis is a result of the combined action of α-1,4- and α-1,6-specific enzymes (*i.e.,* type I pullulanases and amylopullulanases), originating from three major phyla – *Actinobacteria*, *Bacteroidetes* and *Firmicutes*, together accounting for 95% of the total mammalian gut microflora.[82] Several important gram-positive and negative microbial species, such as *Ruminococcus bromii*, *Bacteroides thetaiotaomicron* and *Bifidobacteria* species, have been shown to be capable of both resistant starch degradation, and of utilising partial products of starch digestion, such as di-, trisaccharides and maltodextrins.[294,295]

Most British and United States Pharmacopoeia (BP and USP, respectively) utilised methods of simulating solid dosage forms' dissolution and disintegration under *in vitro* conditions focus primarily on the gastric or small intestinal environments.[280,296] This approach fails to account for physiological concentrations of hydrolytic enzymes and salts across the human upper GIT, leading to an overestimation of the ability of pharmaceutical excipients to reach the large intestine structurally intact.

In our previous work, we showed how amylose content and preparation methods dictate starch hydrogels' bulk and molecular level properties. Low-amylose containing starches, such as normal maize (NM) produced structurally weaker gels, with higher degree of molecular mobility, compared to high-amylose starch hydrogels, such as Hylon VII® (H7).[64] In this study, we probe the viability of NM and H7 starch hydrogels as orally administrable colonic drug delivery vehicles, linking gel structure with its functional properties in the human GIT. We integrate two widely accepted models of *in vitro* digestion – the INFOGEST protocol[112], and colonic fermentation – the batch fermentation model[217,297], accounting for *in vivo* concentrations of hydrolytic enzymes, providing a complete representation of the *in vivo* behaviour of starch gels as pharmaceutical excipients, compared to previous studies.[101,105,298] We demonstrate how to use this insight for the design of hydrogel pharmaceutical excipients from easily accessible and affordable materials, which resist upper GIT degradation, and achieve sustained drug release confined exclusively to the colon.

Furthermore, we show how structure governs interactions of starch gel systems with host's commensal bacteria, and their ability to utilise the hydrogel excipient as a substrate for the production of important physiologically relevant microbial

metabolites, such as SCFAs.[130,299] To the best of our knowledge, this is the first work to apply the INFOGEST protocol of *in vitro* digestion, the batch colon model, as well as high-resolution NMR spectroscopy to the context of targeted colonic pharmaceutical excipients. Our work provides insight for the development of superior orally administrable targeted drug delivery platforms with auxiliary physiologically relevant properties.

4.2 Materials and Methods

4.2.1 *Preparation of Drug-loaded Starch Hydrogels*

Starch hydrogels (10% w/v) intended to be used as controls (without the presence of small drug molecules) were prepared by making up 10% (w/v) starch/deionised water suspensions in 25.0 mL Pyrex® screw top vials, vortex mixed and autoclaved (121 °C, 15 psig) for 20 min, followed by storage for 8 days at 4 °C, forming opaque white gels.

Drug-loaded starch hydrogels were prepared by mixing vanillin (VNL), 5-fluorouracil (5FU) or doxorubicin (DOX) into the starch/water suspensions, at 1% (w/v) prior to gelatinisation. NM and H7 starch hydrogels containing the small molecules are referred to as NM-VNL, NM-5FU and NM-DOX, H7-VNL, H7-5FU and H7-DOX respectively.

VNL, 5FU and DOX were chosen for drug loading because of two reasons – they have been shown to be able to act as a colonic health promoter (VNL)[300], and are regularly employed in the localised treatment of colorectal cancer (5FU and DOX)[275,301,302]; as well as they have ^{1}H peaks, the chemical shift of which is in a spectral region where no bacterial metabolites or fermentation media ingredients have peaks, making them easily distinguishable in quantitative ^{1}H NMR spectra.

All hydrogels intended for simulated digestion, fermentation and micromechanical analyses were carefully excised using a 10 mm cork borer (Breckland Scientific Supplies Ltd., Stafford, UK) and cut into cylinders, 10 mm in height, using a surgical blade (Swann Morton Ltd., Sheffield, UK).

4.3 Results and Discussion

4.3.1 *Starch Hydrogel Bulk Properties and Molecular Organisation through the GIT*

The impact of amylose content on starch' physicochemical properties and susceptibility to amylolytic degradation has been well documented in the literature.[64,255,303,304] In order to probe the viability of low- and high-amylose starch gels as drug delivery vehicles for targeted release in the distal parts of the GIT, it is important to investigate the structural changes occurring in the hydrogel organisation, such as chain length distribution, degree of branching, overall structural integrity – properties important for polymer-based orally administrable excipients' disintegration and drug dissolution profiles.[305,306] Knowledge and control of these parameters would allow for fine tuning of the pharmacokinetic properties of these excipients.[307]

Micromechanical Properties

The extent of the LVE regime of undigested NM and H7 starch hydrogels (*i.e.*, before any enzymatic treatment) was from 0.03 to 0.5% strain (Figure 4.2). It should be noted that the LVE regime is likely to decrease in range and absolute values for the digested and fermented hydrogels, due to decreases in the structural integrity of the gels under the influence of amylolytic enzymes. In order to keep the experimental conditions consistent between samples, we opted for a lower strain value (0.1%) within the gels'

LVE regime, in order to avoid premature fracturing of the digested and fermented hydrogels during the frequency sweeps.

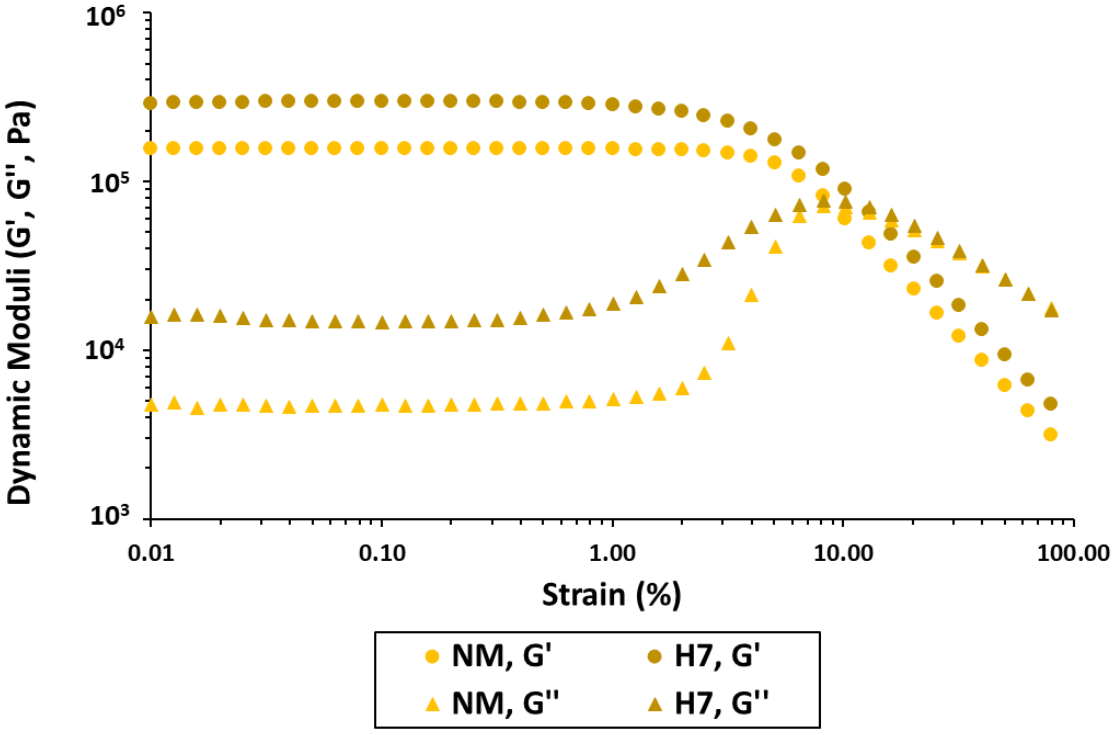

Figure 4.2: Storage and loss moduli (G' and G'', respectively) of NM and H7 starch gels at 37 °C as a function of applied strain, with constant frequency of 0.1 Hz, for ascertaining the hydrogels' linear viscoelastic (LVE) region. Results presented are averages of a minimum of three repeats, where all repeats are within 10% of each other. Error bars have been omitted for visual clarity.

Both NM and H7 starch hydrogels exhibited progressive decrease in their storage moduli (G'), with a significant drop occurring between the 12- and 24-hour fermentation points for NM gels and between 24- and 48-hour points for H7 starch gels (Figures 4.3-4.4).

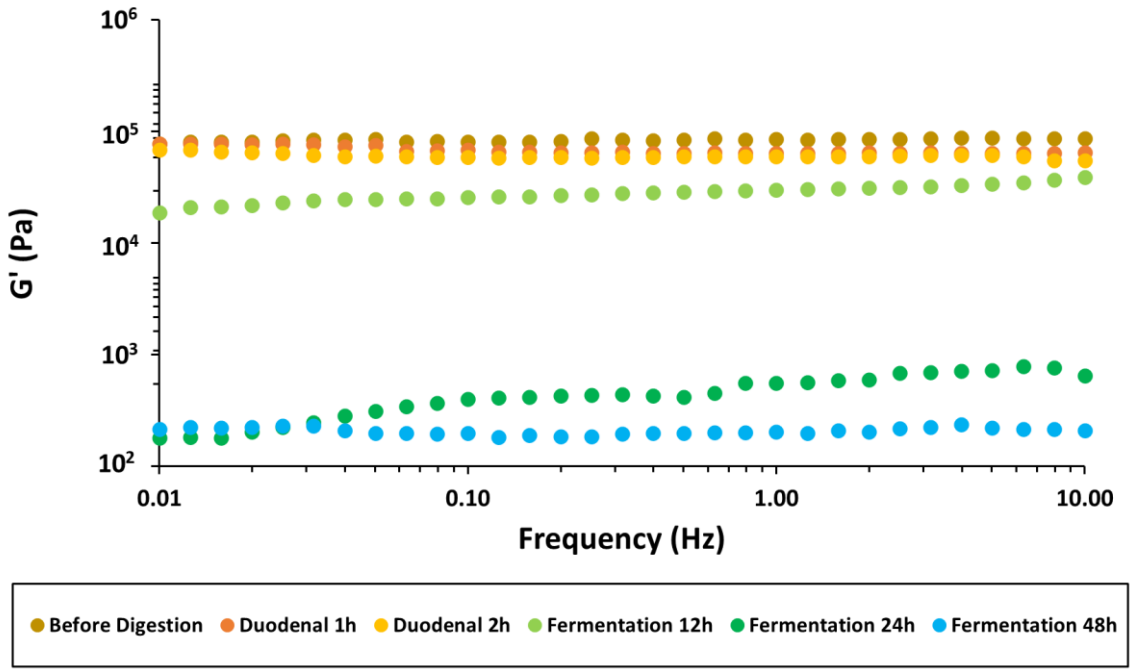

Figure 4.3: Storage and loss moduli (G' and G'', respectively) of NM starch hydrogels at successive *in vitro* digestion and fermentation steps, as a function of applied frequency. Results presented are averages of a minimum of three repeats.

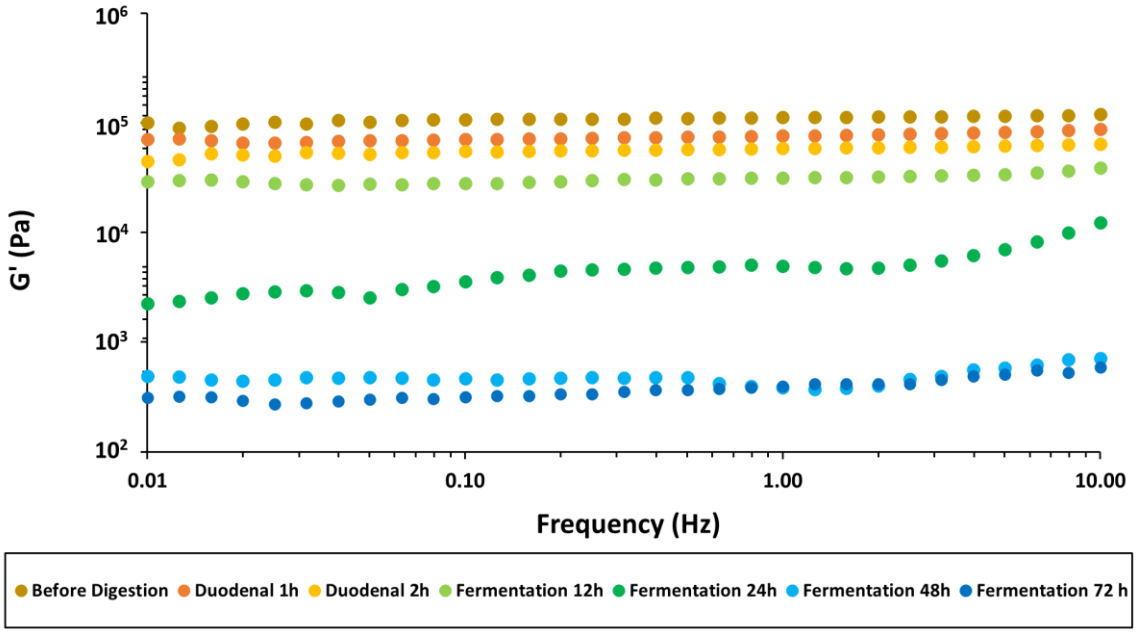

Figure 4.4: Storage and loss moduli (G' and G'', respectively) of H7 maize starch hydrogels at successive *in vitro* digestion and fermentation steps, as a function of applied frequency. Results presented are averages of a minimum of three repeats.

This delayed drop in structural integrity of H7 relative to NM is likely a result of NM's higher susceptibility to enzymatic degradation during the *in vitro* amylolytic digestion, compared to H7 (Figure 4.5). This progressive decrease in the matrices' ability to resist external stressors is likely to have an impact on their role as drug molecule excipients by way of influencing their rate of disintegration and drug release throughout the GIT.

It should be noted that the 72-hour fermentation time point is missing from the micromechanical profile of NM hydrogels (Figure 4.3), as by that point, the hydrogel was no longer exhibiting the properties of a stiff gel, but was closer to a viscous paste, which precluded its positioning between the parallel plates of the rheometer, and subsequent obtaining of the substrate's micromechanical response at variable frequency.

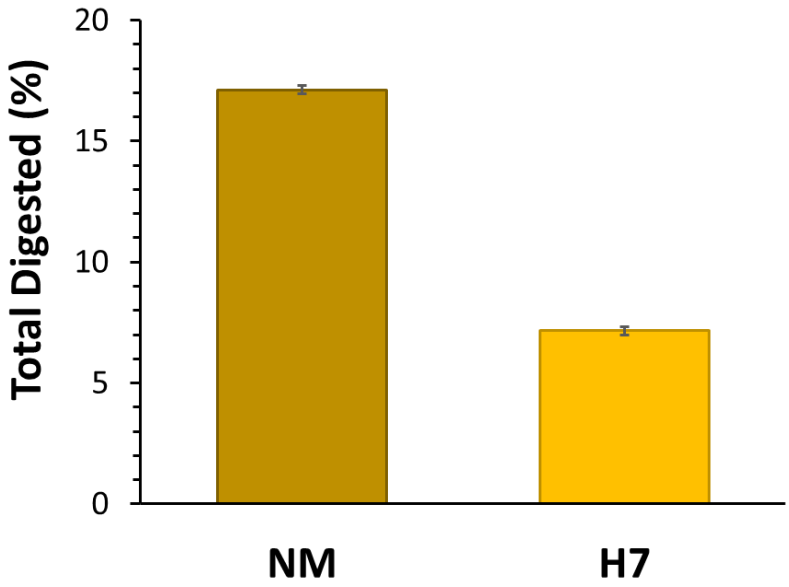

Figure 4.5: Digestibility of NM and H7 starch hydrogels at the end stage of *in vitro* INFOGEST digestion. Results shown are the average of a minimum of three repeats, where error bars are based on the standard deviation across all replicates.

4.3.1.2 *Molecular Structural Parameters*

The molecular size distributions of both branched and debranched gels at successive stages in the simulated GIT (Figures 4.6-4.9) revealed differences in the molecular structural parameters (hydrodynamic radius, R_h for whole molecule size separation; and degree of polymerisation, DP for debranched molecule size separation) between NM and H7 starch hydrogels.

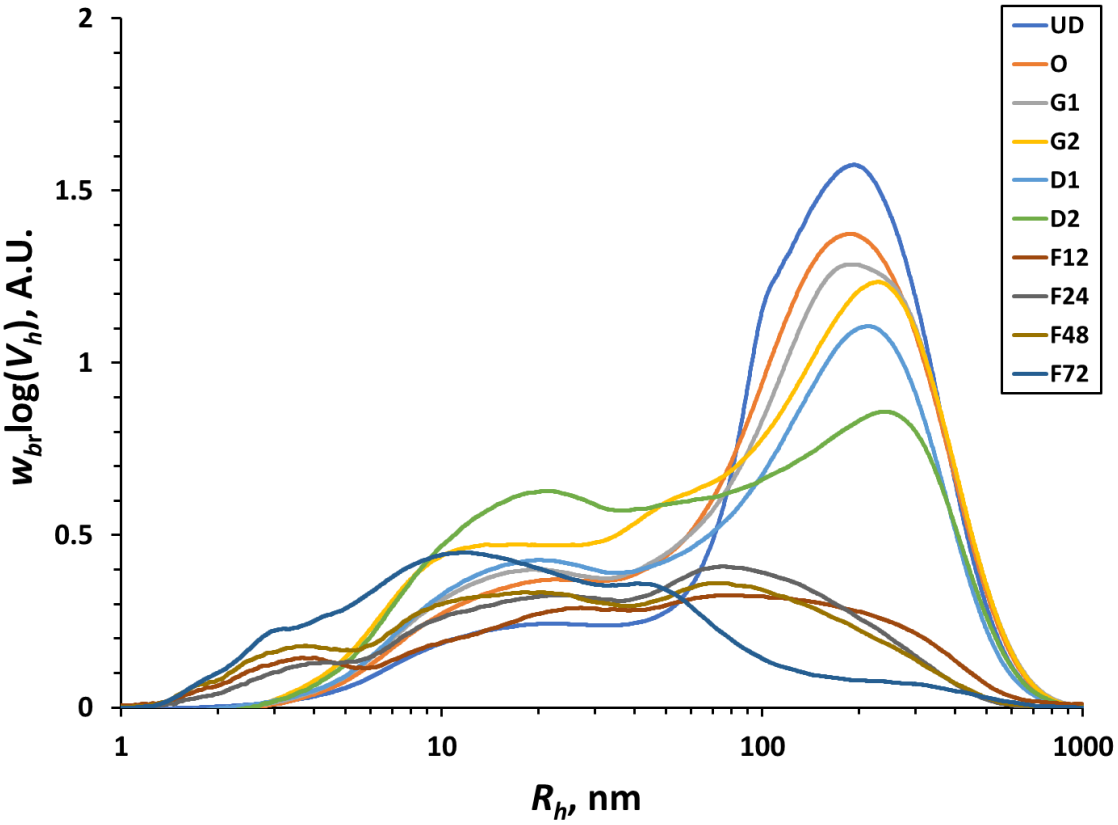

Figure 4.6: Size exclusion chromatography weight distributions of whole NM starch hydrogels, $w_{br}\log(V_h)$ A.U. *vs*. R_h, nm, before (UD), after oral (O), 1 h of gastric (G1), 2 h of gastric (G2), 1 h of duodenal (D1) and after 2 h of duodenal (D2) INFOGEST digestion, and after 12, 24, 48 and 72 hours of *in vitro* fermentation (F12, F24, F48 and F72, respectively), 0-order detrend- and standard normal variate-normalised.

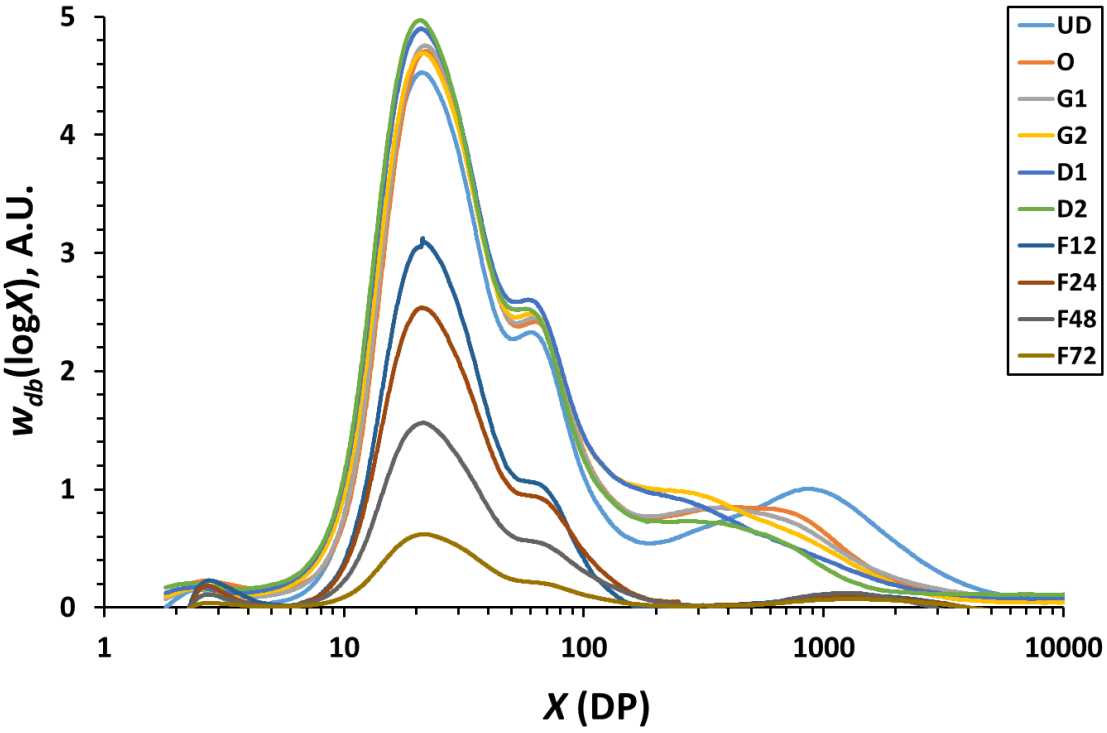

Figure 4.7: Size exclusion chromatography weight distributions of debranched NM starch hydrogels, $w_{br}\log(Rh)$ A.U., before (UD), after oral (O), 1 h of gastric (G1), 2 h of gastric (G2), 1 h of duodenal (D1) and after 2 h of duodenal (D2) INFOGEST digestion, and after 12, 24, 48 and 72 hours of *in vitro* fermentation (F12, F24, F48 and F72, respectively), 0-order detrend- and standard normal variate-normalised.

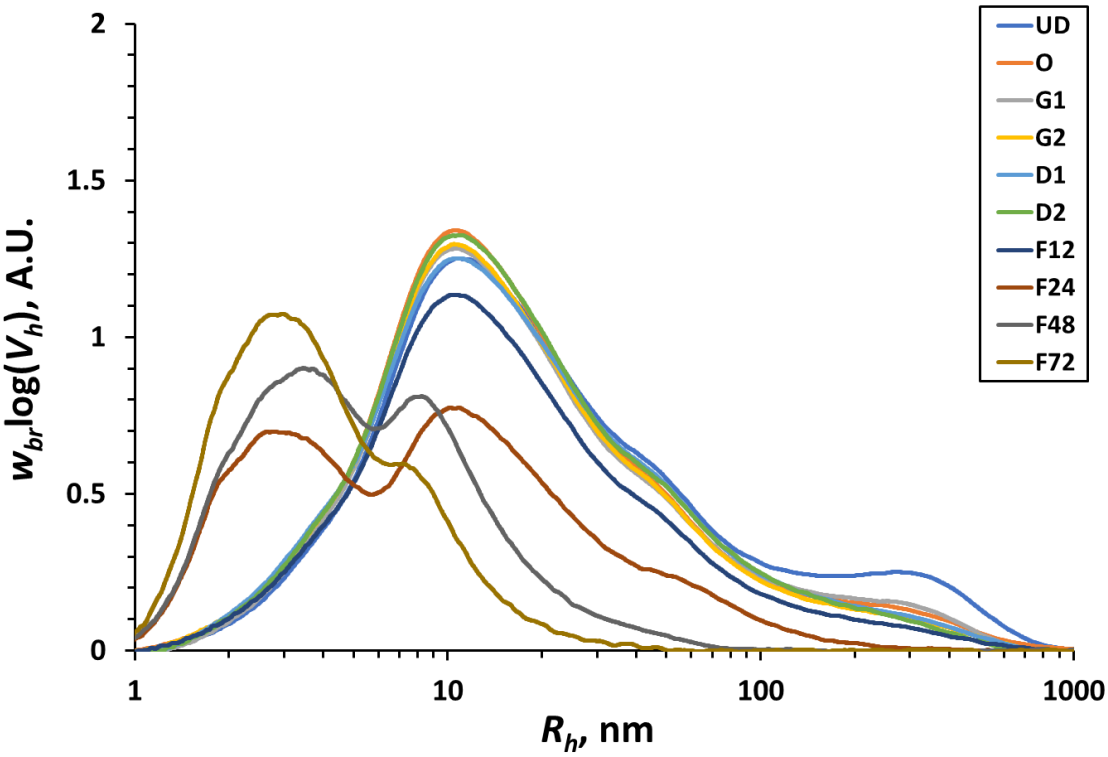

Figure 4.8: Size exclusion chromatography weight distributions of whole H7 starch hydrogels, $w_{br}\log(Rh)$ A.U., before (UD), after oral (O), 1 h of gastric (G1), 2 h of gastric (G2), 1 h of duodenal (D1) and after 2 h of duodenal (D2) INFOGEST digestion, , and after 12, 24, 48 and 72 hours of *in vitro* fermentation (F12, F24, F48 and F72, respectively), 0-order detrend- and standard normal variate-normalised.

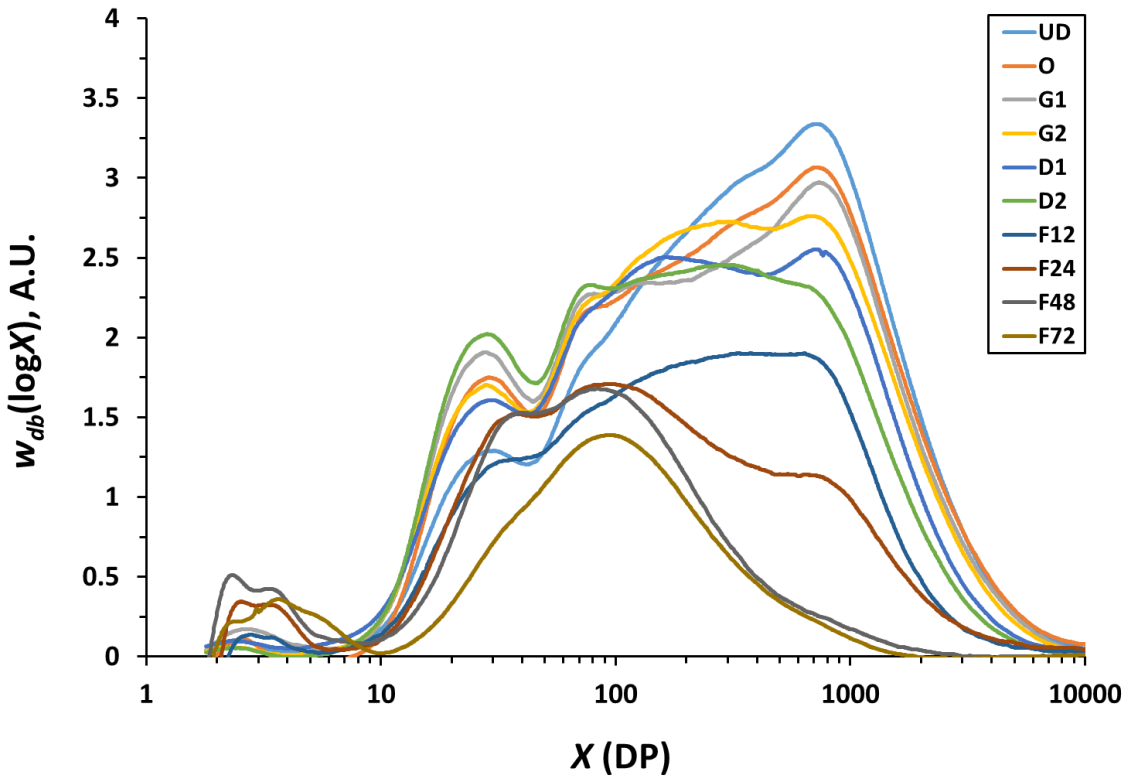

Figure 4.9: Size exclusion chromatography weight distributions of debranched H7 starch hydrogels, $w_{br}\log(Rh)$ A.U., before (UD), after oral (O), 1 h of gastric (G1), 2 h of gastric (G2), 1 h of duodenal (D1) and after 2 h of duodenal (D2) INFOGEST digestion, and after 12, 24, 48 and 72 hours of *in vitro* fermentation (F12, F24, F48 and F72, respectively), 0-order detrend- and standard normal variate-normalised.

The amylopectin fraction (R_h ≈ 200 nm, Figure 4.6)[303] in whole NM gels exhibited a greater susceptibility to upper GIT amylolytic digestion, compared to H7's (Figures 4.6 and 4.8, UD *vs.* D2), as seen in the works of Witt *et al*.[308] Unlike previous works probing the amylolytic susceptibility of ground lyophilised gelatinised starch[221,308], our data showed minimal changes occurring in the upper GIT in the molecular structural parameters of H7 hydrogels (Figure 4.8, UD *vs.* D2), highlighting the impact of the macromolecular hydrogel organisation and structure on its susceptibility to α-amylase digestion and the accessibility of the enzyme to the substrate.[127]

The whole molecular size separation data for both NM and H7 gel samples showed it is the amylopectin region (Figures 4.6 and 4.8, R_h ≈ 200 nm) that experiences greater changes during upper GIT digestion stages, compared to the amylose region (Figures 4.6 and 4.8, R_h ≈ 10-20 nm). This provides further context for the digestibility and micromechanical data, indicating it is the amylopectin fraction's greater susceptibility to α-amylase degradation that has a greater impact on the hydrogels' gradual loss of structural integrity in the upper GIT, compared to amylose.

The size distributions of the debranched NM and H7 gels revealed some decrease in the contribution of longer amylose chains (DP ≈ 1000 – 7000, UD *vs.* D2, Figures 4.7 and 4.9), accompanied by a slight increase in the contribution of shorter chains (DP ≈ 10 – 50, UD *vs.* D2, Figures 4.7 and 4.9) during the upper GIT stages of digestion. This points towards longer chains comprising structural elements more easily accessed by α-amylase, likely a result of their slower and more hindered reassociation into less-digestible structural conformations (*i.e.*, double helices). There was a small population of amylose chains (DP ≈ 1000-1100, Figures 4.7 and 4.9), which was still present after *in vitro* digestion and fermentation, likely to be linked to an increased structural stability, ease of recrystallisation, and lower susceptibility to enzymatic degradation of this linear polymer fraction.[309] The fractions at DP ≈ 2 – 7 are likely to be either the products of enzymatic hydrolysis, having remained trapped within the solvent-filled pores of the hydrogels, amino acids, or small proteins produced by commensal bacterial during the *in vitro* digestion and fermentation.

In both the branched and debranched size distributions of both gels, the most pronounced changes in the hydrogels' molecular structural parameters occurred during

the fermentation stages in the simulated colon (Figures 4.6-4.9, UD *vs.* F72). These are likely to be the result of the cumulative action of multiple hydrolytic enzymes featuring both α(1-4) and α(1-6) specificity, unlike across the upper GIT where starch gels are exposed largely to α(1-4) hydrolytic enzymes (salivary and pancreatic α-amylase).[129,289,310] This is further supported by the preferential cleavage of α(1-4) linkages during the upper GIT digestion stages, followed by preferential cleavage of α(1-6) glycosidic bonds in the large intestinal phase, shown by ^{1}H NMR (Figure 4.10).

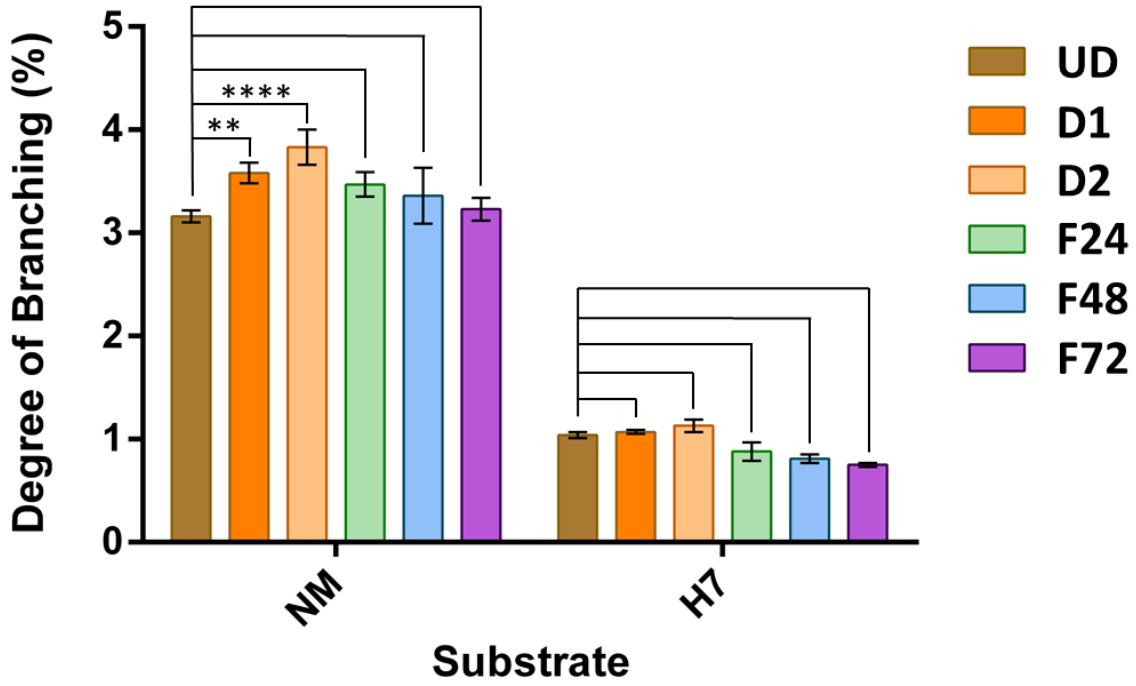

Figure 4.10: Degree of branching, expressed as a percentage of the total number of glucosidic linkages in NM and H7 starch hydrogels before digestion (UD), at 1 and 2 h of small intestinal INFOGEST digestion (D1 and D2, respectively), and at 24, 48 and 72 h of *in vitro* fermentation (F24, F48 and F72, respectively). Error bars are based on the standard deviation across a minimum of three measurements, where ** $p<0.005$, **** $p<0.0001$.

Starch Hydrogel Internal Mobility

We probed the change in the degree of local mobility across all ^{13}C environments in NM and H7 starch hydrogels as they traverse the entire length of the simulated GIT. There was a progressive increase in degree of mobility of solvated chains across all ^{13}C sites with each successive digestion and fermentation stage, accompanied by a simultaneous progressive decrease in their G' (kPa) and strain (%) values at their cross-over point (*i.e.,* point of loss of structural integrity, Figure 4.11).

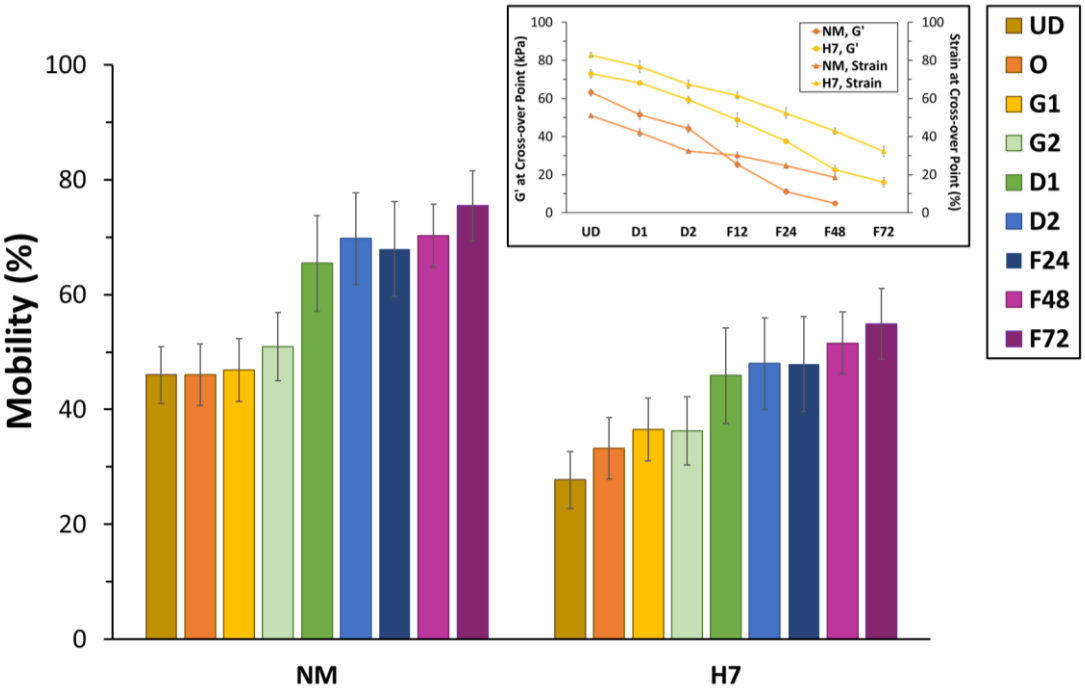

Figure 4.11: Estimated levels of local mobility averaged across all ^{13}C environments in NM and H7 starch hydrogels before digestion (UD), at various INFOGEST digestion (O, G1, G2, D1, D2) and *in vitro* fermentation stages (F24, F48 and F72). Inlay showing cross-over point analysis of NM and H7 gels before and during INFOGEST digestion, and during *in vitro* fermentation, featuring the samples' G' (kPa) and strain (%) values at their respective G cross-over points. Error bars are based on the standard deviation across a minimum of three replicates.

Solid-state NMR spectra (^{1}H-^{13}C CP and CPSP/MAS) of the starch hydrogels at the end of simulated digestion (Figure 4.12, NM, D2) revealed the presence of new sharp peaks in the CPSP spectrum at *ca*. 93 and 96 ppm, the chemical shift of which overlapped with peaks in the solution state NMR spectrum of the digesta at the end of simulated INFOGEST protocol (Figure 4.12, Digesta). Comparison of the ^{1}H-^{13}C CPSP/MAS spectra of the starch gels at the end of *in vitro* digestion, as well as the solution state ^{13}C NMR spectrum of the digesta with the solution-state spectrum of an equimolar (1.0 mM) mixture of reducing sugars (Figure 4.12, glucose, maltose, maltotriose), revealed the identity of the newly observed sharp peaks to be solvated products of digestion (DP ≈ 1 – 3) remaining trapped inside the water-filled pores of the starch hydrogels, as well as remaining in the digesta following simulated upper GIT enzymatic hydrolysis.

The newly observed peaks assigned to a combination of reducing sugars. *i.e*., glucose, maltose and maltotriose, were no longer present after 24 h of *in vitro* fermentation (Figure 4.12, F24). This is likely to be a consequence of their easier utilisation as a carbon source by commensal bacteria[291,311], compared to the pre-digested macromolecular starch matrix.

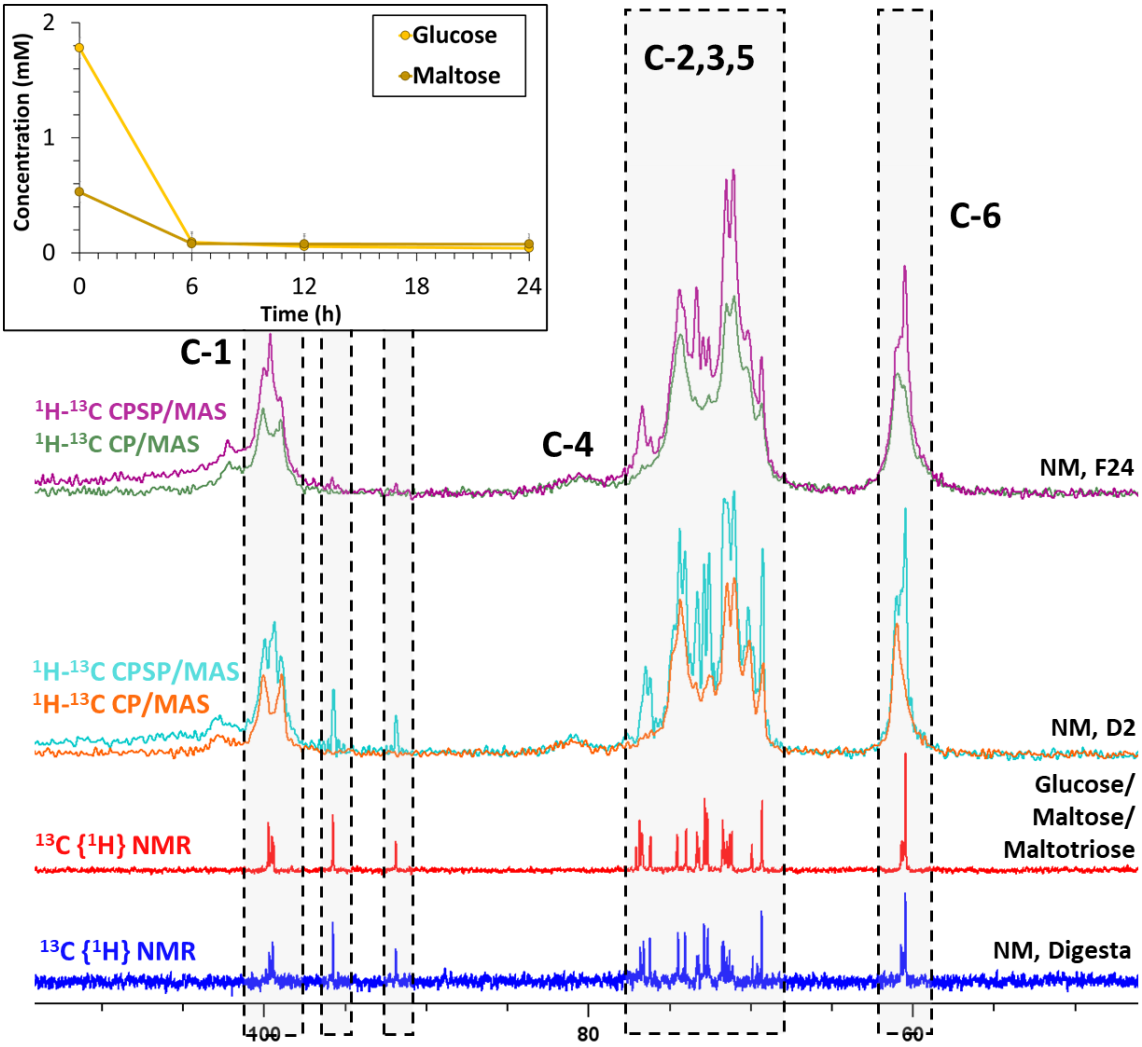

Figure 4.12: ^{1}H-^{13}C CP and CPSP MAS NMR spectra (orange and green, and cyan and magenta, respectively) of H7 starch hydrogels at the end of INFOGEST digestion (D2), and after 24 h of *in vitro* fermentation (F24), $^{13}C\{^{1}H\}$ solution state NMR of glucose, maltose and maltotriose (1.0 mM in D_2O each, red), and of the digesta at the end of INFOGEST digestion (blue). Inlay showing changes in concentration of glucose and maltose (yellow and brown, respectively) across 72 h of *in vitro* fermentation of both NM and H7 substrates (circle and triangle, respectively).

Starch Hydrogels' Viability as Targeted Colonic Drug Delivery Platforms

Across all samples, the drug release was confined to the large intestine with minimal to no release in the upper GIT (Figure 4.13). The drug molecules' release rates were several times lower than other starch-based nanoparticle and polysaccharide hydrogel-type colonic drug delivery platforms of polysaccharide origin[280,312] (*e.g.*, 70-100% drug released from other nanoparticles and gels after 24 hours *vs*. 15-56% from NM and H7 hydrogels, Figure 4.13).[280,312–316] These data highlight starch hydrogels' advantage as targeted colonic drug delivery vehicles with prolonged release, allowing for longer therapeutic windows and lower frequency of drug administration – two important parameters in patients' quality of life. Unlike traditional colonic pharmaceutical excipients, exhibiting sigmoidal release kinetics with rapid release of the guest molecule[317,318], these starch hydrogels show a more gradual pharmacokinetic release profile (1.25-3% *vs.* 0.63-2.1% drug release per hour, respectively).[280,316]

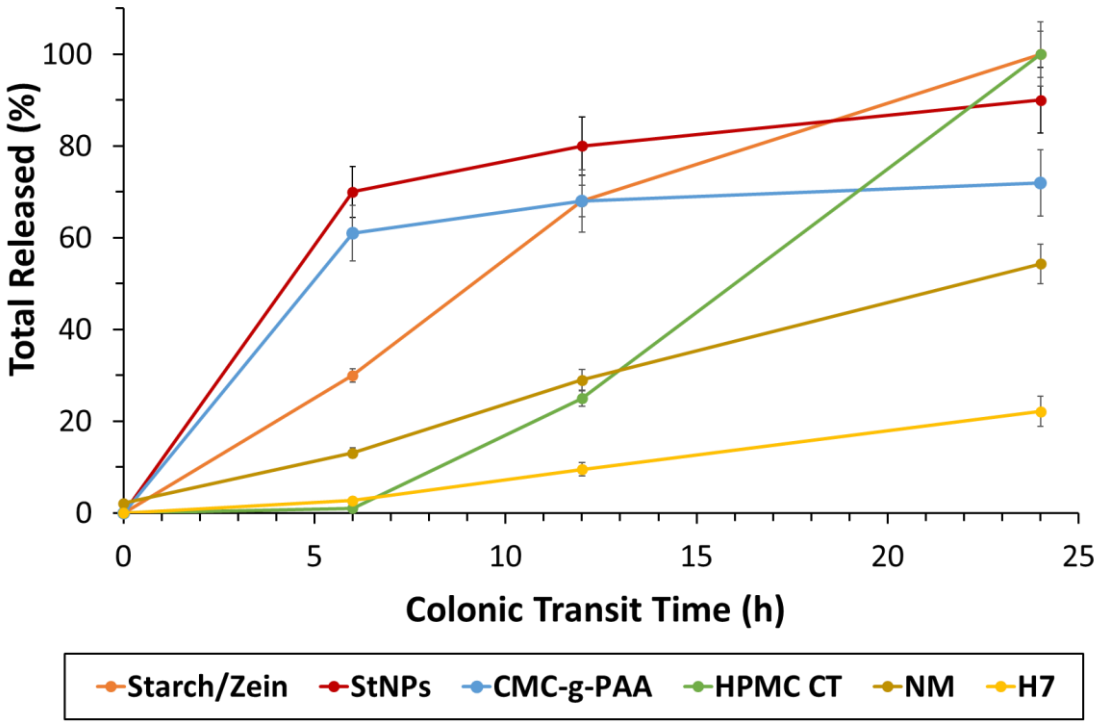

Figure 4.13: Comparative colonic drug release kinetics between VNL-loaded NM and H7 hydrogels, and four competitor drug delivery platforms: starch/zein films[280], amphiphilic starch nanoparticles (StNPs)[316], carboxymethylchitosan-g-polylactic acid (CMC-g-PAA)[318], and hydroxypropyl methylcellulose compression tablets (HPMC CT)[319].

Drug carriers' structural integrity has a significant impact on their role as excipients, as well as on the pharmacokinetic profile of the loaded drug molecules. [276] The NM and H7 hydrogels' drug release kinetics mimic the trends observed in the loss of the excipients' structural integrity (Figure 4.14, inlay). H7's delayed degradation across the entire length of the GIT compared to NM was mirrored by the two hydrogels' pharmacokinetic profiles when loaded with the three guest molecules (Figure 4.14), where all three drugs were consistently released faster from the NM gels compares to the H7 gels. These data show it is matrix disintegration (*a.k.a.* enzymatic erosion[320]) that appears to be the dominating factor in the pharmacokinetic profile of the loaded drug molecules across the GIT.

Each of the three guest molecules showed different release kinetics, with VNL showing the most rapid release kinetics in the *in vitro* colonic phase, followed by DOX and 5FU (Figure 4.14). Differences in release kinetics may be influenced by the small molecules' different degree of physical proximity and interaction with the starch backbone, where the contact between the drugs and the host followed the order of VNL < DOX << 5FU, with interaction strengths estimated by STD NMR (Figures 4.15-4.17). The molecules exhibiting less contact with the starch backbone, such as VNL, showed the most rapid release kinetics, with the drugs showing more contact with the starch backbone, such as 5FU and DOX, being released more slowly and less completely. Guest-host interactions are important when formulating pharmaceutical excipients, as they can have a profound effect on the release kinetics of the API. Chemical modification of both the guest and host are common physicochemical approaches to controlling the degree of interaction between these two species in the formulation of pharmaceutical excipients.[321] It is important to note, however, that in dynamic complexes (and states), STD NMR reports on the contact time of one molecule with another, averaged out across all populations and states the complex undergoes within the experimental time. This means, that in dynamic complexes and states, this methodology reports on an averaged "snapshot" of the dynamic events.

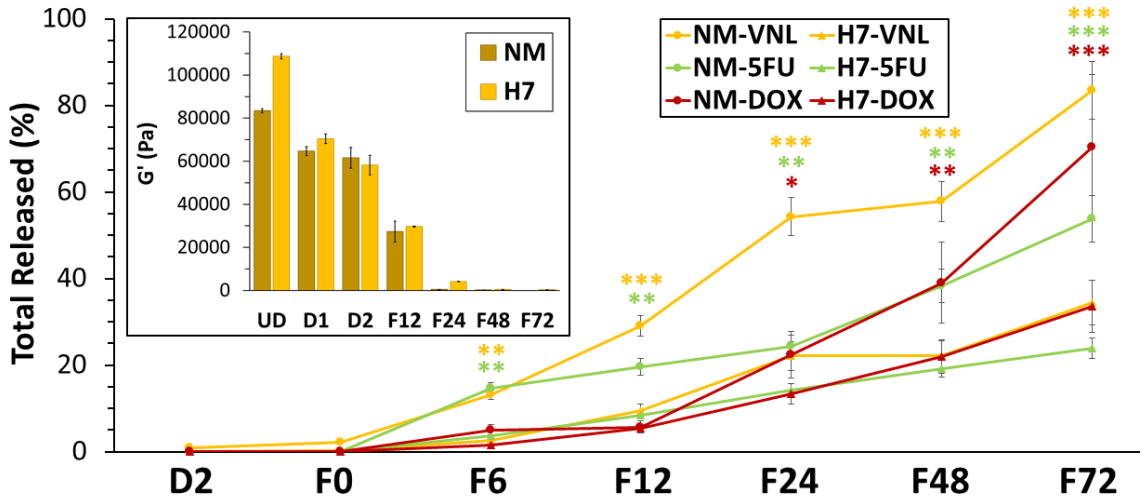

Figure 4.14: Release profiles of 5FU, VNL and DOX from NM and H7 hydrogels during the end of the *in vitro* digestion (D2) and fermentation experiments (F0-72). Inlay showing progressive changes in G' (Pa) of NM and H7 hydrogels before (UD), during *in vitro* digestion (D1 and D2), and fermentation (F12-72). Error bars are based on the standard deviation across a minimum of three replicates. Statistical significance symbols (*) refer to significant differences in the release kinetics between NM and H7 at a given time point (VNL – yellow, 5FU – green, DOX – red), where * ($p<0.05$), ** ($p<0.01$) and *** ($p<0.001$).

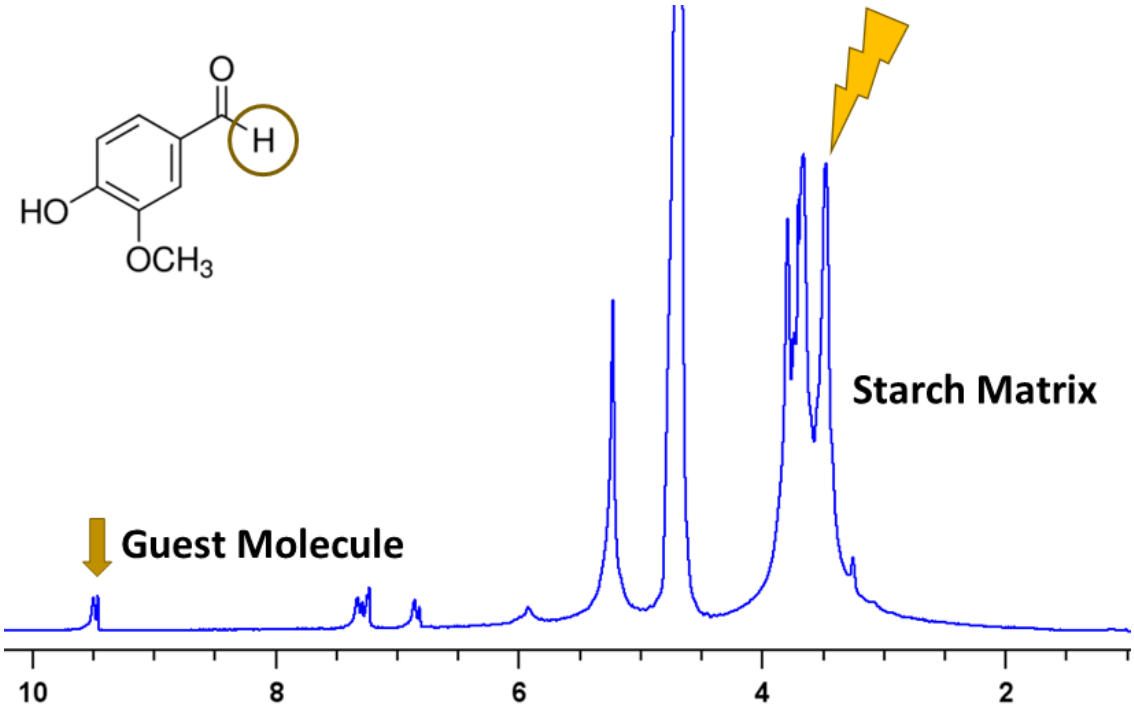

Figure 4.15: Example of the use of ^{1}H STD NMR in investigation of the proximity between guest and host molecules in pharmaceutical excipients. We apply selective saturation to the starch backbone (*ca*. 3.5 ppm) and measure the amount of saturation transferred to the guest molecule (VNL, ^{1}H CHO, *ca*. 9.6 ppm) over a defined time period (mixing time). The rate of STD (%) transfer from the guest to the host by means of intermolecular nuclear Overhauser effect (nOe) is distance dependent (<5Å), hence the rate of STD (%) build-up being proportional to the distance between the guest and the host molecules.

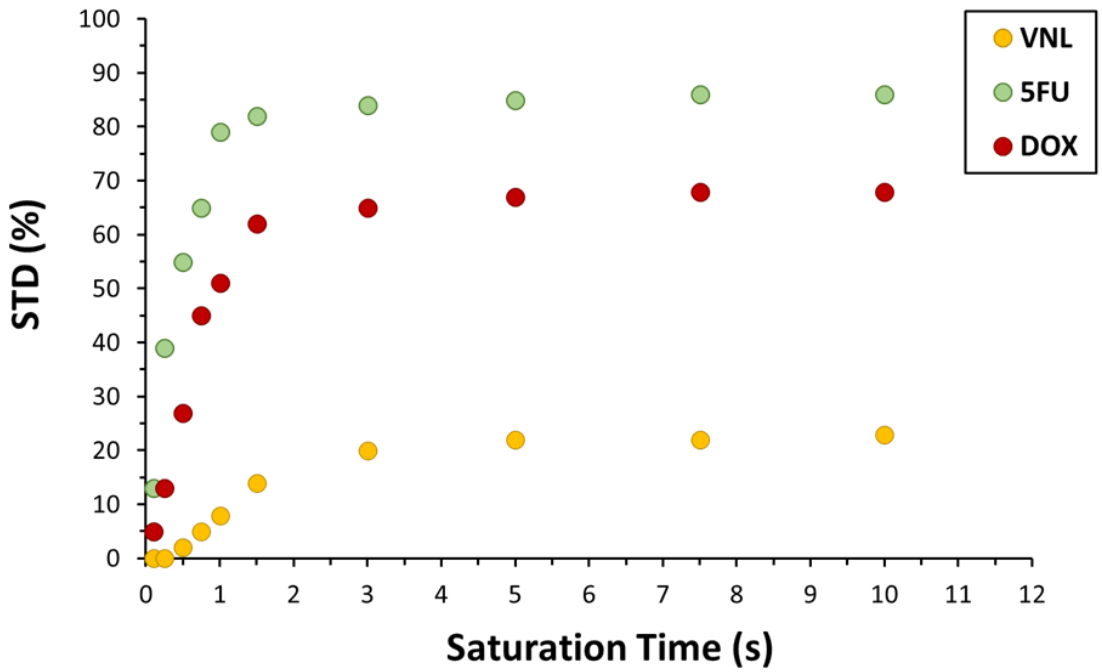

Figure 4.16: STD build-up curves for the three guest molecules VNL, 5FU and DOX binding to the NM starch hydrogel backbone.

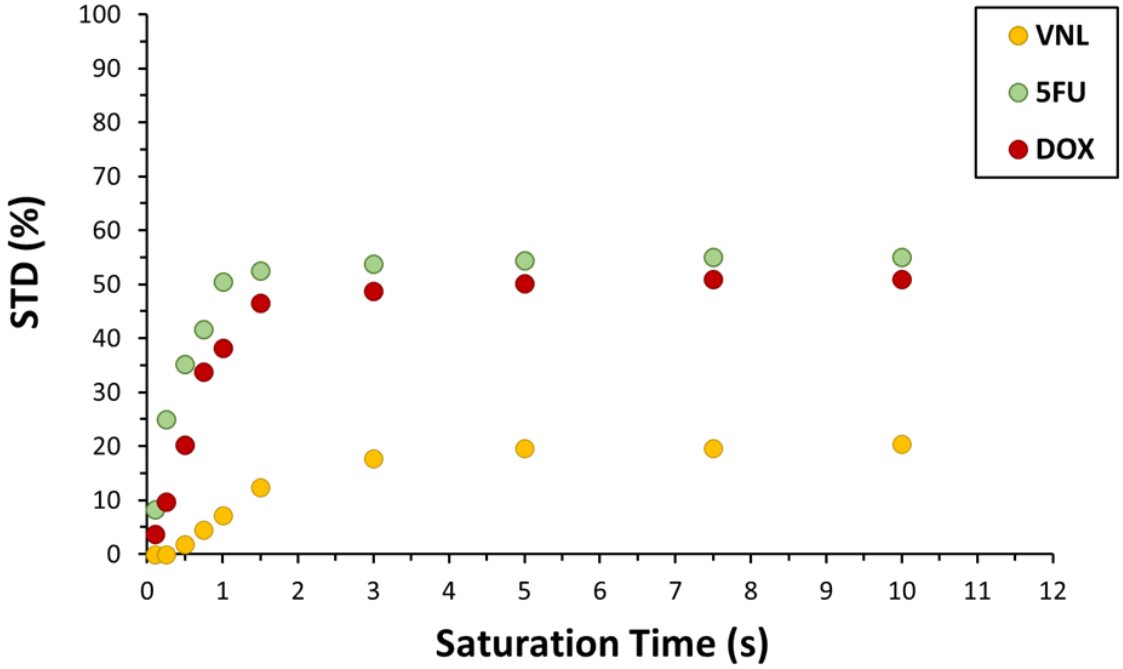

Figure 4.17: STD build-up curves for the three guest molecules VNL, 5FU and DOX binding to the H7 starch hydrogel backbone.

The combined use of the INFOGEST protocol of *in vitro* digestion, and the batch model of *in vitro* fermentation allows for the mimicking of the complete length of the human GIT. This is particularly important in the context of orally administrable pharmaceutical excipients with targeted colonic release. This approach has the advantage of being a more adequate representation of the human gastrointestinal conditions pharmaceutical excipients are exposed to, compared to USP and BSP utilised methods, which can omit the use of hydrolytic enzymes[322], or exclusively focus on one part of the GIT.[322,323]

Our work systematically probes the structure-function links underpinning starch gels' role as pharmaceutical excipients at each individual stage of the human GIT. We link structural parameters defining starch hydrogels' macromolecular organisation, with molecular mobility of internally solvated starch chains, and show how these relate to bulk structural robustness. We have shown how high-amylose starch hydrogels (such as H7) experience a delayed loss of structural integrity under the action of GI hydrolytic enzymes, compared to their low-amylose counterparts (*e.g.*, NM), which directly translates to their delayed drug release kinetics. The delayed loss of structural integrity of H7 results in the small molecular release (VNL, 5FU and DOX) to occur more gradually than its NM counterpart, and exclusively in the large intestine, resisting release in the upper GIT.

Commensal Bacteria's Interaction with Starch Hydrogels

One of the advantages of applying starch hydrogels (*i.e.,* RS III) as pharmaceutical excipients is their health-promoting auxiliary properties, such as their fermentability by commensal bacteria, resulting in the production of physiologically relevant bacterial metabolites (*e.g.,* SCFAs), which have been linked with a range of health benefits.[82,293,324]

Across all participants, NM starch hydrogels led to the production of more SCFAs, compared to H7, where the ratio between acetate, propionate and butyrate was 50:25:25 for NM, and closer to 60:20:20 for the H7 starch gels (Figure 4.18), similar to previous works.[325] Despite the overall comparable concentration of SCFAs produced from the two starch hydrogel types, the more digestible NM substrate led to the production of more than threefold more gas compared to H7 (Figure 4.19). Cumulatively these data show that the more digestible low-amylose NM hydrogel substrate is also more fermentable in the colon. The comparable concentration of SCFAs produced by the two substrates, coupled with the lower production of gas during H7 fermentation has important implications for patients with colorectal pathologies, such as IBD and IBS, who experience increased gas production and retention, leading to debilitating pain and discomfort, compared to healthy individuals. [326,327]

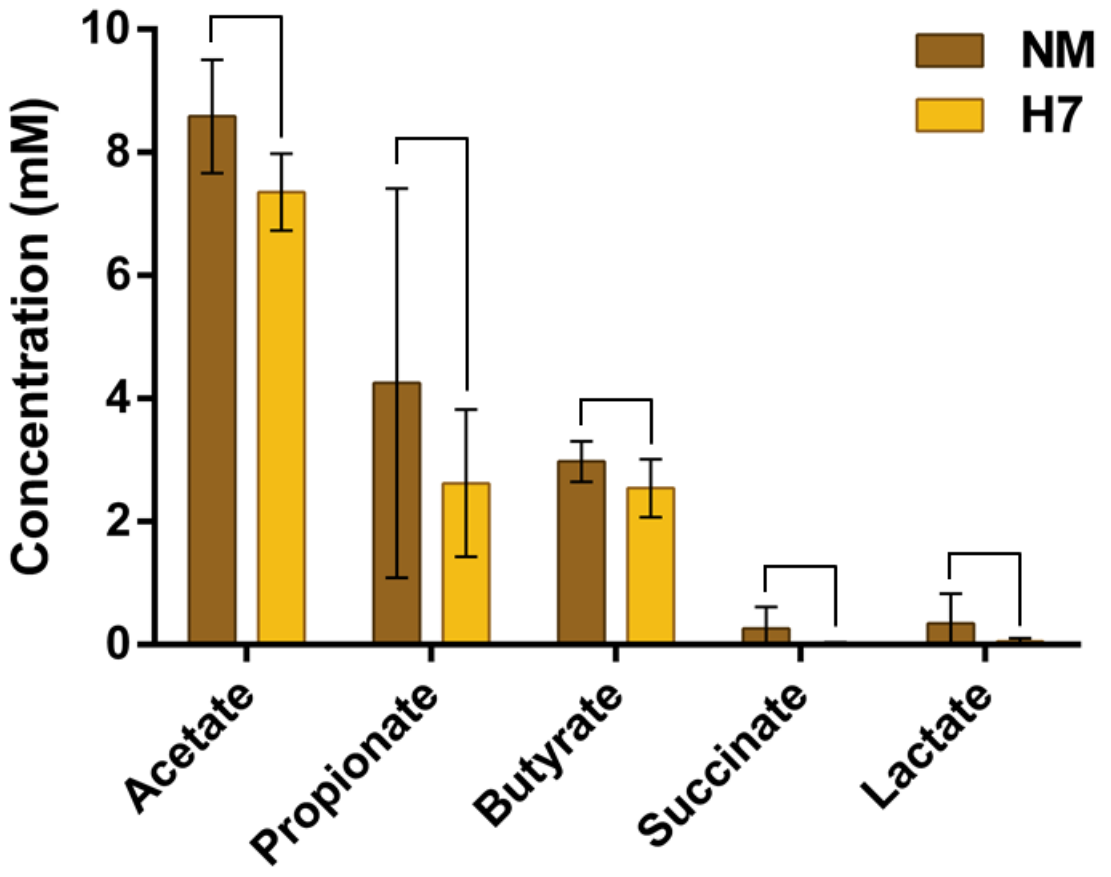

Figure 4.18: Cumulative concentration of SCFAs over 72 h of *in vitro* fermentation of NM and H7 starch hydrogels by bacteria from human faecal donors. All measurements presented are averaged out across 4 different individuals with a minimum of 3 replicates per individual. Error bars are based on the standard deviation between measurements across all samples.

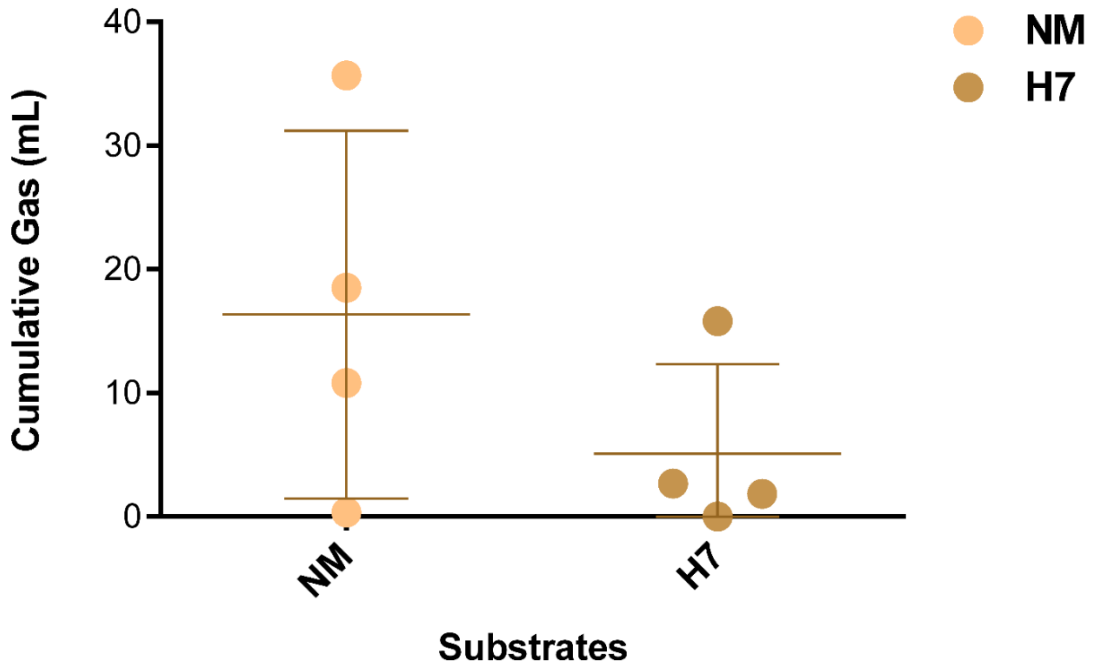

Figure 4.19: Cumulative gas production from NM and H7 maize hydrogels fermented across 72 h, averaged across all four different faecal sample donors, error bars based on a minimum of three replicates per donor. Error bars are based on 95% confidence intervals for each substrate.

There were no significant differences in the concentrations of acetate, butyrate, lactate, and succinate in the presence of VNL, 5FU and DOX, compared to the controls, across all NM and H7 starch hydrogels. The only significant differences observed were the increased production of propionate in the presence of 5FU in both hydrogel excipients (Figures 4.20 and 4.21). These data indicate starch hydrogels are able to provide targeted release of orally administrable drug molecules to the colon, without significantly perturbing commensal bacterial SCFA metabolic pathways.

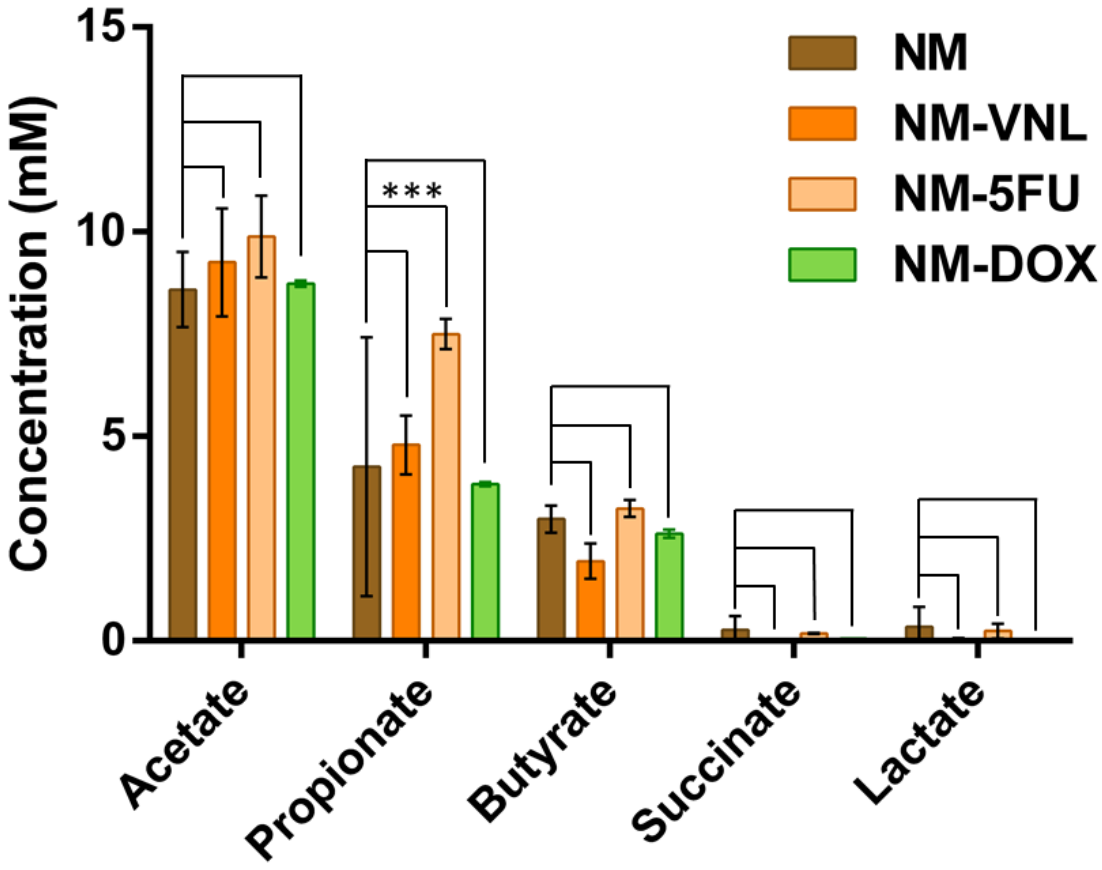

Figure 4.20: Cumulative concentration of SCFAs over 72 h of *in vitro* fermentation of NM, vanillin-, 5-fluorouracil- and doxorubicin-loaded NM (NM-VNL, NM-5FU and NM-DOX, respectively) by bacteria from human faecal donors. All measurements presented are averaged out across 4 different individuals with a minimum of 3 replicates per individual. Error bars are based on the standard deviation between measurements across all samples, where *** $p<0.0005$.

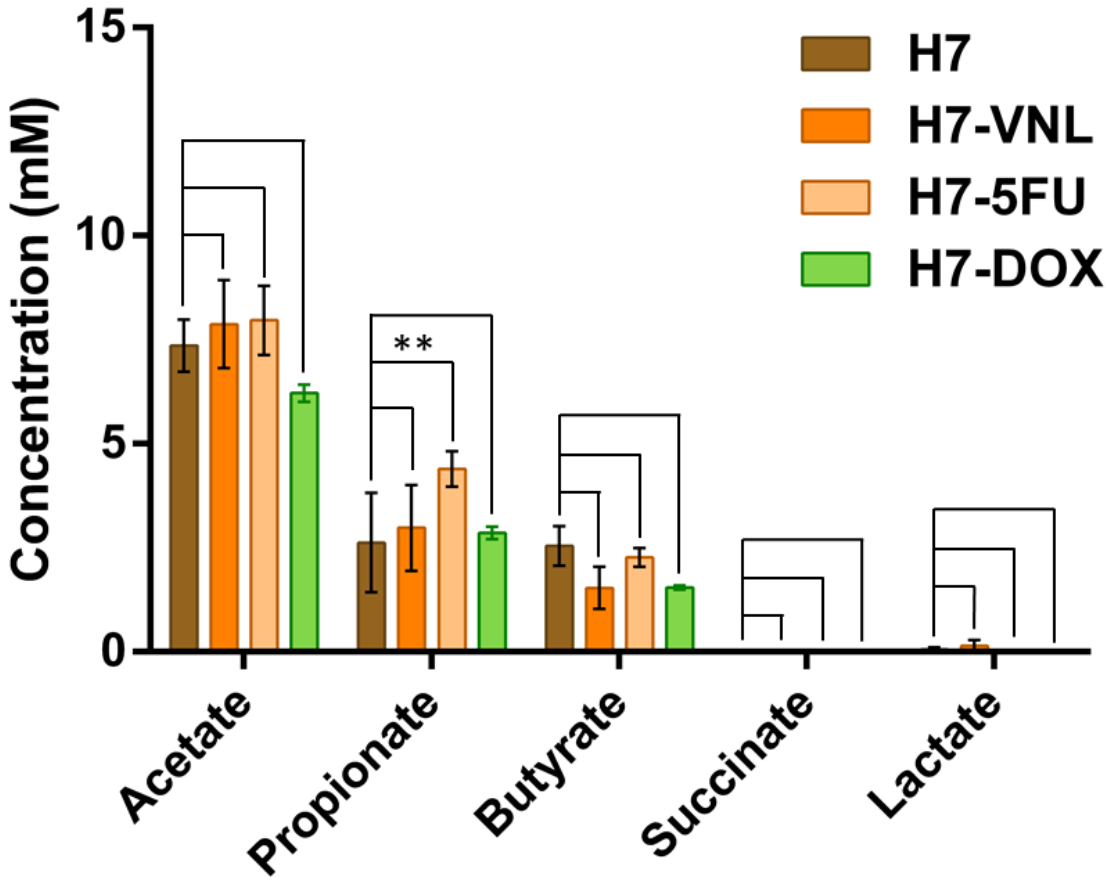

Figure 4.21: Cumulative concentration of SCFAs over 72 h of *in vitro* fermentation of H7, vanillin-, 5-fluorouracil- and doxorubicin-loaded H7 (H7-VNL, H7-5FU and H7-DOX, respectively) by bacteria from human faecal donors. All measurements presented are averaged out across 4 different individuals with a minimum of 3 replicates per individual. Error bars are based on the standard deviation between measurements across all samples, where ** $p<0.005$.

An aspect often neglected in the context of colonic pharmaceutical excipients, is the impact of the commensal microflora on the drug delivery vehicle's stability and the pharmacokinetic profile of the drug molecules.[280]

FISH staining viewed with LSCM revealed differences in how bacteria interact with NM and H7 starch hydrogels – both in the localisation of bacterial colonies, and in the rate

of colonisation of the starch matrix. Unlike *R.bromii* and *Bacteroides*, which do not appear to cluster in larger groups, but rather invade the starch gel matrices in smaller, dispersed colonies, *Bifidobacteria* appear to concentrate along the periphery and surface of the gel matrix (Figures 4.22 and 4.23). This could be a result of the cooperative nature of *Bifidobacterium* communities.[328,329]

The colonisation appears to be time-dependent, irrespective of bacterial species and starch type, where there are fewer commensal bacterial colonies at earlier fermentation times (24 hours), compared to later ones (72 hours, Figures 4.22 and 4.23). In all cases, the colonisation appears to be from the periphery inwards, with *R.bromii* and *Bacteroides* exhibiting a greater rate of colonisation of the matrices, compared to *Bifidobacteria*, and the rate of commensal bacterial invasion into the matrix being greater in NM than in H7 (Figure 4.23). This could be a direct result of the distinctly different morphology of the two gels before and during the different stages of *in vitro* fermentation, where H7 appears as a uniform, cohesive matrix with little-to-no pores or channels throughout its surface, whereas NM hydrogels appear to have numerous channels and "cracks" along their surface. These surface channels are likely to be responsible for the easier accessibility and greater rate of bacterial colonisation of NM starch hydrogels during *in vitro* fermentation. Both hydrogel samples undergo visible changes in their morphology as a function of time during the process of *in vitro* fermentation, which is exhibited as the gradual formation of pores and channels in the hydrogel surface, with the diameter of those increasing towards the later stages of fermentation, where in the case of NM gels, these reach sizes greater than 100 µm (Figure 4.22). These differences in the formation of internal cavities are also likely to play

a role in the loss of bulk structural integrity of the two starch hydrogels (Figures 4.3 and 4.4, and Appendix Figures S9-S12).

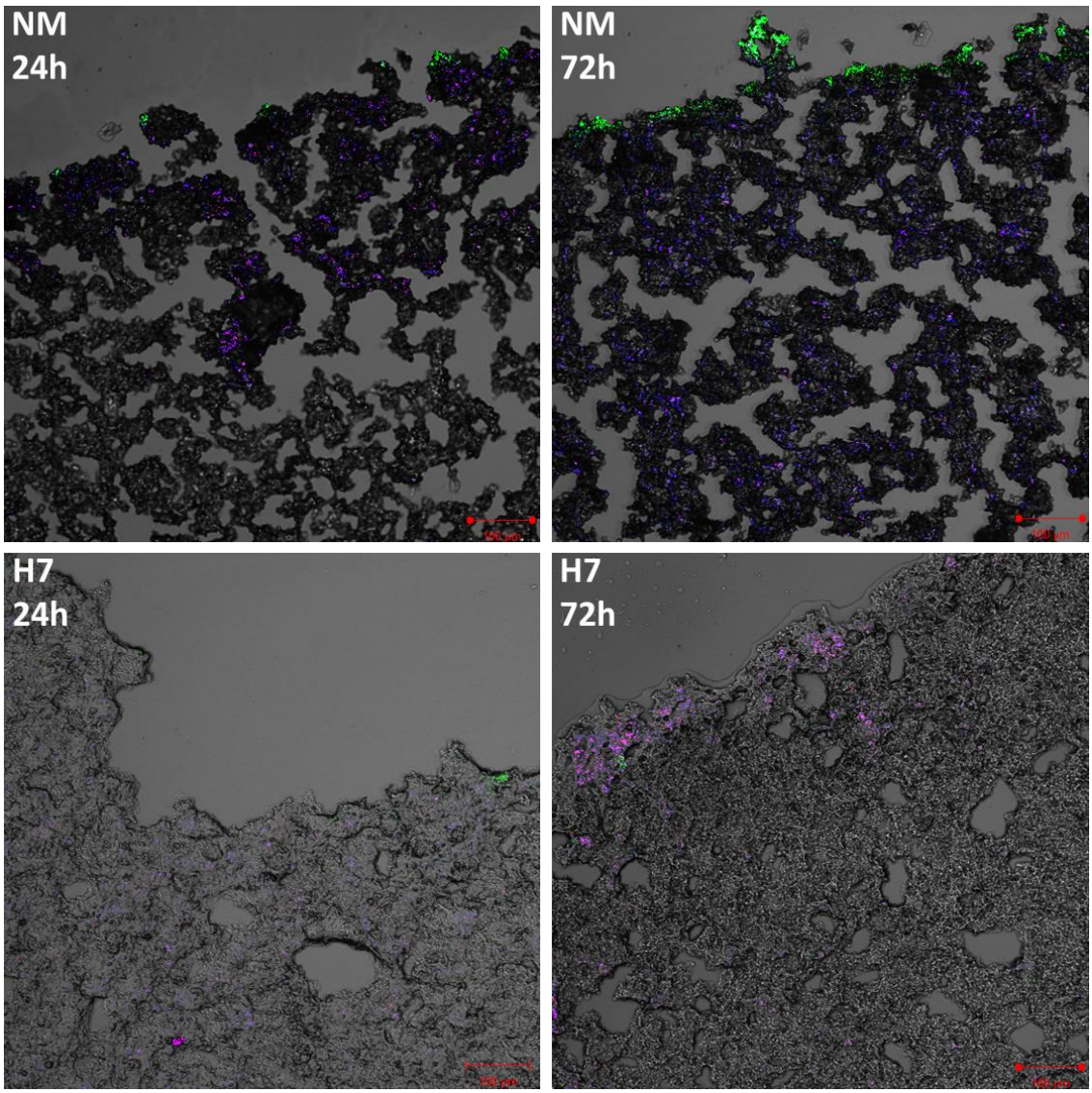

Figure 4.22: Peripheral image of NM and H7 starch hydrogel after 24 hours (NM 24h and H7 24h) and after 72 h (NM 72h and H7 72h) of *in vitro* fermentation, visualised by LSCM at 10x magnification, with the hydrogel morphology and all three bacterial probes: *R.bromii* (blue), *Bacteroides* (red) and *Bifidobacterium* (green).

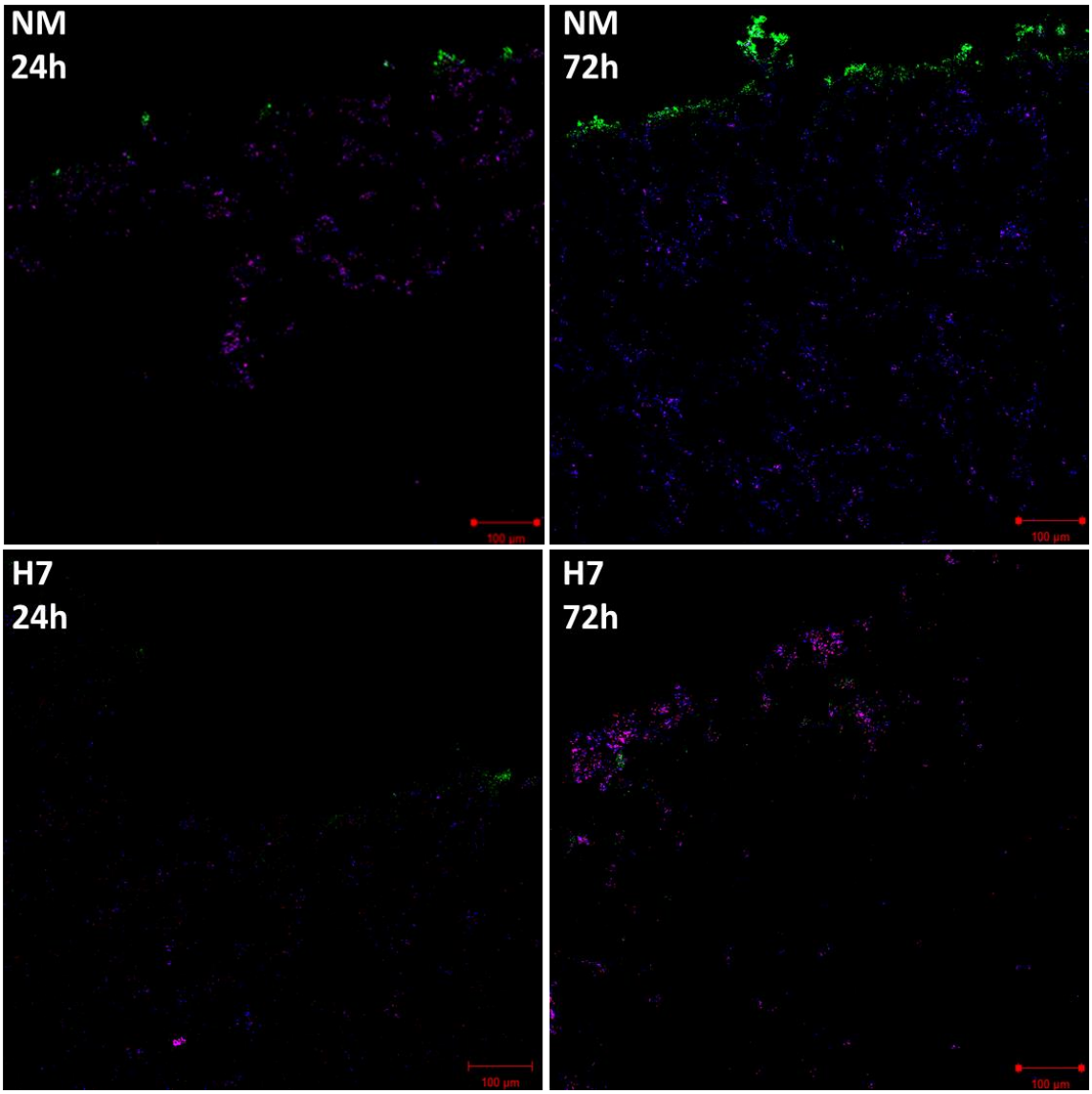

Figure 4.23: Peripheral image of NM and H7 starch hydrogel after 24 hours (NM 24h and H7 24h) and after 72 h (NM 72h and H7 72h) of *in vitro* fermentation, visualised by LSCM at 10x magnification, with all three specific bacterial probes: *R.bromii* (blue), *Bacteroides* (red) and *Bifidobacterium* (green).

On addition of non-specific bacterial probes (Eub338I, Eub338II and Eub338III, Chapter 2, Table 2.1) probes to the combination of *R.bromii*-, *Bacteroides*- and *Bifidobacteria*-specific probes, it was revealed that the combination of the three specific probes accounts for a high proportion (62 – 76%) of the bacteria colonising the starch hydrogel matrices during fermentation (Figure 4.24, and Appendix Figures S13-S16). Once again,

an accumulation of bacterial species was observed around the periphery of the gels, where this proportion was greater in the non-specific bacterial species, compared to the *Bifidobacteria*, likely linked to the colony-forming behaviour of other commensal bacterial species.

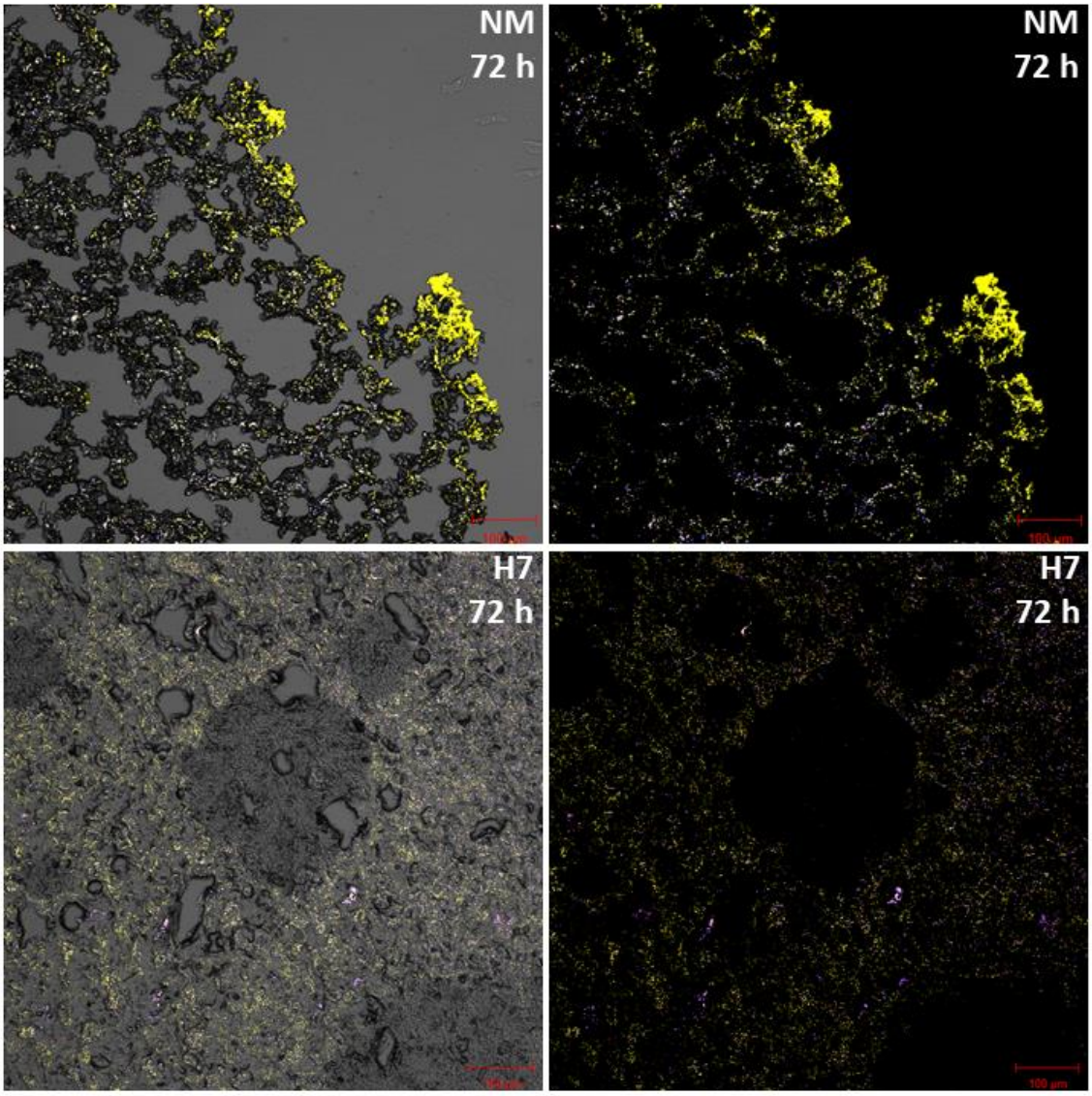

Figure 4.24: Confocal microscopy image of NM and H7 hydrogels after 72 hours of *in vitro* fermentation, visualised at 10x magnification, with the hydrogel morphology and all non-specific bacterial probes (yellow), *R.bromii* (blue), *Bacteroides* (red) and *Bifidobacterium* (green).

4.4 Conclusions

In this study we have probed the bulk- and molecular-level structural changes starch hydrogels undergo as they traverse the entire length of the human GIT, using widely accepted models of *in vitro* digestion and colonic fermentation. We have expanded on the current understanding of RS III hydrolysis across the GIT, by showing how macromolecular structures, such as the ones present in starch hydrogels, can further decrease the susceptibility of RS III to amylolysis.[127,221,308] We have probed the impact of key molecular structural parameters (degree of branching, hydrodynamic radius, degree of polymerisation, and molecular mobility) on the pharmaceutical properties of starch hydrogels as targeted colonic excipients. We have shown how one can modulate their choice of starch to achieve a highly tuned pharmacokinetic profile in the colon. We have probed the interplay between our gel-type systems and commensal bacteria in the gut, and have demonstrated the ability of the colonic microflora to degrade starch hydrogels, leading to the production of health-promoting metabolites, such as SCFAs. We have shown how our soft matter systems compare to currently existing colonic drug delivery platforms.[101,280,330] Our findings provide important information for the application driven design of novel drug delivery platforms for targeted drug release.

It should be noted that end-over-end mixing, as the one employed during the simulated digestion stages, is not a perfect representation of the human peristalsis under *in vivo* settings. That said, our *in vitro* set-up is aimed at providing partial representation of the mechanical stretching and squeezing food stuffs, and orally administered drug delivery platforms are subjected to *in vivo*. This is fundamental matter, which is likely going to

be best addressed by performing *in vivo* experiments involving human volunteers or animal models.

Chapter 5: Solid-state NMR Methodology for Probing Guest-Host Interactions in Small Molecule-Complexed V-Amylose

This chapter focuses on the application of high-resolution solid-state and HR/MAS NMR spectroscopy for the structural characterisation of V-amylose helical complexes, loaded with two small molecules – 1-naphthol and ibuprofen. These data are aimed at providing critical structural understanding of the location of the guest molecules within the V-amylose helices, for the purpose of validation and refining of existing simulation models, based on obtained diffraction (XRD and electron diffraction), and crystallographic data by the group of Professor Jean-Luc Putaux at the Centre de Recherches sur les Macromolécules Végétales (CERMAV) at the Université Grenoble Alpes, France.

5.1 Introduction

Amylose can adopt a left-handed single-helical conformation in the presence of small molecular complexing agents, often referred to as V-amylose.[240] The single-helical arrangement was initially proposed Katz *et al*.[331] working on native starch granules complexed with lipids, and bread dough preparations, and further confirmed using iodine-complexed amylose by means of PXRD and NMR spectroscopy.[67,332] The helical organisation has been argued to be a product of the linear glucan structure, along with the geometry of the α(1-4) glycosidic bonds, with the amylose DP playing an important role in the helicity of the final complex.[333] This leads to the formation of a hydrophobic central cavity capable of accommodating a range of both organic and inorganic small

molecules of hydrophobic and amphiphilic nature, the most commonly reported ones being iodine, short and medium length fatty acids, amino acids, alcohols, carbonyls and esters.[40,334–336]

V-amylose complexes containing small molecular ligands can adopt different conformations, forming crystalline fibres or lamellar crystals, where these can be grouped into 10 allomorphic families according to the helicity of the glucan chain, and XRD and electron diffraction (ED) patterns (Table 5.1).

Table 5.1: V-amylose allomorphs with small organic molecules documented in published works.

Allomorph	**Example Complexing Agents**	**Reference**
$V6_I$	Fatty acids	40,337
$V6_{II}$	*n*-butanol	334,337
$V6_{III}$	Glycerol	337–339
$V6_{IV}$	Hydroxybenzoic acid	337,339
$V7_I$	Borneol	337,339
$V7_{II}$	Butyric acid, Ibuprofen	40,337,340
$V7_{III}$	1-Naphthol	337,341
$V7_{IV}$	Quinoline	337,339
$V8_I$	Salicylic acid	337,338
$V8_{IV}$	Salicylic acid	337

The difference in polymorphism has been attributed largely to the physicochemical properties of the complexing agent and the sample preparation conditions.[337] That said,

the V-amylose allomorph cannot be predicted directly from the physicochemical properties of the guest molecule, as different allomorphs can be obtained with the same complexing agent, and the same polymorph can be obtained using physicochemically distinct guest molecules (*e.g.*, $V7_{II}$ can be obtained using isopropanol, acetone, and thymol). In those cases, it is the recrystallisation conditions that have largely a polymorph-directing effect.[337] Some studies have suggested that the physical dimensions of the guest molecule can be correlated with the helicity of the V-amylose chain.[342] However, no clear relationship can be identified for the successful prediction of whether a molecule would be able to act as a complexing agent for the formation of V-amylose-small molecule complexes.

V-amylose complexation has been used for the encapsulation of a range of small molecules with the purpose of achieving sustained or slow release kinetics following administration of the complex. This has been applied in the area of flavour compounds, nutraceuticals, APIs (*e.g.*, salicylic acid, ibuprofen, praziquantel, rifampicin) and bioactive compounds (*e.g.*, esters of vitamins, genistein).[240,343–351] Amylose has advantages over other drug delivery platforms, as it is affordable, easily renewable, and biocompatible, and also the formation of V-amylose helices has been shown to increase the thermal and oxidative stability of the complexing ligand.[352,353] The latter is a highly advantageous drug delivery platform property, as it opens up pathways for the targeted delivery of oxygen-sensitive, thermally unstable, and highly reactive and volatile molecules. Furthermore, due to the relatively highly crystalline arrangement of V-amylose helices, they have been shown to be resistant to *in vitro* gastric conditions (proteolytic enzymes and low pH), as well as amylolytic conditions (pancreatic α-amylase, β-amylase and amyloglucosidase), allowing for their use as targeted delivery

vehicles capable for release in the distal parts of the human GIT (small and large intestine).[346,350,351,353]

In order to fully utilise V-amylose as a superior drug delivery vehicle, it is important to understand the structural interplay between the guest and the host in these inclusion complexes, as guest-host interactions can impact the drug delivery properties of pharmaceutical excipients.[321] There have been some studies probing the difference in molecular mobility and dynamics of the guest and host molecules in V-amylose complexes[337,340], but not much is known about the interactions between the two, and how these affect the properties of the overall system. In this work, we probe the through-space guest-host interactions in a V-amylose-1-naphthol ($V7_{III}$) and V-amylose-ibuprofen ($V7_{II}$) complexes – two V-amylose complexes with small molecules located exclusively in the hydrophobic cavity of the glucan helix. [337] We probe the structure and interactions in these complexes using high-field solid-state NMR, making use of both homo- and heteronuclear through-space interaction experiments, with the aim of mapping out the spatial proximity between the helical host and its organic ligands.

5.2 Materials and Methods

5.2.1 *Materials*

V-amylose complexed with 1-naphthol (Figures 5.1) and ibuprofen (Figure 5.2) in a $V7_{III}$ and $V7_{II}$ conformation, respectively, were prepared by solubilising amylose (0.5% w/v) in DMSO at 90 °C for 1 hour, following by the addition of 1-naphthol or ibuprofen at saturation, and diluting the mixture with *dd*H_2O to a final DMSO concentration of 30% v/v. The mixture was then incubated at 60 °C for up to 2 weeks, the precipitates were recovered, centrifuged, and washed with *dd*H_2O, heated back up to 90 °C, and then

cooled down to recrystallisation temperature to allow for the crystals to form. [337] These procedures were carried out by the group of Professor Jean-Luc Putaux at the Centre de Recherches sur les Macromolécules Végétales (CERMAV) at the Université Grenoble Alpes, France.

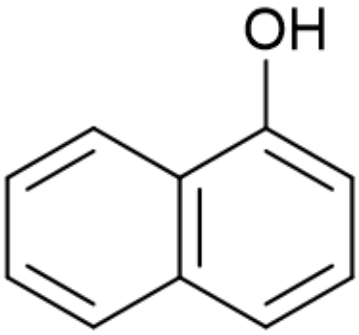

Figure 5.1: Structural formula of 1-naphthol.

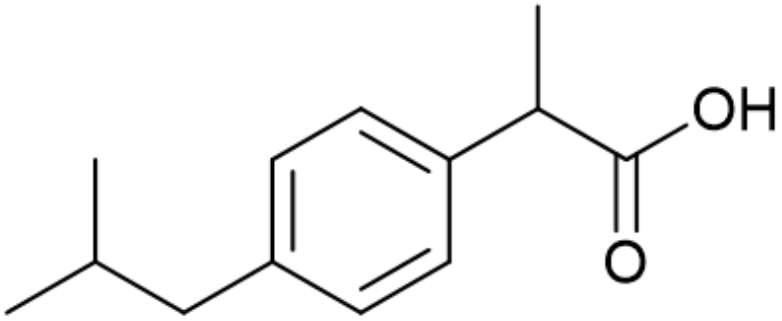

Figure 5.2: Structural formula of ibuprofen.

5.2.2 *Methods*

H_2O/D_2O Exchange

Approximately 300 mg of each of the V-amylose complexes were placed at the bottom of a 1.5 mL centrifuge tube, followed by the addition of D_2O (1.0 mL). The samples were placed on an end-over-end rotator overnight. The following day the free D_2O was pipetted out and discarded without disturbing the pellet. The remaining free solvent

was removed by capillary action using a non-fibrous Kimtech™ tissue (Kimberly-Clark Worldwide, Inc.)

The degree of success of solvent exchange was determined using ^{1}H NMR, comparing the H_2O peak (*ca*. 4.7 ppm) at full width at half height (FWHH) before and after the exchange. The quality of the sample following H_2O/D_2O exchange were verified using ^{1}H-^{13}C CP/MAS NMR spectroscopy, comparing each peak's position, intensity and FWHH before and after solvent exchange.

Proton-Driven Spin Diffusion (PDSD) NMR

Principle

PDSD is a homonuclear correlation experiment, which allows for the cross-polarisation-driven transfer of magnetisation from high-γ nuclei, such as ^{1}H, to low-γ ones, such as ^{13}C, which is then transferred to nearby ^{13}C nuclei predominantly through residual dipolar coupling and chemical exchange.[354] The magnetisation transfer by ^{1}H-^{1}H spin diffusion would be slower at higher spinning speeds. The transfer of magnetisation occurs during a mixing period (t_{mix}), and is distance dependent, so by varying t_{mix}, one can probe the distances between ^{13}C nuclei in a system (Figure 5.3). At very short t_{mix}, cross peaks would result from nearby nuclei, whereas at longer t_{mix}, the distance could extend to ^{13}C centres in different residues (*e.g*., in proteins) or molecules (*e.g*., host-to-guest transfer).

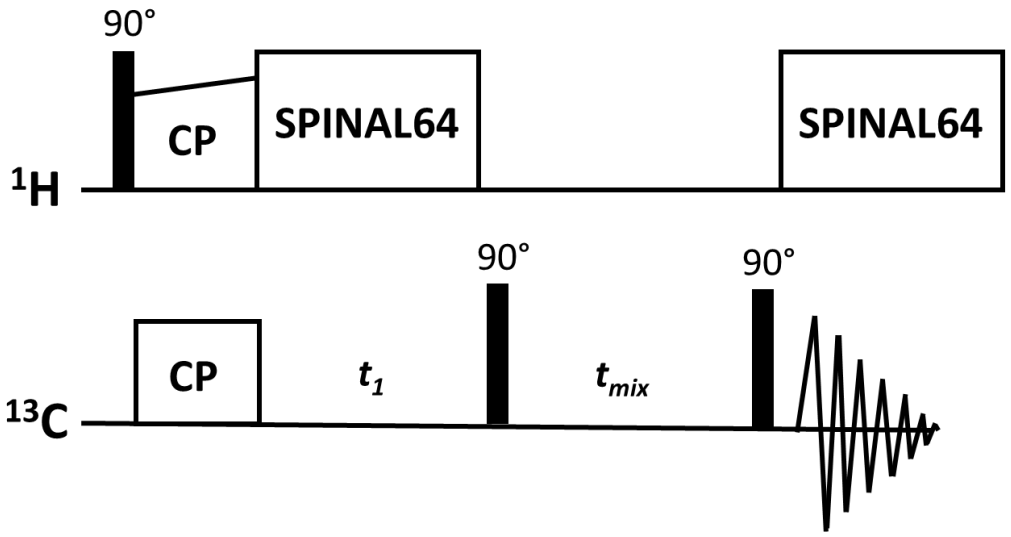

Figure 5.3: Graphical representation of the PDSD pulse train.[355] Pulse phases have been omitted for visual clarity.

Experimental Procedures

PDSD experiments were performed on a Bruker Avance III 400 MHz spectrometer, equipped with a HXY 4-mm probe. The acquisition parameters were π/2 *rf* ^{1}H of 3.2 µs, and ^{13}C of 3.5 µs, contact time of 1.0 ms, t_{mix} 0.05-2 s, recycle delay of 4.5 s, MAS rate of 6 kHz, at 20 °C, using a minimum of 128 scans.

^{1}H-^{13}C Heteronuclear Correlation (HETCOR) NMR

Principle

HETCOR is a heteronuclear correlation experiment in which cross peaks arise from spatially proximal (*i.e.*, through-space experiment) ^{1}H and ^{13}C nuclei, where the transfer of magnetisation occurs through spin diffusion. This is a ^{13}C-detected experiment with simultaneous homonuclear (^{1}H-^{1}H) decoupling during acquisition.

Experimental Procedures

HETCOR experiments were performed on a Bruker AVANCE III 850 MHz solid-state NMR spectrometer (UK National 850 Solid-State NMR facility at the University of Warwick) equipped with a 4 mm HX H13892B probe, using ^{1}H π/2 pulse of 3 μs, contact time of 4 ms, relaxation delay of 3 s, at MAS rate 4.2 kHz, without external temperature control, and with a minimum of 256 scans.

^{1}H-^{1}H NOESY NMR

Principle

NOESY in solids is a homonuclear (^{1}H-^{1}H) exchange experiment, where magnetisation is transferred between like nuclei (^{1}H) through space via residual dipolar coupling and chemical exchange. The transfer of magnetisation is distance-dependent, so by varying t_{mix} one can obtain information on the comparative distance between nuclei.

Experimental Procedures

NOESY NMR experiments were performed on a Bruker AVANCE III 850 MHz solid-state NMR spectrometer (UK National 850 Solid-State NMR facility at the University of Warwick) equipped with a 1.3 mm HXY H13863 probe, using a π/2 rf ^{1}H pulse of 2.5 μs, t_{mix} of 0.005-0.05 s, relaxation delay of 3 s, at MAS rate of 57 kHz, without external temperature control, with a minimum of 64 scans.

Single Quantum-Double Quantum Back-to-Back (SQ-DQ BABA) NMR

Principle

SQ-DQ BABA experiments are predominantly used to probe internuclear distances through spin-pair connectivities under MAS conditions in semi-crystalline and amorphous samples.[188,356] A detailed explanation of the BABA pulse sequence can be found elsewhere[188,356], with details of the zero-order Hamiltonian, and evolution of the DQ Hamiltonian, as well as the toggling frame Hamiltonian. For the purposes of this work, however, the pulse sequence relies on symmetrically placed π/2 ^{1}H pulses in each rotor period (rotor-synchronised pulse train), with the addition of a π ^{1}H pulse in every second rotor period, resulting in refocusing of the CSA and isotropic chemical shift offsets. A π/2 ^{1}H *rf* pulse is applied, followed by an incrementable evolution period under isotropic (^{1}H) chemical shifts. The magnetisation is exchanged between like nuclei (^{1}H-^{1}H) *via* dipolar coupling through radio frequency driven recoupling (RFDR). This is followed by converting SQ to DQ coherence using a BABA pulse sequence, followed by an evolution period of the ^{1}H DQ coherence. The DQ coherences are converted back to SQ coherence by an analogous BABA pulse sequence, followed by a π/2 *rf* ^{1}H pulse and acquisition of the *xy* (*i.e.*, transverse) magnetisation (Figure 5.4).[357] BABA is usually performed at higher spinning speeds in the context of soft matter systems (>5 kHz, *e.g.*, 57 kHz MAS rate used in this chapter), allowing for improved averaging of the strong ^{1}H-^{1}H dipolar coupling, conferring better chemical shift resolution in rigid, solid samples, which would otherwise suffer from broad, non-informative ^{1}H chemical shift distributions.[358]

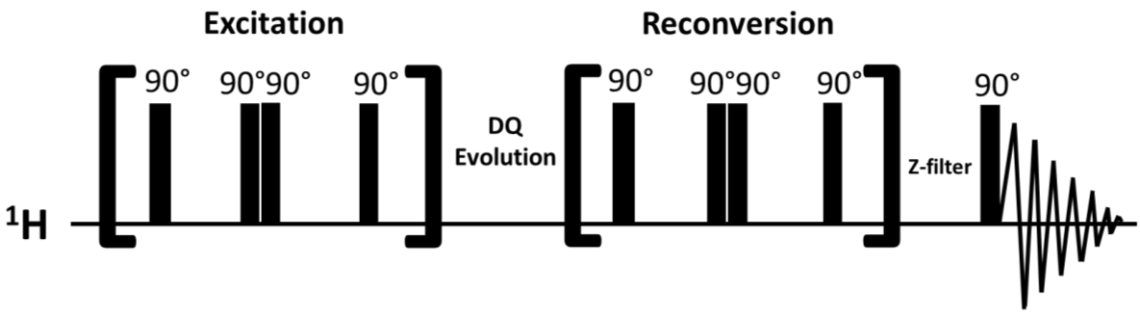

Figure 5.4: Graphical representation of the SQ-DQ BABA pulse train.[357] Pulse phases have been omitted for visual clarity.

Experimental Procedures

SQ-DQ BABA experiments were carried out on a Bruker AVANCE III 850 MHz solid-state NMR spectrometer (UK National 850 Solid-State NMR facility at the University of Warwick) equipped with a 1.3 mm HXY H13863 probe, using a π/2 rf ^{1}H pulse of 2.5 µs, total excitation and reconversion periods of 17.54 µs, DQ evolution period of 1 µs, z-filter of 1 µs, relaxation delay of 3 s, at MAS rate of 57 kHz, without external temperature control, with a minimum of 64 scans.

5.3 Results and Discussion

5.3.1 *V-amylose-1-naphthol ($V7_{III}$)*

In order to decrease the ^{1}H peak contribution of H_2O in the complexes and allow for less ambiguous assignment 2D ^{1}H-^{1}H correlation spectra, part of the solvent was exchanged with D_2O (Figure 5.5). This allowed for better peak separation between the residual H_2O peak and the amylose ^{1}H environment (H-2-6). There were only minor changes in the ^{13}C peaks' intensities and FWHH after solvent exchange, confirming minimal structural changes as a result of the solvent exchange process. This could otherwise be confirmed

by examining the PXRD patterns of the V-amylose complexes before and after H_2O/D_2O exchange. [337]

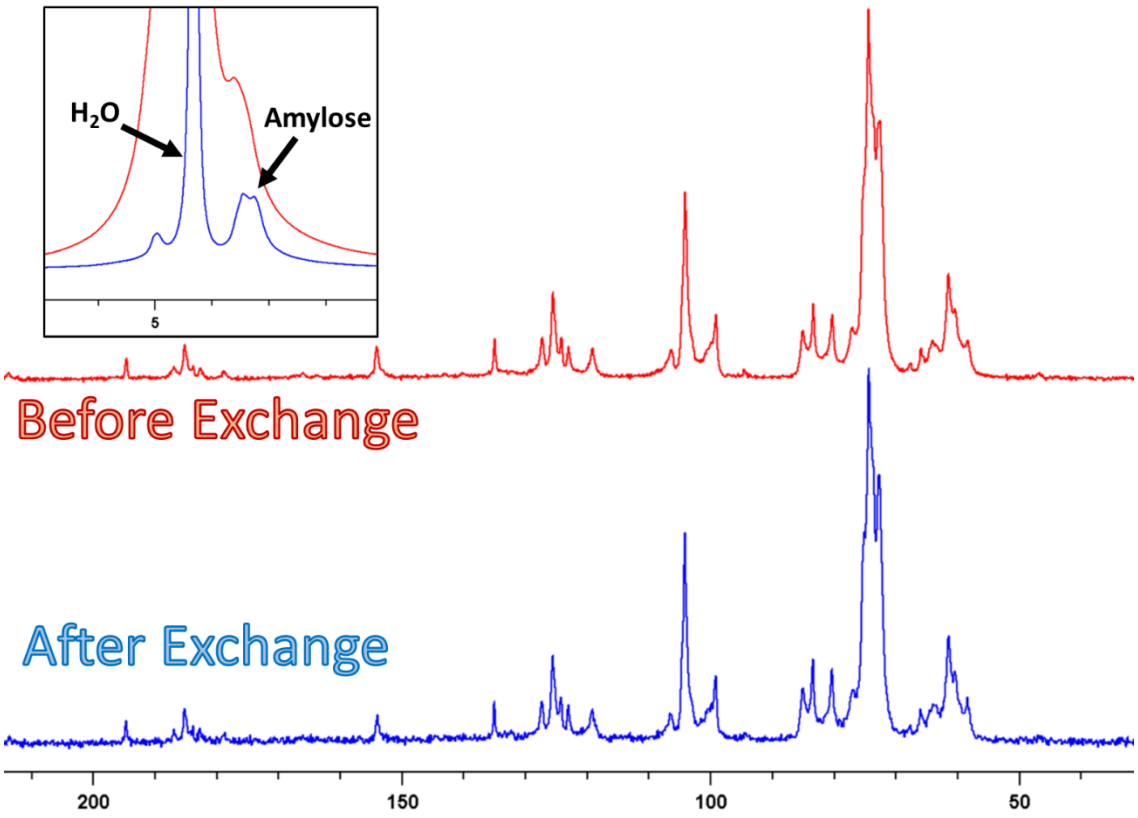

Figure 5.5: ^{1}H-^{13}C CP/MAS NMR spectra of V-amylose-1-naphthol ($V7_{III}$) complex before and after H_2O/D_2O exchange (red and blue, respectively). Inlay showing ^{1}H NMR spectrum of the complex before and after solvent exchange.

The ^{1}H-^{13}C CP/MAS NMR spectrum of the V-amylose-1-naphthol ($V7_{III}$) complex (Figure 5.6) allowed for full peak assignment of the amylose helix (*i.e.*, the host molecule) and 1-naphthol.[337,359]

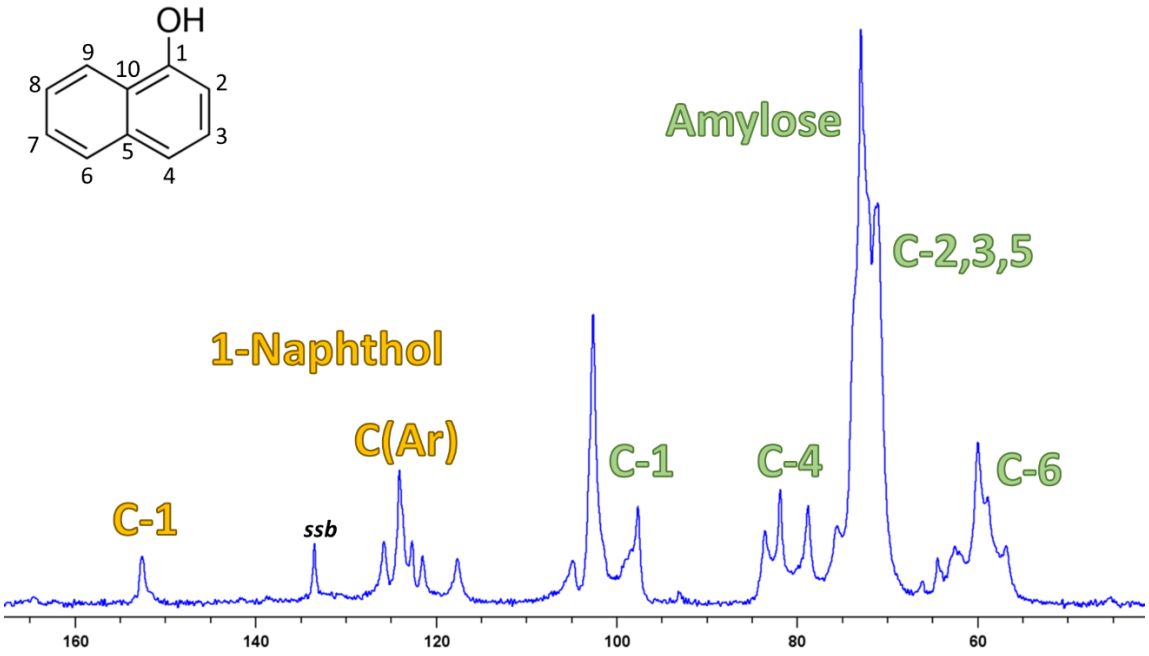

Figure 5.6: ^{1}H-^{13}C CP/MAS NMR solid-state NMR spectrum of V-amylose-1-naphthol ($V7_{III}$) complex, featuring ^{13}C peak assignment. Spinning sideband (*ssb*, *ca.* 134 ppm) denoted.

Comparison of the ^{13}C NMR spectra of pure amylose (from the same batch used for the preparation of the complexes) and one complexed with 1-naphthol in a V7III conformation, revealed differences in the molecular environment around all amylose monomer (D-glucose) nuclei (Figure 5.7). The uncomplexed amylose spectrum exhibited a much more pronounced amorphous contribution, compared to the 1-naphthol-containing complex, as evidenced by the greater peak width in the former.

All ^{13}C nuclear environments (C-1, C-4, C-2,3,5 and C-6) showed multiple peak splittings, likely indicating the presence of multiple different nuclear environments across all ^{13}C centres. This is likely to be the result of different degree of interaction between the guest and the host molecule, arising from differences in the supramolecular organisation of the V-amylose complex. These result in changes in the immediate chemical environment

around each ^{13}C nucleus, changing its degree of shielding and subsequently its effective chemical shift.

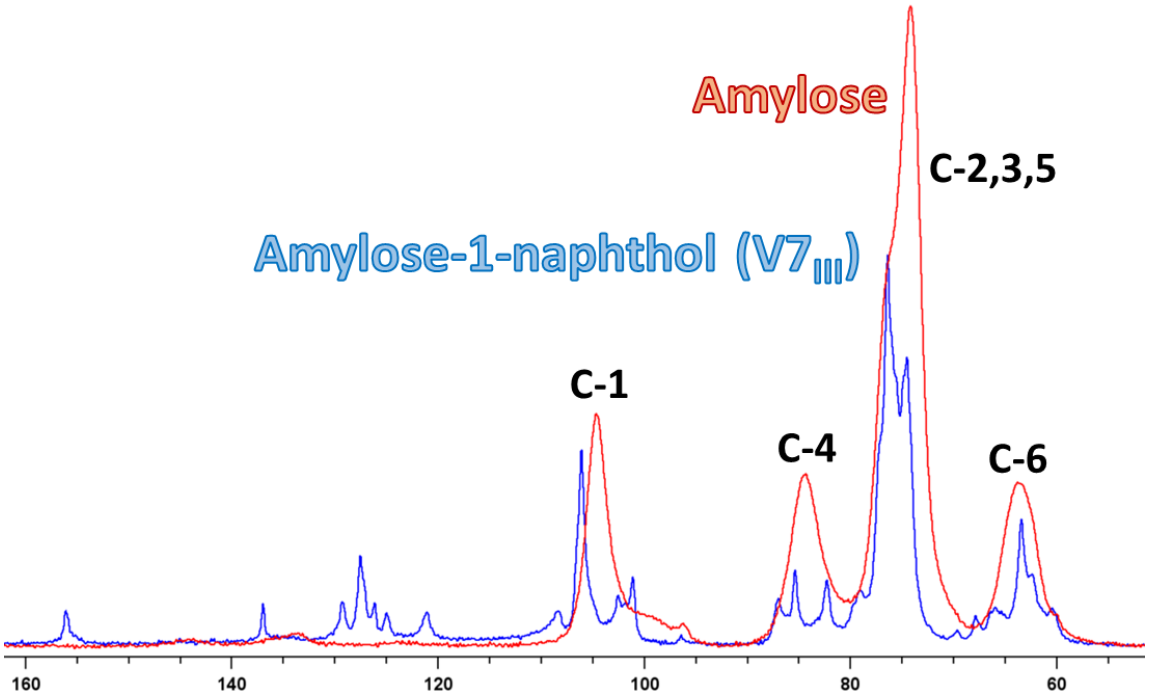

Figure 5.7: ^{1}H-^{13}C CP/MAS NMR spectra of pure amylose (red) and amylose-1-naphthol ($V7_{III}$) complex (blue), with amylose monomer ^{13}C peak assignment.

The ^{13}C-^{13}C PDSD spectra showed close proximity between the aromatic ^{13}C centres in 1-naphthol (C(Ar)) and C-2,3,5 and C-6 of the amylose helix (Figure 5.8).

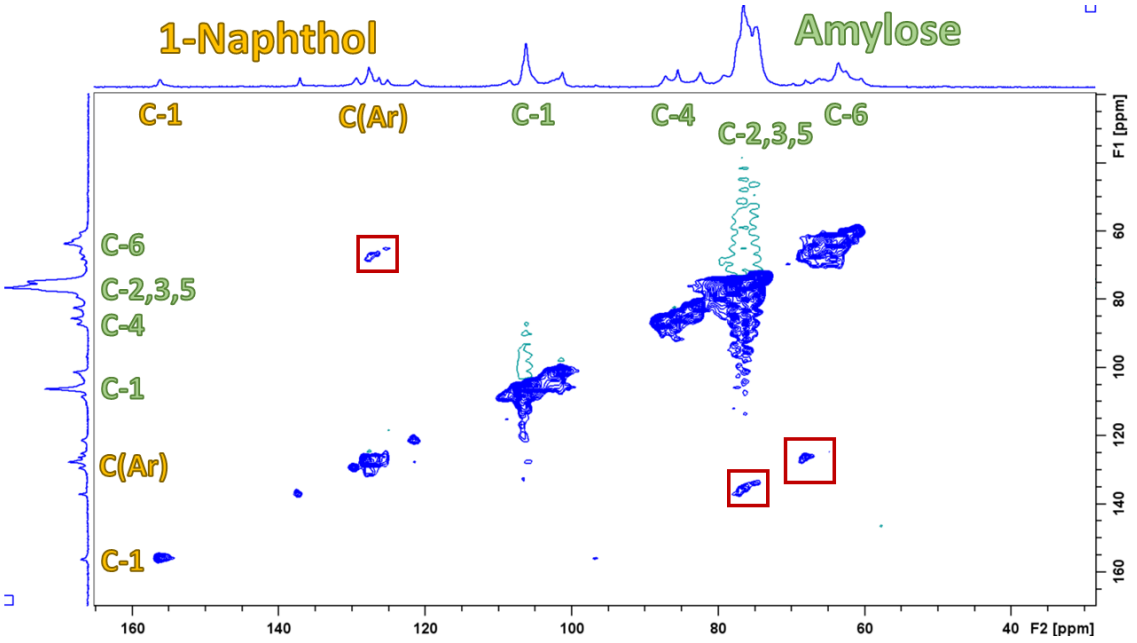

Figure 5.8: ^{13}C-^{13}C PDSD NMR spectrum of V-amylose-1-naphthol ($V7_{III}$) complex at t_{mix} = 0.2 s, featuring peak assignment of both the guest (yellow) and the host molecule (green), with cross peaks between the two shown in red.

The proximity between these environments was further confirmed by the ^{1}H-^{1}H NOESY spectra at variable mixing times (Figure 5.9), which showed the contact time between naphthol and amylose ^{1}H nuclei followed the order of: H(Ar) naphthol – H-2-6 amylose > H-1 naphthol – H-2-6 amylose ≈ H(Ar) naphthol – H-1 amylose (Figure 5.9). It is important to note that in dynamic complexes (and states), NOESY reports on the resident time of one molecule with respect to another in a complex, averaged out across all populations and states the complex undergoes on the experimental timescale.

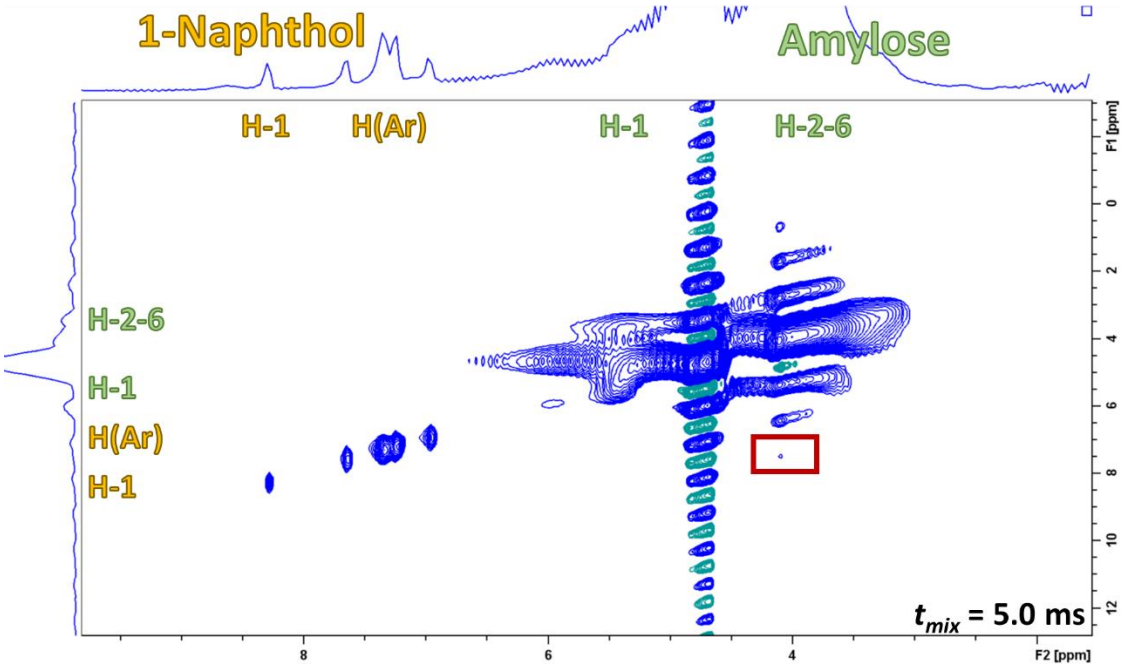
1-Naphthol
Amylose
H-1
H(Ar)
H-1
H-2-6
H-2-6
H-1
H(Ar)
H-1
t_{mix} = 5.0 ms
F1 [ppm]
F2 [ppm]

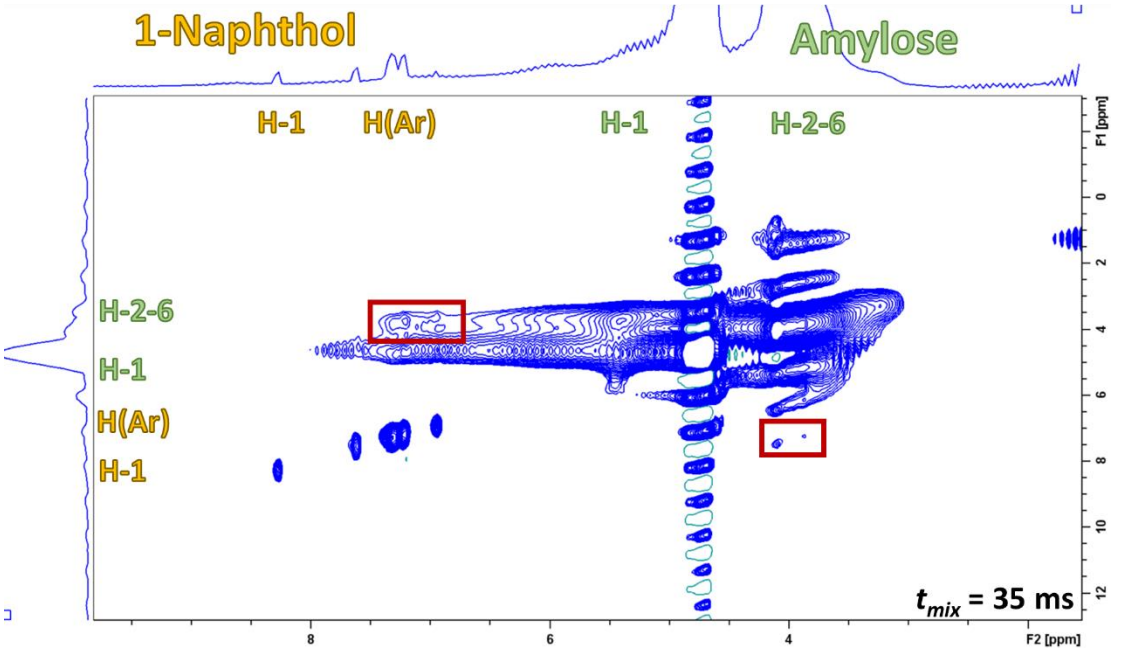
1-Naphthol
Amylose
H-1
H(Ar)
H-1
H-2-6
H-2-6
H-1
H(Ar)
H-1
t_{mix} = 35 ms
F1 [ppm]
F2 [ppm]

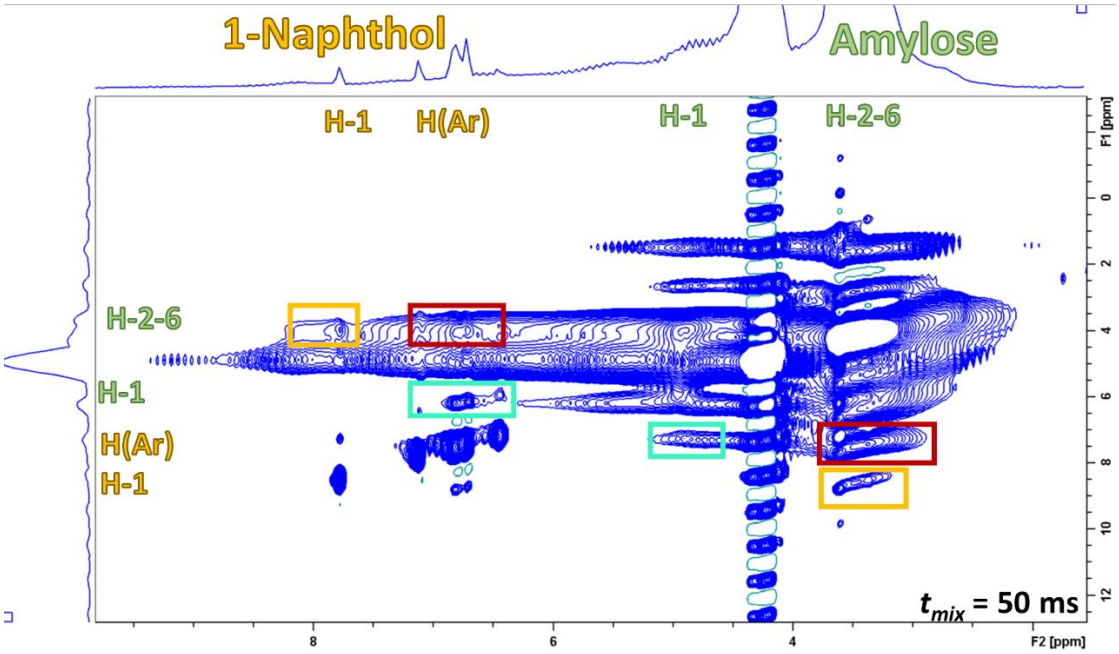

Figure 5.9: ^{1}H-^{1}H NOESY spectra of V-amylose-1-naphthol (V7III) complex at short (5 ms, top), intermediate (35 ms, middle), and long (50 ms, bottom) mixing times, featuring ^{1}H assignment of both 1-naphthol (yellow) and amylose (green). Cross peaks are shown in red, yellow, and cyan. Mirrored cross peaks shown in the same colour.

The above internuclear proximity was further supported by cross peaks in the ^{1}H-^{1}H SQ-DQ BABA NMR spectral data (Figure 5.10), but due to the experiment being carried out at only one mixing time, it precluded obtaining quantitative information of the SQ-DQ spectrum.

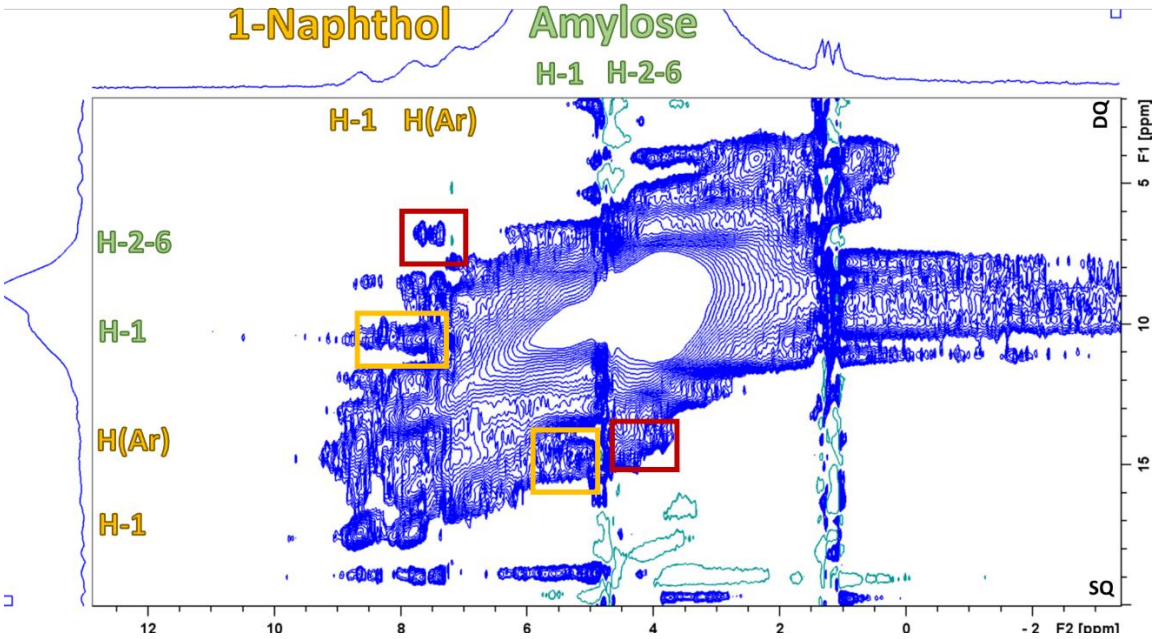

Figure 5.10: ^{1}H-^{1}H homonuclear SQ-DQ BABA NMR spectrum of V-amylose-1-naphthol ($V7_{III}$) complex, at t_{mix} = 20 ms, featuring assignment of the ^{1}H environments across both amylose and 1-naphthol. Cross peaks shown in red and yellow.

5.3.2 *V-amylose-ibuprofen ($V7_{II}$)*

There were practically no changes in the ^{13}C peaks' intensities and FWHH after solvent exchange, confirming minimal structural changes as a result of the solvent exchange process in the V-amylose-ibuprofen ($V7_{II}$) complex (Figure 5.11). Changes in the structuring of the complexed system could have alternatively been probed by means of PXRD. [337]

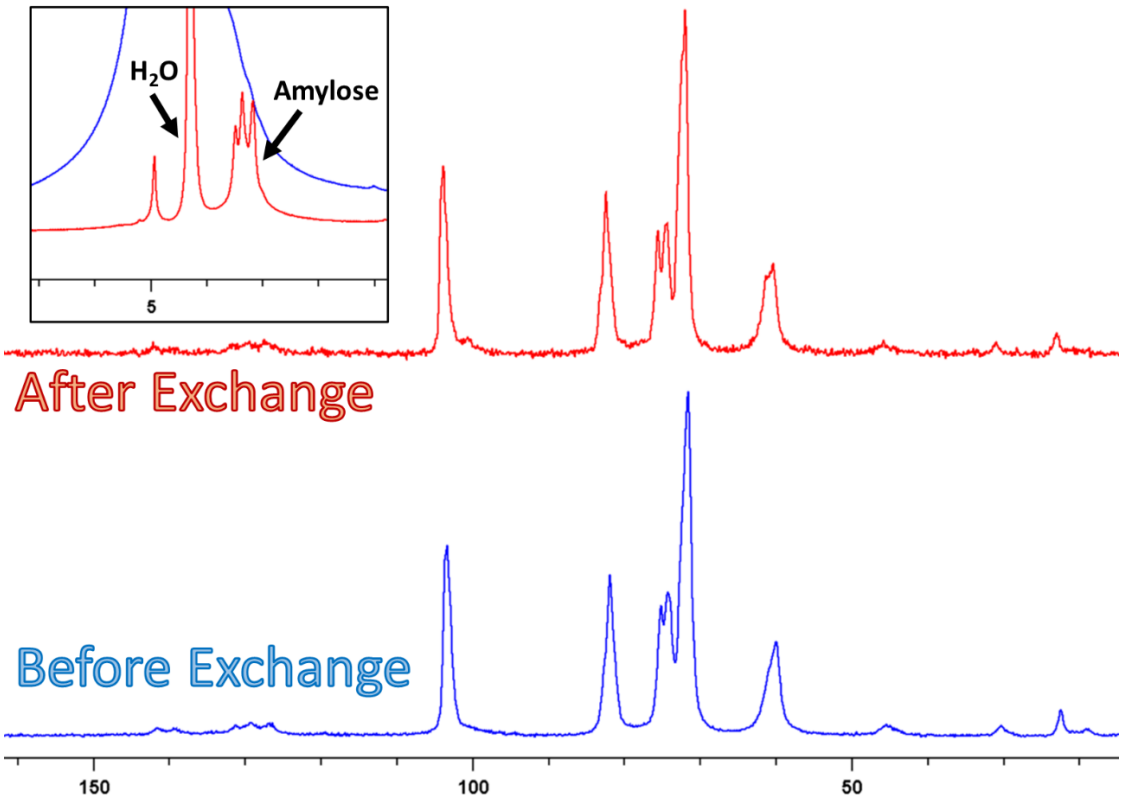

Figure 5.11: ^{1}H-^{13}C CP/MAS NMR spectra of V-amylose-ibuprofen ($V7_{II}$) complex before and after H_2O/D_2O exchange (blue and red, respectively). Inlay showing ^{1}H NMR spectrum of the complex before and after solvent exchange.

The ^{1}H-^{13}C CP/MAS NMR spectrum of the V-amylose-naphthol ($V7_{II}$) complex (Figure 5.12) allowed for full peak assignment of the amylose helix (*i.e.*, the host molecule) and ibuprofen.[337,340]

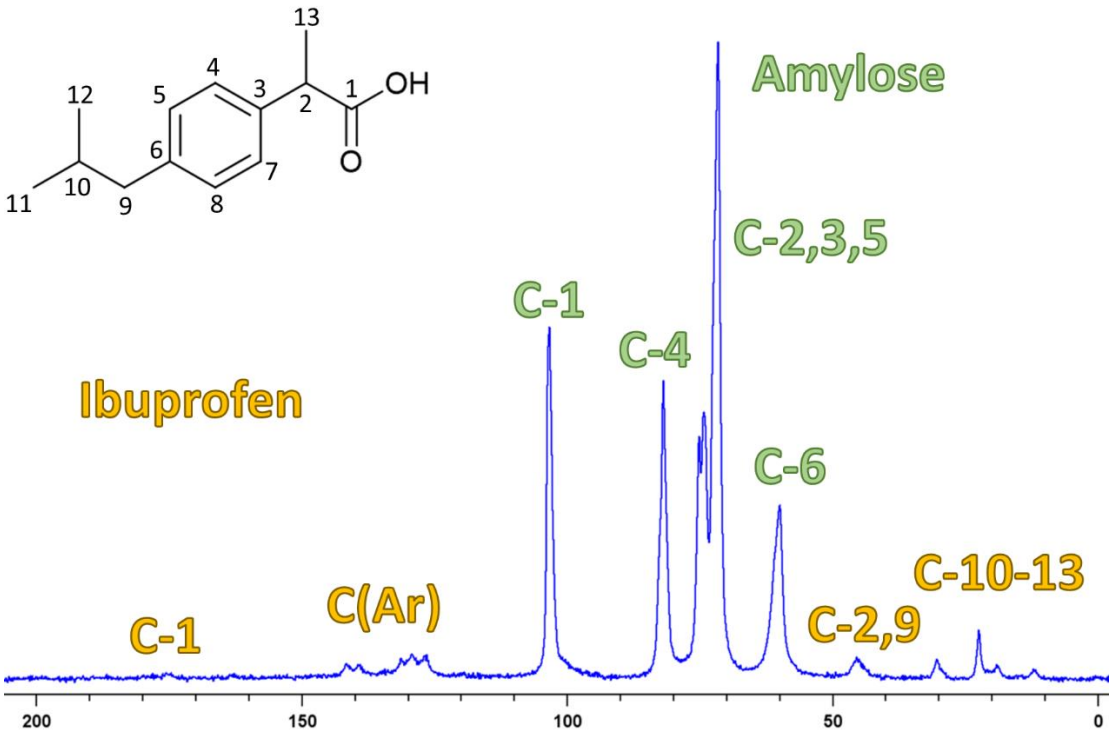

Figure 5.12: ^{1}H-^{13}C CP/MAS solid-state NMR spectrum of V-amylose-ibuprofen ($V7_{II}$) complex, featuring ^{13}C peak assignment.

Similar to the case of the 1-naphthol-complexed amylose, the V-amylose-ibuprofen complex exhibited higher degree of order, compared to amylose alone, as evidenced by the narrower peaks (Figure 5.13). All ^{13}C nuclear environments (C-1, C-4, C-2,3,5 and C-6) showed multiple peak splittings, likely indicating the presence of multiple different nuclear environments across all ^{13}C centres, similar to the V-amylose-1-naphthol complex.

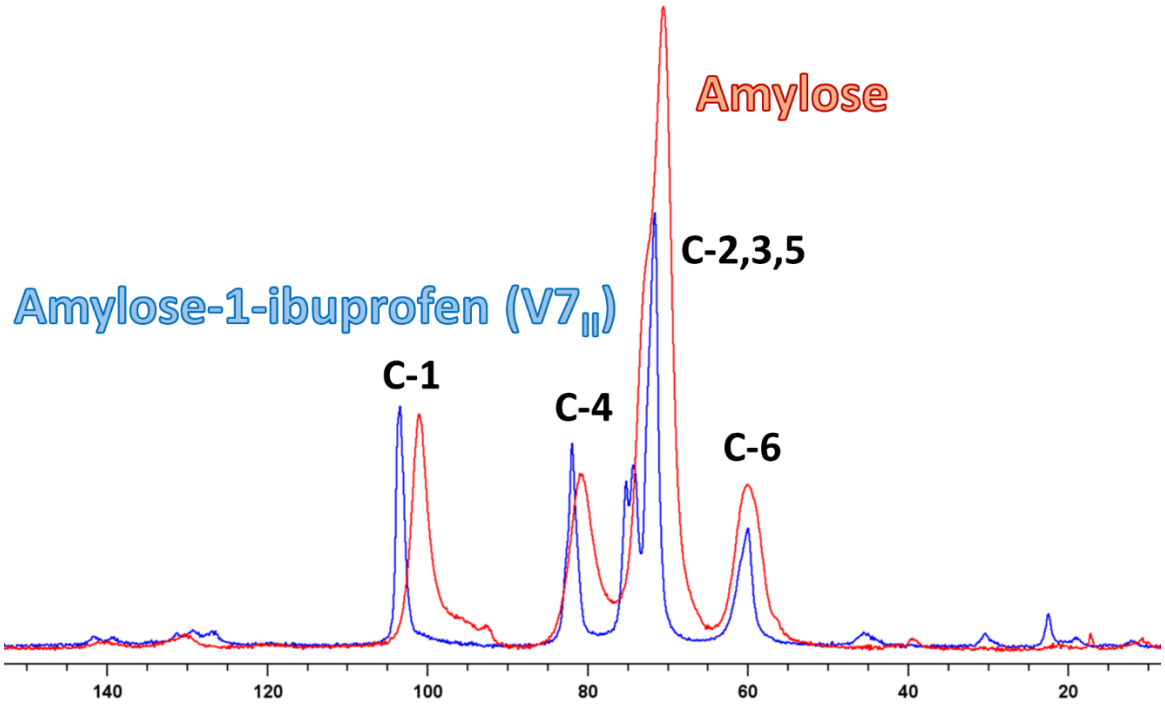

Figure 5.13: ^{1}H-^{13}C CP/MAS NMR spectra of pure amylose (red) and amylose-ibuprofen ($V7_{II}$) complex (blue), with amylose monomer ^{13}C peak assignment.

^{1}H-^{1}H NOESY NMR spectra at variable mixing times (Figure 5.14) revealed spatial proximity between several ^{1}H environments in the guest and host molecules. The guest-host ^{1}H contact followed the order of: H-10-13 ibuprofen – H-1 amylose ≈ H(Ar) ibuprofen – H-1 amylose < H(Ar) ibuprofen – H-2-6 amylose ≈H-10-13 ibuprofen – H-2-6 amylose. As in the case with the 1-naphthol complex, it is important to keep in mind that in dynamic complexes, NOESY reports on the resident time of one molecule with respect to another, averaged out across all populations and states the complex undergoes within the experimental time.

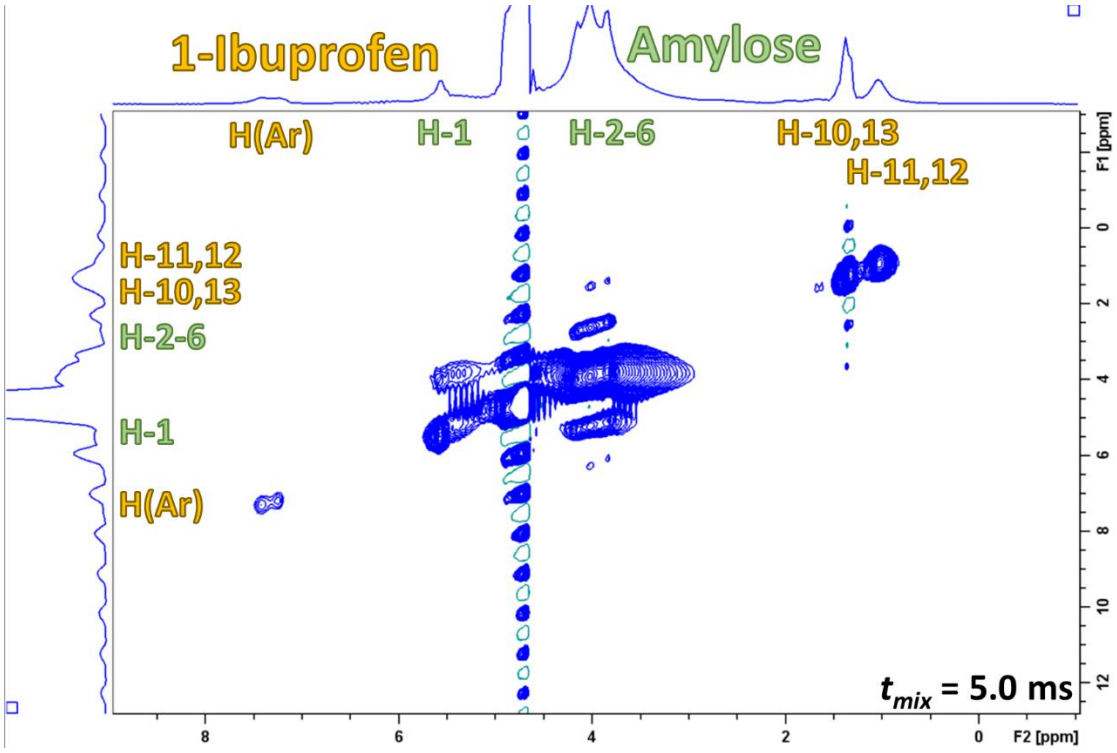
1-Ibuprofen
Amylose
H(Ar)
H-1
H-2-6
H-10,13
H-11,12
H-11,12
H-10,13
H-2-6
H-1
H(Ar)
t_{mix} = 5.0 ms
F1 [ppm]
F2 [ppm]

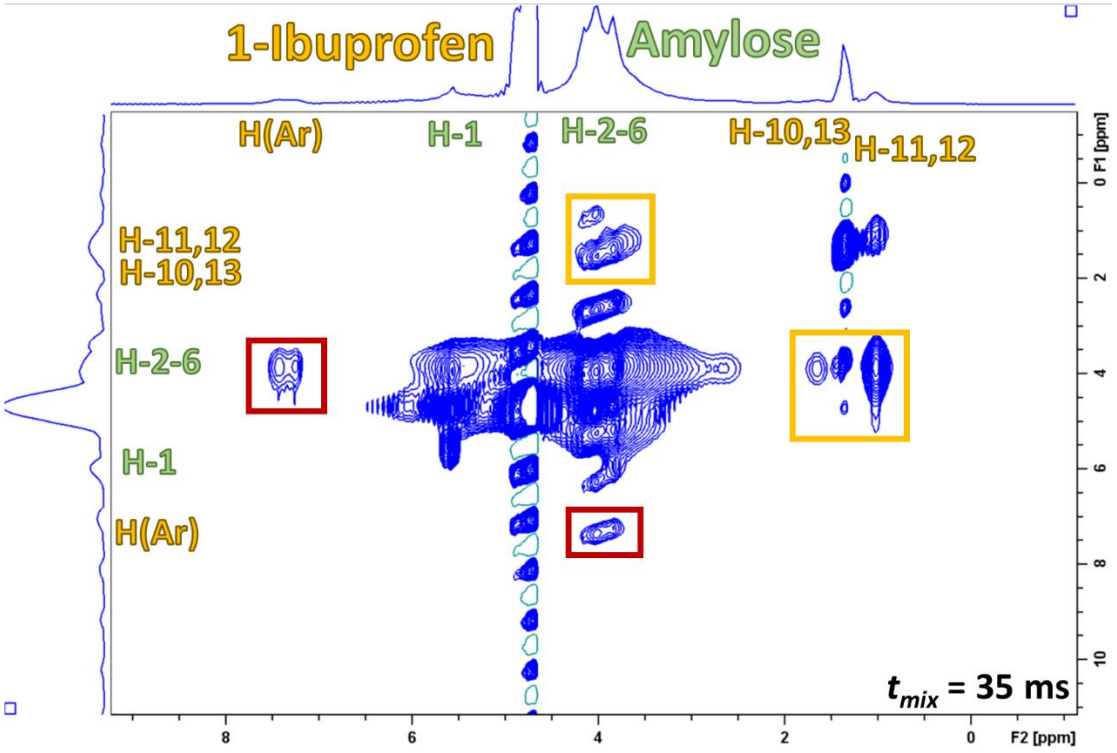
1-Ibuprofen
Amylose
H(Ar)
H-1
H-2-6
H-10,13
H-11,12
H-11,12
H-10,13
H-2-6
H-1
H(Ar)
t_{mix} = 35 ms
F1 [ppm]
F2 [ppm]

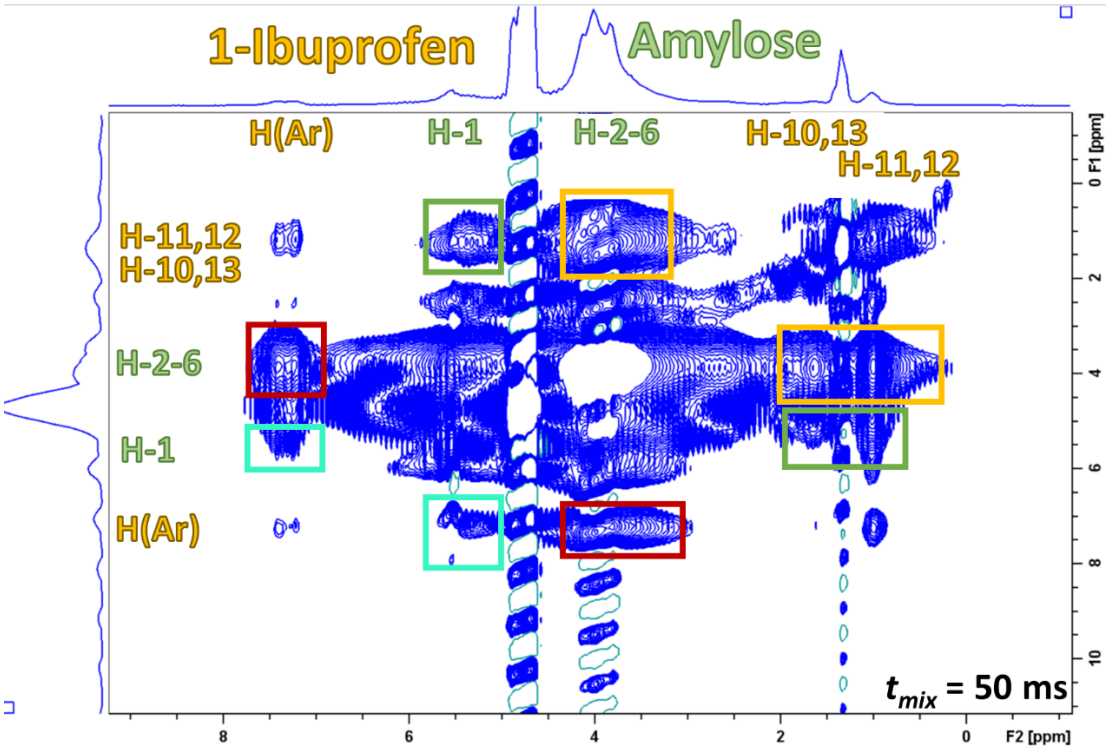

Figure 5.14: ^{1}H-^{1}H NOESY spectral overlay of V-amylose-ibuprofen (V7II) complex at short (5 ms, top), intermediate (35 ms, middle), and long (50 ms, bottom) mixing times, featuring ^{1}H assignment of both ibuprofen (yellow) and amylose (green). Cross peaks shown in red, yellow, green, and cyan. Mirrored cross peaks shown in the same colour.

The above internuclear proximity was partially supported by cross peaks in the ^{1}H-^{1}H SQ-DQ BABA NMR spectral data (Figure 5.15), but due to the experiment being carried out at only one mixing time, it precluded obtaining quantitative information of the SQ-DQ spectrum.

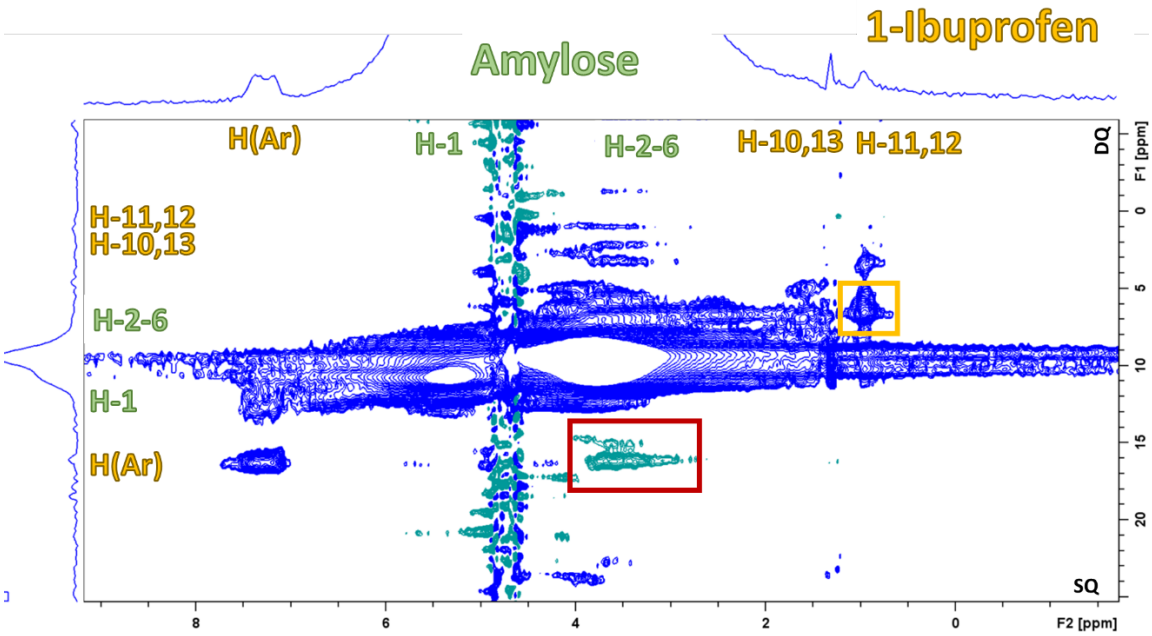

Figure 5.15: ^{1}H-^{1}H homonuclear SQ-DQ BABA NMR spectrum of V-amylose-ibuprofen ($V7_{II}$) complex, at t_{mix} = 20 ms, featuring assignment of the ^{1}H environments across both amylose and ibuprofen. Cross peaks shown in red and yellow.

5.4 Conclusion

Previous works combining geometrical modelling and stoichiometric analyses have pointed towards the interhelical space in $V7_{II}$ and $V7_{III}$-type complexes unable to accommodate guest molecules, but for the guests to be localised exclusively inside the hydrophobic cavity within V-amylose helices.[337] Apart from the matter of guest molecule localisation with respect to the V-amylose host helices, however, there has been no data on potential interactions between guest and host molecules in V-amylose complexes. We have probed the through-space interactions between the host amylose helix, and the guest molecules 1-naphthol and ibuprofen, using advanced solid-state NMR techniques.

We have shown that it is the aromatic rings of 1-naphthol and the aliphatic *iso*butyl tail of ibuprofen that are more proximal to the H-2-6 centres in the amylose helix, whereas H-1 in naphthol and H(Ar) in ibuprofen are further away from the V-amylose host. These data can be applied to the refinement of current molecular models on these complexes, such as the tentative model of V-amylose-ibuprofen ($V7_{II}$) seen in Khanh Le *et al*.[340] (Figure 5.18), which discusses a complex supercell containing a total of 84 glucosyl residues in the V-amylose helix, 8 intrahelical ibuprofen molecules and 56 interhelical water (H_2O) molecules.

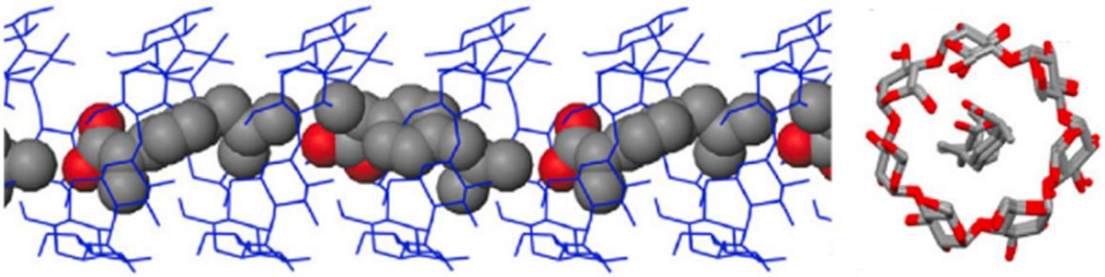

Figure 5.18: Longitudinal (left) and axial (right) views of V-amylose-ibuprofen ($V7_{II}$) complex, with suggested orientation of the guest molecule with respect to the host amylose helix. Figures derived, and geometries optimised and refined using a combination of GROMACS, VMD and SHELX software, and adapted from Cong Anh Khanh Le. [337]

Our methodology can be added to the arsenal of currently existing techniques for studying guest-host interactions and organisation within complex molecules.

5.5 Future Work

This work would be followed by measuring ^1H-^1H SQ-DQ BABA experiments at variable times in order to probe through-space interactions in the above complexes, in support of the ^1H-^1H NOESY experiments. This would be followed by integration of the area

under each cross peak expressed as a percentage of the area under a cross peak resulting from atoms with known interatomic distance at the same mixing time, allowing for approximation of the distance between nuclei belonging to the guest and host. This would further refine currently existing molecular models of these complexes.

Chapter 6: Overall Conclusions and Future Work

This project aimed at furthering our knowledge of how starch structure influences its ability to form hydrogels, and at probing the inter-component interactions within these heterogeneous soft matter systems, governing their bulk and molecular-level properties. We employed an array of characterisation techniques – on a range of length scales, with an emphasis on solid-, solution-state and high-resolution magic angle spinning (HR-MAS) NMR spectroscopy, to probe the molecular-level structural parameters of maize starch gels of different amylose content, ranging from less than 1% to *ca*. 70%, and how these contribute to the bulk structural behaviour of the starch hydrogel systems. We probed the effect of glucan (amylose and amylopectin) composition, short- and long-range molecular order, molecular mobility, molecular structural parameters (hydrodynamic radius, R_h, degree of polymerisation, DP, and chain length distribution, CLD), and the role of water in macromolecular hydrogel assembly and structural integrity.

We discuss our findings in the context of existing models of starch hydrogel organisation, originated by Jane and Robyt[164] and Leloup *et al*.[161] In particular, we expand on the continuous model of amylose gels made up of closely packed helices, interconnected by amorphous "dangling" chains within the porous cavities of the gel matrices, by providing

quantitative data on the mobile nature of these moieties, and how this relates to the gels' bulk system properties.

Furthermore, we explore how the structure of starch hydrogels impacts their physicochemical properties and behaviour in the human gastrointestinal tract (GIT), by investigating how individual structural moieties impact the bulk hydrogel's interactions with GI enzymes and commensal bacteria in the gut.

By employing two widely accepted models of *in vitro* digestion (INFOGEST protocol)[360] and colonic fermentation (batch colon model)[297], we have shown that starch gels resist upper GIT hydrolysis and reach the large intestine structurally intact. We have demonstrated their ability to serve as targeted colonic drug delivery platforms of small organic molecules with variable physicochemical properties (*e.g.*, solubility, hydrophilicity). We have probed the degree of interactions between guest molecules and the hydrogel host, and have demonstrated how these may impact the drug release kinetics of the guest-host system. We have shown how one can modulate their choice of starch in order to achieve the optimum drug release kinetics in the large intestine, and have demonstrated how our starch hydrogel systems compare to other competitor platforms (*e.g.*, other starch-based delivery platforms, mixed polysaccharide systems, enteric coatings, and compression tablets) by achieving sustained API release over prolonged colon transit time (up to 72 hours).

We then extended these investigations to semi-crystalline V-amylose complexes with small molecules (1-naphthol and ibuprofen), probing the structural arrangement and internal organisation of these complexes, and guest-host interactions. These data

provide critical information for the refinement of currently existing tentative molecular models of these complexes.[337]

Thus far, all our drug release data has been acquired under *in vitro* conditions, using widely accepted models of the human upper GIT and large intestine. A logical continuation of this work would be to investigate how our *in vitro* pharmacokinetic data translates to *in vivo* settings. We would probe the effect of starch hydrogels pre-loaded with colorectal cancer (CRC) treatment compounds (*e.g.*, DOX, 5FU) on the emergence and progression of CRC in a mouse model (APC^{min} – commonly used animal model for studying human small intestinal and CRC).[361] Our primary research interests would be whether the APIs reach the target site of intestinal neoplasia, following oral administration; what the effect of the delivery matrix and the APIs would be on the metabolic profile of the mouse gut microbial communities; what the effect of the APIs would be on the morphology of the neoplastic growth, and on the surrounding healthy intestinal lining; and how the cellular metabolite profile in the large intestine changes before, during and following drug administration.

References

(1) Bertoft, E. Understanding Starch Structure: Recent Progress. *Agronomy* **2017**, *7* (3), 56. https://doi.org/10.3390/agronomy7030056.

(2) Seung, D.; Smith, A. M. Starch Granule Initiation and Morphogenesis — Progress in Arabidopsis and Cereals. *J. Exp. Bot.* **2019**, *70* (3), 771–784. https://doi.org/10.1093/jxb/ery412.

(3) Tomlinson, K.; Denyer, K. *Starch Synthesis in Cereal Grains*; 2003.

(4) Smith, A. M. Prospects for Increasing Starch and Sucrose Yields for Bioethanol Production. *Plant J.* **2008**, *54*, 546–558. https://doi.org/10.1111/j.1365-313X.2008.03468.x.

(5) Kammerer, B.; Fischer, K.; Hilpert, B.; Schubert, S.; Gutensohn, M.; Weber, A.; Flügge, U. Molecular Characterization of a Carbon Transporter in Plastids from Heterotrophic Tissues : The Glucose 6-Phosphate / Phosphate Antiporter. **1998**, *10* (January), 105–117.

(6) Tjaden, J.; Möhlmann, T.; Kampfenkel, K.; Henrichs, G.; Neuhaud, H. E. Altered Plastidic ATPADP-transporter Activity Influences Potato (Solanum TuberosumL) Tuber Morphology, Yield and Composition of Tuber Starch. *Plant J.* **1998**, *16* (5), 531–540.

(7) Ball, S. G.; Morell, M. K. From Bacterial Glycogen to Starch: Understanding the Biogenesis of the Plant Starch Granule. *Annu. Rev. Plant Biol.* **2003**, *54*, 207–233. https://doi.org/10.1146/annurev.arplant.54.031902.134927.

(8) Tetlow, I. J.; Morell, M. K.; Emes, M. J. Recent Developments in Understanding the Regulation of Starch Metabolism in Higher Plants. **2004**, *55* (406), 2131–2145. https://doi.org/10.1093/jxb/erh248.

(9) Hawkins, E.; Chen, J.; Watson-Lazowski, A.; Ahn-Jarvis, J.; Barclay, J. E.; Fahy, B.; Hartley, M.; Warren, F. J.; Seung, D. STARCH SYNTHASE 4 Is Required for Normal Starch Granule Initiation in Amyloplasts of Wheat Endosperm. *New Phytol.* **2021**, *230* (6), 2371–2386. https://doi.org/10.1111/nph.17342.

(10) Denyer, K.; Waite, D.; Edwards, A.; Martin, C.; Smith, A. M. Interaction with Amylopectin Influences the Ability of Granule-Bound Starch Synthase I to Elongate Malto-Oligosaccharides. *Biochem. J.* **1999**, *342*, 647–653.

(11) Nakamura, Y. *Starch - Metabolism and Structure*; Springer Japan, 2015.

(12) Pfister, B.; Zeeman, S. C. Formation of Starch in Plant Cells. *Cell. Mol. Life Sci.* **2016**, *73* (14), 2781–2807. https://doi.org/10.1007/s00018-016-2250-x.

(13) Goren, A.; Ashlock, D.; Tetlow, I. J. Starch Formation inside Plastids of Higher Plants. **2018**, 1855–1876.

(14) Dumez, S.; Wattebled, F.; Rolda, I.; Berbezy, P.; Colonna, P.; Delvalle, D. Soluble Starch Synthase I : A Major Determinant for the Synthesis of Amylopectin in Arabidopsis Thaliana Leaves. **2005**, 398–412. https://doi.org/10.1111/j.1365-313X.2005.02462.x.

(15) Zhang, X.; Szydlowski, N.; Delvallé, D.; Hulst, C. D.; James, M. G.; Myers, A. M. Overlapping Functions of the Starch Synthases SSII and SSIII in Amylopectin Biosynthesis in Arabidopsis. **2008**, *18*, 1–18. https://doi.org/10.1186/1471-2229-8-96.

(16) Fujita, N.; Yoshida, M.; Asakura, N.; Ohdan, T.; Miyao, A. Function and Characterization of Starch Synthase I Using Mutants in Rice. **2020**, *140* (March 2006), 1070–1084. https://doi.org/10.1104/pp.105.071845.1070.

(17) Streb, S.; Delatte, T.; Umhang, M.; Eicke, S.; Schorderet, M.; Reinhardt, D.; Zeeman, S. C. Starch Granule Biosynthesis in Arabidopsis Is Abolished by Removal of All Debranching Enzymes but Restored by the Subsequent Removal

of an Endoamylase. *Plant Cell* **2008**, *20* (December), 3448–3466. https://doi.org/10.1105/tpc.108.063487.

(18) Denyer, K.; Barber, L. M.; Burton, R.; Hedley, C. L.; Hylton, C. M.; Johnson, S.; Jones, D. A.; Marshall, J.; Smith, A. M.; Tatge, H.; Tomlinson, K.; Wang, T. L. The Isolation and Characterization of Novel Low-amylose Mutants of Pisum Sativum L..Pdf. *Ptant, Cett Er}viror}ment* **1995**, *18*, 1019–1026.

(19) Tester, R. F.; Karkalas, J.; Qi, X. Starch - Composition, Fine Structure and Architecture. *J. Cereal Sci.* **2004**, *39* (2), 151–165. https://doi.org/10.1016/j.jcs.2003.12.001.

(20) Morrison, W. R.; Tester, R. F.; Snape, C. E.; Law, R.; Gidley, M. J. Swelling and Gelatinisation of Cereal Starches. IV. Some Effects of Lipid-Complexed Amylose and Free Amylose in Waxy and Normal Barley Starches. *Cereal Chemistry*. 1995, pp 385–391.

(21) Baldwin, P. M. Starch Granule-Associated Proteins and Polypeptides - A Review.Pdf. *Starch/Stärke* **2001**, *53*, 475–503.

(22) Gérard, C.; Barron, C.; Colonna, P.; Planchot, V. Amylose Determination in Genetically Modified Starches. *Carbohydr. Polym.* **2001**, *44* (1), 19–27. https://doi.org/10.1016/S0144-8617(00)00194-6.

(23) Defloor, I.; Dehing, I.; Delcour, J. A. Physico-Chemical Properties of Cassava Starch. *Starch - Stärke* **1998**, *50* (2–3), 58–64. https://doi.org/10.1002/(SICI)1521-379X(199803)50:2/3<58::AID-STAR58>3.0.CO;2-N.

(24) Genkina, N. K.; Noda, T.; Koltisheva, G. I.; Wasserman, L. A.; Tester, R. F.; Yuryev, V. P. Effects of Growth Temperature on Some Structural Properties of Crystalline Lamellae in Starches Extracted from Sweet Potatoes (Sunnyred and Ayamurasaki). *Starch - Stärke* **2003**, *55* (8), 350–357. https://doi.org/10.1002/star.200300145.

(25) Yusuph, M.; Tester, R. F.; Ansell, R.; Snape, C. E. Composition and Properties of Starches Extracted from Tubers of Different Potato Varieties Grown under the Same Environmental Conditions. *Food Chem.* **2003**, *82* (2), 283–289. https://doi.org/10.1016/S0308-8146(02)00549-6.

(26) Svihus, B.; Uhlen, A. K.; Harstad, O. M. Effect of Starch Granule Structure, Associated Components and Processing on Nutritive Value of Cereal Starch: A Review. *Anim. Feed Sci. Technol.* **2005**, *122* (3–4), 303–320. https://doi.org/10.1016/j.anifeedsci.2005.02.025.

(27) Copeland, L.; Blazek, J.; Salman, H.; Tang, M. C. Form and Functionality of Starch. *Food Hydrocoll.* **2009**, *23* (6), 1527–1534. https://doi.org/10.1016/j.foodhyd.2008.09.016.

(28) Lindeboom, N.; Chang, P. R.; Tyler, R. T. Analytical, Biochemical and Physicochemical Aspects of Starch Granule Size, with Emphasis on Small Granule Starches: A Review. *Starch - Stärke* **2004**, *56* (34), 89–99. https://doi.org/10.1002/star.200300218.

(29) Vamadevan, V.; Bertoft, E. Structure-Function Relationships of Starch Components. *Starch - Stärke* **2015**, *67* (1–2), 55–68. https://doi.org/10.1002/star.201400188.

(30) Biliaderis, G.; Grant, D. R.; Vose, J. R. Molecular Weight Distributions of Legume Starches by Gel Chromatography. *Cereal Chemistry*. 1979, pp 475–480.

(31) Hoover, R. Composition, Molecular Structure, and Physicochemical Properties of Tuber and Root Starches: A Review. Carbohydrate Polymers,. **2001**, *45*, 253–267.

(32) Morrison, W. R.; Milligan, T. P.; Azudin, M. N. A Relationship between the Amylose and Lipid Contents of Starches from Diploid Cereals. *J. Cereal Sci.* **1984**, *2* (4), 257–271. https://doi.org/10.1016/S0733-5210(84)80014-4.

(33) Verwimp, T.; Vandeputte, G. E.; Marrant, K.; Delcour, J. A. Isolation and Characterisation of Rye Starch. *J. Cereal Sci.* **2004**, *39* (1), 85–90. https://doi.org/10.1016/S0733-5210(03)00068-7.

(34) Pérez, S.; Bertoft, E. The Molecular Structures of Starch Components and Their Contribution to the Architecture of Starch Granules: A Comprehensive Review. *Starch - Stärke* **2010**, *62* (8), 389–420. https://doi.org/10.1002/star.201000013.

(35) Vesterinen, E.; Suortti, T.; Autio, K. Effects of Preparation Temperature on Gelation Properties and Molecular Structure of High-Amylose Maize Starch. *Cereal Chem.* **2001**, *78* (4), 442–446. https://doi.org/10.1094/CCHEM.2001.78.4.442.

(36) Nishiyama, Y.; Mazeau, K.; Morin, M.; Cardoso, M. B.; Chanzy, H.; Putaux, J. L. Molecular and Crystal Structure of 7-Fold V-Amylose Complexed with 2-Propanol. *Macromolecules* **2010**, *43* (20), 8628–8636. https://doi.org/10.1021/ma101794w.

(37) Gidley, M. J.; Bociek, S. M. 13C CP/MAS NMR Studies of Amylose Inclusion Complexes, Cyclodextrins, and the Amorphous Phase of Starch Granules: Relationships Between Glycosidic Linkage Conformation and Solid-State 13C Chemical Shifts. *J. Am. Chem. Soc.* **1988**, *110* (12), 3820–3829. https://doi.org/10.1021/ja00220a016.

(38) Knutson, C. A. A Simplified Colorimetric Procedure for Determination of Am in Maize Starches.Pdf. *Cereal chem*. 1985, pp 89–92.

(39) Morrison, W. R.; Laignelet, B. An Improved Colorimetric Procedure for Determining Apparent and Total Amylose in Cereal and Other Starches. *J. Cereal Sci.* **1983**, *1* (1), 9–20. https://doi.org/10.1016/S0733-5210(83)80004-6.

(40) Le, C. A. K.; Choisnard, L.; Wouessidjewe, D.; Putaux, J. L. Polymorphism of Crystalline Complexes of V-Amylose with Fatty Acids. *Int. J. Biol. Macromol.* **2018**, *119*, 555–564. https://doi.org/10.1016/j.ijbiomac.2018.07.163.

(41) Kasemsuwan, T.; Jane, J. L. Location of Amylose in Normal Starch Granules. II Location of Phosphodiester Cross-Linking Revealed by Phosphorous-31 Nuclear Magnetic Resonance. *Cereal chemistry*. 1994, pp 282–287.

(42) Jane, J. lin; Shen, J. J. Internal Structure of the Potato Starch Granule Revealed by Chemical Gelatinization. *Carbohydr. Res.* **1993**, *247* (C), 279–290. https://doi.org/10.1016/0008-6215(93)84260-D.

(43) Bertoft, E.; Piyachomkwan, K.; Chatakanonda, P.; Sriroth, K. Internal Unit Chain Composition in Amylopectins. *Carbohydr. Polym.* **2008**, *74* (3), 527–543. https://doi.org/10.1016/j.carbpol.2008.04.011.

(44) Morris, V. Starch Gelation and Retrogradation. *Trends Food Sci. Technol.* **1990**, *July*.

(45) Warren, F. J.; Gidley, M. J.; Flanagan, B. M. Infrared Spectroscopy as a Tool to Characterise Starch Ordered Structure - A Joint FTIR-ATR, NMR, XRD and DSC Study. *Carbohydr. Polym.* **2016**, *139*, 35–42. https://doi.org/10.1016/j.carbpol.2015.11.066.

(46) Gidley, M. J.; Hanashiro, I.; Hani, N. M.; Hill, S. E.; Huber, A.; Jane, J. L.; Liu, Q.; Morris, G. A.; Rolland-Sabaté, A.; Striegel, A. M.; Gilbert, R. G. Reliable Measurements of the Size Distributions of Starch Molecules in Solution: Current Dilemmas and Recommendations. *Carbohydr. Polym.* **2010**, *79* (2), 255–261. https://doi.org/10.1016/j.carbpol.2009.07.056.

(47) Limited, W. P. *Starch in Food*; 2018. https://doi.org/10.1016/C2015-0-01896-2.

(48) Bradbury, A. G. W.; Bello, A. B. T. Determination of Molecular Size Distribution of Starch and Debranched Starch by a Single Procedure Using High-Performance Size-Exclusion Chromatography. *Cereal Chemistry*. 1993, pp 543–547.

(49) Wang, Y. J.; White, P.; Pollak, L.; Jane, J. Characterization of Starch Structures of 17 Maize Endosperm Mutant Genotypes with Oh43 Inbred Line Background. *Cereal Chem.* **1993**, *70* (2), 171–179.

(50) Arai, Y.; Baba, T. Structural Characterization of Amylopectin and Intermediate Material in Amylomaize Starch Granules. *Agric. Biol. Chem.* **1984**, *48* (7), 1763–1775. https://doi.org/10.1080/00021369.1984.10866395.

(51) Bertoft, E.; Koch, K.; Åman, P. Building Block Organisation of Clusters in

Amylopectin from Different Structural Types. *Int. J. Biol. Macromol.* **2012**, *50* (5), 1212–1223. https://doi.org/10.1016/j.ijbiomac.2012.03.004.

(52) Hanashiro, I.; Abe, J. I.; Hizukuri, S. A Periodic Distribution of the Chain Length of Amylopectin as Revealed by High-Performance Anion-Exchange Chromatography. *Carbohydr. Res.* **1996**, *283*, 151–159. https://doi.org/10.1016/0008-6215(95)00408-4.

(53) Hizukuri, S. Polymodal Distribution of the Chain Lengths of Amylopectins, and Its Significance. *Carbohydr. Res.* **1986**, *147*, 342–347.

(54) Bertoft, E.; Koch, K.; Åman, P. Structure of Building Blocks in Amylopectins. *Carbohydr. Res.* **2012**, *361*, 105–113. https://doi.org/10.1016/j.carres.2012.08.012.

(55) Bertoft, E.; Piyachomkwan, K.; Chatakanonda, P.; Sriroth, K. Internal Unit Chain Composition in Amylopectins. **2008**, *74*, 527–543. https://doi.org/10.1016/j.carbpol.2008.04.011.

(56) Buléon, A.; Pontoire, B.; Riekel, C.; Chanzy, H.; Helbert, W.; Vuong, R.; Bule, A.; Pontoire, B.; Riekel, C.; Chanzy, H.; Helbert, W.; Vuong, R.; Buléon, A.; Pontoire, B.; Riekel, C.; Chanzy, H.; Helbert, W.; Vuong, R. Crystalline Ultrastructure of Starch Granules Revealed by Synchrotron Radiation Microdiffraction Mapping. *Macromolecules* **1997**, *30* (13), 3952–3954. https://doi.org/10.1021/ma970136q.

(57) Bogracheva, T. Y.; Wang, Y. L.; Hedley, C. L. The Effect of Water Content on the Ordered / Disordered. *Biopolymers* **2001**, *58*, 247–259.

(58) Cairns, P.; Bogracheva, T. Y.; Ringa, S. G.; Hedley, C. L.; Morris, V. J. Determination of the Polymorphic Composition of Smooth Pea Starch. **1997**, *32*.

(59) Zobel, H. F.; Young, S. N.; Rocca, L. A. Starch Gelatinization: An X-Ray Diffraction Study. *Cereal Chem.* **1988**, *65* (6), 443–446.

(60) Waigh, T. a; Donald, A. M.; Heidelbach, F.; Riekel, C.; Gidley, M. J. Analysis of the Native Structure of Starch Granules with Small Angle X-Ray Microfocus Scattering. *Biopolymers* **1999**, *49* (97), 91. https://doi.org/10.1002/(SICI)1097-0282(199901)49:1<91::AID-BIP9>3.3.CO;2-0.

(61) Gidley, M. J. Factors Affecting the Crystalline Type (AC) of Native Starches and Model Compounds: A Rationalisation of Observed Effects in Terms of Polymorphic Structures. *Carbohydr. Res.* **1987**, *161* (2), 301–304. https://doi.org/10.1016/S0008-6215(00)90087-9.

(62) Veregin, R. P.; Fyfe, C. A.; Marchessault, R. H. Investigation of the Crystalline “V” Amylose Complexes by High-Resolution13C CP/MAS NMR Spectroscopy. *Macromolecules* **1987**, *20* (12), 3007–3012. https://doi.org/10.1021/ma00178a010.

(63) Horii, F.; Yamamoto, H.; Hirai, A.; Kitamaru, R. Structural Study of Amylose Polymorphs by Cross Polarisation-Magic Angle Spinning 13C NMR Spectroscopy. *Carbohydr. Res.* **1987**, *160*, 29–40.

(64) Koev, T. T.; Muñoz-García, J. C.; Iuga, D.; Khimyak, Y. Z.; Warren, F. J. Structural Heterogeneities in Starch Hydrogels. *Carbohydr. Polym.* **2020**, *249* (July), 116834. https://doi.org/10.1016/j.carbpol.2020.116834.

(65) Cooke, D.; Gidley, M. J. Loss of Crystalline and Molecular Order during Starch Gelatinisation: Origin of the Enthalpic Transition. *Carbohydr. Res.* **1992**, *227* (C), 103–112. https://doi.org/10.1016/0008-6215(92)85063-6.

(66) Jenkins, P. J.; Donald, A. M.; Jenkins, P.J., Donald, A. M. The Influence of Amylose on Starch Granule Structure. *Int. J. Biol. Macromol.* **1995**, *17* (6), 315–321. https://doi.org/10.1016/0141-8130(96)81838-1.

(67) Gidley, M. J.; Bociek, S. M. Molecular Organization in Starches: A 13C CP/MAS NMR Study. *J. Am. Chem. Soc.* **1985**, *107* (24), 7040–7044. https://doi.org/10.1021/ja00310a047.

(68) Htoon, A.; Shrestha, A. K.; Flanagan, B. M.; Lopez-Rubio, A.; Bird, A. R.; Gilbert, E. P.; Gidley, M. J. Effects of Processing High Amylose Maize Starches under Controlled Conditions on Structural Organisation and Amylase Digestibility. *Carbohydr. Polym.* **2009**, *75* (2), 236–245. https://doi.org/10.1016/j.carbpol.2008.06.016.

(69) Donald, A. M.; Waigh, T. A.; Jenkins, P. J.; Gidley, M. J.; Debet, M.; Smith, A. Internal Structure of Starch Granules Revealed by Scattering Studies. Royal Society of Chemistry 1997.

(70) Buléon, A.; Colonna, P.; Planchot, V.; Ball, S. Starch Granules: Structure and Biosynthesis. *Int. J. Biol. Macromol.* **1998**, *23* (2), 85–112. https://doi.org/10.1016/S0141-8130(98)00040-3.

(71) Kozlov, S. S.; Krivandin, A. V.; Shatalova, O. V.; Noda, T.; Bertoft, E.; Fornal, J.; Yuryev, V. P. Structure of Starches Extracted from Near-Isogenic Wheat Lines. *J.*

Therm. Anal. Calorim. **2007**, *87* (2), 575–584. https://doi.org/10.1007/s10973-006-7880-z.

(72) Franco, C. M. L.; José, S.; Ciacco, C. F.; Tavares, D. Q.; Brasil, C.-. The Structure of Waxy Corn Starch : Effect of Granule Size. *Starch - Stärke* **1998**, *50* (5), 193–198. https://doi.org/papers://590F92D9-0B76-4B88-8729-9AF064BE5AC8/Paper/p2369.

(73) Oostergetel, G. T.; van Bruggen, E. F. J. The Crystalline Domains in Potato Starch Granules Are Arranged in a Helical Fashion. *Carbohydr. Polym.* **1993**, *21* (1), 7–12. https://doi.org/10.1016/0144-8617(93)90110-P.

(74) Waigh, T. A.; Perry, P.; Riekel, C.; Gidley, M. J.; Donald, A. M. Chiral Side-Chain Liquid Crystalline Polymeric Properties of Starch. *Macromolecules* **1998**, 7980–7984.

(75) Wang, S. S.; Li, C.; Copeland, L.; Niu, Q.; Wang, S. S. Starch Retrogradation: A Comprehensive Review. *Compr. Rev. Food Sci. Food Saf.* **2015**, *14* (5), 568–585. https://doi.org/10.1111/1541-4337.12143.

(76) Gallant, D. J.; Bouchet, B.; Baldwin, P. M. Microscopy of Starch: Evidence of a New Level of Granule Organisation. *Carbohydr. Polym.* **1997**, *32* (3–4), 177–191. https://doi.org/10.1016/S0144-8617(97)00008-8.

(77) Baldwin, P. M.; Adler, J.; Davies, M. C.; Melia, C. D. High Resolution Imaging of Starch Granule Surfaces by Atomic Force Microscopy. *J. Cereal Sci.* **1998**, *27* (3), 255–265. https://doi.org/10.1006/jcrs.1998.0189.

(78) Ohtani, T.; Yoshino, T.; Hagiwara, S.; Maekawa, T. High-Resolution Imaging of

Starch Granule Structure by Atomic Force Microscopy. *Starch - Stärke* **2000**, *52* (5), 150–153.

(79) Tang, H.; Mitsunaga, T.; Kawamura, Y. Molecular Arrangement in Blocklets and Starch Granules Architecture. *Carbohydr. Polym.* **2006**, *63*, 555–560.

(80) Waigh, T. A.; Kato, K. L.; Donald, A. M.; Gidley, M. J.; Clarke, C. J.; Riekel, C. Side-Chain Liquid-Crystalline Model for Starch. *Starch - Stärke* **2000**, *52*, 450–460.

(81) Bogracheva, T. Y.; Wang, Y. L.; Wang, T. L.; Hedley, C. L. Structural Studies of Starches with Different Water Contents. *Biopolymers* **2002**, *64* (5), 268–281. https://doi.org/10.1002/bip.10190.

(82) Birt, D. F.; Boylston, T.; Hendrich, S.; Jane, J.-L.; Hollis, J.; Li, L.; McClelland, J.; Moore, S.; Phillips, G. J.; Rowling, M.; Schalinske, K.; Scott, M. P.; Whitley, E. M. Resistant Starch: Promise for Improving Human Health. *Adv. Nutr.* **2013**, *4* (6), 587–601. https://doi.org/10.3945/an.113.004325.

(83) Perry, G. H.; Dominy, N. J.; Claw, K. G.; Lee, A. S.; Fiegler, H.; Redon, R.; Werner, J.; Villanea, F. A.; Mountain, J. L.; Misra, R.; Carter, N. P.; Lee, C.; Stone, A. C. Diet and the Evolution of Human Amylase Gene Copy Number Variation. *Nat. Genet.* **2007**, *39* (10), 1256–1260. https://doi.org/10.1038/ng2123.

(84) Ragunath, C.; Manuel, S. G. a.; Kasinathan, C.; Ramasubbu, N. Structure-Function Relationships in Human Salivary Alpha-Amylase: Role of Aromatic Residues in a Secondary Binding Site. *Biologia (Bratisl).* **2008**, *63* (6), 1028–1034. https://doi.org/10.2478/s11756-008-0163-3.

(85) Meisler, M. H.; Ting, C. N. The Remarkable Evolutionary History of the Human

Amylase Genes. *Crit. Rev. oral Biol. Med.* **1993**, *4* (3–4), 503–509. https://doi.org/10.1177/10454411930040033501.

(86) Cummings, J. H.; Beatty, E. R.; Kingman, S. M.; Bingham, S. A.; Englyst, H. N. Digestion and Physiological Properties of Resistant Starch in the Human Large Bowel. *Br. J. Nutr.* **1996**, *75* (05), 733. https://doi.org/10.1079/BJN19960177.

(87) World Health Organisation (WHO). The Top 10 Leading Causes of Death. *WHO Annu. Reports* **2017**.

(88) Ells, L. J.; Seal, C. J.; Kettlitz, B.; Bal, W.; Mathers, J. C. Postprandial Glycaemic, Lipaemic and Haemostatic Responses to Ingestion of Rapidly and Slowly Digested Starches in Healthy Young Women. *Br. J. Nutr.* **2005**, *94* (06), 948. https://doi.org/10.1079/BJN20051554.

(89) Jenkins, D. J. A.; Kendall, C. W. C.; Augustin, L. S. A.; Franceschi, S.; Hamidi, M.; Marchie, A. Glycaemic Index : Overview of Implications in Health and Disease 1 – 4. **2002**, *76*, 266–273.

(90) Frost, G.; Leeds, A.; Trew, G.; Margara, R.; Dornhorst, A. Insulin Sensitivity in Women at Risk of Coronary Heart Disease and the Effect of a Low Glycemic Diet. *Metabolism* **1998**, *47* (10), 1245–1251. https://doi.org/10.1016/S0026-0495(98)90331-6.

(91) Mann, J. Dietary Carbohydrate: Relationship to Cardiovascular Disease and Disorders of Carbohydrate Metabolism. *Eur. J. Clin. Nutr.* **2007**, *61*, S100–S111. https://doi.org/10.1038/sj.ejcn.1602940.

(92) Jensen, M. K.; Koh-banerjee, P.; Hu, F. B.; Franz, M.; Sampson, L.; Grønbæk, M.

Intakes of Whole Grains , Bran , and Germ and the Risk of Coronary Heart Disease in Men 1 – 3. *Am. J. Clin. Nutr.* **2004**, No. 7, 1492–1499.

(93) Siddique, K. *The Food and Agricultural Research Challenge*; 2008.

(94) Carvalho, A. J. F. Chapter 15 - Starch: Major Sources, Properties and Applications as Thermoplastic Materials A2 - Belgacem, Mohamed Naceur. In *Monomers, Polymers and Composites from Renewable Resources*; Gandini Polymers and Composites from Renewable Resources, A. B. T.-M., Ed.; Elsevier: Amsterdam, 2008; pp 321–342. https://doi.org/https://doi.org/10.1016/B978-0-08-045316-3.00015-6.

(95) Burrell, M. M. Starch: The Need for Improved Quality or Quantity - An Overview. *J. Exp. Bot.* **2003**, *54* (382), 451–456. https://doi.org/10.1093/jxb/erg049.

(96) Shen, L.; Worrell, E.; Patel, M. Present and Future Development in Plastics from Biomass Li. *Biofuels, Bioprod. Biorefining* **2009**, *6* (3), 246–256. https://doi.org/10.1002/bbb.

(97) Doutch, J.; Bason, M.; Franceschini, F.; James, K.; Clowes, D.; Gilbert, E. P. Structural Changes during Starch Pasting Using Simultaneous Rapid Visco Analysis and Small-Angle Neutron Scattering. *Carbohydr. Polym.* **2012**, *88* (3), 1061–1071. https://doi.org/10.1016/j.carbpol.2012.01.066.

(98) Wang, T. L.; Bogracheva, T. Y.; Hedley, C. L.; Centre, J. I.; Nr, N. Starch : As Simple as A , B , C ? **1998**, *49* (320), 481–502.

(99) Reddy, K.; Mohan, G. K.; Satla, S.; Gaikwad, S. Natural Polysaccharides: Versatile Excipients for Controlled Drug Delivery Systems. *Asian J. Pharm. Sci.* **2011**, *6* (6),

275–286.

(100) Ghanbarzadeh, B.; Almasi, H.; Entezami, A. A. Physical Properties of Edible Modified Starch/Carboxymethyl Cellulose Films. *Innov. Food Sci. Emerg. Technol.* **2010**, *11* (4), 697–702. https://doi.org/10.1016/j.ifset.2010.06.001.

(101) Bagliotti Meneguin, A.; Stringhetti Ferreira Cury, B.; Evangelista, R. C. Films from Resistant Starch-Pectin Dispersions Intended for Colonic Drug Delivery. *Carbohydr. Polym.* **2014**, *99*, 140–149. https://doi.org/10.1016/j.carbpol.2013.07.077.

(102) Shalviri, A.; Liu, Q.; Abdekhodaie, M. J.; Wu, X. Y. Novel Modified Starch-Xanthan Gum Hydrogels for Controlled Drug Delivery: Synthesis and Characterization. *Carbohydr. Polym.* **2010**, *79* (4), 898–907. https://doi.org/10.1016/j.carbpol.2009.10.016.

(103) Outline, C. Starch and Derivatives as Pharmaceutical Excipients. **2015**. https://doi.org/10.1016/B978-1-907568-45-9.00002-0.

(104) Steckel, H.; Ph, D.; Eskandar, F.; Witthohn, K.; Ph, D. Effect of Excipients on the Stability and Aerosol Performance of Nebulized Aviscumine. **2003**, *16* (4), 417–432.

(105) Ali, A. E.; Alarifi, A. Characterization and in Vitro Evaluation of Starch Based Hydrogels as Carriers for Colon Specific Drug Delivery Systems. *Carbohydr. Polym.* **2009**, *78* (4), 725–730. https://doi.org/10.1016/j.carbpol.2009.06.009.

(106) Chourasia, M. K.; Jain, S. K. Polysaccharides for Colon Targeted Drug Delivery. *Drug Deliv. J. Deliv. Target. Ther. Agents* **2004**, *11* (2), 129–148.

https://doi.org/10.1080/10717540490280778.

(107) Meneguin, A. B.; Ferreira Cury, B. S.; dos Santos, A. M.; Franco, D. F.; Barud, H. S.; da Silva Filho, E. C. Resistant Starch/Pectin Free-Standing Films Reinforced with Nanocellulose Intended for Colonic Methotrexate Release. *Carbohydr. Polym.* **2017**, *157*, 1013–1023. https://doi.org/10.1016/j.carbpol.2016.10.062.

(108) Builders, P. F.; Arhewoh, M. I. Pharmaceutical Applications of Native Starch in Conventional Drug Delivery. *Starch/Stärke* **2016**, *68*, 864–873. https://doi.org/10.1002/star.201500337.

(109) Emblem, A.; Hardwidge, M. Adhesives for Packaging. In *Packaging Technology Fundamentals, Materials and Processes*; 2012; pp 381–394. https://doi.org/10.1533/9780857095701.2.381.

(110) Blennow, A.; Bay-Smidt, A. M.; Leonhardt, P.; Bandsholm, O.; Hadsen, M. H. Starch Paste Stickiness Is a Relevant Native Starch Selection Criterion for Wet-end Paper Manufacturing. *Starch/Stärke* **2003**, *55*, 381–389.

(111) BeMiller, J. N.; Whistler, R. *Starch Chemistry and Technology*, Third.; 2009; Vol. 1. https://doi.org/10.1017/CBO9781107415324.004.

(112) Minekus, M.; Alminger, M.; Alvito, P.; Ballance, S.; Bohn, T.; Bourlieu, C.; Carrière, F.; Boutrou, R.; Corredig, M.; Dupont, D.; Dufour, C.; Egger, L.; Golding, M.; Karakaya, S.; Kirkhus, B.; Le Feunteun, S.; Lesmes, U.; MacIerzanka, A.; MacKie, A.; Marze, S.; McClements, D. J.; Ménard, O.; Recio, I.; Santos, C. N.; Singh, R. P.; Vegarud, G. E.; Wickham, M. S. J.; Weitschies, W.; Brodkorb, A. A Standardised Static in Vitro Digestion Method Suitable for Food-an International

Consensus. *Food Funct.* **2014**, *5* (6), 1113–1124. https://doi.org/10.1039/c3fo60702j.

(113) Gorham, J. B.; Williams, B. A.; Gidley, M. J.; Mikkelsen, D. Visualization of Microbe-Dietary Remnant Interactions in Digesta from Pigs, by Fluorescence in Situ Hybridization and Staining Methods; Effects of a Dietary Arabinoxylan-Rich Wheat Fraction. *Food Hydrocoll.* **2016**, *52*, 952–962. https://doi.org/10.1016/j.foodhyd.2015.09.011.

(114) Brodkorb, A.; Egger, L.; Alminger, M.; Alvito, P.; Assunção, R.; Ballance, S.; Bohn, T.; Bourlieu-lacanal, C.; Boutrou, R.; Carrière, F.; Clemente, A.; Corredig, M.; Dupont, D.; Dufour, C.; Edwards, C.; Golding, M.; Karakaya, S.; Kirkhus, B.; Le Feunteun, S.; Lesmes, U.; Macierzanka, A.; Mackie, A. R.; Martins, C.; Marze, S.; McClements, D. J.; Menard, O.; Minekus, M.; Portmann, R.; Santos, C. N.; Souchon, I.; Singh, R. P.; Vegarud, G. E.; Wickham, M. S. J.; Weitschies, W.; Recio, I. INFOGEST Static in Vitro Simulation of Gastrointestinal Food Digestion. *Nat. Protoc.* **2019**, *14* (April), 991–1014.

(115) Maldonado-Valderrama, J.; Gunning, A. P.; Wilde, P. J.; Morris, V. J. In Vitro Gastric Digestion of Interfacial Protein Structures: Visualisation by AFM. *Soft Matter* **2010**, *6* (19), 4908–4915. https://doi.org/10.1039/c0sm00300j.

(116) Kaukonen, A. M.; Boyd, B. J.; Charman, W. N.; Porter, C. J. H. Drug Solubilization Behavior during in Vitro Digestion of Suspension Formulations of Poorly Water-Soluble Drugs in Triglyceride Lipids. *Pharm. Res.* **2004**, *21* (2), 254–260. https://doi.org/10.1023/B:PHAM.0000016283.87709.a9.

(117) Butterworth, P. J.; Warren, F. J.; Ellis, P. R. Human α-Amylase and Starch

Digestion: An Interesting Marriage. *Starch - Stärke* **2011**, *63* (7), 395–405. https://doi.org/10.1002/star.201000150.

(118) Brayer, G. D.; Sidhu, G.; Maurus, R.; Rydberg, E. H.; Braun, C.; Wang, Y.; Nguyen, N. T.; Overall, C. M.; Withers, S. G. Subsite Mapping of the Human Pancreatic α-Amylase Active Site through Structural, Kinetic, and Mutagenesis Techniques. *Biochemistry* **2000**, *39* (16), 4778–4791. https://doi.org/10.1021/bi9921182.

(119) Svensson, B. Protein Engineering in the α-Amylase Family: Catalytic Mechanism, Substrate Specificity, and Stability. *Plant Molecular Biology*. 1994, pp 141–157. https://doi.org/10.1007/BF00023233.

(120) Janeček, Š.; Svensson, B.; MacGregor, E. A. α-Amylase: An Enzyme Specificity Found in Various Families of Glycoside Hydrolases. *Cellular and Molecular Life Sciences*. 2014, pp 1149–1170. https://doi.org/10.1007/s00018-013-1388-z.

(121) Machovič, M.; Janeček, Š. The Invariant Residues in the α-Amylase Family - Just the Catalytic Triad.Pdf. *Biol. Bratislava* **2003**, *58* (6), 1127–1132.

(122) Aghajari, N.; Feller, G.; Gerday, C.; Haser, R. Structural Basis of α-Amylase Activation by Chloride. *Protein Sci.* **2002**, *11*, 1435–1441.

(123) Levitzki, A.; Steer, M. The Allosteric Activation of Mammalian α-Amylase by Chloride. *Eur. J. Biochem.* **1974**, *41*, 171–180.

(124) Qian, M.; Haser, R.; Payan, F. Carbohydrate Binding Sites in a Pancreatic A-Amylase-Substrate Complex, Derived from X-Ray Structure Analysis at 2.1Å. *Protein Sci.* **1995**, *4*, 747–755.

(125) Gilles, C.; Astier, J.-P.; Marchis-Mouren, G.; Cambillau, C.; Payan, F. Crystal

Structure of Pig Pancreatic α-Amylase Isoenzyme II, in Complex with the Carbohydrate Inhibitor Acarbose. *Eur. J. Biochem.* **1996**, *238*, 561–569.

(126) Butterworth, P. J.; Warren, F. J.; Grassby, T.; Patel, H.; Ellis, P. R. Analysis of Starch Amylolysis Using Plots for First-Order Kinetics. *Carbohydr. Polym.* **2012**, *87* (3), 2189–2197. https://doi.org/10.1016/j.carbpol.2011.10.048.

(127) Dhital, S.; Warren, F. J.; Butterworth, P. J.; Ellis, P. R.; Gidley, M. J.; Dhital, S.; Warren, F. J.; Butterworth, P. J.; Ellis, P. R. Mechanisms of Starch Digestion by α -Amylase — Structural Basis for Kinetic Properties. *Crit. Rev. Food Sci. Nutr.* **2017**, *57* (5), 875–892. https://doi.org/10.1080/10408398.2014.922043.

(128) Edwards, C. H.; Warren, F. J.; Milligan, P. J.; Butterworth, P. J.; Ellis, P. R. A Novel Method for Classifying Starch Digestion by Modelling the Amylolysis of Plant Foods Using First-Order Enzyme Kinetic Principles. *Food Funct.* **2014**, *5* (11), 2751–2758. https://doi.org/10.1039/C4FO00115J.

(129) Flint, H. J.; Scott, K. P.; Duncan, S. H.; Louis, P.; Forano, E. Microbial Degradation of Complex Carbohydrates in the Gut. *Gut Microbes* **2012**, *August*, 289–306. https://doi.org/10.4161/gmic.19897.

(130) Lockyer, S.; Nugent, A. P. Health Effects of Resistant Starch. *Nutr. Bull.* **2017**, *42* (1), 10–41. https://doi.org/10.1111/nbu.12244.

(131) Warren, F. J.; Fukuma, N. M.; Mikkelsen, D.; Flanagan, B. M.; Williams, B. A. Food Starch Structure Impacts Gut Microbiome Composition. *Am. Soc. Microbiol. Msph.* **2018**, *3* (3), 1–13.

(132) Englyst, H.; Wiggins, H. S.; Cummings, J. H. Determination of the Non-Starch

Polysaccharides in Plant Foods by Gas = Liquid Chromatography of Constituent Sugars as Alditol Acetates. **1982**, *107*, 307–318.

(133) Ashwar, B. A.; Gani, A.; Shah, A.; Wani, I. A.; Masoodi, F. A. Preparation, Health Benefits and Applications of Resistant Starch - A Review. *Starch - Stärke* **2016**, *68* (3–4), 287–301. https://doi.org/10.1002/star.201500064.

(134) Raigond, P.; Ezekiel, R.; Raigond, B. Resistant Starch in Food: A Review. *J. Sci. Food Agric.* **2015**, *95* (10), 1968–1978. https://doi.org/10.1002/jsfa.6966.

(135) Zhang, B.; Dhital, S.; Flanagan, B. M.; Gidley, M. J. Mechanism for Starch Granule Ghost Formation Deduced from Structural and Enzyme Digestion Properties. *J. Agric. Food Chem.* **2014**, *62* (3), 760–771. https://doi.org/10.1021/jf404697v.

(136) BeMiller, J. N. Pasting, Paste, and Gel Properties of Starch –Hydrocolloid Combinations. *Carbohydr. Polym.* **2011**, *86* (2), 386–423. https://doi.org/10.1016/j.carbpol.2011.05.064.

(137) Tester, R. F.; Morrison, W. R. Swelling and Gelatinization of Cereal Starches. I. Effects of Amylopectin, Amylose, and Lipids. *Cereal Chem.* **1990**, *67* (6), 551–557.

(138) Buléon, A.; Pontoire, B.; Riekel, C.; Chanzy, H.; Helbert, W.; Vuong, R. Crystalline Ultrastructure of Starch Granules Revealed by Synchrotron Radiation Microdiffraction Mapping. *Macromolecules* **1997**, *30* (13), 3952–3954. https://doi.org/10.1021/ma970136q.

(139) Perry, P. A.; Donald, A. M. The Effect of Sugars on the Gelatinisation of Starch. *Carbohydr. Polym.* **2002**, *49* (2), 155–165. https://doi.org/10.1016/S0144-

8617(01)00324-1.

(140) Liu, H.; Yu, L.; Chen, L.; Li, L. Retrogradation of Corn Starch after Thermal Treatment at Different Temperatures. *Carbohydr. Polym.* **2007**, *69* (4), 756–762. https://doi.org/10.1016/j.carbpol.2007.02.011.

(141) Tester, R. F.; Morrison, W. R. Swelling and Gelatinization of Cereal Starches. I. Effects of Amylopectin, Amylose, and Lipids. *Cereal Chem.* **1990**, *67* (6), 551–557.

(142) Fredriksson, H.; Silverio, J.; Andersson, R.; Eliasson, A.-C. C.; Åman, P. The Influence of Amylose and Amylopectin Characteristics on Gelatinization and Retrogradation Properties of Different Starches. *Carbohydr. Polym.* **1998**, *35* (3–4), 119–134. https://doi.org/10.1016/S0144-8617(97)00247-6.

(143) Russell, P. L. Gelatinisation of Starches of Different Amylose/Amylopectin Content. A Study by Differential Scanning Calorimetry. *J. Cereal Sci.* **1987**, *6* (2), 133–145. https://doi.org/10.1016/S0733-5210(87)80050-4.

(144) Morrison, W. R.; Tester, R. F.; Gidley, M. J.; Karkalas, J. Resistance to Acid Hydrolysis of Lipid-Complexed Amylose and Lipid-Free Amylose in Lintnerised Waxy and Non-Waxy Barley Starches. *Carbohydr. Res.* **1993**, *245* (2), 289–302. https://doi.org/10.1016/0008-6215(93)80078-S.

(145) Goesaert, H.; Brijs, K.; Veraverbeke, W. S.; Courtin, C. M.; Gebruers, K.; Delcour, J. A. Wheat Flour Constituents: How They Impact Bread Quality, and How to Impact Their Functionality. *Trends Food Sci. Technol.* **2005**, *16* (1–3), 12–30. https://doi.org/10.1016/j.tifs.2004.02.011.

(146) Klucinec, J. D.; Thompson, D. B. Amylose and Amylopectin Interact in Retrogradation of Dispersed High- Amylose Starches. *Cereal Chem.* **1999**, *76* (2), 282–291. https://doi.org/10.1094/CCHEM.1999.76.2.282.

(147) Kalichevsky, M. T.; Orford, P. D.; Ring, S. G. The Retrogradation and Gelation of Amylopectins from Various Botanical Sources. *Carbohydr. Res.* **1990**, *198* (1), 49–55. https://doi.org/10.1016/0008-6215(90)84275-Y.

(148) Liu, H.; Yu, L.; Xie, F.; Chen, L. Gelatinization of Cornstarch with Different Amylose/Amylopectin Content. *Carbohydr. Polym.* **2006**, *65* (3), 357–363. https://doi.org/10.1016/j.carbpol.2006.01.026.

(149) Tester, R. F. Influence of Growth Conditions on Barley.Pdf. *Int. J. Biol. Macromol.* **1997**, *21*, 37–45.

(150) Vamadevan, V.; Bertoft, E.; Seetharaman, K. On the Importance of Organization of Glucan Chains on Thermal Properties of Starch. *Carbohydr. Polym.* **2013**, *92* (2), 1653–1659. https://doi.org/10.1016/j.carbpol.2012.11.003.

(151) Tester, R. F.; Qi, X. Molecular Basis of the Gelatinisation and Swelling Characteristics of Waxy Barley Starches Grown in the Same Location during the Same Season. Part I. Composition and Alpha-Glucan Fine Structure. *J. Cereal Sci.* **2004**, *39* (1), 47–56. https://doi.org/10.1016/S0733-5210(03)00065-1.

(152) Matignon, A.; Tecante, A. Starch Retrogradation: From Starch Components to Cereal Products. *Food Hydrocoll.* **2017**, *68*, 43–52. https://doi.org/10.1016/j.foodhyd.2016.10.032.

(153) Sasaki, T.; Takeshi, Y.; Matsuki, J. Effect of Amylose Content on Gelatinization,

Retrogradation, and Pasting Properties of Starches from Waxy and Nonwaxy Wheat and Their F1 Seeds. *Cereal Chem.* **2000**, *77* (1), 58–63.

(154) Biliaderis, C. G.; Zawistowsi, J. Viscoelastic Behavior of Aging Starch Gels : Effects of Concentration, Temperature, and Starch Hydrolysates on Network Properties. *Cereal Chem.* **1990**, *67*, 240–246.

(155) Slade, L.; Levine, H. Recent Advances in Starch Retrogradation. *Ind. Polysaccharides* **1987**, No. May, 387–430.

(156) Yu, L.; Christie, G. Microstructure and Mechanical Properties of Orientated Thermoplastic Starches. *J. Mater. Sci.* **2005**, *40* (1), 111–116.

(157) Bulpin, P. V.; Gidley, M. J. Crystallisation of Malto-Oligosaccharides as Models of the Crystalline Forms of Starch: Minimum Chain-Length Requirement for Theformation of Double Helices. *Carbohydr. Res.* **1987**, *161*, 291–300.

(158) Gidley, M. J.; Cooke, D.; Darke, A. H.; Hoffmann, R. A.; Russell, A. L.; Greenwell, P. Molecular Order and Structure in Enzyme Resistant Retrograded Starch. *Carbohydr. Polym.* **1995**, *28* (95), 23–31.

(159) Tang, M. C.; Copeland, L. Investigation of Starch Retrogradation Using Atomic Force Microscopy. **2007**, *70*, 1–7. https://doi.org/10.1016/j.carbpol.2007.02.025.

(160) Leloup, V. M.; Colonna, P.; Ring, S. G. Studies on Probe Diffusion and Accessibility in Amylose Gels. *Macromolecules* **1990**, *23* (3), 862–866. https://doi.org/10.1021/ma00205a028.

(161) Leloup, V. M.; Colonna, P.; Ring, S. G.; Roberts, K.; Wells, B. Microstructure of

Amylose Gels. *Carbohydr. Polym.* **1992**, *18* (3), 189–197. https://doi.org/10.1016/0144-8617(92)90063-V.

(162) Imberty, A.; Perez, S. A Revisit to the Three-Dimensional Structure of B-Type Starch. *Biopolymers* **1988**, *27*, 1205–1221.

(163) Kalichevsky, M. T.; Ring, S. G. Incompatibility of Amylose and Amylopectin in Aqueous Solution. *Carbohydr. Res.* **1987**, *162*, 323–328.

(164) Jane, J. L.; Robyt, J. F. Structure Studies of Amylose-V Complexes and Retrograded Amylose by Action of Alpha Amylases, and a New Method for Preparing Amylodextrins. *Carbohydr. Res.* **1984**, *132* (1), 105–118. https://doi.org/10.1016/0008-6215(84)85068-5.

(165) Gong, B.; Cheng, L.; Gilbert, R. G.; Li, C. Distribution of Short to Medium Amylose Chains Are Major Controllers of in Vitro Digestion of Retrograded Rice Starch. *Food Hydrocoll.* **2019**, *96* (March), 634–643. https://doi.org/10.1016/j.foodhyd.2019.06.003.

(166) IAACC. Approved Methods of Analysis of Cereals & Grains. In *iAACC Approved Methods of Analysis of Cereals & Grains*; 2009. https://doi.org/10.1094/AACCIntMethods.

(167) Knutson, C. A. A Simplified Colorimetric Procedure for Determination of Amylose in Maize Starches. *Cereal Chemistry*. 1986, pp 89–92.

(168) Leach, H. W.; McCowen, L. D.; Scoch, T. J. Structure of Starch Granule I. Swelling and Solubility Patterns of Various Starches. *Cereal Chem.* **1959**, *36*, 534–543.

(169) Zhou, X.; Baik, B. K.; Wang, R.; Lim, S. T. Retrogradation of Waxy and Normal

Corn Starch Gels by Temperature Cycling. *J. Cereal Sci.* **2010**, *51* (1), 57–65. https://doi.org/10.1016/j.jcs.2009.09.005.

(170) Xie, Y. Y.; Hu, X. P.; Jin, Z. Y.; Xu, X. M.; Chen, H. Q. Effect of Temperature-Cycled Retrogradation on in Vitro Digestibility and Structural Characteristics of Waxy Potato Starch. *Int. J. Biol. Macromol.* **2014**, *67*, 79–84. https://doi.org/10.1016/j.ijbiomac.2014.03.007.

(171) Sopade, P. A.; Halley, P. J.; Junming, L. L. Gelatinisation of Starch in Mixtures of Sugars. II. Application of Differential Scanning Calorimetry. *Carbohydr. Polym.* **2004**, *58* (3), 311–321. https://doi.org/10.1016/j.carbpol.2004.07.007.

(172) Warren, F. J.; Perston, B. B.; Royall, P. G.; Butterworth, P. J.; Ellis, P. R. Infrared Spectroscopy with Heated Attenuated Total Internal Re Fl Ectance Enabling Precise Measurement of Thermally Induced Transitions in Complex Biological Polymers. *Anal. Chem.* **2013**, *85*, 3999–4006.

(173) Menczel, J. D.; Prime, R. B.; Gallagher, P. K.; Menczel, J. D.; Judovits, L.; Prime, R. B.; Bair, H. E.; Reading, M.; Swier, S.; Prime, R. B.; Bair, H. E.; Vyazovkin, S.; Gallagher, P. K.; Riga, A.; Bair, H. E.; Akinay, A. E.; Menczel, J. D.; Prime, R. B.; Jaffe, M.; Chartoff, R. P.; Menczel, J. D.; Dillman, S. H.; Vassilikou-Dova, A.; Kalogeras, I. M.; Gorbunov, V. V; Grandy, D.; Reading, M.; Tsukruk, V. V. *Thermal Analysis of Polymers: Fundamentals and Applications*; Menczel, J. D., Prime, R. B., Eds.; Wiley Online Books; 2008. https://doi.org/https://doi.org/10.1002/9780470423837.fmatter.

(174) Khan, S. A.; Royer, J. R.; Raghavan, R. Rheology Tools & Methods. In *Fuels with Improved Fire Safety: A Preceedings*; North Carolina, 1997; pp 31–46.

(175) Morrison, F. A. *Understanding Rheology*; Oxford University Press: Oxford, UK, 2001.

(176) Steffe, J. F. *Rheological Methods in Food Process Engineering*; Freenman Press, 1996.

(177) Marangoni, A. G.; Peyronel, M. F. *Controlled-Stress Rheometry*; 2014. https://doi.org/10.21748/lipidlibrary.40883.

(178) Dobrynin, A. V; Colby, R. H.; Rubinstein, M. Scaling Theory of Polyelectrolyte Solutions. *Macromolecules* **1995**, *28* (6), 1859–1871. https://doi.org/10.1021/ma00110a021.

(179) Dobrynin, A. V; Rubinstein, M.; Obukhov, S. P. Cascade of Transitions of Polyelectrolytes in Poor Solvents. *Macromolecules* **1996**, *29* (8), 2974–2979. https://doi.org/10.1021/ma9507958.

(180) Dobrynin, A. V; Rubinstein, M. Hydrophobic Polyelectrolytes. *Macromolecules* **1999**, *32* (3), 915–922. https://doi.org/10.1021/ma981412j.

(181) Rheology Tools & Methods, Textbook.Pdf.

(182) Yu, G.; Yan, X.; Han, C.; Huang, F. Characterization of Supramolecular Gels. *Chem. Soc. Rev.* **2013**, *42* (16), 6697. https://doi.org/10.1039/c3cs60080g.

(183) Xie, F.; Halley, P. J.; Avérous, L. Rheology to Understand and Optimize Processibility, Structures and Properties of Starch Polymeric Materials. *Prog. Polym. Sci.* **2012**, *37* (4), 595–623. https://doi.org/10.1016/j.progpolymsci.2011.07.002.

(184) Bragg, W. H.; Bragg, W. L. The Reflection of X-Rays by Crystals. *Nature* **1913**, *23* (17), 428–438.

(185) Driemeier, C.; Calligaris, G. A. Theoretical and Experimental Developments for Accurate Determination of Crystallinity of Cellulose i Materials. *J. Appl. Crystallogr.* **2011**, *44* (1), 184–192. https://doi.org/10.1107/S0021889810043955.

(186) Lopez-Rubio, A.; Flanagan, B. M.; Gilbert, E. P.; Gidley, M. J. A Novel Approach for Calculating Starch Crystallinity and Its Correlation with Double Helix Content: A Combined XRD and NMR Study. *Biopolymers* **2008**, *89* (9), 761–768. https://doi.org/10.1002/bip.21005.

(187) Lopez-Rubio, A.; Flanagan, B. M.; Gilbert, E. P.; Gidley, M. J. A Novel Approach for Calculating Starch Crystallinity and Its Correlation with Double Helix Content: A Combined XRD and NMR Study. *Biopolymers* **2008**, *89* (9), 761–768. https://doi.org/10.1002/bip.21005.

(188) Duer, M. J. *Introduction to Solid-State NMR Spectroscopy*, First Edit.; Blackwell, 2005.

(189) Keeler, J. *Understanding NMR Spectroscopy*; Springer, 2002. https://doi.org/10.1007/SpringerReference_67582.

(190) Günther, H. *NMR Spectroscopy - Basic Principles, Concepts and Applications in Chemistry*, Third Edit.; Wiley-VCH, 2013.

(191) Chapter 3 Practical Aspects of High-Resolution NMR. *High-Resolution NMR Techniques in Organic Chemistry*. Elsevier 1999, pp 45–110.

https://doi.org/https://doi.org/10.1016/S1460-1567(99)80006-3.

(192) Keshari, K. R.; Wilson, D. M. *Chemistry and Biochemistry of 13C Hyperpolarized Magnetic Resonance Using Dynamic Nuclear Polarization*; 2014; Vol. 43. https://doi.org/10.1039/c3cs60124b.

(193) Widdifield, C. M.; Schurko, R. W. Understanding Chemical Shielding Tensors Using Group Theory, MO Analysis, and Modern Density-Functional Theory. *Concepts Magn. Reson. Part A Bridg. Educ. Res.* **2009**, *34* (2), 91–123. https://doi.org/10.1002/cmr.a.20136.

(194) Forse, A. C. Nuclear Magnetic Resonance Studies of Ion Adsorption On Titanium Carbide-Derived Carbons, 2013. https://doi.org/10.1149/ma2013-02/9/674.

(195) Jochum, M.; Werner-Zwanziger, U.; Zwanziger, J. W. Observable Effects of Mechanical Stress Induced by Sample Spinning in Solid State Nuclear Magnetic Resonance. *J. Chem. Phys.* **2008**, *128* (5). https://doi.org/10.1063/1.2823130.

(196) Brus, J. Heating of Samples Induced by Fast Magic-Angle Spinning. *Solid State Nucl. Magn. Reson.* **2000**, *16* (3), 151–160. https://doi.org/10.1016/S0926-2040(00)00061-8.

(197) Chapter 4 One-Dimensional Techniques. *High-Resolution NMR Techniques in Organic Chemistry*. Elsevier 1999, pp 111–146. https://doi.org/https://doi.org/10.1016/S1460-1567(99)80007-5.

(198) Shu, J.; Li, P.; Chen, Q.; Zhang, S. Quantitative Measurement of Polymer Compositions by NMR Spectroscopy:Targeting Polymers with Marked Difference in Phase Mobility. *Macromolecules* **2010**, *43* (21), 8993–8996.

https://doi.org/10.1021/ma101711f.

(199) Courtier-Murias, D.; Farooq, H.; Longstaffe, J. G.; Kelleher, B. P.; Hart, K. M.; Simpson, M. J.; Simpson, A. J. Cross Polarization-Single Pulse/Magic Angle Spinning (CPSP/MAS): A Robust Technique for Routine Soil Analysis by Solid-State NMR. *Geoderma* **2014**, *226–227* (1), 405–414. https://doi.org/10.1016/j.geoderma.2014.03.006.

(200) Power, W. P. *High-Resolution Magic Angle Spinning-Enabling Applications of NMR Spectroscopy to Semi-Solid Phases*, 1st ed.; Elsevier Ltd., 2011; Vol. 72. https://doi.org/10.1016/B978-0-12-385857-3.00003-7.

(201) Campos E Menezes Jorge Ramalhete, S. Molecular Level Understanding of Supramolecular Gels, 2017.

(202) Claridge, T. D. W. Chapter 9 Experimental Methods. *High-Resolution NMR Techniques in Organic Chemistry*. Elsevier 1999, pp 341–372. https://doi.org/https://doi.org/10.1016/S1460-1567(99)80012-9.

(203) Claridge, T. D. W. Chapter 4 - One-Dimensional Techniques. In *High-Resolution NMR Techniques in Organic Chemistry (Third Edition)*; Claridge, T. D. W., Ed.; Elsevier: Boston, 2016; pp 133–169. https://doi.org/https://doi.org/10.1016/B978-0-08-099986-9.00004-X.

(204) Kobayashi, T.; Nishiyama, Y.; Pruski, M. Chapter 1 Heteronuclear Correlation Solid-State NMR Spectroscopy with Indirect Detection under Fast Magic-Angle Spinning. In *Modern Methods in Solid-state NMR: A Practitioner's Guide*; The Royal Society of Chemistry, 2018; pp 1–38.

https://doi.org/10.1039/9781788010467-00001.

(205) Chapter 8 Correlations through Space: The Nuclear Overhauser Effect. *High-Resolution NMR Techniques in Organic Chemistry*. Elsevier 1999, pp 277–339. https://doi.org/https://doi.org/10.1016/S1460-1567(99)80011-7.

(206) Claridge, T. D. W. Chapter 7 - Correlations Through the Chemical Bond II: Heteronuclear Shift Correlation. In *High-Resolution NMR Techniques in Organic Chemistry (Third Edition)*; Claridge, T. D. W., Ed.; Elsevier: Boston, 2016; pp 243–294. https://doi.org/https://doi.org/10.1016/B978-0-08-099986-9.00007-5.

(207) Flanagan, B. M.; Gidley, M. J.; Warren, F. J. Rapid Quantification of Starch Molecular Order through Multivariate Modelling of C-13 CP/MAS NMR Spectra. *Chem. Commun.* **2015**, *51* (80), 14856–14858. https://doi.org/10.1039/c5cc06144j.

(208) White, P. B.; Wang, T.; Park, Y. B.; Cosgrove, D. J.; Hong, M. Water − Polysaccharide Interactions in the Primary Cell Wall of Arabidopsis Thaliana from Polarization Transfer Solid-State NMR. *J. Am. Chem. Soc.* **2014**. https://doi.org/10.1021/ja504108h.

(209) Claridge, T. D. W. Chapter 2 - Introducing High-Resolution NMR. In *High-Resolution NMR Techniques in Organic Chemistry (Third Edition)*; Claridge, T. D. W., Ed.; Elsevier: Boston, 2016; pp 11–59. https://doi.org/https://doi.org/10.1016/B978-0-08-099986-9.00002-6.

(210) Ramalhete, S. M.; Nartowski, K. P.; Sarathchandra, N.; Foster, J. S.; Round, A. N.; Angulo, J.; Lloyd, G. O.; Khimyak, Y. Z. Supramolecular Amino Acid Based

Hydrogels: Probing the Contribution of Additive Molecules Using NMR Spectroscopy. *Chem. - A Eur. J.* **2017**, *23* (33), 8014–8024. https://doi.org/10.1002/chem.201700793.

(211) Viegas, A.; Manso, J.; Nobrega, F. L.; Cabrita, E. J. Saturation-Transfer Difference (STD) NMR: A Simple and Fast Method for Ligand Screening and Characterization of Protein Binding. *J. Chem. Educ.* **2011**, *88* (7), 990–994. https://doi.org/10.1021/ed101169t.

(212) Gabrielli, V.; Kuraite, A.; Alves, M.; Edler, K. J.; Nepravishta, R.; García, J. C. M.; Khimyak, Y. Z. Spin Diffusion Transfer Difference (SDTD) NMR : An Advanced Method for the Characterisation of Water Structuration within Particle Networks. *J. Colloid Interface Sci.* **2021**. https://doi.org/10.1016/j.jcis.2021.02.094.

(213) Moretti, R.; Thorson, J. S. A Comparison of Sugar Indicators Enables a Universal High-Throughput Sugar-1-Phosphate Nucleotidyltransferase Assay. *Anal. Biochem.* **2008**, *377* (2), 251–258. https://doi.org/10.1016/j.ab.2008.03.018.

(214) Minekus, M.; Alminger, M.; Alvito, P.; Ballance, S.; Bohn, T.; Bourlieu, C.; Carrière, F.; Boutrou, R.; Corredig, M.; Dupont, D.; Dufour, C.; Egger, L.; Golding, M.; Karakaya, S.; Kirkhus, B.; Le Feunteun, S.; Lesmes, U.; MacIerzanka, A.; MacKie, A.; Marze, S.; McClements, D. J.; Ménard, O.; Recio, I.; Santos, C. N.; Singh, R. P.; Vegarud, G. E.; Wickham, M. S. J.; Weitschies, W.; Brodkorb, A. A Standardised Static in Vitro Digestion Method Suitable for Food-an International Consensus. *Food Funct.* **2014**, *5* (6), 1113–1124. https://doi.org/10.1039/c3fo60702j.

(215) Orringer, D.; Lauber, F. U.; Hollander, F. Use of Dried Bovine Hemoglobin Powder in the Anson and Mirsky Methods for Pepsin and Trypsin. *Science (80-.).* **1950**, *111* (2874), 88. https://doi.org/10.1126/science.111.2874.88.

(216) Petropoulou, K.; Salt, L. J.; Edwards, C. H.; Warren, F. J.; Garcia-Perez, I.; Chambers, E. S.; Alshaalan, R.; Khatib, M.; Perez-Moral, N.; Cross, K. L.; Kellingray, L.; Stanley, R.; Koev, T.; Khimyak, Y. Z.; Narbad, A.; Penney, N.; Serrano-Contreras, J. I.; Charalambides, M. N.; Miguens Blanco, J.; Castro Seoane, R.; McDonald, J. A. K.; Marchesi, J. R.; Holmes, E.; Godsland, I. F.; Morrison, D. J.; Preston, T.; Domoney, C.; Wilde, P. J.; Frost, G. S. A Natural Mutation in Pisum Sativum L. (Pea) Alters Starch Assembly and Improves Glucose Homeostasis in Humans. *Nat. Food* **2020**, *1* (11), 693–704. https://doi.org/10.1038/s43016-020-00159-8.

(217) Williams, B. A.; Bosch, M. W.; Boer, H.; Verstegen, M. W. A.; Tamminga, S. An in Vitro Batch Culture Method to Assess Potential Fermentability of Feed Ingredients for Monogastric Diets. *Anim. Feed Sci. Technol.* **2005**, *123-124 Pa*, 445–462. https://doi.org/10.1016/j.anifeedsci.2005.04.031.

(218) Tizzotti, M. J.; Sweedman, M. C.; Tang, D.; Schaefer, C.; Gilbert, R. G. New 1H NMR Procedure for the Characterization of Native and Modified Food-Grade Starches. *J. Agric. Food Chem.* **2011**, *59* (13), 6913–6919. https://doi.org/10.1021/jf201209z.

(219) Vignoli, A.; Ghini, V.; Meoni, G.; Licari, C.; Takis, P. G.; Tenori, L.; Turano, P.; Luchinat, C. High-Throughput Metabolomics by 1D NMR. *Angew. Chemie - Int. Ed.* **2019**, *58* (4), 968–994. https://doi.org/10.1002/anie.201804736.

(220) Cave, R. A.; Seabrook, S. A.; Gidley, M. J.; Gilbert, R. G. Characterization of Starch by Size-Exclusion Chromatography: The Limitations Imposed by Shear Scission. *Biomacromolecules* **2009**, *10* (8), 2245–2253. https://doi.org/10.1021/bm900426n.

(221) Gong, B.; Cheng, L.; Gilbert, R. G.; Li, C. Distribution of Short to Medium Amylose Chains Are Major Controllers of in Vitro Digestion of Retrograded Rice Starch. *Food Hydrocoll.* **2019**, *96* (March), 634–643. https://doi.org/10.1016/j.foodhyd.2019.06.003.

(222) Tao, K.; Li, C.; Yu, W.; Gilbert, R. G.; Li, E. How Amylose Molecular Fine Structure of Rice Starch Affects Functional Properties. **2019**, *204* (October 2018), 24–31. https://doi.org/10.1016/j.carbpol.2018.09.078.

(223) Li, H.; Yu, L.; Yu, W.; Li, H.; Gilbert, R. Autoclaved Rice: The Textural Property and Its Relation to Starch Leaching and the Molecular Structure of Leached Starch. *Food Chem.* **2019**, *283* (November 2018), 199–205. https://doi.org/10.1016/j.foodchem.2019.01.030.

(224) Gilbert, R. G. Size-Separation Characterization of Starch and Glycogen for Biosynthesis-Structure-Property Relationships. *Anal. Bioanal. Chem.* **2011**, *399* (4), 1425–1438. https://doi.org/10.1007/s00216-010-4435-8.

(225) Wu, A. C.; Li, E.; Gilbert, R. G. Exploring Extraction/Dissolution Procedures for Analysis of Starch Chain-Length Distributions. *Carbohydr. Polym.* **2014**, *114*, 36–42. https://doi.org/10.1016/j.carbpol.2014.08.001.

(226) Li, H.; Prakash, S.; Nicholson, T. M.; Fitzgerald, M. A.; Gilbert, R. G. The

Importance of Amylose and Amylopectin Fine Structure for Textural Properties of Cooked Rice Grains. *Food Chem.* **2016**, *196*, 702–711. https://doi.org/10.1016/j.foodchem.2015.09.112.

(227) Vilaplana, F.; Gilbert, R. G. Characterization of Branched Polysaccharides Using Multiple-Detection Size Separation Techniques. *J. Sep. Sci.* **2010**, *33* (22), 3537–3554. https://doi.org/10.1002/jssc.201000525.

(228) Morell, M. K.; Samuel, M. S.; O'Shea, M. G. Analysis of Starch Structure Using Fluorophore-Assisted Carbohydrate Electrophoresis. *Electrophoresis* **1998**, *19* (15), 2603–2611. https://doi.org/10.1002/elps.1150191507.

(229) O'Shea, M. G.; Samuel, M. S.; Konik, C. M.; Morell, M. K. Fluorophore-Assisted Carbohydrate Electrophoresis (FACE) of Oligosaccharides: Efficiency of Labelling and High-Resolution Separation. *Carbohydr. Res.* **1998**, *307* (1–2), 1–12. https://doi.org/10.1016/S0008-6215(97)10085-4.

(230) Lourdin, D.; Valle, G. Della; Colonna, P. Influence of Amylose Content on Starch Films and Foams. *Carbohydr. Polym.* **1995**, *27* (4), 261–270. https://doi.org/10.1016/0144-8617(95)00071-2.

(231) Patindol, J.; Gu, X.; Wang, Y.-J. Chemometric Analysis of the Gelatinization and Pasting Properties of Long-grain Rice Starches in Relation to Fine Structure.Pdf. *Starch - Stärke* **2009**, *61*, 3–11.

(232) Pérez, S.; Bertoft, E. The Molecular Structures of Starch Components and Their Contribution to the Architecture of Starch Granules: A Comprehensive Review. *Starch/Staerke* **2010**, *62* (8), 389–420. https://doi.org/10.1002/star.201000013.

(233) Us, F.; Gonenc, I.; Kibar, A.; Aytunga, E. . Gelatinization of Waxy , Normal and High Amylose Corn Starches. *J. Food* **2010**, *35*, 237–244.

(234) Donovan, J. W. Phase Transitions of the Starch–Water System. *Biopolymers* **1979**, *18* (2), 263–275.

(235) Liu, H.; Yu, L.; Simon, G.; Dean, K.; Chen, L. Effects of Annealing on Gelatinization and Microstructures of Corn Starches with Different Amylose/Amylopectin Ratios. *Carbohydr. Polym.* **2009**, *77* (3), 662–669. https://doi.org/10.1016/j.carbpol.2009.02.010.

(236) Waigh, T. A.; Gidley, M. J.; Komanshek, B. U.; Donald, A. M. The Phase Transformations in Starch during Gelatinisation: A Liquid Crystalline Approach. *Carbohydr. Res.* **2000**, *328* (2), 165–176. https://doi.org/10.1016/S0008-6215(00)00098-7.

(237) White, P. J.; Abbas, I. R.; Johnson, L. A. Freeze-Thaw Stability and Refrigerated-Storage Retrogradation of Starches. *Starch - Stärke* **1989**, *41* (5), 176–180. https://doi.org/10.1002/star.19890410505.

(238) Wronkowska, M.; Soral-Smietana, M.; Komorowska-Czepirska, E.; Lewandowicz, G. Thermal and Water Sorption Isotherm Characteristics of Starch Preparations with High Content of Resistant Starch. In *Starch: From polysaccharides to granules, simple and mixture gels*; 2004; pp 105–118.

(239) Leloup, V. M.; Colonna, P.; Ring, S. G.; Roberts, K.; Wells, B. Microstructure of Amylose Gels. *Carbohydr. Polym.* **1992**, *18* (3), 189–197. https://doi.org/10.1016/0144-8617(92)90063-V.

(240) Putseys, J. A.; Lamberts, L.; Delcour, J. A. Amylose-Inclusion Complexes: Formation, Identity and Physico-Chemical Properties. *J. Cereal Sci.* **2010**, *51* (3), 238–247. https://doi.org/10.1016/j.jcs.2010.01.011.

(241) Zhou, Y.; Hoover, R.; Liu, Q. Relationship between α-Amylase Degradation and the Structure and Physicochemical Properties of Legume Starches. *Carbohydrate Polymers*. 2004, pp 299–317. https://doi.org/10.1016/j.carbpol.2004.05.010.

(242) Błaszczak, W.; Fornal, J.; Kiseleva, V. I.; Yuryev, V. P.; Sergeev, A. I.; Sadowska, J. Effect of High Pressure on Thermal, Structural and Osmotic Properties of Waxy Maize and Hylon VII Starch Blends. *Carbohydr. Polym.* **2007**, *68* (3), 387–396. https://doi.org/10.1016/j.carbpol.2006.12.023.

(243) Fredriksson, H.; Silverio, J.; Andersson, R.; Eliasson, A. C.; Åman, P. The Influence of Amylose and Amylopectin Characteristics on Gelatinization and Retrogradation Properties of Different Starches. *Carbohydr. Polym.* **1998**, *35* (3–4), 119–134. https://doi.org/10.1016/S0144-8617(97)00247-6.

(244) Park, E. Y.; Baik, B. K.; Lim, S. T. Influences of Temperature-Cycled Storage on Retrogradation and in Vitro Digestibility of Waxy Maize Starch Gel. *J. Cereal Sci.* **2009**, *50* (1), 43–48. https://doi.org/10.1016/j.jcs.2009.02.004.

(245) Burchard, W. M.; Ross-Murphy, S. B. *Physical Networks. Polymers and Gels*; Burchard, W., Ross-Murphy, S. B., Eds.; Elsevier Applied Science: London; New York;, 1990.

(246) Almdal, K.; Dyre, J.; Hvidt, S.; Kramer, O. Towards a Phenomenological Definition of the Term "Gel." *Polym. Gels Networks* **1993**, *1* (1), 5–17.

https://doi.org/10.1016/0966-7822(93)90020-I.

(247) Van Den Bulcke, A. I.; Bogdanov, B.; De Rooze, N.; Schacht, E. H.; Cornelissen, M.; Berghmans, H. Structural and Rheological Properties of Methacrylamide Modified Gelatin Hydrogels. *Biomacromolecules* **2000**, *1* (1), 31–38. https://doi.org/10.1021/bm990017d.

(248) Franck, A. J. Understanding Rheology of Structured Fluids. *B. TA instruments* **2004**, 1–11.

(249) Chartoff, R. P.; Menczel, J. D.; Dillman, S. H. Dynamic Mechanica Analysis. In *Thermal Analysis of Polymers: Fundamentals and Applications*; Wiley, 2009.

(250) Harrats, C. *Multiphase Polymer-Based Materials - An Atlas of Phase Morphology at the Nano & Micro Scale*; 2009.

(251) Xie, F.; Yu, L.; Su, B.; Liu, P.; Wang, J.; Liu, H.; Chen, L. Rheological Properties of Starches with Different Amylose/Amylopectin Ratios. *J. Cereal Sci.* **2009**, *49* (3), 371–377. https://doi.org/10.1016/j.jcs.2009.01.002.

(252) Lewen, K. S.; Paeschke, T.; Reid, J.; Molitor, P.; Schmidt, S. J.; Ewen, K. E. S. L.; Aeschke, T. E. R. I. P.; Eid, J. O. R.; Olitor, P. A. U. L. M.; Chmidt, S. H. J. S.; Lewen, K. S.; Paeschke, T.; Reid, J.; Molitor, P.; Schmidt, S. J. Analysis of the Retrogradation of Low Starch Concentration Gels Using Differential Scanning Calorimetry, Rheology, and Nuclear Magnetic Resonance Spectroscopy. *J. Agric. Food Chem.* **2003**, *51* (8), 2348–2358. https://doi.org/10.1021/jf020866j.

(253) Hoover, R. Starch Retrogradation. *Food Rev. Int.* **1995**, *11* (2), 331–346. https://doi.org/10.1080/87559129509541044.

(254) Amiri, F.; Kabiri, K.; Bouhendi, H.; Abdollahi, H.; Najafi, V.; Karami, Z. High Gel-Strength Hybrid Hydrogels Based on Modified Starch through Surface Cross-Linking Technique. *Polym. Bull.* **2018**, *76*, 4047–4068.

(255) Gong, B.; Cheng, L.; Gilbert, R. G.; Li, C. Distribution of Short to Medium Amylose Chains Are Major Controllers of in Vitro Digestion of Retrograded Rice Starch. *Food Hydrocoll.* **2019**, *96* (March), 634–643. https://doi.org/10.1016/j.foodhyd.2019.06.003.

(256) Wenwen, Y.; Tao, K.; Gidley, M. J.; Fox, G. P.; Gilbert, R. G.; Wenwen, Y.; Fox, G. P.; Gidley, M. J. Molecular Brewing: Molecular Structural Effects Involved in Barley Malting and Mashing. *Carbohydr. Polym.* **2018**, *206* (September 2018), 583–592. https://doi.org/10.1016/j.carbpol.2018.11.018.

(257) Tao, K.; Li, C.; Yu, W.; Gilbert, R. G.; Li, E. How Amylose Molecular Fine Structure of Rice Starch Affects Functional Properties. *Carbohydr. Polym.* **2019**, *204* (July 2018), 24–31. https://doi.org/10.1016/j.carbpol.2018.09.078.

(258) Cave, R. A.; Seabrook, S. A.; Gidley, M. J.; Gilbert, R. G. Characterization of Starch by Size-Exclusion Chromatography: The Limitations Imposed by Shear Scission. *Biomacromolecules* **2009**, *10* (8), 2245–2253. https://doi.org/10.1021/bm900426n.

(259) Liu, Y.; Xie, H.; Shi, M. Effect of Ethanol–Water Solution on the Crystallization of Short Chain Amylose from Potato Starch. *Starch - Stärke* **2016**, *68* (7–8), 683–690. https://doi.org/10.1002/star.201500300.

(260) Jayakody, L.; Hoover, R. Effect of Annealing on the Molecular Structure and

Physicochemical Properties of Starches from Different Botanical Origins - A Review. *Carbohydr. Polym.* **2008**, *74* (3), 691–703. https://doi.org/10.1016/j.carbpol.2008.04.032.

(261) Tester, R. F.; Debon, S. J. J.; Sommerville, M. D. Annealing of Maize Starch. *Carbohydr. Polym.* **2000**, *42* (3), 287–299. https://doi.org/10.1016/S0144-8617(99)00170-8.

(262) Gidley, M. J.; Bociek, S. M. Molecular Organization in Starches: A Carbon 13 CP/MAS NMR Study. *J. Am. Chem. Soc.* **1985**, *107* (24), 7040–7044. https://doi.org/10.1021/ja00310a047.

(263) Tan, I.; Flanagan, B. M.; Halley, P. J.; Whittaker, A. K.; Gidley, M. J. A Method for Estimating the Nature and Relative Proportions of Amorphous, Single, and Doubled-Helical Components in Starch Granules by 13C CP/MAS NMR. *Biomacromolecules* **2007**, *8* (3), 885–891. https://doi.org/10.1021/bm060988a.

(264) Poulhazan, A.; Arnold, A. A.; Warschawski, D. E.; Marcotte, I. Unambiguous Ex Situ and in Cell 2D 13 C Solid-State Nmr Characterization of Starch and Its Constituents. *Int. J. Mol. Sci.* **2018**, *19* (12). https://doi.org/10.3390/ijms19123817.

(265) Tang, H.; Hills, B. P. Use of 13C MAS NMR to Study Domain Structure and Dynamics of Polysaccharides in the Native Starch Granules. *Biomacromolecules* **2003**, *4* (5), 1269–1276. https://doi.org/10.1021/bm0340772.

(266) Baik, M.-Y. Y.; Dickinson, L. C.; Chinachoti, P. Solid-State 13C CP/MAS NMR Studies on Aging of Starch in White Bread. *J. Agric. Food Chem.* **2003**, *51* (5),

1242–1248. https://doi.org/10.1021/jf025776t.

(267) Baik, M. Y.; Dickinson, L. C.; Chinachoti, P. Solid-State 13C CP/MAS NMR Studies on Aging of Starch in White Bread. *J. Agric. Food Chem.* **2003**, *51* (5), 1242–1248. https://doi.org/10.1021/jf025776t.

(268) Tsukiashi, A.; Min, K. S.; Kitayama, H.; Terasawa, H.; Yoshinaga, S.; Takeda, M.; Lindoy, L. F.; Hayami, S. Application of Spin-Crossover Water Soluble Nanoparticles for Use as MRI Contrast Agents. *Sci. Rep.* **2018**, *8* (1), 6–11. https://doi.org/10.1038/s41598-018-33362-6.

(269) Larsen, F. H.; Blennow, A.; Engelsen, S. B. Starch Granule Hydration-A MAS NMR Investigation. *Food Biophys.* **2008**, *3* (1), 25–32. https://doi.org/10.1007/s11483-007-9045-4.

(270) Colquhoun, I. J.; Parker, R.; Ring, S. G.; Sun, L.; Tang, H. R. An NMR Spectroscopic Characterisation of the Enzyme-Resistant Residue from α-Amylolysis of an Amylose Gel. *Carbohydr. Polym.* **1995**, *27* (4), 255–259. https://doi.org/10.1016/0144-8617(95)00085-2.

(271) Leloup, V. M.; Colonna, P.; Ring, S. G.; Roberts, K.; Wells, B. Microstructure of Amylose Gels. *Carbohydr. Polym.* **1992**, *18* (3), 189–197. https://doi.org/10.1016/0144-8617(92)90063-V.

(272) Williams, J. K.; Hong, M. Probing Membrane Protein Structure Using Water Polarization Transfer Solid-State NMR. *J. Magn. Reson.* **2014**, *247*, 118–127. https://doi.org/10.1016/j.jmr.2014.08.007.

(273) Huang, R.-M.; Chang, W.-H.; Chang, Y.-H.; Lii., C.-Y. Phase Transitions of Rice

Starch and Flour Gels. *Cereal Chemistry*. 1994, pp 202–207.

(274) Leloup, V. M.; Colonna, P.; Ring, S. G.; Roberts, K.; Wells, B. Microstructure of Amylose Gels. *Carbohydr. Polym.* **1992**, *18* (3), 189–197. https://doi.org/10.1016/0144-8617(92)90063-V.

(275) Amidon, S.; Brown, J. E.; Dave, V. S. Colon-Targeted Oral Drug Delivery Systems: Design Trends and Approaches. *AAPS PharmSciTech* **2015**, *16* (4), 731–741. https://doi.org/10.1208/s12249-015-0350-9.

(276) Peppas, N. A., Bures, P. Leobandung, W. Ichikawa, H. Hydrogel In Pharmaceutical Formulations. *Eur. J. Pharm. Biopharm.* **2000**, *50*, 27–46. https://doi.org/10.16953/deusbed.74839.

(277) Rocha-García, D.; Guerra-Contreras, A.; Rosales-Mendoza, S.; Palestino, G. Role of Porous Silicon/Hydrogel Composites on Drug Delivery. *Mesoporous Biomater* **2016**, *3* (1), 93–101. https://doi.org/10.1515/mesbi-2016-0011.

(278) Varum, F.; Freire, A. C.; Bravo, R.; Basit, A. W. OPTICORE ™ , an Innovative and Accurate Colonic Targeting Technology. *Int. J. Pharm.* **2020**, *583* (February), 119372. https://doi.org/10.1016/j.ijpharm.2020.119372.

(279) Thakral, S.; Thakral, N. K.; Majumdar, D. K. Eudragit®: A Technology Evaluation. *Expert Opin. Drug Deliv.* **2013**, *10* (1), 131–149. https://doi.org/10.1517/17425247.2013.736962.

(280) Bisharat, L.; Barker, S. A.; Narbad, A.; Craig, D. Q. M. In Vitro Drug Release from Acetylated High Amylose Starch-Zein Films for Oral Colon-Specific Drug Delivery. *Int. J. Pharm.* **2019**, *556* (October 2018), 311–319.

https://doi.org/10.1016/j.ijpharm.2018.12.021.

(281) Englyst, H. N.; Kingman, S. M.; Cummings, J. H. Classification and Measurement of Nutritionally Important Starch Fractions. *Eur. J. Clin. Nutr.* **1992**, *46* (2), 30–50.

(282) Edwards, C. H.; Grundy, M. M. L.; Grassby, T.; Vasilopoulou, D.; Frost, G. S.; Butterworth, P. J.; Berry, S. E. E.; Sanderson, J.; Ellis, P. R. Manipulation of Starch Bioaccessibility in Wheat Endosperm to Regulate Starch Digestion, Postprandial Glycemia, Insulinemia, and Gut Hormone Responses: A Randomized Controlled Trial in Healthy Ileostomy Participants. *Am. J. Clin. Nutr.* **2015**, *102* (4), 791–800. https://doi.org/10.3945/ajcn.114.106203.

(283) Silvester, K. R.; Englyst, H. N.; Cummings, J. H. Ileal Recovery of Starch from Whole Diets Containing Resistant Starch Measured in Vitro and Fermentation of Ileal Effluent. *Am. J. Clin. Nutr.* **1995**, *62* (2), 403–411. https://doi.org/10.1093/ajcn/62.2.403.

(284) Topping, D. L.; Clifton, P. M. Short-Chain Fatty Acids and Human Colonic Function: Roles of Resistant Starch and Nonstarch Polysaccharides. *Physiol. Rev.* **2001**, *81* (3), 1031–1064. https://doi.org/10.1152/physrev.2001.81.3.1031.

(285) Ze, X.; Duncan, S. H.; Louis, P.; Flint, H. J. Ruminococcus Bromii Is a Keystone Species for the Degradation of Resistant Starch in the Human Colon. *ISME J.* **2012**, *6* (8), 1535–1543. https://doi.org/10.1038/ismej.2012.4.

(286) Le Leu, R. K.; Brown, I. L.; Hu, Y.; Morita, T.; Esterman, A.; Young, G. P. Effect of Dietary Resistant Starch and Protein on Colonic Fermentation and Intestinal Tumourigenesis in Rats. *Carcinogenesis* **2007**, *28* (2), 240–245.

https://doi.org/10.1093/carcin/bgl245.

(287) Deo, P. N.; Deshmukh, R. Oral Microbiome: Unveiling the Fundamentals. *J. oral Maxillofac. Pathol.* **2017**, *21* (3), 244–251. https://doi.org/10.4103/jomfp.JOMFP.

(288) Martinez-guryn, K.; Hubert, N.; Frazier, K.; Urlass, S.; Mark, W.; Ojeda, P.; Pierre, J. F.; Miyoshi, J.; Sontag, T.; Cham, C.; Reardon, C.; Leone, V.; Chang, E. B. Small Intestine Microbiota Regulate Host Digestive and Absorptive Adaptive Responses to Dietary Lipids. *Cell Host Microbe* **2019**, *23* (4), 458–469. https://doi.org/10.1016/j.chom.2018.03.011.Small.

(289) Kaoutari, A. El; Armougom, F.; Gordon, J. I.; Raoult, D.; Henrissat, B. The Abundance and Variety of Carbohydrate-Active Enzymes in the Human Gut Microbiota. *Nat. Rev. Microbiol.* **2013**, *11* (7), 497–504. https://doi.org/10.1038/nrmicro3050.

(290) Cerf-Bensussan, N.; Gaboriau-Routhiau, V. The Immune System and the Gut Microbiota: Friends or Foes? *Nat. Rev. Immunol.* **2010**, *10* (10), 735–744. https://doi.org/10.1038/nri2850.

(291) Durica-Mitic, S.; Göpel, Y.; Görke, B. Carbohydrate Utilization in Bacteria: Making the Most Out of Sugars with the Help of Small Regulatory RNAs. *Regul. with RNA Bact. Archaea* **2018**, No. 1, 229–248. https://doi.org/10.1128/9781683670247.ch14.

(292) Purchiaroni, F.; Tortora, A.; Gabrielli, M.; Bertucci, F.; Gigante, G.; Ianiro, G.; Ojetti, V.; Scarpellini, E.; Gasbarrini, A. The Role of Intestinal Microbiota and the

Immune System. *Eur. Rev. Med. Pharmacol. Sci.* **2013**, *17* (3), 323–333.

(293) Cryan, J. F.; O'Mahony, S. M. The Microbiome-Gut-Brain Axis: From Bowel to Behavior. *Neurogastroenterol. Motil.* **2011**, *23* (3), 187–192. https://doi.org/10.1111/j.1365-2982.2010.01664.x.

(294) Ze, X.; David, Y. Ben; Laverde-Gomez, J. A.; Dassa, B.; Sheridan, P. O.; Duncan, S. H.; Louis, P.; Henrissat, B.; Juge, N.; Koropatkin, N. M.; Bayer, E. A.; Flint, H. J. Unique Organization of Extracellular Amylases into Amylosomes in the Resistant Starch-Utilizing Human Colonic Firmicutes Bacterium Ruminococcus Bromii. *MBio* **2015**, *6* (5), 1–11. https://doi.org/10.1128/mbio.01058-15.

(295) Reeves, A. R.; D'Elia, J. N.; Frias, J.; Salyers, A. A. A Bacteroides Thetaiotaomicron Outer Membrane Protein That Is Essential for Utilization of Maltooligosaccharides and Starch. *J. Bacteriol.* **1996**, *178* (3), 823–830. https://doi.org/10.1128/jb.178.3.823-830.1996.

(296) Souliman, S.; Beyssac, E.; Cardot, J. M.; Denis, S.; Alric, M. Investigation of the Biopharmaceutical Behavior of Theophylline Hydrophilic Matrix Tablets Using Usp Methods and an Artificial Digestive System. *Drug Dev. Ind. Pharm.* **2007**, *33* (4), 475–483. https://doi.org/10.1080/03639040601128654.

(297) Williams, C. F.; Walton, G. E.; Jiang, L.; Plummer, S.; Garaiova, I.; Gibson, G. R. Comparative Analysis of Intestinal Tract Models. *Annu. Rev. Food Sci. Technol.* **2015**, *6* (14). https://doi.org/10.1146/annurev-food-022814-015429.

(298) Namazi, H.; Fathi, F.; Dadkhah, A. Hydrophobically Modified Starch Using Long-Chain Fatty Acids for Preparation of Nanosized Starch Particles. *Sci. Iran.* **2011**,

18 (3 C), 439–445. https://doi.org/10.1016/j.scient.2011.05.006.

(299) Le Gall, G.; Noor, S. O.; Ridgway, K.; Scovell, L.; Jamieson, C.; Johnson, I. T.; Colquhoun, I. J.; Kemsley, E. K.; Narbad, A. Metabolomics of Fecal Extracts Detects Altered Metabolic Activity of Gut Microbiota in Ulcerative Colitis and Irritable Bowel Syndrome. *J. Proteome Res.* **2011**, *10* (9), 4208–4218. https://doi.org/10.1021/pr2003598.

(300) Bao, C.; Jiang, P.; Chai, J.; Jiang, Y.; Li, D.; Bao, W.; Liu, B.; Liu, B.; Norde, W.; Li, Y. The Delivery of Sensitive Food Bioactive Ingredients: Absorption Mechanisms, Influencing Factors, Encapsulation Techniques and Evaluation Models. *Food Res. Int.* **2019**, *120*, 130–140. https://doi.org/10.1016/j.foodres.2019.02.024.

(301) Minhas, M. U.; Ahmad, M.; Anwar, M.; Khan, S. Synthesis and Characterization of Biodegradable Hydrogels for Oral Delivery of 5- Fluorouracil Targeted to Colon: Screening with Preliminary. *Adv. Polym. Technol.* **2016**, *37* (1), 221–229. https://doi.org/10.1002/adv.21659.

(302) Gulbake, A.; Jain, A.; Jain, A.; Jain, A.; Jain, S. K. Insight to Drug Delivery Aspects for Colorectal Cancer. *World J. Gastroenterol.* **2016**, *22* (2), 582–599. https://doi.org/10.3748/wjg.v22.i2.582.

(303) Tao, K.; Li, C.; Yu, W.; Gilbert, R. G.; Li, E. How Amylose Molecular Fine Structure of Rice Starch Affects Functional Properties. *Carbohydr. Polym.* **2019**, *204*, 24–31. https://doi.org/10.1016/j.carbpol.2018.09.078.

(304) Fredriksson, H.; Silverio, J.; Andersson, R.; Eliasson, A.-C.; Åman, P. The Influence of Amylose and Amylopectin Characteristics on Gelatinization and

Retrogradation Properties of Different Starches. *Carbohydr. Polym.* **1998**, *35* (3–4), 119–134. https://doi.org/10.1016/S0144-8617(97)00247-6.

(305) Peppas, N. A.; Bures, P.; Leobandung, W.; Ichikawa, H. Hydrogels in Pharmaceutical Formulations. *Eur. J. Pharm. Biopharm.* **2000**, *50* (1), 27–46. https://doi.org/10.1016/S0939-6411(00)00090-4.

(306) Koetting, M. C.; Peters, J. T.; Steichen, S. D.; Peppas, N. A. Stimulus-Responsive Hydrogels: Theory, Modern Advances, and Applications. *Mater. Sci. Eng. R Reports* **2015**, *93*, 1–49. https://doi.org/10.1016/j.mser.2015.04.001.

(307) Philip, A.; Philip, B. Colon Targeted Drug Delivery Systems: A Review on Primary and Novel Approaches. *Oman Med. J.* **2010**, *25* (2), 70–78. https://doi.org/10.5001/omj.2010.24.

(308) Witt, T.; Gidley, M. J.; Gilbert, R. G. Starch Digestion Mechanistic Information from the Time Evolution of Molecular Size Distributions. *J. Agric. Food Chem.* **2010**, *58* (14), 8444–8452. https://doi.org/10.1021/jf101063m.

(309) Clark, A. H.; Gidley, M. J.; Richardson, R. K.; Ross-murphy, S. B. Rheological Studies of Aqueous Amylose Gels : The Effect of Chain Length and Concentration on Gel Modulus. *Macromolecules* **1989**, *351* (29), 346–351. https://doi.org/10.1021/ma00191a063.

(310) Butterworth, P. J.; Warren, F. J.; Ellis, P. R. Human α-Amylase and Starch Digestion: An Interesting Marriage. *Starch/Staerke* **2011**, *63* (7), 395–405. https://doi.org/10.1002/star.201000150.

(311) Barrangou, R.; Azcarate-Peril, M. A.; Duong, T.; Conners, S. B.; Kelly, R. M.;

Klaenhammer, T. R. Global Analysis of Carbohydrate Utilization by Lactobacillus Acidophilus Using CDNA Microarrays. *Proc. Natl. Acad. Sci. U. S. A.* **2006**, *103* (10), 3816–3821. https://doi.org/10.1073/pnas.0511287103.

(312) Vashist, A.; Vashist, A.; Gupta, Y. K.; Ahmad, S. Recent Advances in Hydrogel Based Drug Delivery Systems for the Human Body. *J. Mater. Chem. B* **2014**, *2* (2), 147–166. https://doi.org/10.1039/C3TB21016B.

(313) Jacobs, D.M., Deltimple, N., van Velzen, E., van Dorsten, F.A., Bingham, M., Vaughan, E.E., van Duynhoven, J. 1H NMR Metabolite Profiling of Feces as a Tool to Assess the Impact of Nutrition on the Human Microbiome. *NMR Biomed.* **2008**, *21* (3), 615–626. https://doi.org/10.1002/nbm.

(314) Chaichi, M.; Hashemi, M.; Badii, F.; Mohammadi, A. Preparation and Characterization of a Novel Bionanocomposite Edible Film Based on Pectin and Crystalline Nanocellulose. *Carbohydr. Polym.* **2017**, *157*, 167–175. https://doi.org/10.1016/j.carbpol.2016.09.062.

(315) Sintov, A.; Di-Capua, N.; Rubinstein, A. Cross-Linked Chondroitin Sulphate: Characterization for Drug Delivery Purposes. *Biomaterials* **1995**, *16* (6), 473–478. https://doi.org/10.1016/0142-9612(95)98820-5.

(316) Phan, V. H. G.; Trang Duong, H. T.; Tran, P. T.; Thambi, T.; Ho, D. K.; Murgia, X. Self-Assembled Amphiphilic Starch Based Drug Delivery Platform: Synthesis, Preparation, and Interactions with Biological Barriers. *Biomacromolecules* **2021**, *22* (2), 572–585. https://doi.org/10.1021/acs.biomac.0c01430.

(317) Rujivipat, S.; Bodmeier, R. Modified Release from Hydroxypropyl

Methylcellulose Compression-Coated Tablets. *Int. J. Pharm.* **2010**, *402* (1–2), 72–77. https://doi.org/10.1016/j.ijpharm.2010.09.021.

(318) Tu, H.; Qu, Y.; Hu, X.; Yin, Y.; Zheng, H.; Xu, P.; Xiong, F. Study of the Sigmoidal Swelling Kinetics of Carboxymethylchitosan-g-Polyacrylic Acid Hydrogels Intended for Colon-Specific Drug Delivery. *Carbohydr. Polym.* **2010**, *82*, 440–445. https://doi.org/10.1016/j.carbpol.2010.04.086.

(319) Rujivipat, S.; Bodmeier, R. Modified Release from Hydroxypropyl Methylcellulose Compression-Coated Tablets. *Int. J. Pharm.* **2010**, *402* (1–2), 72–77. https://doi.org/10.1016/j.ijpharm.2010.09.021.

(320) Lesmes, U.; Julian, D. Structure e Function Relationships to Guide Rational Design and Fabrication of Particulate Food Delivery Systems. *Trends Food Sci. Technol.* **2009**, *20* (10), 448–457. https://doi.org/10.1016/j.tifs.2009.05.006.

(321) Rodell, C. B.; Mealy, J. E.; Burdick, J. A. Supramolecular Guest-Host Interactions for the Preparation of Biomedical Materials. *Bioconjug. Chem.* **2015**, *26* (12), 2279–2289. https://doi.org/10.1021/acs.bioconjchem.5b00483.

(322) Agüero, L.; Zaldivar-Silva, D.; Peña, L.; Dias, M. Alginate Microparticles as Oral Colon Drug Delivery Device: A Review. *Carbohydr. Polym.* **2017**, *168*, 32–43. https://doi.org/10.1016/j.carbpol.2017.03.033.

(323) Rubinstein, A.; Radai, R.; Ezra, M.; Pathak, S.; Rokem, J. S. In Vitro Evaluation of Calcium Pectinate: A Potential Colon-Specific Drug Delivery Carrier. *Pharmaceutical Research: An Official Journal of the American Association of Pharmaceutical Scientists*. 1993, pp 258–263.

https://doi.org/10.1023/A:1018995029167.

(324) Cotter, P.; Lopez-Exposito, I.; Kleiveland, C.; Lea, T.; Mackie, A.; Requena, T.; Swiatecka, D.; Witchers, H. *The Impact of Food Bioactives on Health*; Cotter, P., Kleiveland, C., Mackie, A., Swiatecka, D., Eds.; 2015. https://doi.org/10.1007/978-3-319-16104-4.

(325) Den Besten, G.; Van Eunen, K.; Groen, A. K.; Venema, K.; Reijngoud, D. J.; Bakker, B. M. The Role of Short-Chain Fatty Acids in the Interplay between Diet, Gut Microbiota, and Host Energy Metabolism. *J. Lipid Res.* **2013**, *54* (9), 2325–2340. https://doi.org/10.1194/jlr.R036012.

(326) Kalantar-Zadeh, K.; Berean, K. J.; Burgell, R. E.; Muir, J. G.; Gibson, P. R. Intestinal Gases: Influence on Gut Disorders and the Role of Dietary Manipulations. *Nat. Rev. Gastroenterol. Hepatol.* **2019**, *16* (December), 733–747. https://doi.org/10.1038/s41575-019-0193-z.

(327) Ohman, L.; Simren, M. New Insights into the Pathogenesis and Pathophysiology of Irritable Bowel Syndrome. *Dig. Liver Dis.* **2006**, *39*, 201–215. https://doi.org/10.1016/j.dld.2006.10.014.

(328) Callaghan, A. O.; Sinderen, D. Van. Bifidobacteria and Their Role as Members of the Human Gut Microbiota. *Front.* **2016**, *7* (June). https://doi.org/10.3389/fmicb.2016.00925.

(329) Lawson, M. A. E.; Neill, I. J. O.; Kujawska, M.; Wijeyesekera, A.; Flegg, Z.; Chalken, L.; Hall, L. J. Infant Diet Promotes Bifidobacterium Community Cooperation within a Single Ecosystem . *bioRXiv* **2019**, *July*, 1–42.

https://doi.org/https://doi.org/10.1101/711234.

(330) Phan, V. H. G.; Thuy, H.; Duong, T.; Tran, P.; Thambi, T.; Ho, D.; Murgia, X. Self-Assembled Amphiphilic Starch Based Drug Delivery Platform : Synthesis , Preparation , and Interactions with Biological Barriers. **2020**. https://doi.org/10.1021/acs.biomac.0c01430.

(331) Katz, J.; van Itallie, T. Alle Starkearten Haben Das Gleiche Retrogradationsspektrum. *Z. Phys. Chem.* **1930**, *150*, 90–99.

(332) Rundle, R. E.; Edwards, F. C. The Configuration of Starch in the Starch-Iodine Complex. IV. An X-Ray Diffraction Investigation of Butanol-Precipitated Amylose. *J. Am. Chem. Soc.* **1943**, *65* (5), 2200–2203.

(333) French, A. Allowed and Preferred Shapes of Amylose. *Bak. Dig.* **1979**, *53* (1), 39–46.

(334) Le, C. A. K.; Choisnard, L.; Wouessidjewe, D.; Putaux, J. L. Single Crystals of V-Amylose Complexed with Bicyclic Organic Compounds. *Macromol. Symp.* **2019**, *386* (1), 1–7. https://doi.org/10.1002/masy.201900007.

(335) Gotanda, R.; Yamamoto, K.; Kadokawa, J. I. Amylose Stereoselectively Includes Poly(d-Alanine) to Form Inclusion Complex in Vine-Twining Polymerization A Novel Saccharide–Peptide Supramolecular Conjugate. *Macromol. Chem. Phys.* **2016**, *217* (9), 1074–1080.

(336) Kadokawa, J. I.; Kaneko, Y.; Nagase, S. I.; Takahashi, T.; Tagaya, H. Vine-Twining Polymerization: Amylose Twines around Polyethers to Form Amylose-Polyether Inclusion Complexes. *Chem. - A Eur. J.* **2002**, *8* (15), 3321–3326.

https://doi.org/10.1002/1521-3765(20020802)8:15<3321::AID-CHEM3321>3.0.CO;2-E.

(337) Anh, C.; Le, K. Inclusion Complexes of Amylose: Morphogenesis, Crystal Structure and Release of Bioactive Molecules, 2019.

(338) Le, C. A. K.; Choisnard, L.; Wouessidjewe, D.; Putaux, J. L. Polymorphism of V-Amylose Cocrystallized with Aliphatic Diols. *Polymer (Guildf).* **2021**, *213* (December 2020), 123302. https://doi.org/10.1016/j.polymer.2020.123302.

(339) Putaux, J. L.; Cardoso, M. B.; Dupeyre, D.; Morin, M.; Nulac, A.; Yang, H. Single Crystals of V-Amylose Inclusion Complexes. *Macromol. Symp.* **2008**, *273* (1), 1–8. https://doi.org/10.1002/masy.200851301.

(340) Anh, C.; Le, K.; Ogawa, Y.; Grimaud, F.; Mazeau, K.; Ziegler, G. R.; Tanwar, S.; Nishiyama, Y.; Potocki-veronese, G.; Choisnard, L.; Wouessidjewe, D.; Putaux, J. Crystal and Molecular Structure of V-Amylose Complexed with Ibuprofen. *Carbohydr. Polym.* **2021**, *261* (February). https://doi.org/10.1016/j.carbpol.2021.117885.

(341) Cardoso, M. B.; Putaux, J. L.; Nishiyama, Y.; Helbert, W.; Hÿtch, M.; Silveira, N. P.; Chanzy, H. Single Crystals of V-Amylose Complexed with α-Naphthol. *Biomacromolecules* **2007**, *8* (4), 1319–1326. https://doi.org/10.1021/bm0611174.

(342) Rutschmann, M. A.; Solms, J. Formation of Inclusion Complexes of Starch with Different Organic Compounds. IV, Ligand Binding and Variability in Helical Conformations of V Amylose Complexes. *Food Sci. Technol.* **1990**, *23* (1), 84–87.

(343) Kasemwong, K.; Itthisoponkul, T. Encapsulation of Flavor Compounds as Helical Inclusion Complexes of Starch. *ACS Symp. Ser.* **2013**, *1143*, 235–245. https://doi.org/10.1021/bk-2013-1143.ch014.

(344) Conde-Petit, B.; Escher, F.; Nuessli, J. Structural Features of Starch-Flavor Complexation in Food Model Systems. *Trends Food Sci. Technol.* **2006**, *17* (5), 227–235. https://doi.org/10.1016/j.tifs.2005.11.007.

(345) Kong, L.; Ziegler, G. R. Molecular Encapsulation of Ascorbyl Palmitate in Preformed V-Type Starch and Amylose. *Carbohydr. Polym.* **2014**, *111*, 256–263. https://doi.org/10.1016/j.carbpol.2014.04.033.

(346) Zhang, L.; Cheng, H.; Zheng, C.; Dong, F.; Man, S.; Dai, Y.; Yu, P. Structural and Release Properties of Amylose Inclusion Complexes with Ibuprofen. *J. Drug Deliv. Sci. Technol.* **2016**, *31*, 101–107. https://doi.org/10.1016/j.jddst.2015.12.006.

(347) Cohen, R.; Orlova, Y.; Kovalev, M.; Ungar, Y.; Shimoni, E. Structural and Functional Properties of Amylose Complexes with Genistein. *J. Agric. Food Chem.* **2008**, *56* (11), 4212–4218. https://doi.org/10.1021/jf800255c.

(348) Oguefai, T.; Yamasato, H.; Limmatvapirat, S.; Yonemochi, E.; Yamamoto, K. Structural Change and Complexation of Strictly Linear Amloose Induced by Sealed-Heaing with Salicylyclic Acid. *J. Chem. Soc. - Faraday Trans.* **1998**, *94* (7), 923–927. https://doi.org/10.1039/a707848j.

(349) Ribeiro, A. C.; Rocha, Â.; Soares, R. M. D.; Fonseca, L. P.; da Silveira, N. P. Synthesis and Characterization of Acetylated Amylose and Development of

Inclusion Complexes with Rifampicin. *Carbohydr. Polym.* **2017**, *157*, 267–274. https://doi.org/10.1016/j.carbpol.2016.09.064.

(350) Carbinatto, F. M.; Ribeiro, T. S.; Colnago, L. A.; Evangelista, R. C.; Cury, B. S. F. Preparation and Characterization of Amylose Inclusion Complexes for Drug Delivery Applications. *J. Pharm. Sci.* **2016**, *105* (1), 231–241. https://doi.org/10.1002/jps.24702.

(351) Yang, L.; Zhang, B.; Yi, J.; Liang, J.; Liu, Y.; Zhang, L. M. Preparation, Characterization, and Properties of Amylose-Ibuprofen Inclusion Complexes. *Starch/Staerke* **2013**, *65* (7–8), 593–602. https://doi.org/10.1002/star.201200161.

(352) Yang, Y.; Zhengbiao, G. U.; Zhang, G. Delivery of Bioactive Conjugated Linoleic Acid with Self-Assembled Amylose-CLA Complex. *Journal of Agricultural and Food Chemistry*. 2009, pp 7125–7130. https://doi.org/10.1021/jf9016306.

(353) Lalush, I.; Bar, H.; Zakaria, I.; Eichler, S.; Shimoni, E. Utilization of Amylose-Lipid Complexes as Molecular Nanocapsules for Conjugated Linoleic Acid. *Biomacromolecules*. 2005, pp 121–130. https://doi.org/10.1021/bm049644f.

(354) Grommek, A.; Meier, B. H.; Ernst, M. Distance Information from Proton-Driven Spin Diffusion under MAS. *Chem. Phys. Lett.* **2006**, *427* (4–6), 404–409. https://doi.org/10.1016/j.cplett.2006.07.005.

(355) Veshtort, M.; Griffin, R. G. Proton-Driven Spin Diffusion in Rotating Solids via Reversible and Irreversible Quantum Dynamics. *J. Chem. Phys.* **2011**, *135* (13). https://doi.org/10.1063/1.3635374.

(356) Zhang, R.; Pandey, M. K.; Nishiyama, Y.; Ramamoorthy, A. A Novel High-Resolution and Sensitivity-Enhanced Three-Dimensional Solid-State Nmr Experiment under Ultrafast Magic Angle Spinning Conditions. *Sci. Rep.* **2015**, *5* (May), 1–9. https://doi.org/10.1038/srep11810.

(357) Alam, T. M.; Tischendorf, B. C.; Brow, R. K. High-Speed 1H MAS NMR Investigations of the Weathered Surface of a Phosphate Glass. *Solid State Nucl. Magn. Reson.* **2005**, *27* (1–2), 99–111. https://doi.org/10.1016/j.ssnmr.2004.08.006.

(358) Cherry, B.; Fujimoto, C.; Cornelius, C.; Alam, T. Investigation of Domain Size in Polymer Membranes Using Double-Quantum-Filtered Spin Diffusion Magic Angle Spinning NMR. *Macromolecules* **2005**, *38* (4), 1201–1206. https://doi.org/10.1021/ma047885.

(359) Federov, L. A.; Rebrov, A. I.; Hu, J. Z.; Shen, L. F. 13C NMR and Structural Study of Solid-State 1-Naphthol and 2-Naphthol Arylazo-Derivatives. *Chinese J. Chem.* **1991**, *9* (3), 2–7.

(360) Minekus, M.; Alminger, M.; Alvito, P.; Ballance, S.; Bohn, T.; Bourlieu, C.; Carrière, F.; Boutrou, R.; Corredig, M.; Dupont, D.; Dufour, C.; Egger, L.; Golding, M.; Karakaya, S.; Kirkhus, B.; Le Feunteun, S.; Lesmes, U.; MacIerzanka, A.; MacKie, A.; Marze, S.; McClements, D. J.; Ménard, O.; Recio, I.; Santos, C. N.; Singh, R. P.; Vegarud, G. E.; Wickham, M. S. J.; Weitschies, W.; Brodkorb, A. A Standardised Static in Vitro Digestion Method Suitable for Food-an International Consensus. *Food Funct.* **2014**, *5* (6), 1113–1124. https://doi.org/10.1039/c3fo60702j.

(361) Lefebvre, A. M.; Chen, I.; Desreumaux, P.; Najib, J.; Fruchart, J. C.; Geboes, K.; Briggs, M.; Heyman, R.; Auwerx, J. Activation of the Peroxisome Proliferator-Activated Receptor γ Promotes the Development of Colon Tumors in C57BL/6J-APC(Min)/+ Mice. *Nature Medicine*. 1998, pp 1053–1057. https://doi.org/10.1038/2036.

(362) Johnsson, H.; Gabrielsson, J. *Comprehensive Chemometrics: Chemical and Biochemical Data Analysis*; Brown, S. D., Ed.; Elsevier, 2009.

Appendix

Standard normal variate and zero-order normalisation of SEC data

Standard normal variate (SNV) and 0-order normalisation, commonly employed in comparative spectral and chromatographic data, consists of subtracting the mean of the entire data set from each data point, followed by dividing each data point by the data set's standard deviation. One of the main advantages of this data transformation strategy is its correction for both baseline shifts and global intensity variations. [362]

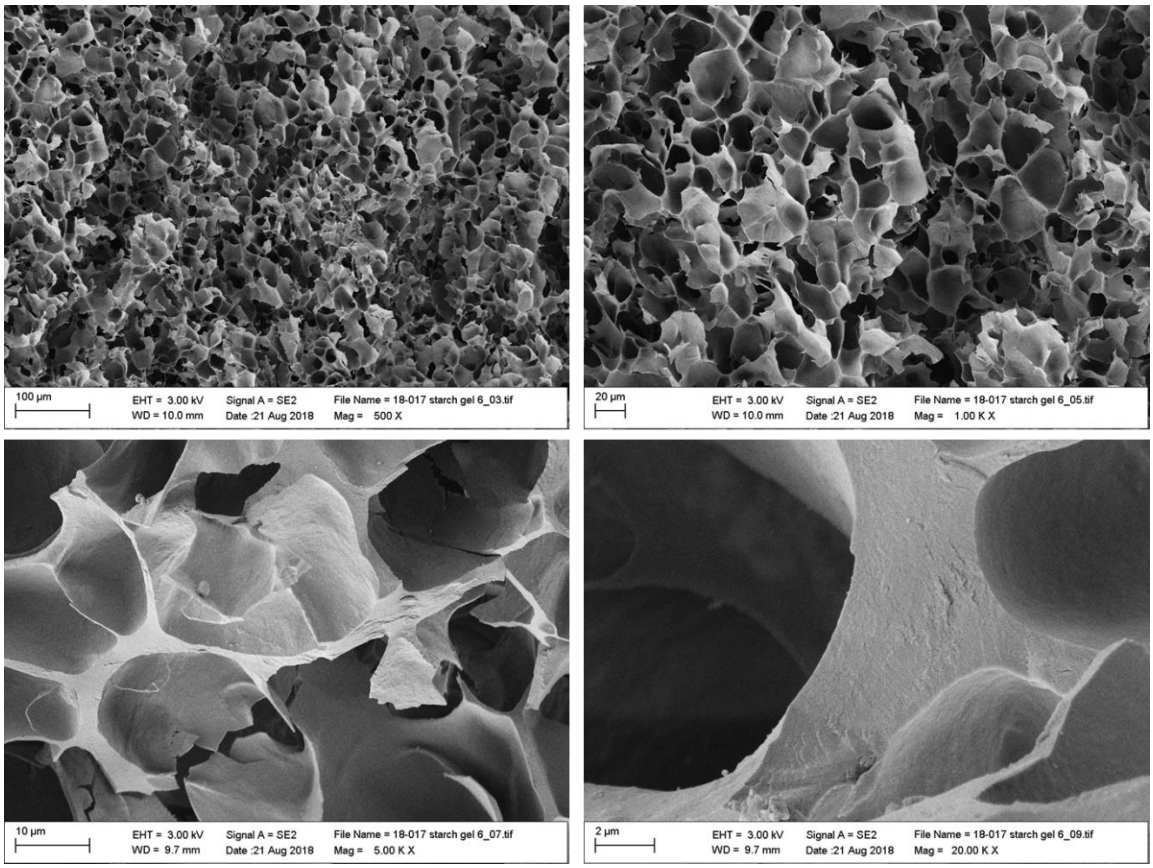

Figure S1: Environmental scanning electron microscopy images of normal maize (NM) starch hydrogels at 500x, 1000x, 5000x and 20000x magnification, acquired at a working distance of *ca*. 10 mm, and electron beam voltage of 3.0 kV.

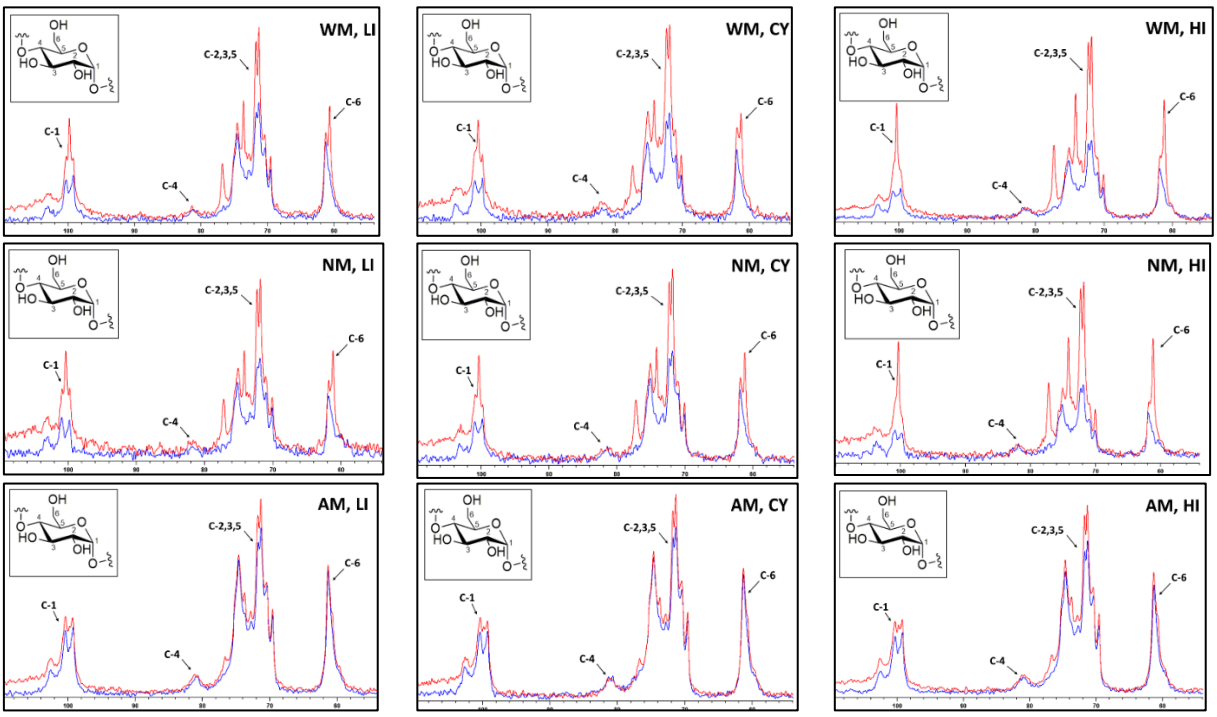

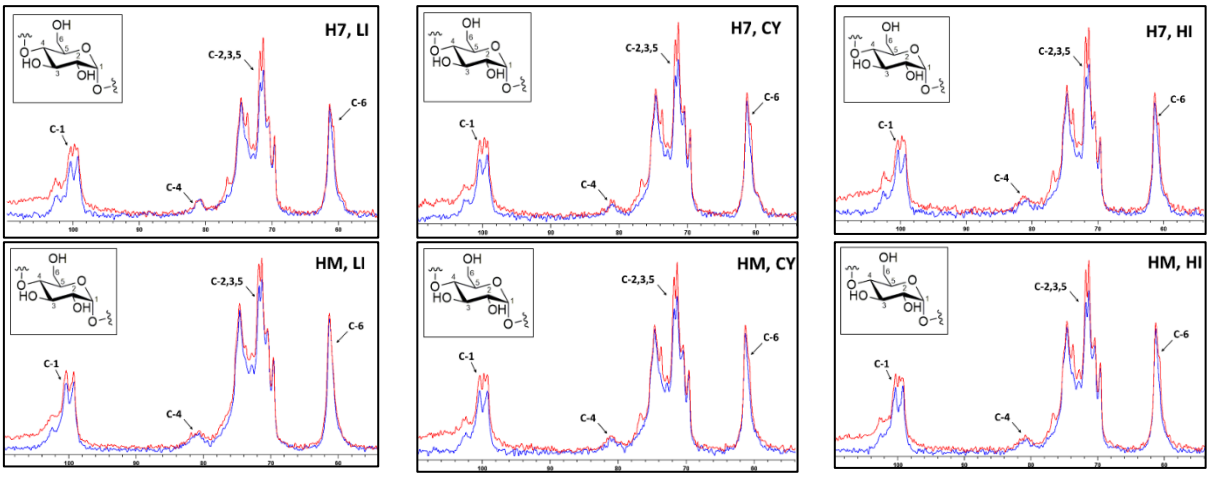

Figure S2: ^{1}H-^{13}C CP and CPSP/MAS NMR spectra (blue and red, respectively) of waxy maize (WM), normal maize (NM), amylomaize (AM), Hylon VII™ (H7) and Hi-Maize 260™ (HM) hydrogels, prepared in three different conditions – low isothermal (LI), thermocycled (CY) and high isothermal (HI) storage. Inlays showing the glucose monomer with ^{13}C atomic numbering.

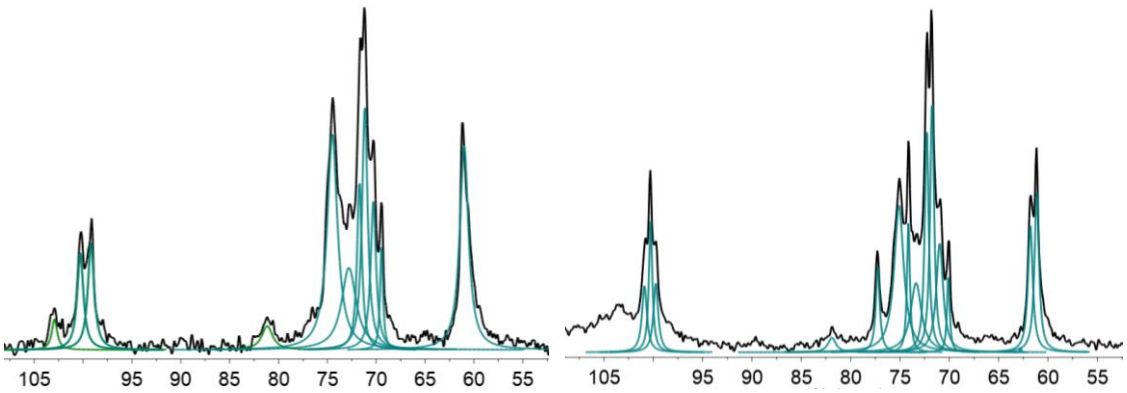

Figure S3: Spectral deconvolution of the ^{1}H-^{13}C CP (left) and CPSP/MAS NMR spectra (left and right, respectively) of waxy maize (WM) hydrogels, using MNova global spectral deconvolution algorithm.

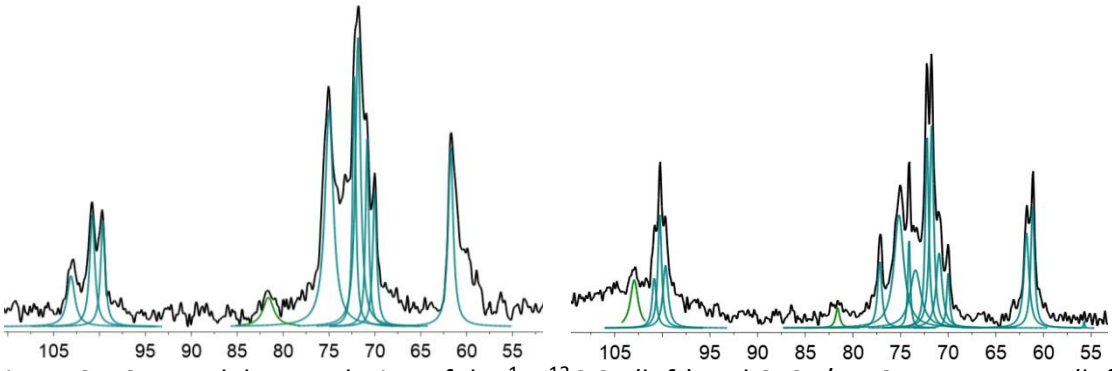

Figure S4: Spectral deconvolution of the ^{1}H-^{13}C CP (left) and CPSP/MAS NMR spectra (left and right, respectively) of normal maize (NM) hydrogels, using MNova global spectral deconvolution algorithm.

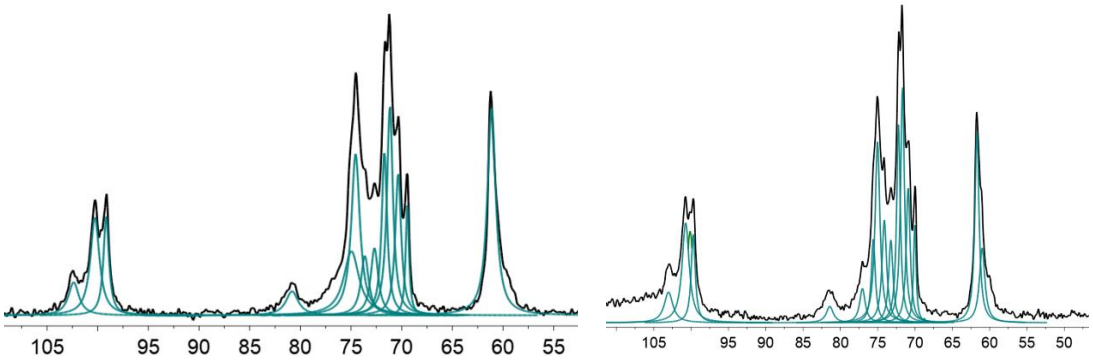

Figure S5: Spectral deconvolution of the ^{1}H-^{13}C CP (left) and CPSP/MAS NMR spectra (left and right, respectively) of amylomaize (AM) hydrogels, using MNova global spectral deconvolution algorithm.

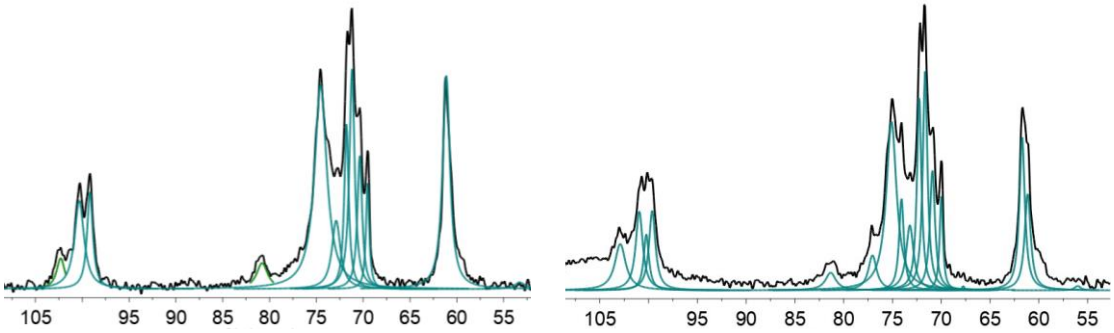

Figure S6: Spectral deconvolution of the ^{1}H-^{13}C CP (left) and CPSP/MAS NMR spectra (left and right, respectively) of Hylon VII® (H7) starch hydrogels, using MNova global spectral deconvolution algorithm.

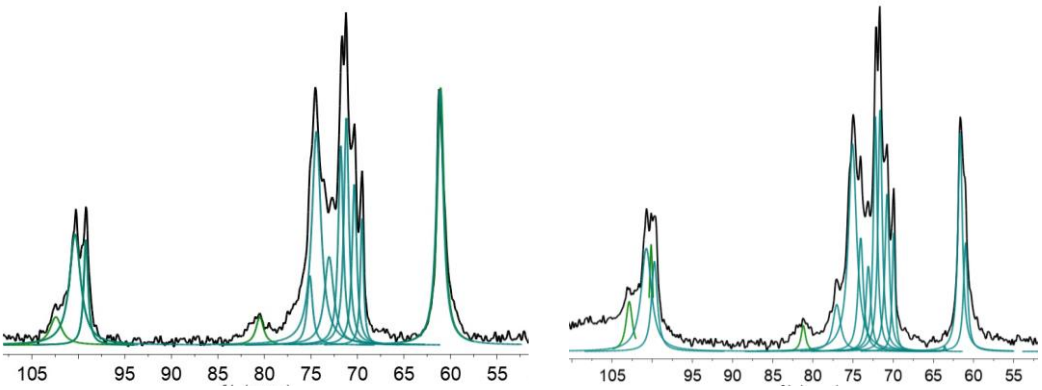

Figure S7: Spectral deconvolution of the ^{1}H-^{13}C CP (left) and CPSP/MAS NMR spectra (left and right, respectively) of Hi-maize 260® (HM) hydrogels, using MNova global spectral deconvolution algorithm.

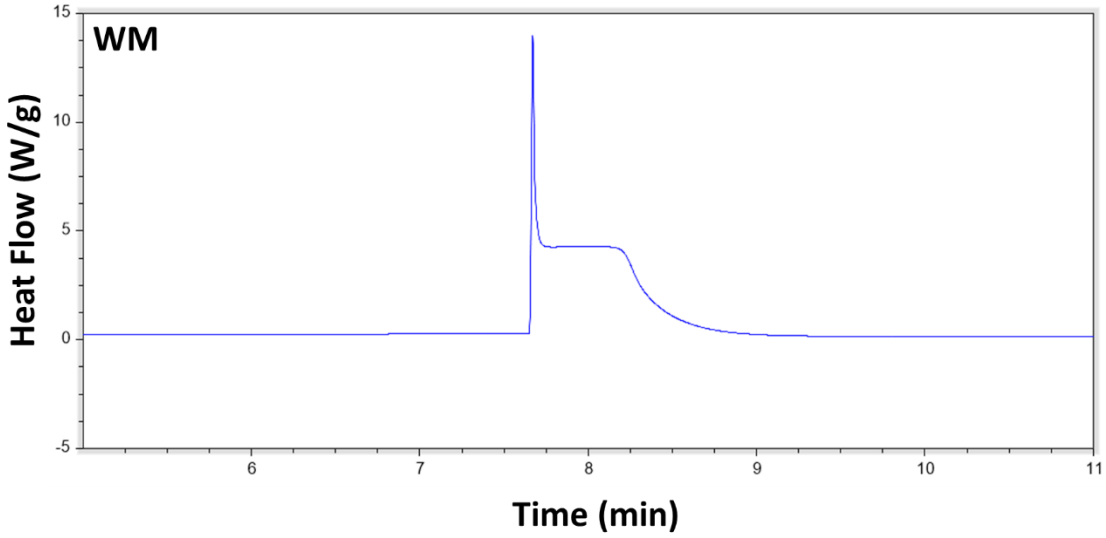

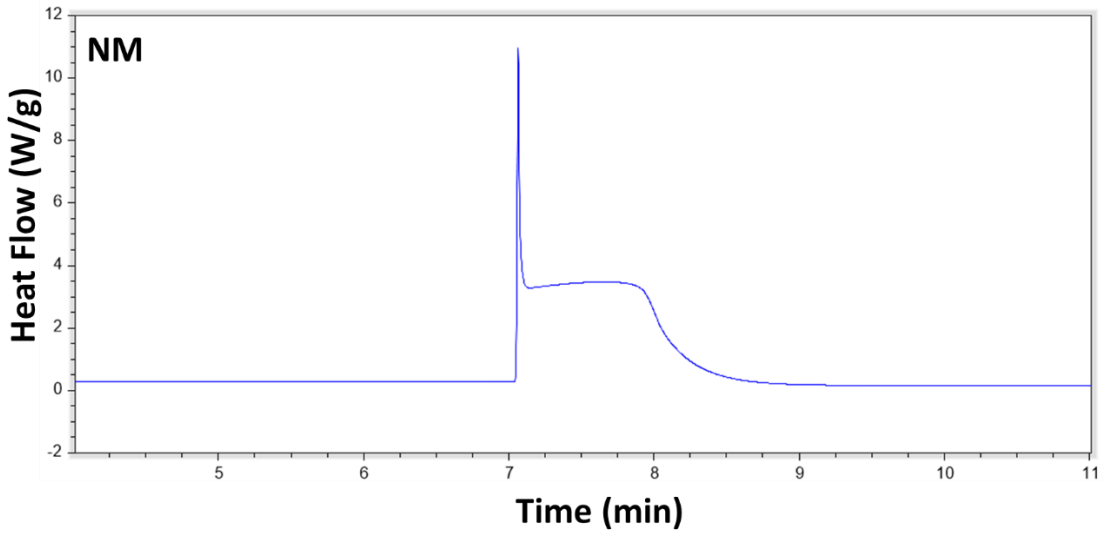

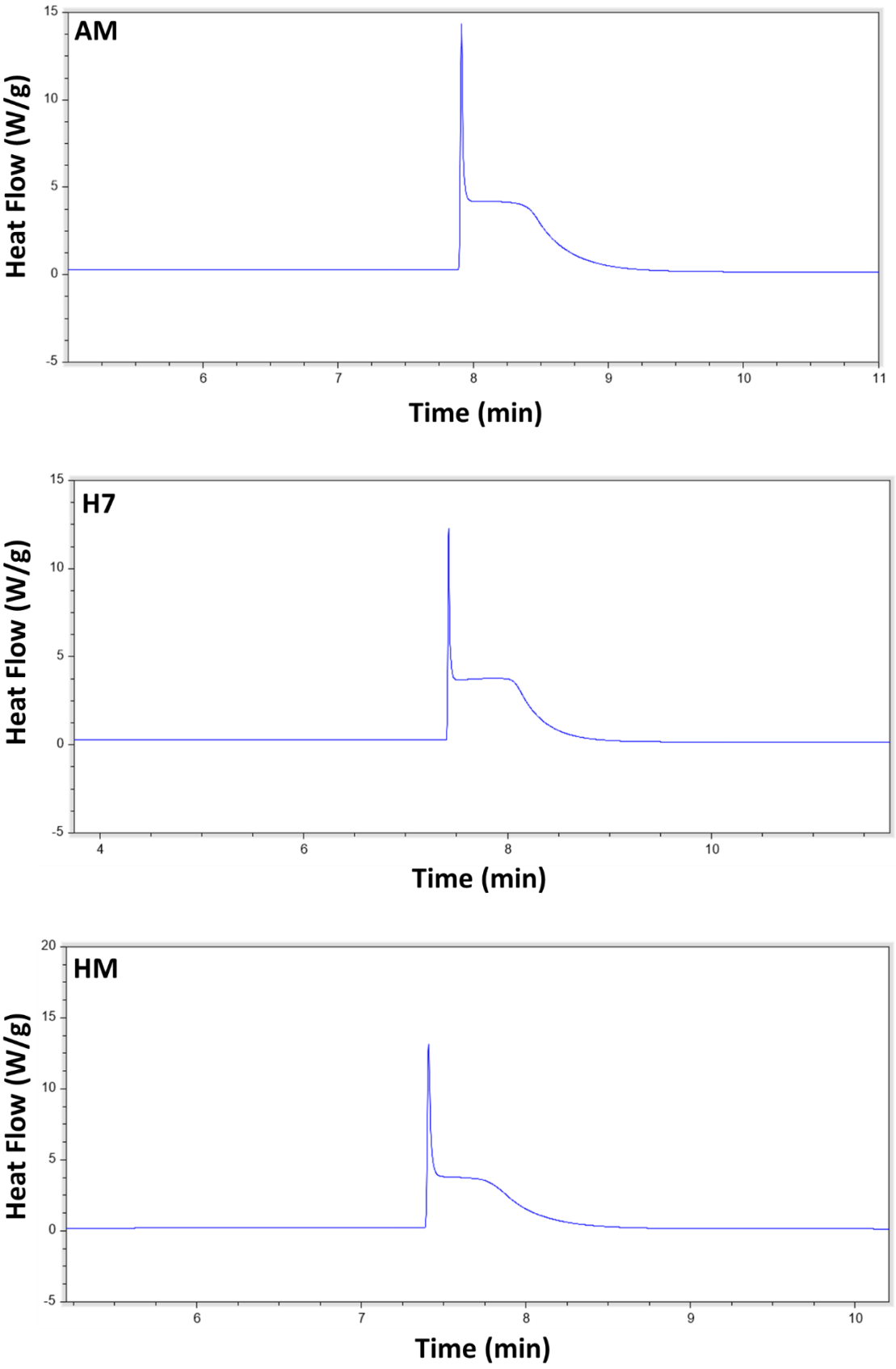

Figure S8: Sub-ambient DSC thermograms of WM, NM, AM, H7 and HM starch hydrogels, showing the endothermic freezing event of the freezable bound H_2O population within all five starch gels. Data presented as heat flow *vs.* time.

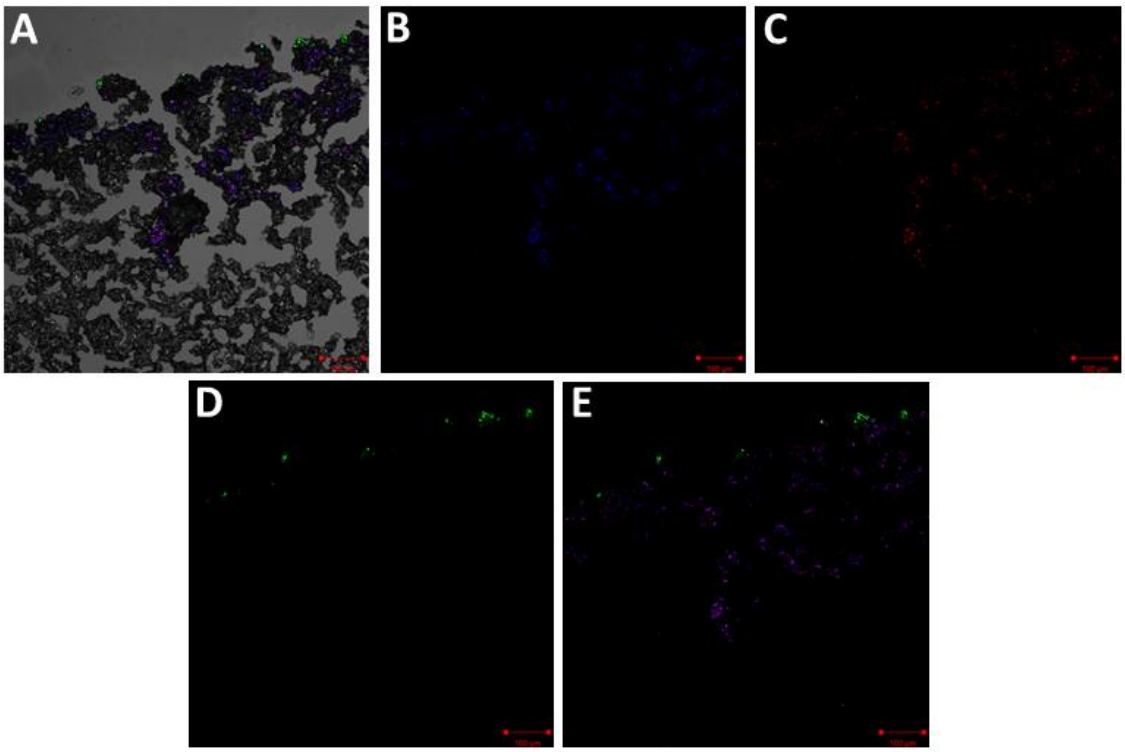

Figure S9: Peripheral image of normal maize starch hydrogel after 24 hours of in vitro fermentation, visualised by LSCM at 10x magnification, with the hydrogel morphology and all three bacterial probes (A), *R.bromii* (blue, B), *Bacteroides* (red, C) and *Bifidobacterium* (green, D), and all three (E).

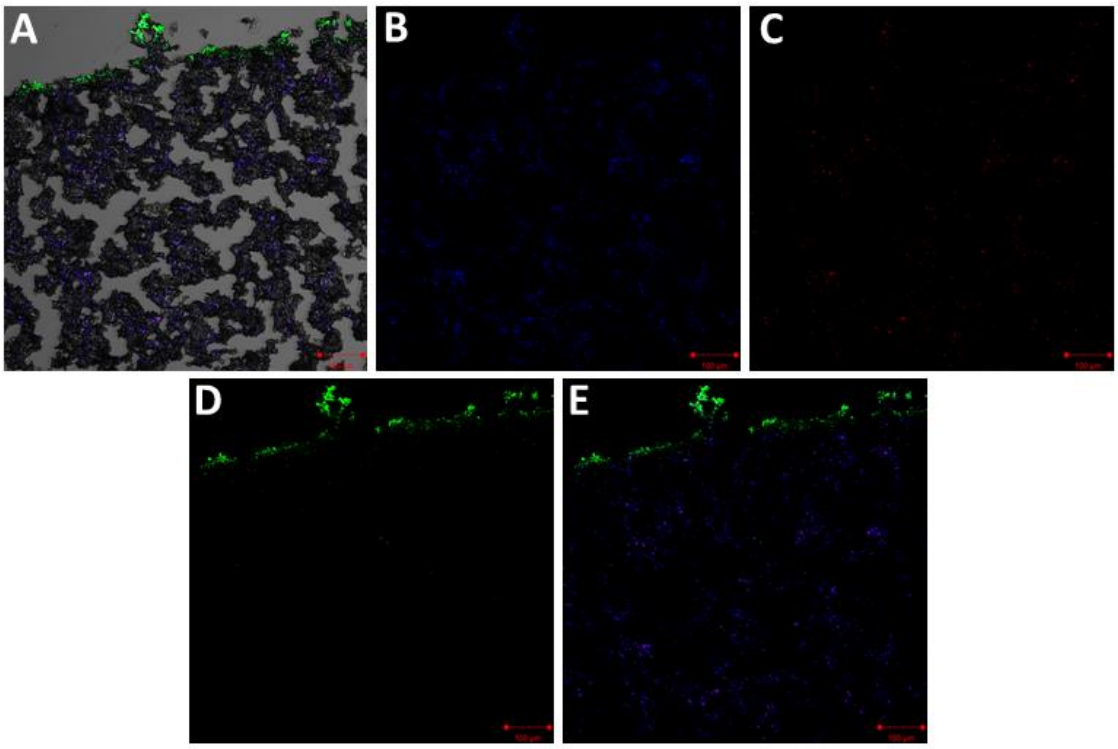

Figure S10: Peripheral image of normal maize starch hydrogel after 72 hours of in vitro fermentation, visualised by LSCM at 10x magnification, with the hydrogel morphology and all three bacterial probes (A), *R.bromii* (blue, B), *Bacteroides* (red, C) and *Bifidobacterium* (green, D), and all three (E).

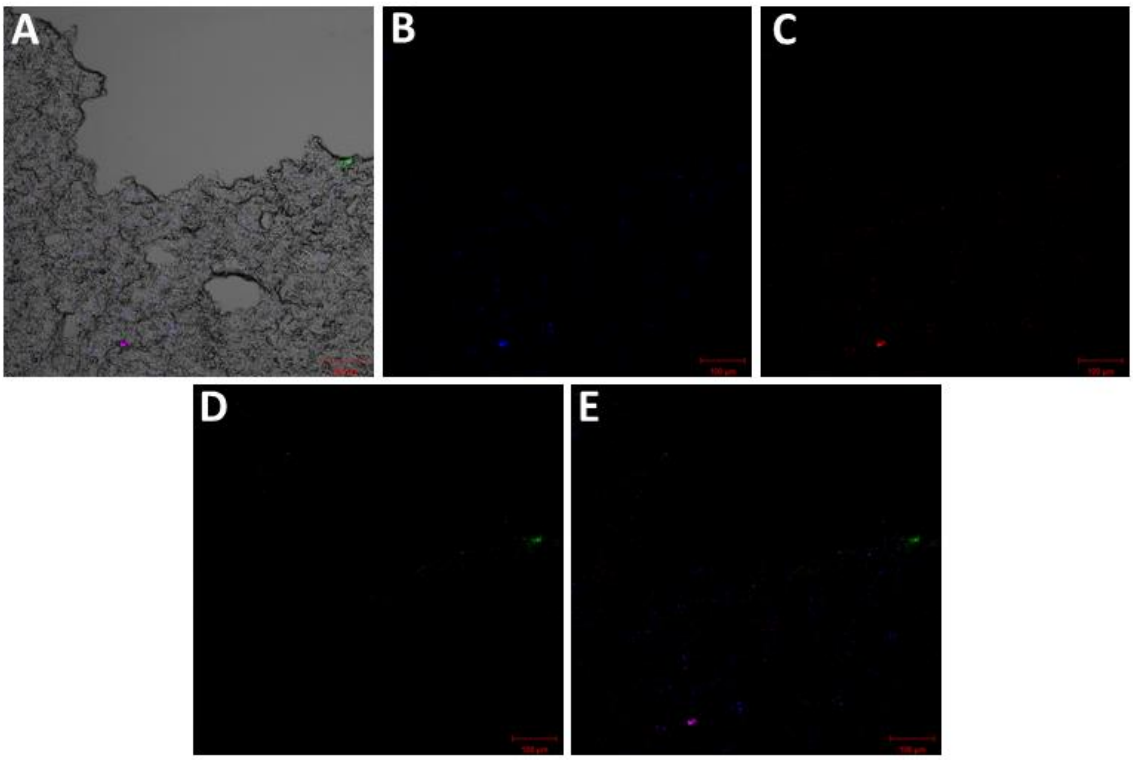

Figure S11: Peripheral image of Hylon VII® starch hydrogel after 24 hours of in vitro fermentation, visualised by LSCM at 10x magnification, with the hydrogel morphology and all three bacterial probes (A), *R.bromii* (blue, B), *Bacteroides* (red, C) and *Bifidobacterium* (green, D), and all three (E).

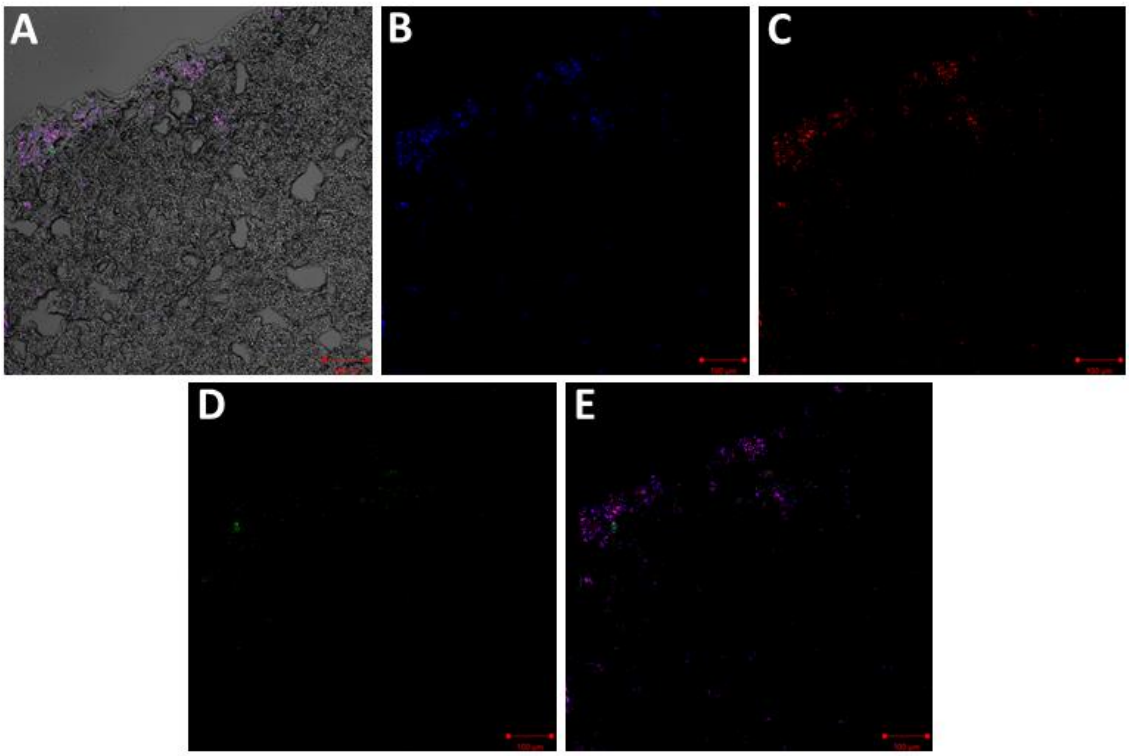

Figure S12: Peripheral image of Hylon VII® starch hydrogel after 72 hours of in vitro fermentation, visualised by LSCM at 10x magnification, with the hydrogel morphology and all three bacterial probes (A), *R.bromii* (blue, B), *Bacteroides* (red, C) and *Bifidobacterium* (green, D), and all three (E).

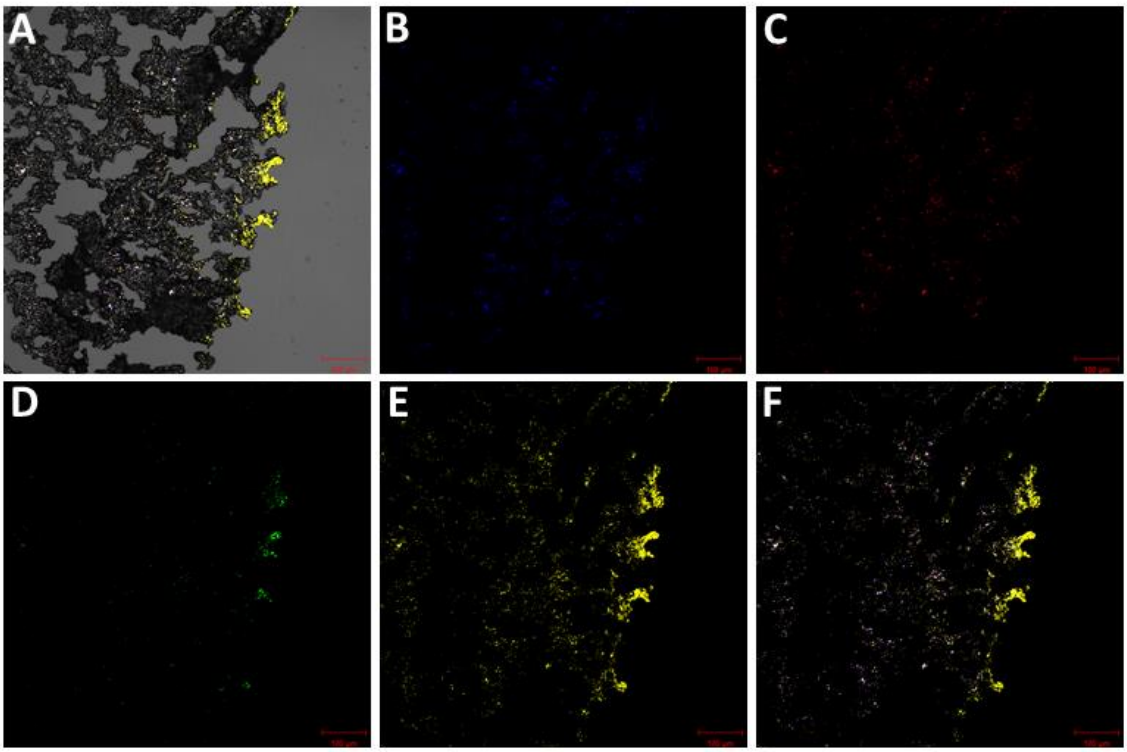

Figure S13: Peripheral image of normal maize starch hydrogel after 24 hours of in vitro fermentation, visualised by LSCM at 10x magnification, with the hydrogel morphology and all bacterial probes (A), *R.bromii* (blue, B), *Bacteroides* (red, C) and *Bifidobacterium* (green, D), non-specific probes (E), all bacteria (F).

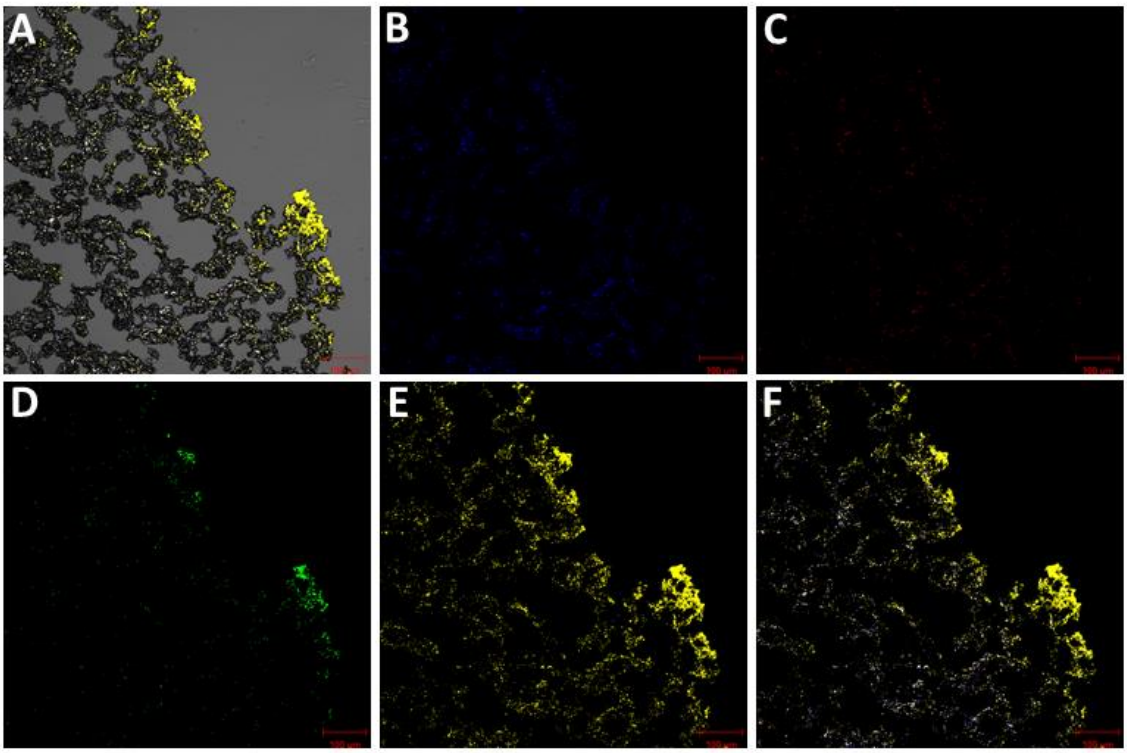

Figure S14: Peripheral image of normal maize starch hydrogel after 72 hours of in vitro fermentation, visualised by LSCM at 10x magnification, with the hydrogel morphology and all three bacterial probes (A*), R.bromii* (blue, B), *Bacteroides* (red, C) and *Bifidobacterium* (green, D), non-specific probes (E), all bacteria (F).

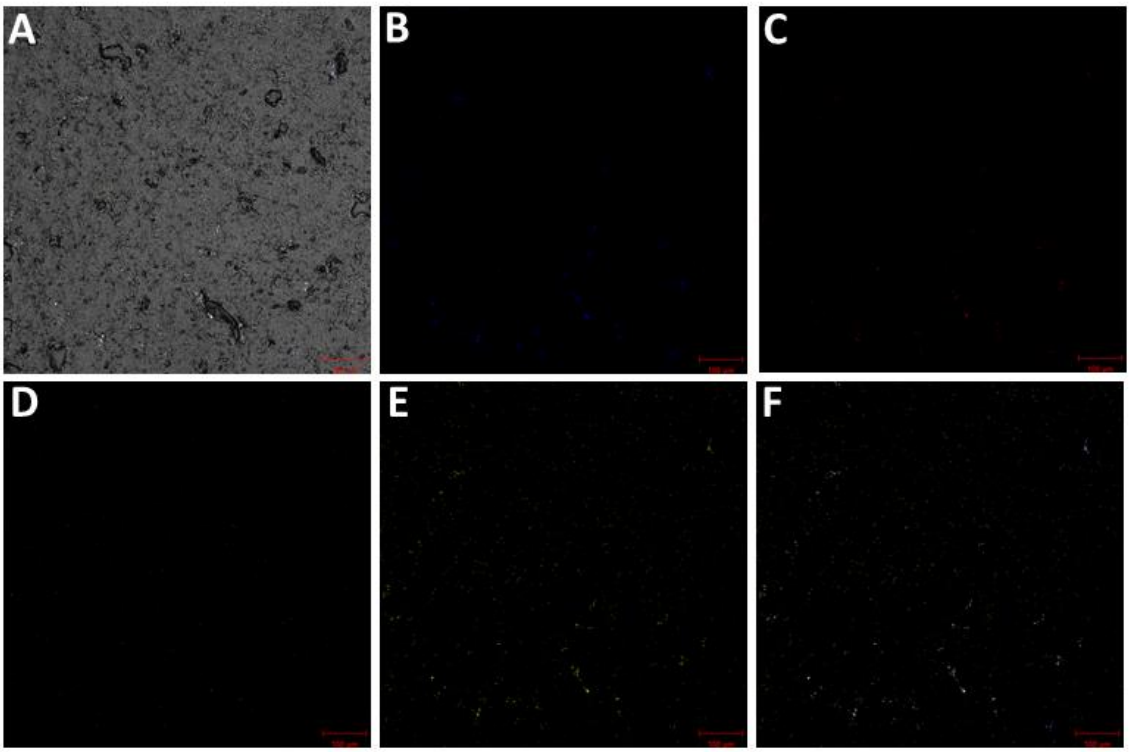

Figure S15: Surface image of Hylon VII® starch hydrogel after 24 hours of in vitro fermentation, visualised by LSCM at 10x magnification, with the hydrogel morphology and all three bacterial probes (A), *R.bromii* (blue, B), *Bacteroides* (red, C) and *Bifidobacterium* (green, D), non-specific probes (E), all bacteria (F).

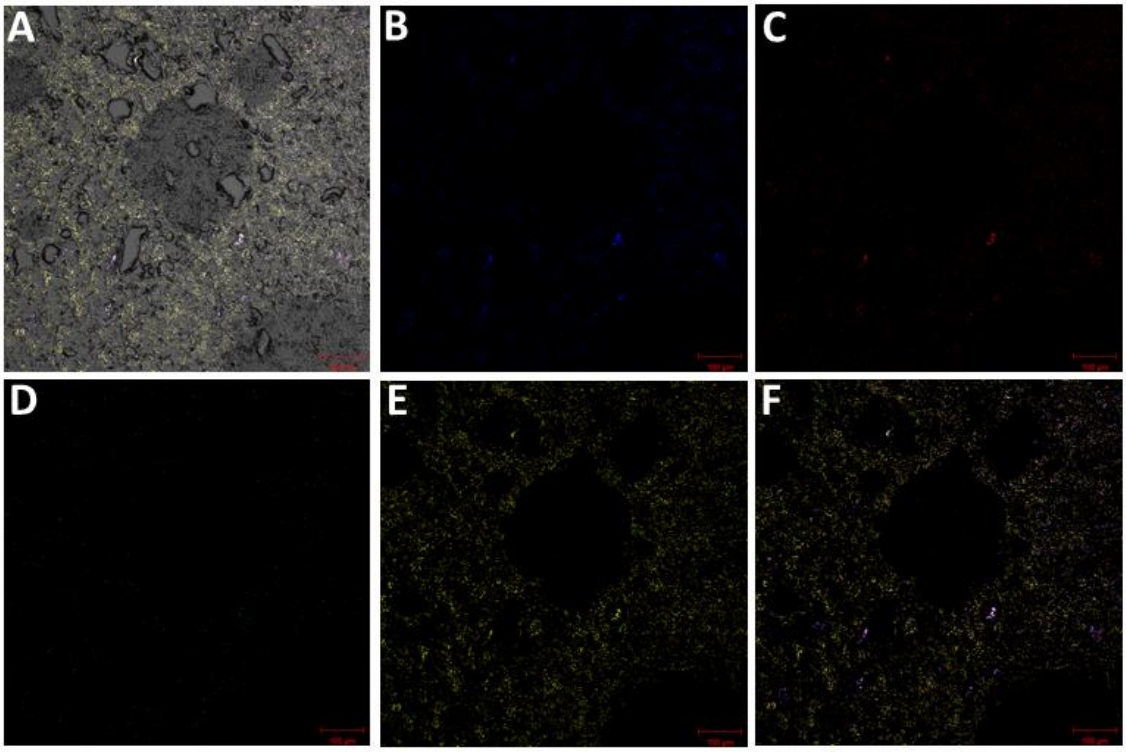

Figure S16: Surface image of Hylon VII® starch hydrogel after 72 hours of in vitro fermentation, visualised by LSCM at 10x magnification, with the hydrogel morphology and all three bacterial probes (A), *R.bromii* (blue, B), *Bacteroides* (red, C) and *Bifidobacterium* (green, D), non-specific probes (E), all bacteria (F).